Evolution of Alpha Phase Alumina in Agglomerates upon Addition to Cryolitic Melts

by

N. Peter Østbø

Thesis submitted in partial fulfilment of the
requirements for the degree
Doktoringeniør

Norwegian University of Science and Technology
Department of Materials Technology and Electrochemistry

May 2002

Adventure with Alumina

Perkin Medal Lecture 1946

Francis C. Frary, Director of Alcoa Research Laboratory

"Aluminum oxide and its hydrates present a variety of amazing contrasts. From the hardness of sapphire to a softness similar to that of talc, from an apparent density of over 200 pounds to one of about 5 pounds per cubic foot, from high insolubility and inertness to ready solubility in acids or alkalis and marked activity, the properties can be varied over wide limits. Some forms flow and filter like sand; others are viscous, thick, unfilterable, or even thixotropic. Crystals may be of any size down to a fraction of a micron in diameter, with various allotropic forms, and there are also amorphous forms. Some varieties have a high adsorptive power, others none at all. Some are catalytically active, others inactive. But they are all converted into α - alumina (corundum) if heated hot enough and long enough."

Cited in "Industrial Alumina Chemicals",
by Chanakya Misra [118]

Summary

Rapid dissolution of alumina upon addition to the cryolitic melt is crucial for the modern Hall-Héroult process for aluminium production. The formation of slow - dissolving alumina agglomerates may be detrimental, and irregular dissolution kinetics may cause the loss of process control. So-called anode effects may subsequently ignite, which are a major source of green-house gases from the primary aluminium industry.

A literature review and the study of the theory of sintering provides the background for discussing the present work. The most probable mass transport mechanism in the transition alumina-fluoride-moisture system studied here is surface diffusion. Surface diffusion is a non-densifying mass transport mechanism that will result in coarsening (alumina grain growth) but only weak interparticle bonding since no macroscopic shrinkage is involved. Rapid mass transport is known to result when there is a simultaneous phase transformation, and this is the case when transition alumina transforms to α-alumina, catalyzed by the presence of fluorides.

The main experimental techniques used in the present work were powder X-ray diffraction (XRD) and Scanning Electron Microscopy (SEM). Supporting techniques used have been specific area determination by the BET method and simple thermo-gravimetric techniques. An optical furnace was designed and built in order to study the dissolution of tablet alumina agglomerates.

A preliminary agglomeration study of preformed cylindrical alumina samples served to map some of the most important mechanisms involved when alumina powder interacts with alumina-saturated cryolitic melt. The conditions at the alumina-melt interface were studied, but it is concluded that the experimental method could not provide the necessary parameter control in order to study the agglomeration mechanism in further detail.

The tablet agglomerate study is the major experimental contribution of the present work. The experimental method provided good control of the sample chemistry and well defined temperature and time variables. It is concluded that liquid cryolitic melt ($NaAlF_4$) provides an effective mass transport route for the transformation assisted growth of α-alumina platelets. The platelets that initially form will provide the limited mechanical strength necessary for agglomerate formation and their persistence in a cryolitic melt. Alumina agglomeration may therefore take place with only partial, initial phase transformation. It is concluded that differences in the agglomeration

behavior of various qualities of alumina may be the rate determining property for alumina dissolution kinetics in cryolitic melts. Differences in the agglomeration behavior may be due to a number of physical properties of alumina. It is argued here that the fundamental, but difficult to measure, alumina nano-structure may be most important.

The alumina nano-structure is correlated to secondary alumina properties such as the α-alumina content, specific surface area (BET) and moisture content (MOI, LOI). In this study an X-ray diffraction line profile analysis using the Warren-Averbach method shows that there is a significant difference in the nano-structure of the two smelter grade alumina qualities under study. This may explain the different agglomeration behavior that is observed.

An optical study of tablet agglomerate dissolution in cryolitic melt proved to be largely unsuccessful due to severe corrosion of the quartz crucibles used. However, a proposed mechanism for the tendency for disintegration of alumina agglomerates, thus dissolving as "snow-flakes" is supported.

The temperature response time in the tablet alumina samples was studied in order to determine the experimental limit of the shortest time period possible in the experiments. The exothermal $\gamma \rightarrow \alpha$ transformation is observed for secondary alumina samples containing adsorbed fluorides. An interesting effect of the carbon content in secondary alumina is also shown.

The moisture content of smelter grade alumina is a function of the alumina quality, in particular the technology used for the calcination of the aluminium trihydrate precursor. In the current study the moisture content is shown to be a dynamic function of the ambient temperature and relative humidity. The moisture content is an important variable for the study of alumina agglomeration, and for the fluoride emission from the Hall-Héroult process. The kinetics of moisture desorption and absorption for various alumina qualities is studied. The desorption kinetics is concluded to be significantly different, while it is also shown that practical absorption kinetics is a function of the sample size and available surface area.

Preface

The present work was carried out at the Department of Materials Science and Electrochemistry (IME) at the Norwegian University of Science and Technology (NTNU), Trondheim, from January 1998 to October 2001. In addition to the compulsory courses in advanced materials technology and science, the work also included short courses on neutron spectroscopy at Kjeller, March 1998, and in electrochemistry in Southampton during the summer of 1998.

Initially, a study of the mechanism of deformations of anodes during electrolysis was a part of the doctoral work, but that subject was discontinued mid-term. The work included a short research collaboration with Dr. Peter Witt at CSIRO in Melbourne, Australia over the course of a few weeks in March 1999, involving finite element modeling. The collaboration was initiated by Prof. Jomar Thonstad, my supervisor, who spent his sabbatical year there.

We found that some ceramic theory became a necessary part of the thesis in progress, and I became a student member of the American Ceramic Society (ACerS) at the end of 1999. Support and encouragement was found in Prof. Tor Grande and the "ceramics group" at NTNU, and a poster was presented during the ACerS meeting in St. Louis in May, 2000. Parts of the work described in this thesis was also presented at the conference on Molten Salts in Denmark, August 2000.

The moisture content of smelter grade alumina became an important subject during the course of this work, and the experimental work reported in the final chapter of this thesis is the result of a collaboration with Senior Researcher Kjell Hamberg and his colleagues at the Hydro Research Center in Porsgrunn (HRE), who were also very hospitable during my stay there in the spring of 2001. Based on our results, work continues in Hydro Aluminium and at the Alunorte alumina refinery in Brazil to further explore the effect of alumina structure and moisture content.

In addition to the moisture study in chapter 8, supportive experimental work is also reported in chapter 7 on the thermal response in the tablet agglomerate samples studied in chapter 5. An introduction to the major experimental techniques used is given in Chapter 3, while chapter 4 serves as a partial reproduction of earlier results and forms the experimental basis for the research angle covered in the following chapters.

An extensive literature review, chapter 2, was necessary in order to include discussions of relevant work in the vast research field of ceramics. The reader will find that the literature review lends a great deal to the current study of smelter grade alumina agglomeration. Together with the tablet agglomerate study in chapter 5, chapter 2, - and the accompanying bibliography - takes up most of the space in this thesis, partly reflecting that these are perhaps the most important contributions of this work. A study of alumina agglomeration during feeding could not be complete without a study of agglomerate dissolution, and, though mostly unsuccessful, a contribution to this field is reported in chapter 6.

N. Peter Østbø

Acknowledgements

The Research Council of Norway (NFR) and the aluminium industry in Norway cosponsored the work as a part of the PROSMAT research program. In particular, Bjørn P. Moxnes at Hydro Aluminium provided funding and support for some of the basic alumina analysis work in Årdal. The Dept. of Materials Science and Electrochemistry at NTNU is also acknowledged for financial support towards the critical finale of this project. My participation at the ACerS meeting and conference in May, 2000, was sponsored by the Faculty of Chemistry and Biology.

Professor emeritus Jomar Thonstad[1] has been my supervisor during these years, and I am grateful for his support, advice and criticism. It was a great inspiration to be guided by him into the field of aluminium electrolysis, though also frustrating not to possess the same insight - especially when the project skewed off the traditional course. I also want to thank dr. ing. Sverre Rolseth[2], who has been my co-supervisor for his encouragement and inspiration, not least when experiments failed. Dr. ing. Ove Kobbeltvedt[3] was also a co-supervisor, startet me off on this work and kept interest from the industrial viewpoint.

Professor Tor Grande at the Dept. of Chemistry deserves a special thanks for his interest in my work and progress, and for his helpful guidance on ceramics theory. The platform of this thesis rests partly on his shoulders.

Finally, Martha Bjerknes[1] deserves a special thanks for all her friendly support during these years- and keeping not just myself, but all things great and small together at IME. Of course, many thanks go to my friends and colleagues at IME and SINTEF, especially Sarbjyot, Odd-Arne, Trond Eirik and Elke, for memorable years-and some friendships that will surely outlast the memory of lesser details - such as the many rainy days and working nights “på Gløshaugen” in Trondheim.

[1]Department of Materials Science and Electrochemistry
[2]SINTEF, Materials Technology
[3]Hydro Aluminium, Karmøy

List of Symbols and Abbreviations

Symbol	Unit	Explanation
α-Al_2O_3		Alpha alumina phase (aluminium oxide), corundum
γ-Al_2O_3		Specific and generic transition alumina phase
AI		Attrition Index (SGA grain strength)
C, C^*, C_∞	wt %	Alumina concentration in bath, local, bulk
C_p	$Jmol^{-1}K^{-1}$	Molar heat capacity at constant pressure
CE	%	Current efficiency
CR		Cryolite Ratio of electrolyte, molar ratio NaF:AlF_3
D	cm^2/s	Diffusion coefficient
E,E°	V	Potential, standard potential
E_a	kJ/mol	Activation Energy
h	$Wm^{-2}K^{-1}$	Heat transfer coefficient
k	$kgm^{-2}s^{-1}$	Mass transfer coefficient
ν,ν_∞	m/s	Relative fluid velocity, in bulk
ΔH_{diss}	kJ/mol	Enthalpy of dissolution (alumina in bath)
ΔH_{fus}	kJ/mol	Enthalpy of fusion
ΔG°	kJ/mol	Change in standard Gibbs energy
T	K, °C	Temperature
t	s, min, h	Time
ρ	g/cm^3	Density
LOI	%	Loss on Ignition, SGA loss of mass 300<T<1000,1100 °C
MOI	%	Moisture on Impact, SGA loss of mass, RT<T<300 °C
RH	%	Relative Humidity
RT	°C	Room Temperature (∼20 °C)
SGA, PSD		Smelter Grade Alumina, Particle Size Distribution
SSA	m^2/g	Specific Surface Area
BET		Method of Brunauer, Emmet and Teller for determining SSA
DTA		Differential Thermal Analysis (characterization technique)
SEM		Scanning Electron Microscopy (char. techn.)
XRD		Powder X-ray Diffraction (char. techn.)
XRF		Powder X-ray Fluorescence Spectroscopy (char. techn.)

Contents

Chapter 1

Introduction

1.1 Aluminium Production

A basic description of aluminium and it's history may be found in Encyclopædia Britannica [1]. Aluminium (Al) is the most abundent metal element in the earth's crust, but has a very strong affinity to oxygen and is mainly found in the many alumino-silicate minerals, chemically bonded to silicon and oxygen. The atomic number is 13, and the atomic weight is 26.98. Aluminium metal crystallizes in the face centered cubic structure and melts at 660 °C. Originally aluminium was called aluminum by Sir Humphry Davy in 1809 and, indeed, the metal name is aluminum in American English. H.C. Ørstedt, the famous Danish scientist, was the first to isolate metallic aluminium, in 1825.

Aluminium remained an exotic and extremely expensive metal for many years. However, in 1886, independently (!), the American C.M. Hall and the Frenchman P.L.T. Héroult invented a process suitable for large scale commercial production at the time of increasing availability of hydro-electric powerplants. The process involves the use of electrolysis of pure alumina (aluminium oxide) dissolved in molten cryolite, a mineral found naturally on Greenland, which also was the electrolyte, and the use of carbon as electrodes and cell-lining material. In 1888 the Bayer process for the production of refined alumina was developed for the now established Hall-Héroult process. Well into the second century of use, the Hall-Héroult process and the Bayer process have been continuously improved and will probably not

be replaced in the foreseeable future[1].

Aluminium is an attractive metal for use as a sustainable material, and there is an increasing use of recycled, (so-called secondary) aluminium. It may be speculated that the demand for primary aluminium will almost cease some time in the future.

In 2000 the world production of primary aluminium surpassed 24 million tons, and Norway is a major producer [29]. Aluminium has been the most widely used non-ferrous metal since the 1960's, finding many technological applications due to its qualities of light weight, good mechanical properties, high thermal and electrical conductivity and being naturally protected by a tough layer of aluminium oxide which forms upon contact in air. Aluminium alloys are now replacing major structural parts in automobiles world-wide, thus further increasing the demand for aluminium.

1.2 The Hall-Héroult Process

A schematic cut-through view of a typical modern point-fed prebake aluminium electrolysis cell is shown in figure 1.1. The basic principle of the Hall-Héroult process remain the same today as in the beginning, but technological improvements and increasing scientific knowledge have resulted in a much more efficient and environmentally clean industry.

1.2.1 Process Fundamentals

The fundamentals of the process are descibed in the literature [49, 176, 92]. Alumina is dissolved in the Na_3AlF_6-AlF_3-CaF_2-Al_2O_3 electrolyte (often called bath) as ionic complexes such as $Al_2OF_6^{2-}$ and $Al_2O_2F_4^{2-}$ [91, 49, 176]. The electrolyte is a molten salt that mainly consists of positive Na^+ and negative $AlF_x^{(3-x)-}$, (for x = 4, 5 and 6), ions - though the ionic structure is still being debated [94, 2, 176]. The electrolyte composition is variable (and may contain LiF and MgF_2) but most smelters use about 5 wt % CaF_2, 3 wt % Al_2O_3 and about 12 wt % excess AlF_3. The molar ratio of NaF:AlF_3 (being 3:1 in cryolite) is termed the cryolite ratio (CR). The electrolyte acidity is determined by the concentration of AlF_3 with respect to cryolite,

[1] Unless efforts to produce an inert anode are successful, in which case considerable changes will be made.

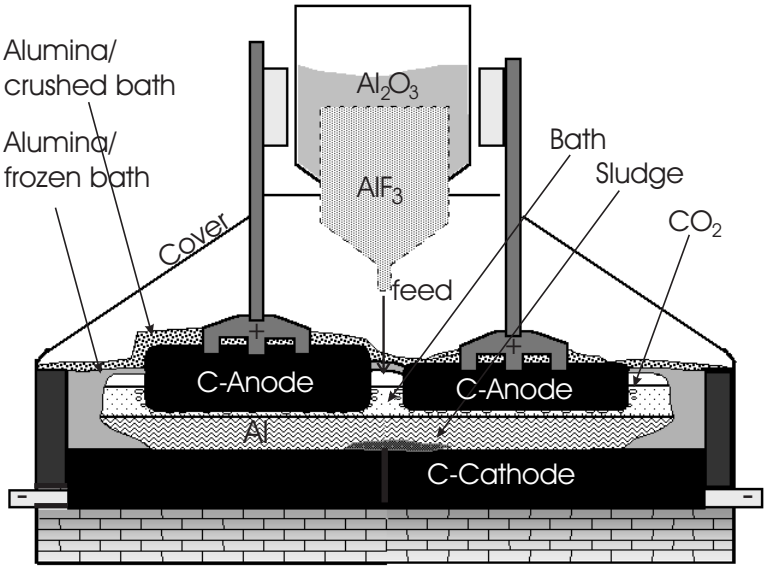

Figure 1.1: *Schematic cut-through view of a modern point-fed prebake aluminium electrolysis cell.*

and a 12 wt % excess equates to CR = 2.17, (which is quite acidic) when corrected for the CaF_2 and Al_2O_3 content.

Aluminium acts as the cathode while the anode carbon reacts with the oxygen-containing alumina, - thus the anodes are being consumed in the process. The carbon anodes have to be replaced at regular intervals of about 1 anode per day (out of a typical total of 20 anodes per cell). The best available (modern) technology requires about 13.0 kWh of electric energy per kg of aluminium produced, with a current efficiency in excess of 95 %. The cell reaction is usually written as;

$$Al_2O_{3(diss.)} + \frac{3}{2}C_{(s)} \rightarrow 2Al_{(liq)} + \frac{3}{2}CO_{2(g)}$$

The total cell voltage of a modern Hall-Héroult cell is about 4.2 V, while the typical operating temperature is 960 °C. A modern production line (pot-line) for aluminium production consists of 180-260 electrolysis cells (also called pots), connected in series, and represents a considerable capital investment. By increasing the size of each cell and the line current (modern Hydro Aluminium technology uses 250 kA) the production cost is decreased. However, larger, maximum efficiency cells are more difficult to control and

operate steadily- so that further research and developement is needed. The alumina feeding strategy, dissolution and distribution is very critical.

1.2.2 Three Major Roles of Alumina

Apart from being the raw material, in which 1.89 kg is consumed for every kg of aluminium produced, alumina also plays an important role in the heat balance of the cell. Alumina, often mixed with crushed bath,- is used as an insulating cover on top of the top-crust, which also consists of alumina and bath. The insulating material also ensures that excessive air oxidation of the carbon anodes is avoided.

Furthermore, alumina is used for environmental control in the dry scrubbing process, in which it picks up harmful flouride emissions (HF and $NaAlF_4$), [176]. Fluorides are subsequently recycled, since it is normally the secondary (reacted, dry scrubber) alumina that is used to feed the electrolysis cells. Along with the fluorides, however, the secondary alumina also recycles less desirable volatile impurities and excess atmospheric moisture [49, 176].

1.3 The Bayer Process

Smelter grade alumina (SGA) used in the production of aluminium is produced by the Bayer process. An excellent review is given by Hudson [64]. The process depends on the selective dissolution of aluminous hydrates present in bauxite, which contains aluminous hydrate ore, equivalent to 45-60 wt % Al_2O_3. In addition to alumina, the ore contains mainly Si, Fe and Ti oxides and some organic material, which be filtered out during the "Bayer cycle", shown in figure 1.2. The residue is dumped and dried as so-called "red mud" and should be recovered by top-soil and later replanted where the bauxite ore was removed.

Crushed ($\sim$ 1 mm) and washed bauxite is dissolved in a strong caustic solution (140-250 g Na_20/l) under pressure and at a temperture of about 100-250 °C, depending on the bauxite quality and Na_2O/Al_2O_3 concentration, [64]. Dissolved SiO_2 may be removed from the solution by precipitation and washing, in reaction with added CaO, or in the form of various sodium-zeolites (alumino-silicates).

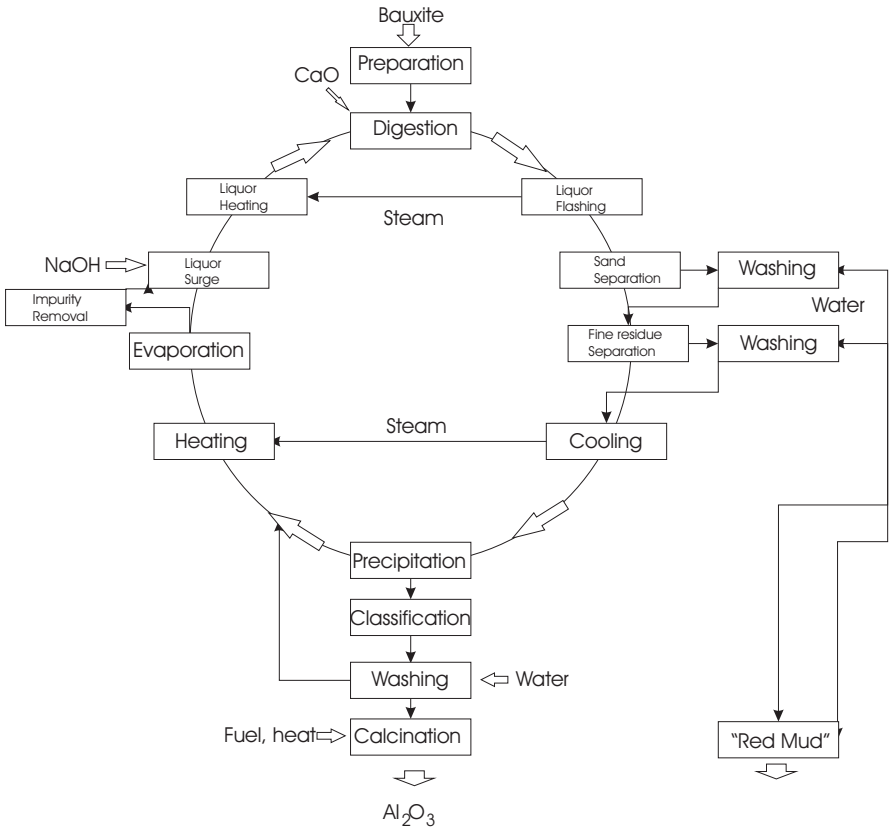

Figure 1.2: *Bayer Process flowsheet, "Bayer Cycle", redrawn from [64].*

Quite pure crystalline $Al(OH)_3$ is precipitated and filtered out of the process cycle when the crystal agglomerates have reached the desired size. The final precipitated $Al(OH)_3$ (gibbsite) agglomerates typically consist of about 100 crystals, while the subsequent calcination process results in a nano-crystalline structure of α- and transition alumina phases, see chapter 2. An important point of the process cycle is the fact that the input and output material flow of bauxite and alumina respectively is relatively small compared to the material present in the cycle. This implies that process parameters vary slowly and rapid process changes are difficult.

1.3.1 Alumina Calcination and Quality

The calcination of the Bayer process product, $Al(OH)_3$, represents the interface between the Bayer process and the Hall-Héroult process. About 10 % of Bayer alumina is calcined to specialty grade alumina or hydrate used mainly by the ceramics industry. Modern so-called "fluid flash" calciners are much more efficient, and produce a more consistent high quality product, than the older fluidized bed and particularily rotary kiln type calciners, [64, 191, 137, 193]. The resulting SGA powder grains produced are hard agglomerates (secondary particles) made up of polycrystalline and polymorphic aluminium oxide (primary particles).

The most important alumina quality parameters today, apart from chemical purity (*XRF*), are consistency, flowability (particle size distribution (PSD) and attrition index (AI)), specific surface area (SSA, *BET*), moisture and hydrate content (MOI, LOI), unpacked bulk density (UPBD) and the α-alumina content (*XRD*). The common abbreviation and *characterization method* normally used is stated in paranthesis. The α-alumina content, SSA and LOI are closely interrelated properties – and good correlations exist for single alumina qualities, [20, 134].

The optimum alumina quality may vary between smelter technologies, and there is no doubt that the alumina refineries optimize quality with respect to cost, sometimes in conflict with the needs of the aluminium producer. The alumina specifications from the smelter are also a compromise between cost and the various roles of alumina. Since the advent of the dry scrubbing process, the specific surface area for SGA is usually specified as minimum 55 m^2g^{-1}- while the moisture content should be kept low, and the α-alumina content in the range 5-15 % [173, 3, 134]. Though most critical alumina properties may be reasonably controlled, and many aluminium producers rely on buying alumina on the spot market – there are still considerable advantages for an aluminium producer to control it's own sources of alumina for quality control purposes. However, a continuous improvement in characterization methods and efforts in basic research is closing the knowledge gap between the requirements of the Hall-Héroult process and the specifications of the alumina produced by the Bayer process plants around the world.

Chapter 2

Literature Review

2.1 Introduction

It is critical that the raw material for aluminium production, smelter grade alumina (SGA), behaves consistently and predictably upon addition to the melt in the modern Hall-Héroult process. The primary aluminium industry requires the alumina supplier to provide a product within certain specifications. Nevertheless, product quality may vary upon switching from one type of alumina to another, or when handling different stocks of the same alumina. Variations within a single batch of alumina may be due to particle size segregation during handling and storage.

Basic requirements for the dissolution of an alumina particle in cryolitic melts are;

1. The alumina particle must be (partly) wetted by liquid melt.
2. The local alumina content in the melt must be below saturation.
3. There must be sufficient heat available for the endothermic process of heating and dissolution.

In modern smelters, the alumina has usually been used to clean pot off-gases in the dry scrubbers, so variations in the cleaning process may also lead to variable secondary alumina quality. Out of bounds specifications may lead to serious operational problems, loss of current efficiency (CE) and increased emissions. There is thus still much industry motivated work

towards the further understanding of the critical alumina properties for primary aluminium production.

The design and operation of modern pot-lines seem increasingly sensitive regarding the limit of alumina dissolution in spite of and, ironically, because of better feeder control. As one wishes to maximize productivity, energy efficiency and CE by design and operating conditions the optimal conditions for rapid alumina dissolution are compromised. By operating with a stable, and relatively low, electrolyte temperature close to the liquidus, both the CE and the cell life expectancy is optimized. A good heat balance ensures that a stable side-ledge (frozen electrolyte) is maintained which protects the side-lining from corrosion by the electrolyte. CE may be optimized by limiting the back reaction, and this may be achieved by minimizing the amount of aluminium metal dispersed in the electrolyte by operating a quiet bath and a stable non-turbulent metal pad. A low anode to cathode distance (ACD) minimizes the cell voltage drop due to electrical resistivity in the electrolyte thereby reducing the energy consumption, but may decrease the CE, and is detrimental to rapid alumina dissolution.

Optimal conditions for rapid alumina dissolution include;

1. High temperature and superheat[1] in the melt which ensures ample heat for dissolution and high alumina solubility

2. A comparatively large dissolution volume which also ensures ample available heat and avoiding local alumina saturation

3. Vigorous electrolyte convection including turbulence

If the *alumina concentration* drops below a certain level, around 1 wt % [49, 176], an anode effect (AE) may ignite resulting in reduced productivity, disrupted heat balance, and the emission of unwanted green-house gases (CF_4 and C_2F_6).

Modern automatic *alumina feeding* controllers rely on the rapid response of the so-called pseudo-resistance of the cell when the alumina concentration is relatively low, at around 3 wt %, [92, 182]. Since an anode effect may ignite if the alumina concentration drops to around 1 wt %, the alumina concentration should be kept well above this level - thus requiring

[1] Superheat is defined as the (positive) difference between the melt temperature and the liquidus temperature of the melt

relatively accurate control. The feeding program is based on consecutive periods of over-feeding and under-feeding compared to the theoretical alumina consumption. Modern cells use point-feeding of small amounts of alumina (typically around 1 kg) to open but restricted areas (typically 2-5 feeders) of each cell at relatively short time intervals (typically 1 min). Thus, point-feeding technology enables the pot-line to operate at close to the optimal conditions by automatic control, partly relying on adequately high rates of alumina dissolution. However, by operating on the alumina dissolution limit, and maximum automation, the impacts of poor or unexpected variations in the alumina dissolution behavior may be particularly critical.

Ideally the *alumina concentration* should be held at a constant level as a function of both time and space in the electrolyte. However, the above mentioned control sequence requires that the alumina concentration is dynamically varied to preset levels above and below an optimal low control level (about 2-3 wt %). An even alumina distribution in a pot is best assured by using many feeding positions and good convective electrolyte transport, but this may be difficult to obtain in practice. The literature reports (permanent) spatial variations of the alumina concentration within a cell of about 0.5 wt % [86, 120, 151, 176] and local variation close to and within the alumina dissolution volume will vary from the bulk concentration (around 2 wt %) to saturation, typically around 7 wt %, [169, 163, 176].

The alumina concentration is dynamic since the raw material is continuously consumed during electrolysis. Expected *dynamic time variations* of the alumina concentration may typically be in excess of 0.13 wt %/min (8 wt %/h) due to consumption [176], while the alumina dissolution kinetics may typically result in variations in excess of 0.3-0.8 wt %/min [6, 7, 76, 90, 149, 86, 176]– depending on the alumina dissolution rate. Local effects due to non-ideal alumina distribution will lead to variations also.

The *distribution of alumina* from the feeding positions is limited by the electrolyte flow, typically of around 5-10 cm/s, and this may be expected to vary according to cell design and operating conditions and indeed from pot to pot, [86]. Higher (by an order of magnitude) flow rates were recorded where anode gas bubbles discharge from under the anodes. For any given cell design a set of preferred circulation patterns will dominate during stable operation driven by a combination of anode gas bubbles and electromagnetically induced flow patterns (circulation) in the liquid aluminium metal.

Modern cell designs aim at providing a stable, flat metal pad by ensuring balanced electromagnetic forces, but the available "stirring" energy which is of value for alumina dissolution is thereby reduced. Large anodes and the practice of using low anode- cathode spacing may have an adverse effect on the distribution of alumina, and stationary concentration gradients may be expected. Some anode positions may be susceptible to particularly poor alumina feeding because of this, making them prone to anode effects or may result in deformations and "spikes" forming on the bottom surface of some anodes [86, 151, 176] if the alumina concentration is permanently deficient. Thus, even though the particular protruding anode surface has a lower potential, which normally would lead to increased current and self-leveling, inadequate alumina feeding may result in permanent deformation and may result in partial short-circuiting of the cell.

2.1.1 Focus

Modern alumina feeding technology is sensitive when it comes to the "lumping" or "agglomerating" properties of the alumina. Not all of the alumina is dispersed as a free-flowing powder. The conditions above the melt and especially upon addition to the melt favor the *formation of agglomerates* with a very different dissolution behavior compared to the loose alumina powder. Lumps of alumina, here called agglomerates, are observed to form (typically as floating "rafts") as the added (secondary) alumina hits the melt and is partially encapsulated by a layer of frozen melt. Indeed, most of the alumina charge will probably interact with the melt in this way before it dissolves and disperses. Liquid melt will penetrate the agglomerates while the frozen layer melts away [195, 196] and will fill interparticle and intra-particle voids of the alumina, thereby increasing the density of the agglomerates so that floating "rafts" become submerged and may sink in the electrolyte [112, 90, 86, 176].

If agglomerates are not broken up and dissolve they may sink to the electrolyte-liquid melt interface and remain suspended by surface tension there during dissolution, as recently discussed by Solheim and Rolseth [168], or form so-called "sludge" under the liquid metal on the carbon cathode surface [176]. Apart from the fact that an insufficient mass of alumina is available for electrolysis, sludge is detrimental to cell performance since it is an electrically insulating material (relatively) and may disrupt current paths and induce horizontal current components that may cause instabilities in the metal pad.

It is generally believed that sludge will to some extent feed alumina (usually determined self-feeding) back to the bulk electrolyte by way of a postulated bath film [176] or even by entrainment by (and through) the liquid metal [184]. Such mechanisms are relatively slow processes but may probably be important during the under-feeding cycles of the alumina control program.

It may be concluded that the formation, break-up and dissolution of alumina agglomerates seems to be crucial for the operation of modern Hall-Héroult cells. The mechanism of formation of agglomerates is the focus of this study. In the following sections a report is given on the published literature relevant for this work.

2.2 Part I: Alumina Dissolution Studies

Most dissolution studies have been performed in the laboratory in order to have parameter control. The problem is complex and many different experimental approaches are reported in the literature. The resulting plethora of cell designs and experimental techniques used by the many researchers in the field has rendered direct comparison between studies very difficult [112, 90, 86, 176].

Kobbeltvedt [86] pointed out the importance of *separating the process of dissolution from the process of agglomeration* in studying the two distinct mechanisms. In many studies the two have been confounded, confusing the discussion of mechanisms and parameters. The actual dissolution mechanism may also be described as a two-step process, single dispersed grains of alumina dissolving before the rather slow dissolution of agglomerates [86], and there seems to be agreement in the literature that the process may be under mass transfer control. On the other hand, the formation and break-up of agglomerates is most likely heat transfer controlled [180, 196, 63, 176]. It is important to keep in mind that the dissolution process is continuous, and most models assume a controlling step or process. As our understanding increases, so might the complexity of the models increase in order to fully describe the truly complex process of alumina-electrolyte interaction and dissolution.

In the following it will become apparent that no general consensus exists regarding the mechanism of alumina dissolution, or the most important alumina parameter(s), apart from consistency [204], illustrating the complexity

as well as the different angle of attack of the many workers that have studied the problem. However, the alumina dissolution rate in the electrolyte may be described by a simple differential equation [77, 85] supposing mass transfer control

$$\frac{dC}{dt} = \frac{kA}{V}(C_{sat} - C) \tag{2.1}$$

where C is the local alumina concentration and C_{sat} is the (local) alumina saturation concentration, a function of the melt composition and temperature. A is the (apparent) contact area between the alumina and electrolyte, k is a dissolution rate constant[2], i. e. the mass transfer rate. The constant k may depend on alumina properties, the degree of convection and also the electrolyte temperature and superheat, though the latter are indicative of heat transfer control. V is the available dissolution volume controlling the concentration gradient but which also determines the heat available for dissolution.

Lubyová and Danék have proposed empirical models that seem to fit their data quite well [188, 187], supporting a physical model of diffusion control for low CR melts, and heat transfer for normal CR melts. The models do not incorporate the driving force of alumina concentration, and though this may not be important for the initial dissolution rate, their work is difficult to discuss further, especially since no comparison is made to other data, and no regression fitting coefficient is quoted.

As will be discussed in the following, there seems to be reasonable agreement in the literature that the most important factors influencing the alumina dissolution, apart from the alumina, are the method of addition and available heat (and heat transfer conditions) in the melt in the dissolution area. It is important to have an optimal dispersion of alumina grains and a large available dissolution area in order to ensure good wetting, heat transfer and avoid local saturation of alumina. The importance of the alumina properties is still not clear, though interest in identifying the key (if there are any) physico-chemical properties still motivates research, including this study. Further study of the formation and break-up of such agglomerates is needed.

The agglomeration, (or lumping) of modern alumina (SGA) has been observed by many workers [112, 90, 86, 176], and may explain many of the conflicting results and conclusions reported in the literature pertaining to

[2]Indeed the proposed model may be simplified by using $k' = \frac{kA}{V}$, a composite but simple mass transfer rate constant.

dissolution kinetics. It may be argued that the tendency to form agglomerates may be the dissolution rate determining property of any alumina [86, 196, 63].

The method of addition of alumina appears to be critical in discussing the many studies, since it will largely determine whether or not agglomerates are formed. The following dissolution process discussed in the literature may be divided into (dissolution) studies of

- dispersed single alumina grains
- alumina agglomerates, pellets, tablets, cubes
- alumina batches giving varying amounts/ conditions of dispersed grains and agglomerates

A review and discussion of the literature which is of relevance for the current study is presented in the following sections.

2.2.1 Dissolution Characterization Methods

A large number of experimental techniques are reported in the literature on studies regarding the dissolution of alumina in cryolite. They may be roughly divided into *in situ* and *ex situ* characterization methods, see table 2.1.

In situ Methods

The qualitative behavior of alumina upon addition to cryolitic melts may be readily observed in laboratory cells, but such observations may be difficult to quantify and relate to the industrial process. However, visual determination is always a good supporting technique in any study, and has been useful for determining the apparent rate of dissolution and qualitative description of the tendency for agglomeration (and crusting) and interaction with melt [38, 180, 90, 86, 99, 75, 80, 112, 185].

A method using fast linear sweep voltammetry, often termed *critical current density (CCD)* or *limiting current* determination technique, recently discussed by Richards *et al.* [140], has been applied by several workers and seems to be the most promising method of *in situ* alumina concentration

Table 2.1: *Dissolution Characterization Methods reported in the literature, based in part on table presented in Richards* et al. *[140]*

Dissolution Characterization Method	Ref.[#]
In situ	
Visual methods	[179, 77, 99, 75, 185, 112, 90]
Various Electrochemical methods	[76, 140, 178, 7, 90, 86]
Temperature monitoring	[90, 106, 147, 35, 86]
X-ray absorption	[196, 107]
Ex situ	
LECO, oxygen analysis	[147, 86]
Wet chemistry techniques	[180, 188]
Optical Microscopy	[77, 45, 185, 124]
Electron Microscopy and Diffraction	[99, 76, 185, 106, 107]
Powder X-ray Diffraction	[185, 76, 7]
Particle Size Determinations	[75, 7]
Pellet/tablet/agglomerate dissolution	[37, 38, 82, 180, 127, 76]

determination. The actual dissolved alumina content is determined using an electrochemical probe and pre-calibrated apparatus. The physico-chemical properties of alumina are routinely determined using a range of increasingly well defined and standardized laboratory analysis techniques, as discussed by Roach *et al.* [143, 145, 142]. As described previously, many of these properties have been correlated to the dissolution rate of a given alumina quality, mostly using the electrochemical CCD-technique.

The temperature depression which results in the electrolyte upon addition of SGA may also be monitored in order to obtain a measure of alumina dissolution kinetics, [90, 106, 147, 86], and even the alumina distribution and circulation pattern in electrolysis cells [86].

A few X-ray studies have also been quite successful, where the absorption contrast of bulk alumina has been shown to be sufficient for visualizing the degree of alumina dispersion in the melt of small (X-ray transparent) laboratory cells [107, 195].

The modern Hall- Héroult process monitors the pseudo-resistance over the anode-cathode distance that shows a well documented and predictable varia-

tion with the concentration of alumina in the electrolyte, though the method is limited regarding absolute quantitative determination, it could be used in a laboratory study as well [197, 49]. Optical Spectroscopy, such as Raman Scattering, has been mentioned as a possible method for deducing the alumina concentration *in situ* in the electrolyte [133]. An obvious benefit of such spectroscopy being that no direct contact between the melt and optical probe is needed.

Ex situ Methods

Ex situ studies, typically involving bath and/or agglomerate sampling and later physical characterization and chemical analysis etc. have so far been more reliable than the *in situ* methods described above - though the CCD technique in particular is now well proven in the laboratory. Though fairly accurate, *ex situ* studies are in general sensitive when it comes to the sampling method used, i. e. taking representative samples, sample quench method and crystallization etc. – and usually detect both dispersed undissolved alumina as well as dissolved alumina, [140].

The standard method of determining the alumina content in quenched melt samples at our laboratory is done by the "LECO" oxygen analysis method based on spectroscopic analysis of CO/ CO_2 from carbo-thermally reduced oxygen compounds in the samples, [147]. The instrument is calibrated with a well known standard material prior to sample characterization. LECO analysis results agreed well with those obtained by the electrochemical CCD-technique in the work by Kobbeltvedt *et al.* [147, 85, 86].

Several researchers have found that the crystal morphology and phase of alumina in quenched samples depends on the CR and the sampling method used, [34, 140]. In addition, un-dissolved alumina may be present. The phase diagram of Foster [34] relates the equilibrium of α- and η-alumina as a function of the alumina concentration and the CR of the melt. Dissolved alumina may solidify to a rather disperse X-ray amorphous (perhaps nano-crystalline) phase rendering analysis by XRD difficult. However, a recent unpublished XRD result by Haverkamp *et al.* [65] indicates that the relative content of α and η in quenched bath samples may be used to discern the amount of dissolved and dispersed, undissolved alumina.

Several microscopy based *ex situ* methods, may give qualitative information on the dissolution mechanism by studying relatively few alumina grains in the collected samples. However, the problem of collecting and studying

representative samples becomes exasperated at high magnification, always limited by the statistics i. e. the number of samples studied. Methods that deduce information from the bulk average of samples, such as powder X-ray diffraction (XRD) are preferred when bulk properties are to be deduced, ref. chapter 3. Microscopy may however be very useful for supporting data obtained by more statistically significant sources.

2.2.2 Discussion

There is substantial evidence supporting a rather simple mass transfer model, such as equation 2.1 or variations thereof. Provided that the cryolitic melt is well above its freezing temperature and far from alumina-saturation, the most important variable seems to be the available contact area between the alumina (powder) and melt [85]. Agglomeration is thus a critical property of alumina. Recent work supports an understanding of the importance of the method of addition, convection and heat transfer on the alumina dissolution rates obtained in the electrolyte, which influences the degree of agglomeration [6, 112, 90, 196, 195, 86, 63].

In the following discussion, a distinction is made between (1): visual and physico-chemical studies and (2): electro-chemical studies. In some cases that distinction is artificial, but such a distinction does to some extent highlight the fact that researchers have attempted to follow the process from at least two points of view.

The visual study of alumina dissolution has been compared to the dissolution of sugar in a cup of coffee or tea. As alumina grains dissolve the melt first becomes opaque, slurried, before the melt regains its translucence. When 1 wt % of alumina is added to a well-stirred melt of fairly high temperature the time needed for the dissolution is within a few seconds, and well calcined α-alumina dissolved more slowly than low-calcined γ-alumina in the well known study by Thonstad *et al.* [179, 180]. On the other hand, the electro-chemical methods, such as CCD, usually show much slower dissolution kinetics, the process of dissolution taking several hundreds of seconds to attain the theoretical alumina concentration after addition [90, 85, 58, 86]. The discrepancy has been attributed to the translucency of alumina crystals [73, 58], but this is a rather unlikely explanation. Dispersed alumina with such small, irregular crystals should be very effective optical scatterers.

However, the conflicting conclusions may be reconciled when the dissolution process is divided into fast dissolution of dispersed grains, and rather

slow dissolution of agglomerates, sometimes referred to as "flakes", "rafts", lumps or sludge [80, 86, 85, 63, 149].

Visual and physico-chemical studies

It is reasonable to assume that if the particle size of alumina could be measured in the electrolyte, the rate of the dissolution process could be directly monitored. Measuring actual particle size *in situ* in cryolitic melts may unfortunately not be conducted using standard (water based) techniques such as the Coulter counter or laser diffraction based analysis (Malvern). Indeed, molten cryolitic melts prevent most probing techniques due to the severe, corrosive environment. Visual studies have usually only reported what is possible to discern from above, i. e. at or near the melt surface.

A few visual studies using see-through cells (quartz) have been reported, [55, 107], providing some qualitative descriptions of the behavior of alumina upon addition to cryolitic melt. Liu *et al.* [107] used specially constructed crucibles with flat surfaces made from quartz plates. As mentioned above, as the alumina grains dissolve, the melt first becomes opaque (slurried), before the melt regains its translucence. The direct observation of single shrinking grains has not been made however. However, alumina agglomerates resembling "snow-flakes" have been observed, probably consisting of interlinked SGA grains perhaps released spalling/disintegration of larger agglomerates in the melt, ref. chapter 6, and [138, 107, 185].

Maeda *et al.* [112] used 50 g melt in Pt-crucibles and 0.5 g alumina (1 wt %) additions. The alumina was fed in two ways, slow and fast, and no forced convection was applied. Normally, the superheat of the melt used was 20 °C. During the slow feeding, alumina grains were allowed to trickle down the feeding tube and largely disperse as discrete grains in the melt, while during fast feeding the alumina grains flowed down the feeding tube as a coherent powder body and tended to form a "lump", (i. e. alumina agglomerate) upon contact with the melt. 28 alumina qualities were tested, and 2-3 copies of each experimental condition were performed. The dissolution time was visually determined. Rapid feeding usually gave crust ("rafts") and always gave more rapid dissolution than slow feeding. During slow feeding the alumina tended to sink and form a pile on the bottom of the crucible. It was concluded that modern "sandy" aluminas dissolved more quickly than floury alumina, and for the sandy aluminas a slight correlation was found with the alumina properties (LOI, BET, α-content) during slow feeding.

No correlation was seen when fast feeding was applied. The dissolution rate was shown to increase with increasing superheat, which was achieved by changing the melt composition (increasing the AlF_3 content), while keeping a constant melt temperature. The dissolution rate decreased for decreasing temperature when the superheat was held constant (at levels of 15, 20 and 25 °C). When using the slow alumina feeding method while the superheat was held constant, the dissolution rate decreased with increasing alumina content.

Noguchi *et al.* [124] studied the behavior of pressed and sintered pellets of alumina in a droplet of cryolite by using a hot thermocouple technique and an optical hot stage microscope. The temperature employed was about 1050 °C. An alumina chip of $0.5\times0.5\times5.0$ mm^3 was set in the 5 mg droplet of cryolite, equating to a factor of 10 times greater mass of alumina compared to the melt (!). Full dissolution was therefore not possible. The authors noted faster "dissolution" for lower calcined alumina and for higher AlF_3 content in the melt, but have probably observed mostly corrosion and shattering of the more porous γ-alumina. The addition of aluminium fluoride to the melt will increase the superheat and may be expected to increase the corrosion rate of the alumina.

Gerlach and Winkhaus and coworkers [38, 204] used a rotating disc method to relate the dissolution rate difference between various calcination grades (phases) of pressed or sintered alumina pellets. The pellets therefore had variable density and strength, see chapter 3. α-Alumina (a dense sintered disc) dissolved the slowest, while a disc of β-alumina had the highest dissolution rate. However, the effect of melt additives and temperature, and SGA grain size were concluded to be more important. The penetration of melt vertically in a tube filled with alumina (as for crust formation) was used to record the exothermal γ to α transition, and showed that low-calcined γ-alumina has a more rapid temperature response upon addition to cryolitic melt. The studies also showed that the crust density decreased when low α-aluminas or only the coarse fraction was used. Interlocking thin alumina platelets of up to 30 μm were recorded (SEM) in crust formed with low α alumina, while calcined 100 % α-aluminas did not form platelets, but retained the original morphology. Crust formation was concluded to be critical for dissolution, and the degree of alumina calcination and heat effects are important.

Jain *et al.* [73, 72] used the CCD technique and argued that the alumina-bath contact area is more crucial for alumina dissolution than the surface

area of alumina as measured by the BET method. It was concluded that the dissolution rate was largely intrinsic to the alumina quality used, but that the effect was confounded with the moisture content (LOI).

Johnston and Richards [76] also used an electroanalytical probe (CCD-technique), and determined the dissolution behavior of cubes of crust made under fairly controlled, near-equilibrium conditions. The density and compressive (cold) strength of the cubes were found to be correlated, while the dissolution rate did not vary significantly. However, the dissolution rate was found to decrease by an order of magnitude after a duration of 20-40 min in the melt, compared to the initial rate.

A "crust-cube" technique, similar to that used by Johnston and Richards [76], was used by Kheiri *et al.* [81, 82], but not in combination with an electrochemical CCD-technique. Cubes of crust were cut from crust that had been exposed to the cryolitic melt for only 20 s, thus the conditions were more relevant for the modern alumina feeding process. The cubes were tested for their integrity (not dissolution) in liquid aluminium at Hall-Héroult process temperatures, simulating perhaps the disintegration of sludge. High α-alumina crust (of high density) samples disintegrated more easily than low α-alumina, low density crusts. The low density (porous structure) of crusts formed by secondary (reacted) alumina was correlated to the content of carbon (soot, anode dust), that may cause pour wetting and the formation of a more porous network of electrolyte and alumina during the exothermal combustion process forming CO_2 [82].

Calculations done by Thonstad *et al.* [180] showed that dispersed alumina grains should dissolve in the order of 10 seconds including the formation and remelting of a layer of frozen bath, in agreement with visual determinations [179]. The experimental work showed a significant difference, of several seconds, between the faster dissolving low-calcined "γ" alumina and the highly calcined α alumina. The study concluded that the dissolution process is very rapid when ample heat, convection and dispersion is assured.

In addition to the heat needed to re-melt frozen melt after (cold) alumina additions, and heating of alumina, the actual dissolution of alumina in cryolitic melts is also a strongly endothermic reaction [180]. Usually, a clear correlation between the maximum temperature drop observed in the melt upon addition of alumina and the dissolution rate of the alumina may be found [73, 72, 90, 58]. The temperature of the cryolitic melt has been found to quickly drop to the new liquidus temperature after the addition of 1 wt % alumina batches [180].

A study by Liu *et al.* [106, 107] included a qualitative description (microscopy, SEM) of single SGA grains shortly after addition to cryolitic melt which revealed that some shattering occurs in low-calcined SGA, but not in calcined α-alumina. Shattering may be expected due to the explosive release of pressure and moisture during the rapid heating [106, 107].

Hovland *et al.* [63] showed that reducing the agglomerate size was more effective than increasing the stirring rate in reducing the time of dissolution of agglomerates that form upon addition, and argued that the formation and dissolution of agglomerates is most likely heat-transfer controlled, in agreement with Walker *et al.* [195, 196].

Kobbeltvedt[86], recorded the temperature at several positions in industrial electrolysis cells (Hydro Aluminium) and determined the *alumina distribution* patterns of several cell designs by the temperature depressions recorded in each position as consecutive charges of alumina were carried away from the feeding positions. Each cell has a fairly constant circulation pattern. A fairly well defined alumina dissolution volume, probably consisting of a mixture of cooled melt (with a relatively high average alumina concentration) and submerged and/ or sinking undissolved alumina agglomerates was assumed to pass the thermocouples.

2.2.3 Electrochemical studies

A fast linear sweep voltammetry technique, employing the principal of *critical current density* (CCD), has been shown to be quite reliable in determining the dissolution rate of alumina. The critical current density (CCD) varies with the alumina concentration and may be calibrated for a predetermined alumina concentration in the laboratory. On a laboratory scale the method has been applied by many workers and has enabled a quite systematic mapping of the most important factors affecting the alumina dissolution rate [76, 73, 6, 7, 90, 147, 85]. Other studies based on the same principle have been discussed [140, 197].

The need for a standard industry test procedure for determining the alumina dissolution kinetics and concentration may be argued, and the CCD method seems to be the best candidate for a reliable and accurate *in situ* sensor [140, 58, 197].

Kobbeltvedt *et al.* [85, 86] concluded that it is important to consider both the actual alumina dissolution process and the process of alumina agglom-

eration. The former is believed, in part, to be nested in the latter. In Kobbeltvedt's study it is argued that alumina dissolution in modern prebake Hall-Héroult cells with point-feeding, may be viewed as a two step process (at least).

1. Dissolution of dispersed alumina particles. Dissolution rate in excess of 0.3 wt %/min [6, 76, 149, 85].

2. Dissolution of alumina agglomerates. Dissolution rate as low as 10^{-4} wt %/min., and even lower if sludge is formed [180, 85].

Alumina properties such as the particle size distribution (PSD) in the ore and content of volatiles (mainly moisture) contributes to the efficiency of alumina dispersion upon addition. A related factor is the extent to which alumina agglomerates are formed and later dissolve, break up or form sludge. Alumina properties such as the volatile content (moisture etc.) and flowability (partially measured by PSD and angle of repose) are very important, along with operational variables relating to the heat transfer rate. The heat transfer rate to the dissolution area is determined by the bath superheat (ΔT above liquidus), sufficient convection in the dissolution area in the bulk of the bath and agitation (undulations) of the bath surface mostly due to anode gas release. The factors controlling the heat transfer to the alumina particles may thus be rate determining for the formation and break-up of alumina agglomerates in the melt.

It seems that a great deal of the discrepancies pertaining to the numerous dissolution studies over the years may be attributed to the differences in methods of addition of alumina, and thus the degree of heat transfer attained [112]. The operational/ experimental factors have probably dominated results ascribed to alumina properties in some cases, especially where the statistics have been rather poor. Bagshaw and Welch [7] and Kuschel and Welch [90] found that the alumina flowability and moisture content (LOI) were the most important alumina properties that influence the alumina dissolution rate. Kuschel and Welch [90] combined temperature recording, electro-chemical (CCD) and optical (video) techniques simultaneously under fairly realistic conditions in the laboratory. They found that high electrolyte velocity (stirred melt), alumina feeding (good alumina dispersion), high temperature of melt (available heat), high LOI (moisture content) in the alumina and good flowability of the alumina were all the most important requirements for rapid alumina dissolution in modern cells

Table 2.2: *Table based on Kuschel and Welch [90], shipment variations in alumina properties and the impact on alumina dissolution times.*

Property	Units	Refinery A	Refinery B	Change in diss. time
α-Al_2O_3	%	14.0-17.5	5-10	< 15 %
LOI	wt %	0.67-1.25	0.5-0.9	< 20 %
BET	m^2/g	76-82	55-65	< 15 %
Bulk density	kg/m^3	928-1004	950-990	< 8 %
$< 45\mu$m	wt %	6.7-11.5	4.5-9	< 5 %
FFT	s/100 g	NA	3.6-7	< 25 %
Dissolution time	s	27-48	20-40	< 50 %

Table 2.3: *Table based on Kuschel and Welch [90], impact of varied cell dynamics (operating conditions) within typical industry range and their impact on alumina dissolution times.*

Property	Units	Range	Typical Value	Change in diss. time τ, $\tau_{norm} = 1.0$
Bath Ratio		1.25-1.08	1.20	$\tau \in \{0.8, 1.8\}$
Superheat	°C	5-15	10	$\tau \in \{0.85, 3.0\}$
Alumina conc.	wt %	1.6-4.5	2.0	$\tau \in \{0.8, 1.2\}$
Bath Velocity	cm/s	4-25	15	$\tau \in \{0, 5.0\}$
Dissolution time	s	13-500	26	$\tau \in \{0.5, 30.0\}$

using point-feeding. The results from that work seem to encompass most of the current knowledge of alumina dissolution, but the agglomeration and crusting properties, though commented – was not looked into.

The study by Kuschel and Welch [90] determined the cell factors to be 5 to 20 times more important for dissolution than the alumina properties when the alumina properties only were allowed to vary between shipments from two suppliers of SGA over a 12 month period, see table 2.2 and table 2.3. When alumina properties were studied, empirically optimum (unspecified) conditions for rapid alumina dissolution were used. However, since the alumina properties were not varied, other than that allowed between different shipments from the suppliers, the specific effect of alumina properties was not reported. That study may thus have given the impression that variations between alumina properties are not as critical as those of the cell operations. Though the importance of alumina properties was noted, the effect of varying alumina properties under adverse dissolution conditions (i. e. low super-heat) was not conducted, so the effect of agglomerates that form upon addition was minimized. The so-called "cell dynamic factors" were varied between likely extremes encountered in industrial cells, though it was noted that other variations due to cell design could not be simulated in a small lab-cell.

In light of the current study, it would have been interesting to see the difference between aluminas A and B studied by Kuschel and Welch [90] at e. g. low superheat. Possible differences in the tendency to agglomerate, or the flowability between alumina A and B might have shown dramatic effects on the dissolution behavior.

Issaeva *et al.* [71] also used a combination of CCD and visual techniques and found that different aluminas may differ by up to a factor of 5 in dissolution rates for a fixed set of experimental conditions. The data indicated that primary and secondary aluminas from high and low α-alumina content SGA behave differently. Further investigation of alumina quality inpact on dissolution kinetics is thus warrented.

2.3 Alumina Agglomeration and Agglomerate Dissolution

Kobbeltvedt *et al.* [147, 85, 86] concluded that the differences in dissolution behavior of aluminas may be related to their tendency to form agglomerates upon addition to the melt, and this conlcusion is supported by most of the available data in the literature, [179, 180, 7, 90, 63, 149]. Rolseth and Thonstad [149] concluded that alumina agglomeration was caused by a combination of cryolite freezing and the transformation from $\gamma \rightarrow \alpha$ alumina which may provide an interlinking network of alumina. Similar descriptions have been given by other workers during studies of crusting or sludge formation and alumina dissolution [99, 75, 76, 80, 185].

Several workers have found a correlation between the content of α-alumina phase and the crusting and/or agglomeration behavior of smelter grade aluminas [99, 75, 76, 80]. Rolseth*et al.* [148] found a clear correlation between the cold strength of crust and the α-content of the SGA qualities tested. Lower α-alumina contents resulted in stronger crust. The literature also reports that very low contents of α-alumina is unwanted in many smelters due to formation of excessively hard crusts [3, 191]. Recent alumina specifications by Aluminium Pechiney call for an α-alumina content in SGA over 4-5 % for this reason [3]. Townsend and Boxall [185] studied 4 types of sandy SGAs with quite similar α-Al_2O_3 contents in the range of 15-20 %, and their dry-scrubber (secondary alumina) derivatives. A simple crusting scale (1-2) with the following nomenclature was used; 1: hard as white ice, 2: soft as wet snow, and a dissolution scale (a-c) described the dissolution behavior; a:(sinking alumina), b-c:(increasing tendency to float and subsequent disintegration as "flakes").

The test for crusting tendency was performed by dropping 2 g alumina samples into cryolitic melt, while wetting tests were performed by picking up 4 g alumina pluss bath after 10 s. Crusting was studied by dropping 8 g alumina into the melt, the samples being wetted for 3 min before they were removed. The crusting tendency for alumina A, which formed a hard crust, and B, forming soft crust, was further discussed in detail. Topographic SEM micrographs of hard crust showed rather large hexagonal crystals of up to 10 μm diameter, while the soft crust had crystals only of up to 3-5 μm diameter. The hard crust had an α-alumina content of 68 % while it was 93 % in the soft crust. The residual "γ"-alumina content was inferred by difference [185].

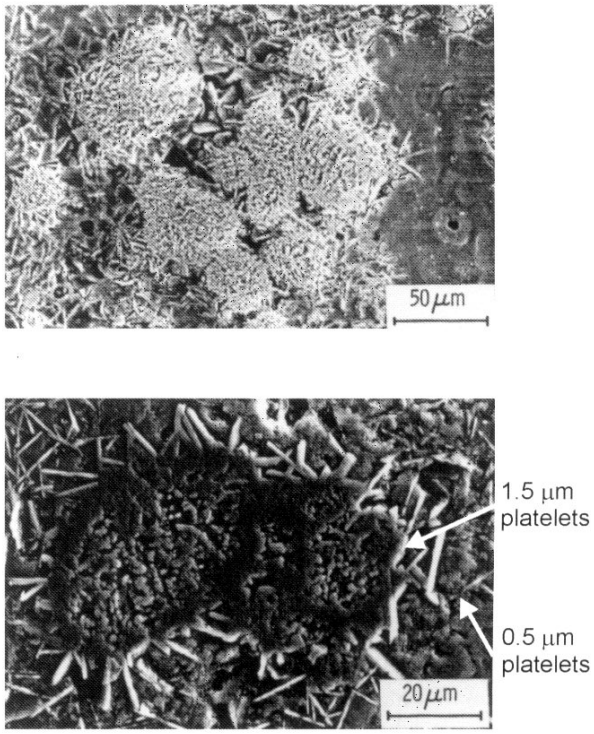

Figure 2.1: *SEM-BSE images of crust after 3 min wetting by melt. Interlinking network of α-alumina platelets evident in lower (cross section). Microstructure is bimodal, thicker 1.5 μm platelets are recrystallized on/from SGA grains, while thinner 0.5 μm platelets precipitate from melt upon quench and are not a part of the interlinking network. From Townsend and Boxall [185], as presented in [176].*

SEM micrographs showed, see fig 2.1, that while α-alumina crystallites (platelets) that precipitate from the melt, during quenching of the samples, have a mean thickness of only 0.5 μm, the cementing (interlinking) platelets are around 1.5 μm in thickness. Platelets were apparently quite uniform in size, and with a near perfect hexagonal shape. The authors concluded that crusting tendancies cannot be correlated with measurable quantities (alumina properties), but that the aluminas' crusting tendency is generally reduced by a high fines content and dry scrubbing. The conversion of γ to α was explained by preferential dissolution of "γ"-alumina and reprecipitation of α-alumina [185].

Townsend and Boxall [185] showed that apparently similar aluminas, with similar flowability, wetting and dispersion by melt, demonstrated very different agglomeration behavior. While alumina B had almost completely recrystallized/ transformed to the α-phase, alumina A produced much larger crystallites and had a considerable residual amount of "γ"-alumina. It may be hypothesized that an equivalent mass transport of alumina may have taken place, only it was concentrated on fewer growth sites in the case of alumina A, which produced the stronger crust by producing larger and stronger α-alumina platelets.

Walker *et al.* [196] and Hovland *et al.* [63] concluded that the formation and break-up of alumina agglomerates in cryolitic melt is heat-transfer controlled. It was shown in the study by Walker *et al.* that melt penetration starts before complete re-melting of the frozen bath, probably due to microscale inhomogeneities of the frozen shell and low melting, low CR melt segregation. The melt temperature in the bulk of the electrolyte, i. e. *the superheat of the electrolyte* and the *heat transfer conditions* to the heat affected area of dissolution will determine the heat transfer rate, and hence the freeze thickness and time of melt-back of the frozen layer that forms on alumina agglomerates upon feeding, [63, 196, 86]. The heat transfer rate will thus largely determine the formation and dissolution kinetics of alumina agglomerates [63, 196].

Kobbeltvedt [86] showed that aggregates of calcined alpha alumina would disperse easily after re-melting of the frozen shell that formed upon addition, while aggregates of SGA, having a high content of transition alumina phases, did not. This effect was attributed to the formation of a network of alpha alumina platelets as reported in the literature on top crust formation [99, 75, 76, 185, 204].

It may be concluded that the literature describing results of observed differences between aluminas of similar α- content has not been satisfactoraly explained [185]. Furthermore, the inherent difficulties of measuring the actual α-alumina content by XRD, accurately and with precision, may not have been fully appreciated by some authors. The related property of alumina microstructure has only been addressed to a very limited extent, basically by qualitative descriptions of micrographs supporting phase identification by XRD. The highly interdependent SGA properties of surface area (BET), α-content, moisture content (MOI,LOI), flowability and particle size distribution (PSD) has complicated the discussion in at least some of the work pertaining to alumina dissolution studies.

2.3.1 Summary of Key Mechanisms

Top crust forms when the cryolitic melt wets and penetrates an excess of alumina, which previously also was the preferred alumina feeding method in the industry. Pieces of crust (alumina agglomerates) with a density greater than that of the electrolyte are a likely source of sludge [80, 176].

Ødegård *et al.* [127] further identified the importance of the $\gamma \rightarrow \alpha$ phase transition in the formation of top crust and the related process of (slow-dissolving) alumina agglomerates. The top crust formation process was studied in further detail by Rye [154, 153]. However, in contrast to previous work, the latter study failed to identify the α-alumina content as having a significant impact on crust properties. Other variables were concluded to be more important, in particular those affecting the density of crust. Llavona *et al.* [108] found that crusts from secondary alumina were softer than those made from primary alumina, which was shown to be correlated to the lower density of crust formed by secondary alumina. The particle size distribution, in particular the content of fines and the moisture content is also likely to influence the packing density of alumina [145, 22].

With reference to the brief discussion of mechanical strength of composites, see chapter 3, it may be noted here that the primary parameter controlling the strength of crust is probably the porosity, and the theory of pore-filling by a liquid phase (cryolitic melt) into a permeable ceramic network (of alumina) seems very relevant, [42]. However, the formation of crust is a very complex process - since the microstructure of SGA, and thus its permeability to liquids, is a function of the exposure to the melt. The process of re-crystallization and crystal coarsening of alumina platelets studied in the current work is thus also relevant for the process of crust formation.

Top cover crust formation, alumina lumping and the clogging of feeder-hammers, alumina feeders and feeder holes are industrial problems related to the process of alumina agglomeration. Industrial smelters that employ the operation of closed alumina feeder holes[3] may experience slow alumina dissolution and distribution upon addition to the electrolyte surface [120]. That mode of operation will probably form slow dissolving agglomerates as the conditions are as required for rather effective alumina agglomeration,

[3]Closed feeder holes: Point feeders in which the alumina is allowed to be suspended above the electrolyte for several minutes between every feeding cycle. The feeder will then push the alumina from the previous cycle into the electrolyte before a fresh alumina charge is allowed to settle in the feeder hole until the next feeding cycle, etc.

the subject of the present work, ref. chapters 4 and 5.

Conditions for effective SGA agglomeration include the presence of liquid bath and gaseous fluorides combined with high temperatures and a body of alumina at rest.

The evolution of volatiles during the heating of the alumina is characterized by LOI and MOI values (in air), both correlated to the specific surface area (BET), again correlated to particle size and the phase composition of the alumina [200, 191, 137, 194, 145, 22, 9, 3, 130]. The release of excess volatiles, including exothermic burning of carbon present in secondary (reacted) alumina, produces a poros agglomerate where the skeletal structure consists of frozen bath components and an interlinking network of α-alumina platelets and alumina grains. Kheiri *et al.* [82] showed that an increasing carbon content added to alumina decreased the density of agglomerates formed upon addition of (secondary) alumina to cryolitic melt.

The permeation of liquid bath vertically through loosely, or lightly vibrated, packed alumina (such as during crust formation) has been found to occur at a rate of about 0.5 mm/s [38, 148]. The process is due to capillary rise, but it is heat transfer controlled for "cold" alumina added to bath [154, 152, 196]. The permeation of water and liquid bath was found to be similar in the study by Rolseth *et al.* [148], at least if alumina is preheated to 1000 °C so that isothermal conditions prevail and the effects of volatiles is minimized. The $\gamma \rightarrow \alpha$ alumina transformation process was assumed to slow down the permeation rate compared to that observed for water, probably due to the release of volatiles etc. during the interaction of SGA and cryolitic melt. A high content of fines was also found to decrease the permeation rate, which is controlled by the available microporosity of a certain size distribution. Large grains and grains with a smaller surface area are more easily wetted by a liquid.

The temperature at the liquid bath penetration front, i. e. in a bed of loose alumina, may be estimated to be around 700 °C from the phase diagram for the system cryolite–AlF_3, [153, 176], which also corresponds to the lowest temperature for conversion of $\gamma \rightarrow \alpha$ alumina when catalyzed by fluorides [86, 127].

Østvold *et al.* [133, 50] found that the *phase transition temperature* is less than 700 °C for alumina samples with added $NaAlF_4$ held at temperature for 20 h. The temperatures measured on top of the dense "sintered" alumina covering the electrolysis cells has been found to be 455±58 °C [50]

indicating that the transformation temperature is in fact even lower [133] - since confirmed by unpublished data [132]. Thus, there seems to be some discrepancies pertaining to the phase transition temperature due, in part, to the different experimental conditions used. The transformation has very sluggish kinetics at low temperature. When the transformation temperature is defined as the temperature at which 50 % has transformed after 30 min, the temperature is found to be 800 °C [127].

The true temperature at the liquid melt front in top crust, or indeed in agglomerates is difficult to determine experimentally [153]. For instance, the cover of alumina is likely to be partly wetted by liquid phase and gas phase fluorides, and the temperature seen by the alumina caused by radiation of heat from the electrolyte may be considerably higher than the temperature measured by a thermocouple immersed through the loose cover onto the "sintered" layer. The heat released from the exothermal oxidation of carbon impurities and the slightly exothermic $\gamma \rightarrow \alpha$ phase transition will also contribute to the available energy, in addition to the heat provided by liquid bath by conduction and radiation, while the vaporization of water will be a heat sink, but also an effective heat transport.

2.3.2 Conclusion Part I

The importance of some form of bonding mechanism of alumina in agglomerates (termed "sintering" by Kobbeltvedt *et al.* and Østvold *et al.*), which provides mechanical strength and dimensional stability to agglomerates after the electrolyte freeze layer has re-melted has been emphasized [127, 149, 63, 85, 86]. Such a transformed, "recrystallized" microstructure, as shown in figure 2.1, consisting partly of an interconnecting skeletal structure of α-alumina platelets – is recognized as crucial in top crust formation and in old technology alumina feeding methods (by crust breaking), [99, 75, 76, 185, 148].

The mechanical strength of the transformed microstructure within alumina agglomerates is likewise probably important for their following break-up and dissolution behavior. It is probably also significant that the altered microstructure may present different liquid melt transportation routes (i. e. permeability to liquid melt), also affecting the dissolution behavior. The evolution of such a *microstructure and the physical mechanism of agglomeration* of the SGA grains, providing mechanical strength also after the frozen bath has remelted, will be further investigated in the current study.

2.4 Part II: "Sintering" Mechanism

The study of particle size and microstructure and the effect of particle growth kinetics is a major subject in the theory of "sintering". The following discussion is based on a rather comprehensive literature study of alumina sintering theory and phase transformations. The α-alumina phase transformation, usually via the transition alumina phases, is an active research field. Most of the relevant literature concerns the use of alumina as a ceramic material, both as a structural material and as a so-called "functional" material, such as a catalytic substrate, electronics insulator, thermal conductor etc. The evolution of microstructure in pure or composite form for some other ceramic systems may also be relevant, as the principles of microstructure and the physical properties are general.

2.4.1 Agglomeration Mechanism Summary

The actual alumina agglomeration mechanism postulated is akin to that suggested for the formation of top crust. The main mechanism is the crystal coarsening of the SGA particle surfaces and the resulting physical attraction by proximity or intergrowth/ "interlinking" of these coarsened surfaces of neighboring alumina grains. A shell of frozen electrolyte serves to hold an alumina agglomerate together during this coarsening. The presence of gaseous and liquid fluorides will act as fluxing agents (mineralizers) that greatly accelerate the $\gamma \rightarrow \alpha$ phase transition and crystal growth, and that control the crystal morphology (hexagonal platelets).

The study of SGA agglomeration (crusting) by Townsend and Boxall serves as a relevant example. While alumina B had almost completely recrystallized/ transformed to the α-phase, alumina A produced much larger crystallites and apparently had a considerable residual amount of "γ"-alumina. It may be deduced that while similar mass transport prevailed, the mass transport was concentrated on fewer growth sites, which were farther apart in the case of alumina A, which thus produced the stronger crust by producing larger and stronger α-alumina platelets.

The formation and break-up of alumina agglomerates must be directly related to the *macroscopic properties* of the alumina agglomerate (size, density, mechanical strength etc.) and these are *determined by the agglomerate microstructure* and microstructure evolution of SGA upon addition to the cryolitic melt. This implies that the alumina's physico-chemical properties,

in particular the nano- and micro- structure of the SGA, will to a great extent control the microstructure of the resulting agglomerates that form upon addition to the melt. This effect of the SGA nano-structure does not preclude the importance of the heat transfer rate in the dissolution area, or other operating-conditions and related variables, that control the material and heat transport in modern Hall-Héroult cells.

2.4.2 Sintering Theory

The process of obtaining a mechanically strong artifact from a powder precursor is termed "sintering". The working definition stated by German [39] is quoted here;

> Sintering is a thermal treatment for bonding particles into a coherent, predominantly solid structure via mass transport events that often occur at the atomic scale. The bonding leads to improved strength and a lower system energy.

The theory of sintering is described by McColm and Clark [116] and by German [39]. A short presentation of the most central concepts is cited here. The thermodynamic driving force of sintering is the reduction of free surface area leading to a lower system energy. The main sintering processes and the stages of sintering are presented in figure 2.2.

As previously described, it has been shown that the alumina microstructure in top crust (from SGA and cryolitic melt), i. e. α- alumina platelets, forms interlinking bridges ("necks") between individual SGA particles, shown in figure 2.1. Neck formation is generally a characterizing feature of partially sintered microstructures, see fig. 2.2. In the relevant case concerning the agglomeration of SGA the bonding forces act between polycrystalline alumina particles, so the situation is very complex and difficult to describe using the classical theory of sintering.

However, the mechanism of agglomeration seems closely related to an initial sintering stage, i. e. a period of wetting by a liquid phase (cryolitic melt), discharge of volatiles (moisture etc.), partial particle rearrangement and rapid crystal coarsening and "recrystallization" during the phase transformation $\gamma \rightarrow \alpha$ of alumina in SGA grains. Basic sintering theory may thus be quite relevant.

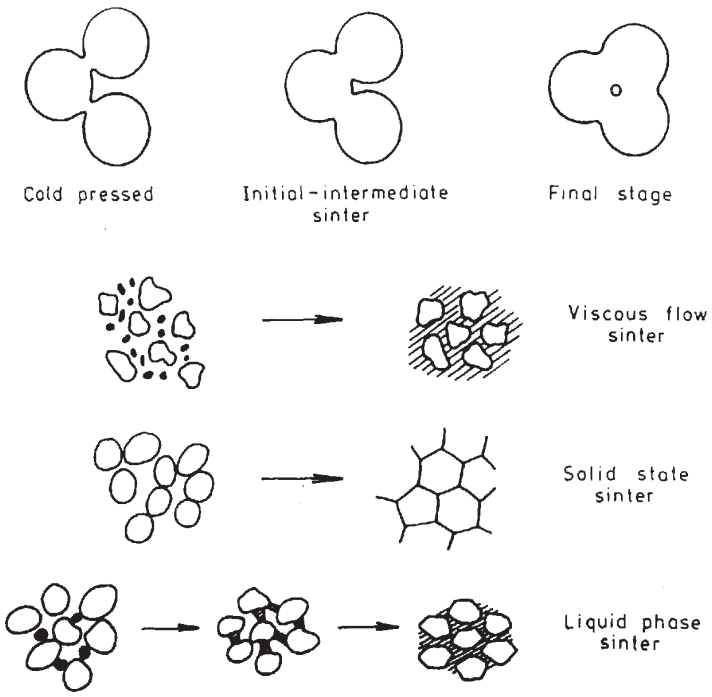

Figure 2.2: *Schematic representation of the stages of sintering and main types of sinter processes. From McColm and Clark [116].*

Sintering Rate and Material Transport

The 6 possible mass transport mechanisms in sintering are presented in table 2.4, [39, 116]. Of these possible mechanisms, (v) surface diffusion, and mechanisms (iii) and (vi) may give rise "neck" growth without densification, [39, 116]. The process of sintering may be divided into 3 distinct stages, [39];

- Initial stage
- Intermediate stage
- Final stage

and liquid phase assisted densification (sintering) may be described by the three stages given in table 2.5, in which the intermediate stage is generally that giving the highest degree of densification [39, 116].

Table 2.4: *Possible mass transport mechanisms in sintering. From [116].*

i	Viscous flow
ii	Plastic flow
iii	Evaporation-condensation
iv	Volume diffusion
v	Surface diffusion
vi	Solution-precipitation

Table 2.5: *Liquid phase sintering may be divided into three stages*

Liquid Phase Sintering (LPS)	Stage
Melting and wetting, rearrangement	Initial
Solution- Reprecipitation	Intermediate
Solid- State Sintering mechanisms (giving final loss of porosity)	Final

The most important parameters governing the sintering kinetics of a sample system, apart from the intrinsic chemistry and particle microstructure (size and shape), are generally the temperature, the time at temperature and the atmosphere and pressure. The rate determining mass transport mechanism is a function of all these. Liquid-phase assisted sintering (LPS) is usually the most efficient method to densify (sinter) a powder at atmospheric pressure.

A physical expression of the sintering rate may be derived by a general approach that considers that the time Δt needed to achieve a given degree of densification or microstructural coarsening is;

$$\Delta t = \frac{V}{JA\Omega} \tag{2.2}$$

where V is volume of mass to be moved, J is the mass flux through the liquid, A is the area proportional to the particle size and the thickness of the liquid film and Ω is the atomic volume. The sintering rate for both liquid phase sintering (LPS) and surface diffusion (SD) derived from such an approach is very sensitive to particle size, being proportional to the fourth power of crystallite size, d;

$$\Delta t_{LPS} = \frac{\beta'' d^4 kT}{D_L \delta_L \gamma_\nu^L \Omega} \tag{2.3}$$

where D_L is the diffusion coefficient of dissolved species in the liquid phase, δ_L is the thickness of the liquid film, β is a combined constant, γ_ν^L is the surface tension of the liquid-solid interface and Ω is the atomic volume of "Al_2O_3". Similarly for surface diffusion;

$$\Delta t_{SD} = \frac{\beta' d^4 kT}{D_{SD} \delta_S \gamma_S \Omega} \tag{2.4}$$

where D_{SD} is the diffusion coefficient in the surface layer of thickness δ_S and γ_S is the surface energy of the disordered surface. The apparent proportionality with temperature T in both eq. 2.3 and eq. 2.4 is somewhat misleading. The expected (logical) inverse proportionality with T is hidden in the diffusion coefficient, which of course increases with temperature. An increase in temperature will usually also increase the solubility in the case of LPS, and increase the liquid volume, which also enhances the mass transport [116, 141, 39].

Surface diffusion if often the dominating mass transport mechanism at the initial stage of sintering, i. e. for relatively low temperatures – resulting in particle coarsening before sintering and densification is achieved, [141, 116].

Crystal Coarsening Mechanism

From such basic sintering theory, we may expect that the dominating mass transport mechanism for the system under study in the present work: i. e. alumina–"cryolitic melt"–moisture, at temperatures in the range 700 - 1000 °C may be expected to be a form of surface diffusion [115, 8]. The complex SGA agglomerate system consists of nano-crystalline α- and transition alumina, the latter with a largely defect, hydroxylated surface, at least partly wetted by liquid phase fluoride ("$NaAlF_4$"), and exposed to an atmosphere with a significant partial pressure of H_2O, HF, AlF_3 and gaseous $NaAlF_4$. Due to the very high surface area of SGA, added liquid phase "$NaAlF_4$" may act more as an adsorbed surface species than a bulk liquid film, unless a large surplus is added. Very limited rearrangement may thus be expected, but the resulting $\gamma \rightarrow \alpha$ phase transformation and crystallite coarsening may be expected to be very rapid.

We may conclude that the dominating mass transport mechanism for the relevant system studied is likely to be surface diffusion, which is non-densifying in nature, and will only lead to partial, initial sintering caused by crystal coarsening, "interlinking" and agglomeration. The kinetics of this mass transport mechanism is very sensitive to particle size, and will greatly increase for decreasing initial particle size (d_0), being proportional to the fourth power (d^4). A coarsening mechanism described in the literature of ceramics where a liquid phase is present is described in the following section.

Crystal Coarsening Theory, LSW

The theory of liquid phase assisted sintering and particle coarsening is described by German [39]. The increasing average crystallite size $\bar{d}$ in a particle-liquid system depends on the initial average particle size ($\bar{d_0}$), on a kinetic parameter K_C which is strongly dependent on temperature, but also on sample system parameters such as the diffusion coefficient, solid-liquid surface energy, solid fraction and the solubility of the solid in the liquid. Assumptions usually made also include spherical particle shape and isotropic surface energy and no particle-particle interaction (!), a mean concentration of solid in the liquid and a quasi-stationary diffusion field. The classic analytical solution to the set of differential equations that apply for liquid phase sintering is known as the Lifshitz-Slyozov-Wagner (LSW) theory, [39]. The theory assumes many factors that are unrealistic for most systems, however,

the assumption of *diffusion- controlled growth* at infinite solid dilution (no particle- particle interaction) leads to an exact solution given as;

$$\bar{d}^3 = \bar{d_0}^3 + \frac{32}{9} K_C t \tag{2.5}$$

and predicts that the maximum grain size will be $\frac{3}{2}\bar{d}$. For more realistic systems the simplified relation becomes;

$$\bar{d}^3 = \bar{d_0}^3 + Kt \tag{2.6}$$

If the rate of crystal growth increases with an increasing liquid volume fraction, it is usually a good indication of diffusion controlled growth. When the system may be described as having *interfacial reaction- controlled growth*, which is more likely in more complex systems, and characterized by irregular or angular grains, the grain-size evolution with time t may be described by

$$\bar{d}^2 = \bar{d_0}^2 + K't \tag{2.7}$$

For such a system, the K''s dependence on temperature will be very strong since the activation energy will usually be high.

For the current study the alumina particle-particle interaction is indeed very crucial since intergrowth and interlinking is the postulated mechanism of agglomeration of alumina grains. According to the theory it seems that the SGA-cryolitic melt system is under interfacial reaction control since the recrystallized, coarse α-alumina platelets have a distinct angular hexagonal morphology. As discussed by German [39], the assumption of infinite dilution is hardly realistic for most systems. A high volume fraction of solids will accelerate grain growth by coalescence through short diffusion distances. In the case of smelter grade alumina, with an exceedingly high surface area, the theory is probably not relevant. It may then be assumed that the liquid fraction of fluorides will spread on the surface, thus increasing its disorder by partial surface "dissolution" and powerful chemical interaction. Thus, within a small "diffusion" layer, the effective surface diffusion of material is likely to enable rapid crystal growth and micro-structure coarsening.

Other Material Transport Effects

As mentioned, the system under study in the present work is very complex, and the literature on the subject usually reports lacking control of

the chemistry, temperature and atmosphere. Two mechanisms that seem relevant for the present work, are mentioned in the literature for complex "sintering" systems involving chemical reactions.

The so-called *Hedvall effect* is observed as an increased reaction rate when material transport, such as during sintering, or a *chemical reaction*, coincides with a phase transformation of one of the reactants. An increase in the reactivity of a reactant during the structural rearrangement of a polymorphic phase transformation is known as *Hedvall's effect* [61]. An example is given as that of the γ-alumina reactant in the reaction with CoO to produce the spinel $CoAl_2O_4$ in which there is a simultaneous transformation above approximately 900 °C [61]. The spinel formed as a layer on the spherical alumina particles.

The reactivity also increases when the contribution of the surface energy of the reactant becomes a significant contribution to the total Gibbs energy of the system. The solubility of γ-alumina may thus be expected to be greater than that of α-alumina since it has a higher surface energy. As proposed by Townsend and Boxall [185], the growth of interlinking platelets of α-Al_2O_3 may be described as preferential dissolution of γ-alumina and reprecipitation on (less soluble) α-alumina. The process in which smaller particles dissolve and larger particles grow is usually termed *Ostwald ripening*, but this is probably not a significant mechanism for the system under study due to the relatively low temperature and short reaction time available.

The so-called *Kirkendall effect* is rather the opposite situation, describing the effect of a chemical reaction dominating the (intended) effect of densification by sintering [39]. The driving force of sintering is usually much lower than a simultaneous chemical reaction, and this may be detrimental to densification in some systems, [39]. Indeed this effect is in general what is seen in the literature on sintering of transition aluminas, to be further discussed later. A transition to the stable corundum phase ("γ"$\rightarrow \alpha$) will largely be completed before a significant densification is possible unless high pressure is used. The transformed microstructure is usually of very high porosity, with a skeletal structure of α-alumina.

2.4.3 "Sintering" Summary

The $\gamma \rightarrow \alpha$ alumina transformation is very rapid when catalyzed by fluorides. Thus, we may conclude that sintering *per se* is probably not the

dominant mechanism operating in the changing microstructure, at least not during the initial stage of agglomeration at a temperature of 700 - 800 °C. However, the combined effect of volatile fluorides and water vapor, both known to catalyze the "γ"$\rightarrow \alpha$ phase transition and to provide rapid mass transport – will provide a very effective mechanism for micro-structural change, i. e. *coarsening*. It may be expected that the mode of mass transport is by surface diffusion, and this assumption is supported in the relevant literature, to be discussed [8, 158].

Based on the available literature and basic theory of sintering, we must assume that the alumina agglomerate microstructure that develops upon interaction with cryolitic melt will depend on;

- Heat Transfer Rate
- Mass Transport Mechanisms, surface diffusion
- Reaction Kinetics
  - Crystal structure of alumina, "nano-structure", seeding
  - Microstructure of alumina, $\gamma \rightarrow \alpha$-alumina
  - Temperature
  - Atmosphere, H_2O, HF, $NaAlF_4$, pressure
  - Chemistry, impurities etc.

The nano- and micro-structure of alumina, including the effect of atmosphere, liquid phase and seeding is the subject of the following sections.

2.4.4 Crystallographic Phases of Alumina

For most smelter grade aluminas (SGA) of the modern, free-flowing "sandy" type, the predominant crystallographic alumina phases are poorly ordered (nano-crystalline) transition aluminas, γ, θ, χ, η, ρ, δ, κ, see [200, 100, 87], that all transform irreversibly to the stable α-phase when heated high enough and long enough. The transformations may also be induced by mechanical activation [183, 208]. The hexagonal/ rhombohedral structure of α-Al_2O_3 is well known, space group $R\bar{3}C$ (167), indeed one of the earliest crystal structures to be determined by X-ray diffraction. Early work on the transition aluminas that form upon dehydration of aluminium hydroxides

is also still quite relevant [105, 203], but work is continuing to elucidate the crystallographic structure models and dynamics of the phase transitions of the less ordered aluminas, ref. [212, 209, 129, 198, 201, 100, 101, 87, 78, 16].

It is now well established that the phase transformation from the transition aluminas to α-Al_2O_3 (corundum) is a nucleation and growth type process [156]. When the crystallites of a θ-alumina matrix reaches a critical size, α-alumina crystals nucleate and grow within the θ alumina matrix [201, 8, 5]. The activation energy E_a for the $\gamma \rightarrow \alpha$ transition in air is around 600 kJ/mol [156]. The E_a will depend somewhat on the method of preparation of the transition γ-alumina and will decrease by increasing the nucleation density, or by efficient mass transfer such as a flux or moisture content in the atmosphere etc. [8, 165]. A study by Simpson *et al.* [161] revealed that the activation energy of the transformations "amorphous-to-γ" and "γ-to-α" in thin films on single crystal sapphire substrates did not depend on the crystallographic orientation of the substrate, though the fastest transformation kinetics were observed to take place on the lowest symmetry orientation due to more effective surface step mobility. The effect of quartz additions illustrates two central features. A cover by amorphous silica on alumina particles impedes crystal growth and hinders the phase transformation, while crystalline quartz provides nucleation sites and enhances the phase transformation and growth kinetics [155].

A recent, comprehensive review of the current state of knowledge concerning the crystallography of the metastable alumina phases is given by Levin and Brandon [100], much based on recent advances in high resolution transition electron microscopy (HRTEM), and structure modeling. The hydrothermal transformation sequences of the transition aluminas and their precursors are given in table 2.6, ordered according to the packing of oxygen anions having either (approximately) hexagonal close packing (hcp) or face centered cubic packing (fcc).

The probable hydro-thermal transformation sequence during calcination of the precursor to SGA, i. e. hydrate from the Bayer process, is [200, 87];

$$\gamma - Al(OH)_3 \rightarrow \gamma - AlOOH \rightarrow \gamma \rightarrow \delta \rightarrow \theta \rightarrow \alpha - Al_2O_3$$

This transformation sequence would seem to be in contradiction to the sequence given in table 2.6. However, the partial pressure of water during calcination of rather coarse Bayer hydrate material seems to favor a transformation involving a boehmite intermediate stage and following sequence given in table 2.6, while in air the sequence via δ and κ is preferred for fine

Table 2.6: *Transformation sequences of the transition aluminas and their precursors, ordered according to the packing of Oxygen Anions being either hcp or fcc., based on Levin and Brandon [100].*

Approximate oxygen packing and transformation sequences (hcp or fcc)
hcp
α-AlOOH (diaspore) $\overset{700^\circ-800^\circ C}{- - - \longrightarrow}$ α-Al_2O_3
γ-$Al(OH)_3$ (gibbsite) $\overset{150^\circ-300^\circ C}{- - - \longrightarrow}$ χ $\overset{650^\circ-750^\circ C}{- - - \longrightarrow}$ κ $\overset{1000^\circ C}{- \longrightarrow}$ α-Al_2O_3
$5Al_2O_3 \cdot H_2O$ (tohdite) $\overset{700^\circ-800^\circ C}{- - - \longrightarrow}$ κ' $\overset{750^\circ C}{- \longrightarrow}$ κ $\overset{900^\circ C}{- \longrightarrow}$ α-Al_2O_3
"Al_2O_3"-Vapor (CVD) $\longrightarrow$ κ $\longrightarrow$ α-Al_2O_3
fcc
γ-AlOOH (boehmite) $\overset{300^\circ-500^\circ C}{-- \longrightarrow}$ γ $\overset{700^\circ-800^\circ C}{-- \longrightarrow}$ δ $\overset{900^\circ-1000^\circ C}{-- \longrightarrow}$ θ $\overset{1000^\circ-1100^\circ C}{-- \longrightarrow}$ α-Al_2O_3
α-$Al(OH)_3$ (bayerite) $\overset{200^\circ-300^\circ C}{- - - \longrightarrow}$ η $\overset{600^\circ-800^\circ C}{- - - \longrightarrow}$ θ $\overset{1000^\circ-1100^\circ C}{- - - \longrightarrow}$ α-Al_2O_3
Amorphous Al_2O_3 (anodic film) $\longrightarrow$ γ $\longrightarrow$ δ $\longrightarrow$ θ $\longrightarrow$ α-Al_2O_3
Al_2O_3 (melt, T $\geq$ 2100°C) $\longrightarrow$ γ $\longrightarrow$ δ, θ $\longrightarrow$ α-Al_2O_3

material, [100, 200]. On the other hand, gibbsite is expected to transform first to ρ-Al_2O_3 in a vacuum [87]. The local nano-structure and atmosphere is clearly decisive in determining the dehydration sequence and final morphology, - consisting of nano-crystallites of transition alumina and voids, [200].

Wefers and Misra [200] point out that the various crystallographic transition aluminas may have been overemphasized in the past as the conversion from hydrate to α-Al_20_3 is a more or less continuous process of solid state reordering in the case of hydrothermal treatment. In particular, various SGA qualities are likely to contain all or any transition phase, including traces of hydrate[4], depending on calcination conditions and technology, but also on the hydrate and bauxite raw material. It is also likely that there will be variations from SGA -grain to grain, even though the microstructure is more

[4]Residual $Al(OH)_3$, aluminium hydrate is unacceptable to most smelters, though traces of the hydrate are not uncommon, especially fines from the alumina refineries' electrostatic precipitators (ESP-dust).

homogenous in modern SGA (using state of the art calciners) than what may be expected from old rotary kiln calciners operating with rather large temperature gradients and material retention times. Liu *et al.* [106, 107] showed that typical modern sandy SGA particles (grains) contain an intimate mixture of α and "γ"-alumina phases. We may conclude that the microstructure and local ordering on the nano-scale level, and atmosphere within the coarse particles, are likely to influence the final structure and crystallography.

Hamberg [51] attempted to correlate the content of different transition aluminas to the (hydrothermal) transformation kinetics of different metallurgical grade aluminas as a function of high-temperature exposure. Unfortunately it was concluded that the results seemed to lack relevance as long as no standard alumina exists for comparison. Furthermore, for a fluoride catalyzed phase transition the hydrothermal transition sequence is probably not directly relevant, since alumina will assumably transform directly to the most stable α-Al_20_3 form, [189, 200].

Bagshaw and Welch [7] found some correlation between the content of certain phases (δ-Al_20_3 in particular) of smelter grade alumina and the alumina's dissolution rate, as determined using the CCD technique. However, the detection of trace amounts of such phases (i. e. δ) by XRD analysis is highly debatable, even using modern full profile analysis [144]. Barton *et al.* [10] discussed the possibility of employing NMR-MAS techniques for the characterization of SGA, which may perhaps provide a better, more relevant description of the content of poorly ordered, X-ray amorphous alumina phases.

SGA contains residual water from the calcination of aluminium trihydrate (gibbsite, $Al(OH)_3$), and modern SGA has a large capacity to absorb moisture in the porous structure, and may thus act as a desiccator. Moisture is an inevitable companion to modern SGA's which have their relatively high specific surface area tailored to meet the requirements of the dry scrubbing process to remove fluorides from the pot off-gases. Apart from fluorinating the alumina with HF and particulate fluoride "$NaAlF_4$", dry scrubbing also enriches the alumina with other volatiles from the pots, including carbon dust, SO_2, Fe, P etc. [176]. The fact that the moisture content is dynamic under normal ambient conditions is the subject of further study in chapter 8.

Moisture, as surface hydroxyl (OH-)groups, is also associated to the transitional crystallographic phases of calcined alumina, which have complex

Table 2.7: *Fluoride assisted transformation mechanisms reported in the literature*

Proposed Reaction Mechanism	Ref.
$2AlF_{3(g)} + 3H_2O_{(g)} \longrightarrow \alpha\text{-}Al_2O_{3(s)} + 6HF_{(g)}$	[158, 61, 127, 189]
$\eta\text{-}Al_2O_{3(s)} + AlF_3 \longrightarrow \{Al_x - O_y - F_z\} \longrightarrow \alpha\text{-}Al_2O_{3(s)} + AlF_3$	[21]
"$\gamma\text{-}Al_2O_{3(sat)}$" $\overset{in Na_3AlF_6}{--\longrightarrow}$ $\alpha\text{-}Al_2O_3$	[185]

surface structures and are catalytically active [119]. Highly porous γ- alumina, which may be phase stabilized with Ce- or La- doping, is widely used as a catalyst support [109, 190]. OH- groups may also adsorb at the highly ordered crystal faces of corundum [123]. There is still some controversy regarding what part the hydroxyl groups/ water play in the transition aluminas crystallographic phase structures, in particular the cubic spinel type structures of γ-,η- and δ- Al_2O_3.

It may be argued that hydroxyl groups are only a part of the surface structure of the various defect cation vacancy structures [167, 206]. The role of H_2O as a probable surface stabilizer for nano-crystalline alumina (both γ- and α-Al_2O_3) is fairly well established [117, 119], explaining some features of porosity and limitations in surface areas. Hydrogen has also been suggested to be a cation component of the bulk structure of the spinel- type transition aluminas, similar to Li in $LiAlO_4$. Sohlberg *et al.* [166] favor the latter view and argue that the transition aluminas γ-,η-, δ- Al_2O_3 are a group of hydrogen spinels, with a propensity for absorbing dissociated water while maintaining stoichiometry and charge neutrality.

Several workers have studied the well known fluoride- assisted/catalyzed alumina phase transition to the stable alpha form [89, 189, 127], and several mechanisms have been suggested, ref. table 2.7. It has been suggested that the transition alumina in SGA is "immediately" transformed to the stable alpha phase upon addition to the industrial, cryolite based, melt [77].

The effective transition temperature in SGA is lowered to about 800 °C in the presence of HF or AlF_3, [89, 127, 189]. Ødegård *et al.* [127] defined the transition temperature (800 °C) to be the temperature at which 50 %

of the sample was converted to α-alumina with 30 min exposure at this temperature. That study used the Greek letter γ (or Υ) as a short notation form of the combination of transition aluminas present in SGA, and this notation is used in the current work as well.

Østvold *et al.* [133] reported that the phase transition temperature is less than 700 °C for SGA samples with added $NaAlF_4$ held at temperature for 20 h. The temperatures measured on top of the dense "sintered" alumina covering the electrolysis cells (i. e. top-crust) has been found to be approximately 400-500 °C, indicating that the transformation temperature is in fact even lower, though the kinetics must be very slow.

For amorphous, sol-gel type, precursors – the formation of α-alumina may be achieved at a much lower temperature, and without the intermediate transition phases and subsequent phase transformation, by seeding and using an HCl, or HF, atmosphere [165, 8].

2.4.5 Microstructure and Particle Size

The typical morphology of α- alumina crystals grown by fluoride mineralizers above 800 °C, such as AlF_3 and HF, are near perfect hexagonal platelets, up to about 1.5 μm thick and approximately 15 μm in diameter [158, 21, 202, 60]. Alumina calcined in air, and at a higher temperature, will generally have a vermicular ("wormlike") morphology where the α- crystal domains form small, porous and irregular colonies of crystals of various orientations [5, 8]. This microstructure in calcined high α-alumina SGA was described as resembling a brain coral by Johnson [75].

Smelter grade alumina of the typical "floury" type (as may be calcined with mineralizers such as AlF_3 or by calcination of fine $Al(OH)_3$ will have grains made up of crystals of a few μm diameter, which greatly reduces the flowability, hence the given name. SGA of the modern typical "sandy" type, as produced by flash calcination of coarse $Al(OH)_3$ agglomerates, have particle grain sizes predominantly of about 45-75 μm, and thus flow and filter like sand. These grains are polycrystalline agglomerates, mostly consisting of transition aluminas with a few % made up of α- alumina crystals. The transition alumina crystallites, probably more accurately described as crystal domains, have an average dimension of around 80 Å as evidenced by line profile broadening in XRD data, while TEM and HRTEM studies report transition alumina crystals more than an order of magnitude larger, in the range 20-100 nm [78, 159, 201].

The typical nano- and micro-structure (if any) of the α-alumina phase in SGA is not known, but this was identified as one interesting starting point for the current study. In any case this phase is the only well defined crystallographic alumina phase present in modern SGA, and may be studied by XRD. Furthermore, the α-alumina crystals will most likely act as seed crystals for the recrystallization process under study.

Since the polymorphic phase transition to α-alumina is a nucleation and growth process, the nucleation density in the alumina precursor matrix phase is very important for the resulting microstructure and particle size of the resulting α-alumina. The nucleation density of α-Al_2O_3 colonies in unseeded boehmite-derived alumina has been reported to be in the range 10^8-10^{10} cm^{-3} [158, 8]. By assuming spherical shape, and that a similar nucleation density might be expected in SGA, and a crystallite-colony size of about 600 nm diameter, the volume of α-alumina would equate to approximately 0.1 % in SGA. The minimum α-content more than an order of magnitude higher than 0.1 % for modern low-α aluminas, and 2 orders of magnitude higher for SGA with intermediate α-alumina contents. A mean crystallite-colony size any larger than 600 nm is probably unlikely, see chapter 5, so we may conclude that the nucleation density, i. e. the number of α-nuclei, is in the order of 10^{13} cm^{-3}, which corresponds to the saturation level found by Shelleman and Messing [160].

Wen and Yen [201] studied the $\theta \rightarrow \alpha$ transition. A controlled heating rate and slow calcination, 1 h at 900 °C, of a boehmite gel produced θ-alumina, which was further heat treated by DTA at 2,5,10 and 20 °C/min and subsequently quenched to RT. The samples were characterized for particle size by XRD (Scherrer line broadening analysis) and by equivalent diameter from the specific surface area (BET) in addition to DTA and TEM. The maximum crystallite size of θ-alumina was determined to be about 20 nm, and the α-nuclei of about 17 nm appeared and underwent rapid growth to a primary crystal size of 45-55 nm, possibly by coalescence of nuclei, when the major transformation to α- alumina also occurred. The size of α-agglomerates, i. e. the secondary particles consisting of the 50 nm primary crystallites, decreased for more rapid heating rates.

A recent study by Kao and Wei [78] also found that the $\theta \rightarrow \alpha$ transition starts by the formation of $\sim$50 nm nuclei α-alumina.

Derdacka-Grzymek *et al.* [26] studied the calcination of industrial aluminium trihydrate, with fixed heat soaking time of 1 h and $1200 < T < 1400$ °C, with and without 0.1-0.2 % fluoride mineralizer additive. Qualita-

tive XRD and SEM was used to characterize the samples, and the authors concluded that samples with fluoride additives gave a smaller particle size. XRD patterns were reported to be identical for all samples, showing only α-alumina. The combination of high temperature and a fluoride mineralizer additive gave regular prismatic, hexagonal, low aspect ratio crystals. The published SEM micrographs appeared to show that the MgF_2 addition gave larger, more well defined crystals than AlF_3, but this was not commented by the authors.

Wójcik *et al.* [205] studied the effect of B and F mineralizers on the morphology of intended specialty alumina (i. e. non-SGA) during calcination of aluminium trihydrate with about half the normal content of Na_2O impurity. The calcination time was varied between 4 levels; 60, 120, 180 and 240 min, while $1250 < T < 1350$ °C. The mineralizers were dissolved in distilled water and intensively mixed (manually) with the hydrate. B was added in the range 1.5-2.25 wt % while the F range was 0.375, 0.5 and 1.0 wt %. After calcination the samples were milled in a rotary vibration mill for 60 min and the d_{50} (i. e. median) particle size was determined by laser-interferometry (CILAS).

SEM micrographs confirmed the particle size, and was used to describe the general morphology of primary crystals. The study showed that the main coarsening effect was noted for F addition, with a saturation level of about 1.0-1.5 wt %, which resulted in platelet crystals with d_{50} of about 6 μm [205]. The addition of B had a limited coarsening effect (max d_{50} about 3 μm) and gave coarse "bean"-shaped crystals, i. e. a form of the so-called "brain coral" or polycrystalline "finger"-shaped crystal colonies described in the literature, [75, 5]. B-addition also showed a greater effect of time and temperature on coarsening, indicating slower kinetics, but this was not commented [205]. Regular solid state diffusion is promoted by B, being more sensitive to effects of temperature and time, and preserving the morphology typical for solid state calcination of α-alumina.

Daimon and Kato [21] reported a SEM-study of the morphology of corundum (α-alumina) crystallized by heating a 4:1 mixture (by weight) of η-Al_2O_3 and reagent grade AlF_3 in air. 20 wt % AlF_3 is obviously a large surplus, [127, 189, 205] . Platelike η-alumina of several hundred microns across was first synthesized by dehydration of a sulfate precursor. Samples were set in a Pt-tube and heated quickly to the set temperature in the range 900 to 1200 °C and held for several hours. Calcined η-alumina (heated to $T > 1200$ °C) was shown to retain the secondary platelike shape of the

precursor sulfate, but consisted of sub-microcrystalline α-alumina, much like calcined SGA which also retains the aluminium trihydrate secondary particle shape.

When the calcined α-alumina was mixed with AlF_3 and heated at 1100 °C for 1 h, the primary crystal size increased (faceted, 2-3 μm) but the secondary platelet structure of the η-alumina precursor still remained intact [21]. Further thermal treatment of the η-Al_2O_3 and reagent grade AlF_3 samples resulted in rather large platelet crystals of α-alumina of random orientation relative to the precursor. The average crystal size after 20 h was largest for 900 °C, at 35 μm, and smallest for 1200 °C (25 μm), while the thickness increased. The samples heated at 1000 and 1100 °C showed intermediate crystal sizes, indicating an approximately linear relationship.

A vapor phase transport model was suggested, in which an intermediate alumina-fluoride species (complex) adsorbs at the basal {0001} plane of the platelets. A similar mechanism has been suggested for the growth of very large platelets from a PbF_2-alumina solution at a temperature near the boiling point of PbF_2 (1293 °C) [202]. The effect of temperature seems to support such a mechanism, since the amount of adsorbed species should decrease with increasing temperature [21]. The platelet orientation and indexes of the nearly perfect center-plane symmetric hexagonal crystals was determined by crystallographic considerations supposing hexagonal symmetry [53]. Differential interference microscopy indicated several trigonal pyramids on the basal plane of crystals formed at 900 °C, and a flatter surface for the 1100 °C samples, indicating a changing growth mechanism with the heating temperature.

Shacklee and Messing [158] studied the effect of seeding, water vapor and HF concentration on the phase transformation $\gamma \rightarrow \alpha$, starting from a boehmite sol and dry γ-alumina powder, using controlled, rapid heating in sealed Pt-Au crucibles. The motivation was to investigate nucleation and growth of monodisperse α-alumina platelets that have a potential commercial use as additives in ceramics and alloys and as abrasives, see chapter 3.

By assuming that the seed concentration determines the number of nuclei and platelet concentration during recrystallization, the average particle hexagonal diameter D, in [cm], is a function of the seed concentration and platelet thickness [158] by;

$$D = \sqrt{\frac{1.24}{Nh}} \tag{2.8}$$

where h is the thickness of the hexagonal platelet. The seeds are assumed to be monodisperse, with a random distribution in a face centered cubic γ-alumina matrix. The highest HF concentration studied, in excess of 2 wt %, gave highly aggregated, thin platelets, while the maximum size of 10-15 μm was achieved with 1.6 wt % HF and a low water content. The study concludes that [158];

> "A system where the water concentration could be kept low, while preventing the buildup of excess reactant vapor (i. e. HF, AlF_3)- and thereby avoiding excessive secondary edge-nucleation- should result in discrete, monodisperse particles, where the particle size is dependent on the number of seed particles"

Block and Lau [13] have patented a method of obtaining α-alumina hexagonal platelets for use as additives to form thermally conductive elastomers. The fixed method uses γ-alumina and 2 wt % AlF_3, samples being held for 30 min at 1200 °C. It is noted that the size and aspect ratio of the platelets depends on the alumina quality used, with a mean (hexagonal) diameter of 2-3 μm for γ-alumina type A to 40 - 50 μm for γ-alumina type B.

Hill *et al.* [60] recently described the effect of HF-concentration, holding time and temperature on the formation of platelets using a method similar to that of Shacklee and Messing [158]. A maximum crystallite size of 30 μm was found for an HF content of 2 wt %, with only 15 μm for higher concentrations (up to 10 wt %).

A method of obtaining rather large α-alumina hexagonal platelets by way of a liquid fluoride flux, such as low melting Li-cryolite, is described in the Elf-Atochem patent by Faure and Bachelard from 1994 [31]. The patent describes a rather wide range of temperature and additives, but the essence of the method resembles the experimental method investigated in the current study, as described in chapter 5.

2.4.6 Sintering of Transition Alumina

The sinterability of alumina has long been known to be increased by using transition alumina, thus exploiting the rapid diffusion processes occuring during the transition to the stable α form. Usually, high pressure is applied in order to obtain dense sinters, and the process may be termed "reactive hot pressure sintering" [39]. Pressure less low temperature sintering, i. e.

T < 1600 °C, of transition alumina exploits the phase transformation and leads to increased sintering rates, but results in a sintered microstructure with high porosity [5]. Further densification is difficult and usually requires a high temperature (T ∼ 1600 °C), as used for the sintering of a conventional α-alumina powder starting material.

In a previous section of this chapter, 2.4.4, it was concluded that the microstructure and local ordering on the nano-scale level, and atmosphere within the coarse particles is likely to influence the final structure and crystallography of SGA by controlling the rate controlling nucleation stage [181]. The nano-structure matrix of α-alumina nuclei and transition phase alumina may well be decisive in the following recrystallization (by α-alumina crystal growth) upon addition to cryolitic melts, and hence important for the postulated agglomeration mechanism of the current study.

Local sintering and grain growth may occur, especially if a polymorphic phase transformation is possible, even in the absence of liquid or gas phase, at a relatively low temperature. The formation of coarse, dense grains (with minimal porosity) will be restricted to the densest part of the aggregates/ agglomerates, first in domains and then in agglomerates [95]. This explains why the sintering of porous transition aluminas produces macro-porous and quite inhomogeneous sintered bodies, with trapped porosity and low bulk density, and may explain why agglomeration may occur even at very low temperatures in SGA.

Tucker [186] observed that the α-phase tended to nucleate and grow at the particle-particle contacts of spherical γ-alumina. The initial sintering and grain growth behavior, and suggested models for sintering in porous alumina, has been studied by Coble and others [19, 95, 181, 48]. Badkar and Bailey [5] and Legros *et al.* [98] have described the increased sintering rate, possible mechanism of pore formation, and limitations of the phase transformation assisted sintering of transition alumina.

Several studies have explored the possibilities of exploiting the phase transformation to promote rapid sintering while avoiding the excessive α-alumina grain growth and porosity, either by seeding, lowering E_a and temperature, or mixing or other form of control of the hydroxide and alumina precursors [25, 52, 98, 93, 115].

Shelleman and Messing [160] studied the combined effect of seeding and liquid phase V_2O_5 (which is liquid at the sintering temperatures used) on the sinterability and greatly increased transformation kinetics of γ-alumina.

A change in the activation energy E_a for 10 wt % V_2O_5 indicated that while the transformation was interface reaction controlled below 850 °C (E_a=402.1 kJ/mol) it is a diffusion controlled solution-precipitation process above 850 °C, with E_a=116.4 kJ/mol. For the 10 wt % V_2O_5 addition, the particle size was one order of magnitude smaller in the maximally seeded material (held 300 s at 1025 °C) compared to the unseeded sample, held 10800 s (i. e. several h) at 1050 °C. At 850 °C, the PSD was largely unchanged in the max. seeded, 10 wt % V_2O_5 system, between 2100 and 7200 s. The absence of Ostwald ripening was argued to be due to a low driving force (high energy activation barrier) of the equilibrium morphology, highly faceted crystal-grains. While the seeding was crucial during the initial phase transformation, the majority of the transformation, by volume, occurs by subsequent crystal growth of α-alumina.

Bagwell and Messing [8] similarly described the increased phase transformation (and sintering) kinetics of γ-alumina by seeding and a controlled water vapor atmosphere. That study found that the E_a was reduced from 567 kJ/mol to 350 kJ/mol in seeded samples in dry air, and further reduced to 177 kJ/mol with water vapor. The transformation temperature for $\gamma \rightarrow \alpha$ was then reduced by about 225 °C. The accelerated kinetics were believed to be due to increased surface diffusion, and the authors concluded that the $\gamma \rightarrow \alpha$ transformation rate could be increased by several orders of magnitude, and was strongly dependent both on nucleation and growth. They conclude by stating that: "water vapor should be minimized during the sintering of α-alumina due to the non-densifying transport mechanism that is accelerated at temperatures ranging from about 800 °C to 1200 °C". We may conclude that water vapor was shown to be an effective coarsening agent, by surface diffusion, in the transition to α-alumina.

Zeng and coworkers [210] found, by applying Herring's scaling law [172], that practical sintering temperatures less than 1000 °C is possible provided that the α-Al_2O_3 particle size is less than 20 nm [210] since the sintering rate is strongly dependent on crystallite size. The initial particle size d_0 is crucial. In solid state sintering the sintering rate is proportional to d^2, while for LPS and for growth by surface diffusion, it is proportional to d^4. Thus the reduction of particle size when gas phase or liquid phase sintering is applied/ occurs produces even greater effects than those of solid state sintering reported by Zeng *et al.* [210]. It may be noted that 20 nm is smaller than the minimum α-crystallite size of about 50 nm when derived via θ-alumina.

2.4.7 Conclusion Part II

The presence of gaseous and liquid fluorides will act as fluxing agents that greatly accelerate the $\gamma \rightarrow \alpha$ phase transition and alumina crystal growth, and that control the crystal morphology (platelets).

Water vapor and seed particles will also influence the kinetics of the transformation and the resulting morphology [158, 8, 61]. Based on studies performed under controlled conditions it may be concluded that the majority phase transformation occurs during the growth phase. While the initial seeding stage is also crucial, and will largely determine the subsequent microstructure (grain size, morphology) - it may be assumed to be intrinsic to the SGA quality and thus largely unaffected by the conditions during alumina feeding in Hall-Héroult process.

2.5 Hypothesis

Based on the literature review and basic theory of sintering and crystal growth, it is proposed that the content of α-phase in each smelter grade alumina (SGA) grain will act as nuclei for further crystal growth. The distribution, size and quantity of these nuclei can best explain the difference between the crust-forming and dissolution behavior of otherwise quite similar SGA, i. e. aluminas having similar measurable physico-chemical properties. Though the process is complex, we propose that it is probably the nano-structure (i. e. sub-micron) of each SGA grain, including the α-alumina seeds, that will determine the agglomeration behavior of a given alumina quality otherwise fulfilling modern, rather tight, SGA specifications.

2.5.1 Model

Basic dissolution kinetics may be assumed to be mass transfer controlled, and may be expressed by a simple differential equation such as eq. 2.1. The rate of dissolution is proportional to the effective (apparent) contact area between the alumina (solute) and the cryolitic melt(solvent), which may be expressed as part of an effective mass transport coefficient k'. The formation and break-up of alumina agglomerates upon addition to the melt is thus crucial for the dissolution rate obtained, since the amount of agglomerates

will largely determine the available (apparent) surface area of each alumina feed.

We propose a model involving the nucleation density available for further growth of large hexagonal platelets of α-Al_2O_3, correlated to the initial content of α-alumina of the SGA, probably in a complex, non-linear manner.

The assumption that alumina agglomeration occurs by partial interlinking of neighboring grains, has been discussed in the literature. We propose that the mechanical strength of such agglomerates, that we may call "agglomerate strength" (AS), should be proportional to the contact area between neighboring alumina grains ($d_{interface}$). Such an interlinking microstructure is the result of the interaction between SGA and the cryolitic melt. While the various variables intrinsic to the cryolitic melt and other process variables have been the subject of many studies, the nano-structure of SGA remains largely an uncharted territory.

The resulting microstructure of the reacted SGA, i. e. the size and density of the resulting α-alumina platelets, may be assumed to be related to the initial "seed concentration", i. e. the nucleation density (N_α) of the α- Al_2O_3 phase in SGA, most likely related to the initial α-content of the SGA, though probably in a complex manor. The simple model may be expressed by the following relation;

$$AS \propto d_{interface} \propto \frac{[Al_2O_{3(transition)}]}{N_\alpha} \tag{2.9}$$

It is assumed that the α-alumina nuclei in the alumina will act as crystal seeds during the further nucleation and growth of the stable alumina phase from the transition aluminas present in SGA. The transition is effectively catalyzed by fluorides, moisture and the high temperature present in the cryolitic melt. The nucleation density N_α is assumed to be related to the content of α-alumina, which is routinely measured, but it may be expected that different alumina qualities have different nano-structures, though the content of α-alumina is similar. Since every grain of smelter grade alumina has a specific volume of transition alumina, the average α-alumina platelet volume of the recrystallized α-alumina microstructure may be expected to be inversely proportional to N_α.

The preferred crystal morphology is the hexagonal platelet form, with the basal plane perpendicular to the [0001]-direction, usually denoted [001], [53]. The stability of the transition alumina matrix should be related to the density, local order and content of the various transition aluminas.

The initial crystallite size distribution within each alumina grain will control the initial rate of transformation and crystal coarsening. The mass transport rate, transport distance and the dominating mechanism of mass-transport, i. e. solid state, vapor phase or liquid phase, is also critical. Environmental factors such as temperature, duration of exposure at the relevant temperature, atmosphere and the presence of impurities may control the preferred mass-transport mechanism, which is probably by some form of surface diffusion in the relevant case. The "steady state" microstructure thus evolved may be specific to each set of these intrinsic and dynamic extrinsic conditions for a given alumina quality and operating conditions of the alumina reduction cell. In practice, the interaction of SGA and cryolitic melt is likely to be chaotic on the micro-scale level. Thus, in order to study such interactions quantitatively, a controlled experiment must be designed – allowing reproducible results.

2.6 Scope of This Study

The current study has an emphasis on the evolution of microstructure of alpha alumina in agglomerates that we consider to be the process of inter-particle bonding and hence an important aspect of alumina agglomeration. The agglomerate microstructure forms during the recrystallization of alumina during the interaction of SGA, volatiles and the electrolyte. The heat transfer rate to the affected dissolution area in the electrolyte may be rate determining for the formation and break-up of agglomerates, though it is not the rate determining step for the dissolution of alumina *per se*. The clogging of feeder-holes and the formation of slow-dissolving agglomerates ("rafts" or lumps) upon addition are related to the alumina's tendency to aggregate and sinter. This mechanism is related to the rapid phase transition from the metastable transitional phases in the alumina to the stable α-Al_2O_3 phase (corundum). The resulting alumina morphology is typically aggregates of hexagonal platelets when the growth of corundum crystals is assisted by the presence of fluorides.

The present study concentrates on the time-scale of the dissolution process (seconds and minutes) and we focus on the kinetics of the evolution of an interconnected network of α-Al_2O_3 platelets. This will retard the dissolution process by;

- Providing mechanical strength to the agglomerates (cm scale)

- reducing the available surface area for dissolution (several orders of magnitude)

Agglomerates of alumina of altered physico-chemical properties and microstructure are thus exposed to the electrolyte. The following dissolution process involves the dissolution of agglomerates with a wettable surface area that is several orders of magnitude less than that of the free-flowing, and ideally dispersed, powder. Together with this reduction in surface area there is a corresponding loss of volatiles of which mainly moisture, OH-groups, carbon and fluorides are considered here. It is generally believed that the presence, and subsequent loss, of volatiles help to disperse the alumina and provide a porous structure in the agglomerates.

The working hypothesis is that the average alpha alumina particle (crystallite) size is expected to increase during the "sintering" and phase transition process. The α-alumina particle growth rate should increase with temperature and be greatly accelerated if (liquid) fluorides are present. The average particle size may depend on the reaction growth mechanism, local chemistry and mass transport conditions. In order to test the hypothesis, the study focuses on the expected correlation of the α-alumina content, crystallite size and strength of alumina agglomerates.

The experimental design chosen for the study is aimed at determining the main microstructural parameters involved in the formation of alumina agglomerates, by controlled laboratory experiments. Different exposure conditions including temperature, atmosphere, melt composition and different alumina quality should then be possible to control. Alumina agglomerate dissolution will also be studied and related to the various microstructures and the resulting strength and/ or dissolution behavior.

Thus, by subsequently attempting to relate the dissolution behavior of alumina agglomerates with a well defined history, we shall attempt to describe the mechanism of agglomerate formation and dissolution, and if possible confirm the observations of what resembles "snow-flakes" of alumina in the electrolyte during dissolution. This would be an important contribution to the understanding of alumina dissolution in cryolitic melt, and may form the basis of a more advanced, more accurate physical – mathematical model than those based on a simple "shrinking grain" model.

The scope of the current study may be summarized as;

- Literature study, including relevant ceramics literature, present chapter

- Sample preparation using relatively simple, proven techniques
- Relatively advanced XRD data-collection and data-analysis.
- Electron microscopy, SEM
- BET and various thermal/ gravimetric techniques.
- Optical Study of Alumina Agglomerate Dissolution

Chapter 3

Characterization Methods

3.1 Introduction

There are many more techniques available today, for the study of a particulate material such as smelter grade alumina (SGA), than there were when the modern study of SGA started, and indeed more techniques than would be possible to persue in a single study. Roach *et al.* in particular, have described most of the common techniques used and several promising methods for "unmasking the mysteries" of aluminium hydrates and alumina, [143, 145, 142, 33].

Many promising characterization tools have been ruled out, at least as routine methods, due to lack of resources, too difficult sample treatment, unwanted fluoride attack of apparatus or experimental relevance. Neutron diffraction was investigated as a possible method, since a sealed sample container in stainless steel may be used to contain smelter grade alumina and cryolitic melt for *in situ* studies of the interaction product: alumina agglomerates. However, such a technique was ruled out due to limited spectral and time resolution. A more conservative approach was chosen for the micro-structural study, using X-ray powder diffraction (XRD), supported by scanning electron microscopy (SEM), surface area determination (BET-method) and various more simple laboratory techniques.

A short description of X-ray diffractometry, scanning electron microscopy and some background for the agglomerate strength determination used in the present study is given here.

3.2 Powder X-ray Diffractometry

The theory of X-ray diffraction and its use in materials research is described at length in various text books, [40, 84, 96], and only the basic concepts and relevant use is presented in this section.

3.2.1 General

All X-ray powder diffraction (XRD) work in this study was carried out using a Siemens D5000 instrument (XRD A at the Department of Chemistry, NTNU) equipped with a graphite monochromator. The incident radiation on the sample is thus stripped of the Cu-$K_{\alpha 2}$ contribution from the Cu X-ray target source, but also has relatively low intensity. Data is collected and analyzed using the Siemens D5000 instrument suite of programs.

Unless otherwise stated, every sample analyzed by XRD was crushed by hand using a small alumina mortar and pestle. Approximately 0.9 g sample was emplaced and lightly pressed in place in the rotating sample holder (60 rpm standard) using a glass microscope sample plate. The XRD instrument has variable slits that ensures a constant irradiated sample area, –which otherwise is a function of the diffraction angle (2θ). The sample rotation ensures that the diffraction data is collected from a truly homogenous, isotropic sample.

The basic theory of X-ray diffraction and the experimental techniques employed in the current study is presented in the following sections. The techniques used are both qualitative and quantitative phase analysis and line profile analysis of the diffraction peaks.

3.2.2 Basic Theory

X-ray diffraction is due to the interaction of incident X-rays with the electron distribution in a crystalline material. The following largely mathematical treatment of diffraction theory is based on Giacovazzo [40].

A crystal is the periodic 3-dimensional arrangement of molecules, or other asymmetric material structure with an electron density ρ_M, within unit cells in a lattice. Mathematically, a 3-dimensional infinite lattice may be

described as;

$$L(\vec{R}) = \sum_{u,v,w=-\infty}^{+\infty} \delta(\vec{R} - \vec{R}_{u,v,w})$$

where the lattice vector $\vec{R}_{u,v,w} = u\vec{a} + v\vec{b} + w\vec{c}$ (u, v, w are integers) and δ is the common δ-function[1]. The electron density function for the infinite crystal is given by;

$$\rho_\infty(\vec{R}) = \rho_M * L(\vec{R})$$

which is the mathematical convolution of ρ_M and $L(\vec{r})$. It may be shown that the amplitude of a photon wave scattered from a collection of electrons in a direction defined by the scattering vector $\vec{K}$ (defined below), may be expressed as the Fourier transform of the electron density;

$$F(\vec{K}) = \int_{j=1}^{N} \rho(\vec{r}) e^{2\pi i \vec{K}\cdot\vec{r}} d\vec{r}$$

F($\vec{K}$) is usually called the atom form factor for a point collection of electron density, such as that of an atom, while F($\vec{K}$) for a crystal is termed the structure factor. Thus, the scattered amplitude, or *structure factor*, for a crystalline material may be written as;

$$\begin{aligned} F_\infty(\vec{K}) &= \rho_M * L(\vec{R}) \\ &= \frac{1}{V} F_M(\vec{G}) \cdot \sum_{h,k,l=-\infty}^{+\infty} \delta(\vec{K} - \vec{G}_{hkl}) \end{aligned}$$

where V is the volume of the unit cell and $\vec{G}$ is the generic reciprocal lattice vector, defined by $\vec{G}_{hkl}$=$h\vec{a*} + k\vec{b*} + l\vec{c*}$, where h, k, l are integers, and $\vec{a*}, \vec{b*}, \vec{c*}$ are the reciprocal lattice vectors related to the (material) lattice vectors by;

$$\begin{aligned} \vec{a*} &= \frac{1}{V}\vec{b}\cdot\vec{c} \\ \vec{b*} &= \frac{1}{V}\vec{c}\cdot\vec{a} \\ \vec{c*} &= \frac{1}{V}\vec{a}\cdot\vec{b} \end{aligned}$$

[1]Dirac's δ-function: $\int_{-\infty}^{+\infty} \delta(t)dt = 1$, and $\delta(t) = 0,\ t \neq 0$.

In crystallography k-space is called reciprocal space, and in a crystal the scattered amplitude is thus only non-zero when $\vec{K} = \vec{G}$. The scattering vector $\vec{K}$ is defined as;

$$\vec{K} = \frac{1}{\lambda}(\vec{s} - \vec{s}_0),$$

and

$$|\vec{K}| = \frac{2sin\theta}{\lambda},$$

where the unit vector $\vec{s}_0$ defines the direction of an incident radiation beam, while the scattered beam has a unit vector $\vec{s}$ at an angle 2θ relative to $\vec{s}_0$. The so-called *Laue conditions* for diffraction are obtained by scalar multiplication with the lattice vectors so that;

$$\begin{aligned} \vec{a}\cdot(\vec{s} - \vec{s}_0) &= h\lambda \\ \vec{b}\cdot(\vec{s} - \vec{s}_0) &= k\lambda \\ \vec{c}\cdot(\vec{s} - \vec{s}_0) &= l\lambda \end{aligned}$$

The electron density function of a finite crystal lattice, ρ_{crys}, may be expressed as;

$$\begin{aligned} \rho_{crys} &= \rho_\infty \Phi(\vec{r}) \\ where & \\ \Phi(\vec{r}) &= 1, inside \\ \Phi(\vec{r}) &= 0, outside \end{aligned}$$

so that the structure factor becomes;

$$\begin{aligned} F(\vec{K}) &= F_\infty(\vec{K}) * D(\vec{K}) \\ where \quad D(\vec{K}) &= \int_S \Phi(\vec{R}) e^{2\pi\vec{K}\cdot\vec{R}} dR \\ &= \int_\Omega e^{2\pi\vec{K}\cdot\vec{R}} dR \end{aligned}$$

and Ω is the volume of the crystal. Furthermore, since $\vec{R}_j = \vec{r}_j + \vec{r}_0$, ($\vec{r}_j$ being the position of a scatterer within a unit cell and $\vec{r}_0$ is the origin of the unit cell with respect to the lattice), then the total scattered amplitude becomes;

$$F(\vec{K}) \propto L_{hkl} \cdot \sum_{j=1}^{N} f_j e^{2\pi\vec{G}\cdot\vec{r}_j} = L_{hkl} \cdot F_{hkl}$$

where f_j is the scattering factor of the j'th scatterer. The *Structure factor* (F_{hkl}) thus only depends on the positions of the scatterers within the unit cell while the *Lattice form function* L_{hkl} only depends on the crystal lattice, having maxima given by the Laue conditions. The structure factor is often written as $F_{\vec{G}} = |F_{\vec{G}}|exp(i\phi_{\vec{G}}$, where $\phi_{\vec{G}})$ is the phase of the structure factor.

For powder diffraction the integrated intensity of an observed diffraction peak may be expressed as, [40];

$$I(\vec{G}) = K_{exp} \cdot |F_{\vec{G}}|^2 \cdot m(\vec{G}) \cdot A_\mu \cdot (LP)$$

where K_{exp} is a scale factor, depending on various experimental parameters. The term $m(\vec{G})$ is the multiplicity of the (hkl) peak corresponding to $(\vec{G})^2$ while A_μ is the X-ray sample absorption factor and (LP) is a factor depending on the angle-dependent Lorentz factor and X-ray beam polarization. The sample is assumed to be free of texture (isotropic). Sample texture will affect the diffraction pattern intensity distribution due to preferred crystallite packing directions of anisotropic powder samples.

Because the peak intensity is proportional to $|F_{\vec{G}}|^2$, all phase information, i.e. the information of the position of each X-ray scatterer, is lost – and this is known as the *phase problem* in crystallography.

A useful picture of the diffraction condition $\vec{K} = \vec{G}$ is that known as the *Ewalds construction*, see fig. 3.1. The angle $2\theta_{hkl}$ defines the position of the reflection on the *Ewalds sphere* of radius equal to the reciprocal of the wavelength λ. The diffraction condition $\vec{K} = \vec{G}$ is equivalent to Bragg's law (eqn. 3.1), since the cord length defined by the scattering vector is;

$$|\vec{K}| = |\vec{G}| = 1/d_{hkl} = \frac{2sin\theta_{hkl}}{\lambda}$$

and it may be seen that the reciprocal lattice vector is perpendicular to the scattering plane (d_{hkl}).

3.2.3 Qualitative XRD

Qualitative phase identification using powder X-ray Diffraction (XRD) is based on the well known diffraction condition known as *Bragg's law*;

$$2d_{hkl}sin\theta_{hkl} = n \cdot \lambda, \qquad n = 1, 2, ... \tag{3.1}$$

[2]Every (hkl) peak in a powder diffractogram may be a combination of some or all of the diffraction conditions/planes given by the integers ±h, ±k and ±l with the same 2θ given by Bragg's law: $d_{hkl} = n\lambda/2sin\theta_{hkl}$

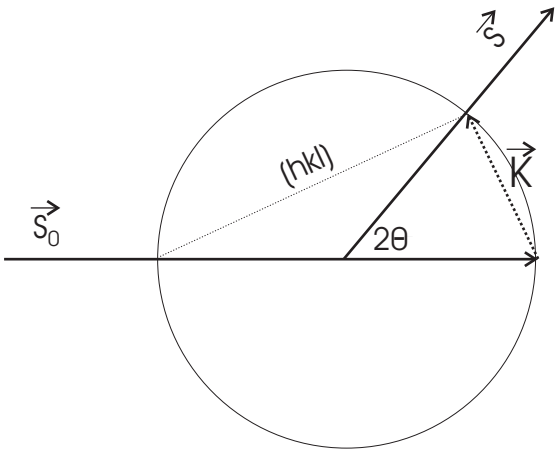

Figure 3.1: *Ewalds construction showing the diffraction condition* $\vec{K} = \vec{G}$.

where d_{hkl} is the plane spacing of the plane corresponding to the observed diffraction peak, θ_{hkl} is the scattering angle corresponding to the observed $2\theta_{hkl}$ peak position (as diffracted intensity is usually recorded as a function of scattering angle) and λ is the wavelength of the X-ray radiation used (λ=1.5418 Å for Cu-K_α). A comprehensive database covering most known crystalline materials is compiled in The Powder Diffraction File which may be used in a search and match routine to identify the presence of crystalline phases in a powder sample.

Experimental

Powder samples were prepared and set in the sample holder as previously described for XRD analysis. Diffraction data was usually collected for $2\theta \in (20, 80)^\circ$ with 40 s per step of 0.04 °2θ.

3.2.4 Quantitative XRD

Quantitative phase determination based on X-ray powder diffraction may be carried out by using a reference material blended with the sample, and a predetermined calibration curve for the relative diffracted intensity. In the case of allotropic compounds, i. e. a polymorphous material of a single chemical compound, such as polycrystalline, polymorphic alumina - the

diffracted intensity of the α-Al_2O_3 phase of the sample, proportional to the phase content, will be proportional to the diffracted intensity of a 100 % α-Al_2O_3 standard;

$$[\alpha] = \frac{I_{024}(sample)}{I_{024}(\alpha - std)} \tag{3.2}$$

The integrated intensity of a single, well defined peak may be used, such as the peak (hkl)=(024), at 2θ=52.5 °.

Experimental

Tablet agglomerate samples obtained by the method described in chapter 5, were analyzed by XRD in order to determine the degree of $\gamma \rightarrow \alpha$ phase transformation attained. Standard 100 % α-Al_2O_3 samples were prepared by calcining primary smelter grade alumina (SGA) at 1200 °C for 5 h in a muffle furnace. The fully transformed samples were confirmed to contain well resolved diffraction peaks of α-Al_2O_3 and no other crystalline phases.

Tablet agglomerates and powder samples were prepared and set in the sample holder as previously described for XRD analysis. Diffraction data of the (024) peaks of α-Al_2O_3 was collected, using identical experimental parameters for both analysis samples and standard. The data was collected for $2\theta \in (51.7, 53.3)°$ with 40 s per step of 0.04 °2θ.

In order to get optimal results a typical data collection procedure involved the collection of 10-15 data-sets with several standard samples spaced at 3-4 sample intervals. It was observed that the XRD instrument intensity decreased linearly during the course of 12-24 h. The diffracted intensity of peaks collected in data-sets from separate days, or even separated by more than 1-2 h should not be used for quantitative phase determination by this procedure. However, by averaging the intensity of all standard data-sets collected during the course of a each sampling procedure campaign (of up to 8-10 h) reproducible, precise and accurate results were obtained. Data collected using this procedure could be compared with that reported for SGA by similar procedures used in the aluminium industry, ref. Australian Standard AS2879.3-1991.

3.2.5 Line Profile Analysis

In theory it is possible to determine the micro-structure and microstrain of a polycrystalline material from the intensity distribution of the X-ray

diffraction peaks, [96, 84, 40].

Modern 3^{rd} generation synchrotron X-ray diffraction instruments, such as that of the beam lines SNBL and BM-16 at the ESRF (in Grenoble, France) have powder diffraction peak line profiles given, in practice, entirely by the sample broadening effects since such X-ray sources gives a nearly perfectly planar, parallel radiation beam. In addition to the vastly greater X-ray flux,- synchrotrons thus provide a very useful, though rather costly, tool for materials research [30, 175, 4, 102]. However, only a standard, though quite modern, XRD instrument (Siemens D5000) was available for this study. Useful work may be performed with a conventional source also, [164, 103, 104, 83], and it was partly the aim of this study to determine this possibility for SGA.

Scherrer Broadening

The best known (and most practical) example of microstructural study using XRD is that the average crystallite size ($\bar{L}$) in a given diffraction plane direction $< hkl >$ may be estimated in [Å] by the classic Scherrer equation;

$$\bar{L} = \frac{0.89\lambda}{\beta cos\theta_{hkl}} \tag{3.3}$$

where 0.89 is a sample crystallographic constant, λ=1.5418 Å is the X-ray wavelength used, β is the diffraction peak width at half maximum (FWHM) corrected for the instrument contribution and θ_{hkl} is the diffraction angle of the peak, approx. 26.25 ° for (hkl)= (024) in the case of α-Al_2O_3.

The Warren-Averbach Method

The *Warren-Averbach method* is a relatively advanced procedure of obtaining information of both crystallite size and strain from the diffracted intensity distribution of well resolved powder diffraction peaks. The method was developed for cold- worked metals (crystalline "powder" materials), and works best for such simple structures with relatively few and well resolved diffraction peaks. An introduction may be found in the review article of Langford and Louër [96], but the method is best described by Warren [199]. The observed intensity distribution of a powder diffraction peak, for every

observation position x, (or observed 2θ), may be expressed as a Fourier series, [199];

$$y_{obs}(x) = \sum_{n=-\infty}^{\infty} \{A_n cos(2\pi nx) + B_n sin(2\pi nx)\} \tag{3.4}$$

where

$$A_n = \frac{N_n}{N_3} < cos(2\pi l Z_n) >$$

Usually the *sine* term is neglected for further analysis. N_3 is the average number of unit cells in the crystallite column perpendicular to the diffraction plane d_{hkl} of the observed peak. The total number of cells of the diffraction domain volume is $N = N_1 N_2 N_3$, where N_1 and N_2 are the number of cells in the two other directions. The average $< cos(2\pi l Z_n) >$ represents the average over pairs of n'th neighbors in all columns of the sample, weighted by the number of cells in the column N_n. The *cosine* coefficient may be expressed as a product of size (S) and strain (D) dependent terms;

$$A_n = A_n^S A_n^D$$

where

$$A_n^S = \frac{N_n}{N_3} \qquad A_n^D < cos(2\pi l Z_n) >$$

and the experimentally determined value of A_n must be normalized to unity (1) for $n = 0$ since $N_n = N_3$ and $Z_n = 0$ for $n = 0$.

By determining the coefficients A_n^S and plotting A_n^S *vs* n, the initial negative slope will directly give the average column length N_3 by;

$$-\left(\frac{dA_n^S}{dn}\right)_{n=0} = \frac{1}{N_3} \tag{3.5}$$

and the distribution of column lengths may be found from the second derivative [199]. If it is assumed that several orders of the same diffraction peak is available, for instance 2 or more peaks $[00l]$, then for small n and l one may write;

$$lnA_n(l) = lnA_n^S - 2\pi l^2 < Z_n > \tag{3.6}$$

stating that the Fourier coefficient is a sum of order independent size terms A_n^S and order dependent strain terms. By plotting $lnA_n(l)$ *vs* l^2 from equation 3.6, the strain broadening term may be found by extrapolating the nearly straight line obtained to $l = 0$.

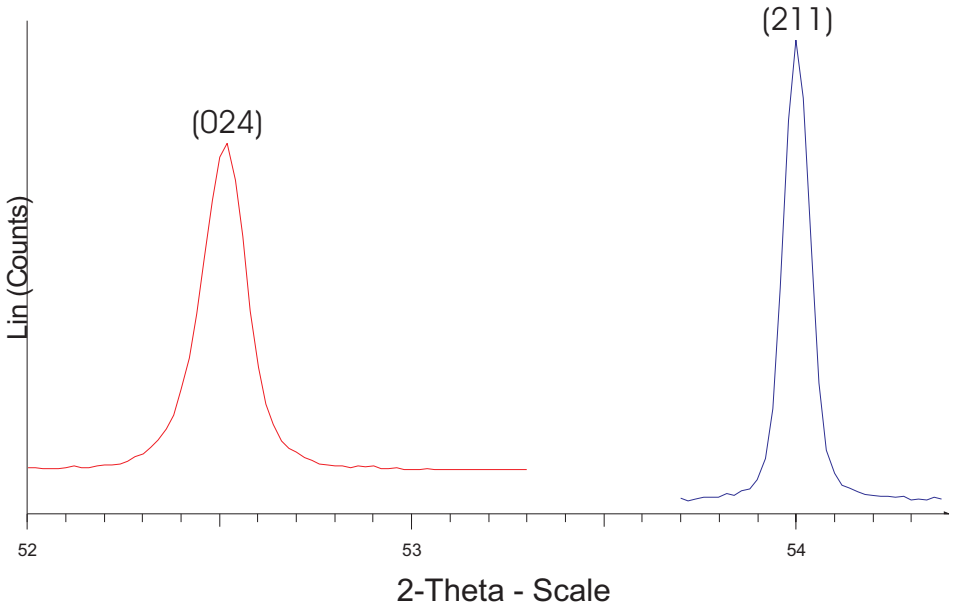

Figure 3.2: *High resolution diffraction peaks used for line profile analysis: (024) peak of α-Al_2O_3 and (211) peak of the LaB_6 standard reference material. See text for details of data collection.*

Experimental

The line shape contributions from the XRD instrument optics must be determined using a standard reference material (SRM), in this case LaB_6 was used. In practice, for materials with limited line profile broadening, a high resolution data collection method and instrument must be used. The instrument used is the same as that for the other XRD work reported here, though the data collection procedure was optimized and very long data collection times had to be used.

Truncation errors resulting from the Fourier analysis are inevitable due to cut-off in the tails of experimental diffraction peaks. It is essential that good diffraction intensity statistics are available, i.e. a high peak to background ratio[3]. The diffraction peaks of the (024) peak of α-Al_2O_3 and (211) peak of the LaB_6 standard reference material are shown in figure 3.2. The measured

[3]Peak-to-background ratio for XRD equates to the signal-to-noise ratio.

FWHM of the peaks is 0.135 and 0.081 °2θ respectively. The LaB_6 peak represents the instrument contribution to the diffraction peak, which is close to what is experimentally possible using an instrument with a conventional closed X-ray tube source. The minimal FWHM of such an XRD instrument is generally assumed to be in the region of 0.07 °2θ, as demonstrated in this work also for lower diffraction angles 2θ.

Tablet agglomerates and powder samples were prepared and set in the sample holder as previously described. Diffraction data of the (012) and (024) peaks of α-Al_2O_3 was collected for $2\theta \in (24.7, 26.3)^\circ$ and $2\theta \in (51.7, 53.3)^\circ$ respectively with up to 3 consecutive scans of 160 s per step of 0.02 °. Several powder diffraction data sets may thus be collected and later treated as a single data-set, (since 3 scans of 160 s per step is equivalent to a single scan of $3 \cdot 160$ s = 480 s), since diffraction data obeys Poisson statistics, ref. [28]. According to Possion statistics the peak to background ratio of diffraction data, i.e. the quality of the data, follows the relation $\sigma \propto 1/\sqrt{N}$ were N is the number of counts. Thus, by increasing the number of counts by a factor of 4 the peak to background ratio is improved by a factor of 2. Practical considerations (instrument counting time) and experimental effects such as the stability of the instrument X-ray intensity and possible sample deterioration may limit the counting statistics obtainable.

The XRD pattern for the LaB_6 standard reference material was collected from a thinly dispersed powder sample fixed to a piece of double sided tape to the sample holder. Data was collected using standard instrument optics for $2\theta \in (20, 80)^\circ$ and 40 s per step of 0.04 °2θ. Diffraction data for the single (211) peak was also collected using the same procedure as that for the single α-Al_2O_3 peaks.

For the Warren-Averbach analysis at least 6 peaks of LaB_6 were fitted to a Pearson VII model function, ref. Appendix C, and used as the standard reference profile of a peak at the position of the α-Al_2O_3 peaks. Diffraction data for the (024) peak of α-Al_2O_3 in the sample was then fitted by a Pearson VII model function Φ such that;

$$y_{calc}(x_i) = \sum_j A_j \Phi(x_i - x_j) + b(x_i),$$

for every position x_i, where A_j is the calculated area of the j'th peak and $b(x)$ is the background. The fitted sample profile function and standard (instrument) profile were then analyzed using the Warren-Averbach method as implemented in the Siemens Crysize computer software. The sample was

assumed to only have particle size broadening effects, so that only the single (024) peak of α-Al_2O_3 was used. The possible presence of strain cannot entirely be ruled out, but this was not studied in the current work. Typical results from Crysize and the profile fitting routines are presented in the Appendix C and D.

3.3 Scanning Electron Microscopy

The theory and practice of scanning electron microscopy (SEM) is thoroughly described in the textbook by Goldstein *et al.* [43]. Only the most basic concepts are presented here.

3.3.1 Theory

In principle a SEM uses electron optics (electro-magnets) in order to focus an electron beam on the surface of a sample. The electron beam may be stationary or scanned across the sample in a similar way as that of the electron beam in a cathode ray tube (CRT) display, [43]. Backscattered electrons (BSE) may be collected by an amplifying scintillation type detector coupled to the scanning rate on the sample so that the detected signal is scanned on a viewing CRT display. A monochrome image of the sample is thus produced on the display since the emission of electrons from the sample will vary according to the sample topography and chemical composition.

Detected Signals

Upon interacting with the sample, the incident high energy electron beam (the accelerating voltage may be varied in the range 1-40 kV) results in a range of signals that may be detected and analyzed, [43]. These signals include back-scattered electrons due to elastic scattering and several signals originating from inelastic scattering processes; secondary electrons, Auger electrons, X-ray and other wavelengths of electromagnetic radiation. Finally the sample current may be monitored since the sample must be grounded in order to avoid charge build-up. Compared to an optical microscope the SEM has a superior depth of focus in addition to increased magnification -

allowing near 3-dimensional images of topographic samples. A rough surface will stay in focus unless the roughness exceeds D given by;

$$D = \frac{1}{\alpha}\left(\frac{\delta}{M} - d\right)$$

where α is the beam divergence, δ is the resolution of the human eye (about 0.1 mm), M is the magnification and d is the beam size (given by the electron-optics). For typical values ($\alpha = 5{\cdot}10^{-3}$ [rad], M= 1000 $\times$ and d= 50 Å) the field/depth of focus D in a SEM is thus approximately D=10 μm.

Basic Optics

The filament current is emitted from a small tungsten or LaB_6 electrode and is typically 100 - 200 μA, while the distance between the sample and the objective condenser (electro-magnetic) lense is termed the "working distance" (WD) of the SEM. An objective aperture is used in order to reduce the divergence of the condenser lense. A short WD and small aperture will minimize the beam size on the sample and result in optimum image resolution, while a longer WD and larger aperture will maximize the depth of focus (field of focus), [43], i.e. in perfect analogy to optical photography. The minimum beam diameter is also a function of the beam current and accelerating voltage (E), minimized for high E and low beam current.

Sample Preparation

Any sample to be examined by SEM must be mounted such that the sample is electrically grounded, and the sample must be stable in the high vacuum, electron-irradiation environment. Usually a non-conducting sample is coated by a thin layer of carbon or gold prior to imaging. In modern environmental SEMs (ESEM) the sample chamber has a relatively high pressure (of around 10^{-2} atm) so that non-conducting and even organic samples may be imaged directly without the need for careful preparation, carbon-copying etc., [43]. Phase contrast imaging and chemical analysis requires flat polished samples.

EDS and WDS

Qualitative and quantitative chemical information may be obtained from the characteristic X-ray emission from the sample under irradiation by the

electron beam [43]. Characteristic radiation is due to specific excitations that are unique to each element. Characteristic X-ray photons may be described by the energy-wavelength relationship;

$$\lambda E = \frac{hc}{e} = 12.4$$

where λ is the photon wavelength in [Å], E is the photon energy in [keV], h is Plank's constant, e is the electron charge and c is the speed of light. Probably the best known characteristic X-ray photon wavelength is that of Cu-K_α produced in X-ray tube sources and used for X-ray instruments such as for XRD previously described in the current chapter. Dedicated SEMs for chemical analysis of samples are usually termed electron probe micro analysis (EPMA) instruments and are equipped with solid state or scintillation type gas chamber detectors based on energy dispersive spectroscopy (EDS) or wavelength dispersive spectroscopy (WDS). Most SEMs are equipped with an EDS analyzer, while the more complex, higher resolution WDS analyzers (which use analyzer crystals) are only found on dedicated EPMA instruments, [43]. Small shifts in the characteristic energy due to chemical bonding may be observed for some elements by using a high resolution WDS instrument, [43]. Quantitative analysis requires the use of well characterized standard samples for relative intensity measurements.

3.3.2 Experimental

All the SEM work reported in this study was conducted on the digital scanning electron microscope Zeiss DSM 940 instrument at the Department of chemistry, NTNU. The instrument uses a standard W filament, an emission current of 0.80 μA and a WD-range of 9-40 mm, allowing a maximum sample height of 20 mm. The instrument has an EDS analyser and TRECOR element analysis software for qualitative chemical determination. The sample chamber is ventilated by N_2 gas prior to evacuation to operational vacuum. Images are recorded on Polaroid 4×5 inch film. The images presented in the current work were subsequently digitally scanned and occasionally enhanced by employing a gamma processing correction [43] for presentation.

Dry powder samples of smelter grade alumina (SGA) were mounted on the SEM sample holder with Cu-tape, or, as for larger crust samples and agglomerates, embedded in carbon glue for increased stability and better electrical grounding. The dry sample was subsequently sputter-covered by a

thin layer of gold ($\sim$ 10 nm) for topography study or evaporation covered by carbon for EDS analysis. In practice the optimal coating thickness had to be found by trial and error, and several thin coatings is generally better. For image recording on photographic Polaroid film the scanning raster speed was reduced in order to improve the signal-to-noise ratio, but the scanning speed was limited to intermediate quality scans for most images of agglomerate samples due to increasing sample charging.

Alumina Agglomerate Topography

A technique was developed for imaging the topography of fine alumina agglomerate samples. Fresh fracture surfaces were exposed by breaking off small pieces of agglomerate (tablets) using cleaned, fine stainless steel tweezers and needle, and setting them in relatively viscous carbon glue and then set to dry over night. The dry sample was then tipped so that excess material fell off or was lightly tapped off. For very weak agglomerates this resulted in further agglomerate breakage since the agglomerates then were pulled apart by their own weight. Interparticle forces in the weakest agglomerates apparently could not support the tensile stress induced by the weight of the part not fixed in carbon glue. This was advantageous since fresh fracture surfaces thus were exposed and sample charging was limited.

Topographic SEM-BSE images are presented in chapters 4 and 5.

3.4 Mechanical Strength

The mechanical properties of a ceramic material will in practice be determined by the microstructure, not least the porosity and other "flaws". A description of the mechanical, thermal, electrical and magnetic properties of ceramic materials is given by Richerson [141].

It may be argued that the most relevant "strength" parameter for agglomerates of smelter grade alumina (SGA) in relation to primary aluminium production is their dissolution rate and behavior in cryolitic melts. The dissolution of tablet agglomerates is the subject of chapter 6. However, some mechanical theory relevant for the present study of tablet-shaped agglomerates is presented here.

3.4.1 Theory

Porosity and Critical Flaw Size

The E-modulus (modulus of elasticity, also known as *Young's modulus*) of a material will decrease with increasing porosity by the relation,

$$E = E_0\left(1 - 1.9P + 0.9P^2\right)$$

which is valid for a relative volume fraction of pores P <0.5, [141]. The effect of porosity on the strength of ceramics is well known, [174, 121, 24], and alumina is an often studied model system. Theoretically, the maximum applied stress on a ceramic material may be expressed as;

$$\sigma_{th} = \left(\frac{E\gamma}{a_0}\right)^{1/2} \tag{3.7}$$

where a_0 is the atomic distance and γ is the fracture (surface) energy. The presence of flaws (pores etc.) will greatly reduce the strength of a ceramic material however. The maximum stress at fracture (σ_m),(when the applied stress is σ_a), and the critical flaw size, may be determined from;

$$\sigma_m = \sigma_a 2\left(\frac{c}{\rho}\right)^{1/2} \tag{3.8}$$

where $2c$ is the length dimension of the flaw (crack or pore) and ρ is its smallest diameter. The fracture stress (σ_f) occurs when $\sigma_m \geq \sigma_t h$, so that by combining 3.8 and 3.7;

$$\sigma_f = A\left(\frac{E\gamma}{c}\right)^{1/2} \tag{3.9}$$

where A is a constant which depends on the sample and flaw geometry. Equation 3.9 is known as *Griffith's postulate*. For a material with at least one pore of the order of 100 μm, Griffith's postulate may be used to estimate the fracture stress to be;

$$\frac{\sigma_f}{\sigma_{th}} = \frac{const.}{10^4}$$

thus, the strength of the material is reduced by a factor of 10 000 (!). Critical flaws cannot be avoided in practice, though their size may be much reduced.

Composites and Platelets

The strength and fracture toughness of ceramic materials may be increased by the addition of e.g. fibers or whiskers with a higher E-modulus than the matrix material, [141, 192], such as the case with steel reinforced concrete. Composite materials formed by mixing metals, ceramics, polymers and glasses (and even liquids or gases) provide a whole new range of possible material properties. The crust that forms on top of the electrolyte in the Hall-Héroult process is a composite of SGA and solidified electrolyte. The properties of crust has been the subject of several studies, further discussed in chapters 2,4 and 5. Obviously, the porosity of the crust will to a large extent determine its strength - but also the microstructure and relative contents of alumina, the formation of a skeletal structure of "interlinking" alumina platelets, and void-filling electrolyte is important. The importance of filling of voids in an alumina matrix of an Al_2O_3/Ni_3Al composite has been described by Skirl *et al.* [162]. The filling of a molten salt (aluminum nitrate nonahydrate) with a low melting point into a matrix of partially sintered zirconia is described by Glass and Green [42], including relevant theory on capillary flow into pores. Regarding the formation of a scheletal structure of alumina platelets/particles, the relative strength of each alumina particle bond is important. A recent study of a novel sintering method showed greatly improved bending strength of a very porous alumina body, which could be attributed to increased bridging due to enhanced neck growth [74].

A structure containing platelet-shaped crystals or grains is known to increase the fracture toughness of ceramics, – basically by absorbing the crack propagation energy, [141]. This effect has been exploited by controlling the amount of α and β phases in Si_3N_4 and SiC ceramics [207, 27, 211].

Alumina platelets have recently been applied as a reinforcing material in some metals and ceramic materials, [114, 146, 213, 36, 136, 126, 97]. As noted by Ledbetter *et al.* [97], the addition of platelets may cause flaws that will soften the ceramic rather than stiffen it, though the culprit in that case was found to be mullite being covered by (soft) silica. A porous alumina coating on alumina powder particles was used by O'Brien and Sheldon [126] for the study of fracture mode and toughness of alumina composites, and for confirming the crack deflection mechanism.

Anisotropic grain growth may occur *in situ* in high purity and liquid phase sintered alumina ceramics with the formation of potentially very large platelike grains ($\sim$ 100 μm in length) and has been studied rather extensively,

[62, 46, 171, 170]. Also, the stacked platelet morphology of clays contributes to the high plasticity and high green-body[4] strength [157]. Alumina platelets may also be used as an additive to polymers for (anisotropic) thermal conduction [13].

Temperature and Reliability

The material properties of ceramics are often superior to those of metals for use in many applications such as in high temperature, corrosive environments. However, there is often a trade-off between high strength and reliability of for instance ceramic structural components. The reliability factor m and fracture strength of a ceramic material may be determined using statistical analysis (Weibull) of the strength determination data of at least $\sim$40 specimen samples. The theory of Weibull statistics used is based on a "weakest link" model, [141]. The mechanical strength and other properties will in practice be determined by the microstructure. Ceramic materials often contain secondary phases that become viscous at high temperature and under pressure, so that "creep" may limit the mechanical strength in some applications. Room temperature strength tests may be of very limited relevance for many applications.

3.4.2 Experimental

The observed mechanical properties of the tablet agglomerates formed by the method described in chapter 5, may be compared to the strength of very weak green bodies of ceramic material prior to sintering, [141]. It is exceedingly difficult to determine the (very low) strength or toughness of such a material, with about 70 % porosity, by conventional methods.

The E-modulus, interparticle contact stiffness and diametral compressive strength (so-called "Brazilian tablet test") are correlated with the velocity of sound in the material, [157, 47]. Recent studies have shown the possibility of characterizing the weak bonding strength occuring in the early stages of sintering, during coarsening and other events that do not involve any significant shrinkage[5]. Experimental techniques based on the use of ultrasound have been reported, [47, 17, 79, 113, 157], and similar methods should

[4]Ceramic green-body = shaped but non-fired, non-sintered ceramic precursor

[5]Macroscopic shrinkage normally involves volume diffusion, see discussion of sintering theory in chapter 2

be considered for further work on similar (tablet) alumina agglomerates. Nonnet *et al.* [125] recently combined ultra-sound and synchrotron radiation to study the simultaneous evolution of microstructure and material strength *in situ* of high-alumina castables subjected to heat treatment and sintering from RT up to 1600 °C.

Such reports are interesting areas for further work, however - the dissolution behavior has been considered to be the most relevant "strength parameter" for the tablet agglomerates of the current study: see chapter 6. Furthermore, the qualitative "sinter"-scale described in chapter 5, was the only practical and reliable technique available for determining a measure of the mechanical strength of the tablet agglomerates in this study. Trained use of the scale allowed quite reproducible, precise results, also between different operators - with an error of no more than ± 1 on the scale from 0 - 10. The method and results are described in chapter 5.

Chapter 4

Agglomeration Part I

4.1 Background

The relevant literature and theoretical background for the present study is presented chapter 2. A brief motivation is stated here.

Kobbeltvedt [86] concluded that the agglomeration of smelter grade alumina (SGA) upon addition to cryolitic melt, will determine much of the dissolution behavior of a particular alumina quality.

In order to understand the interlinking and recrystallization process, one must study the advancing front of (bulk, unsaturated) melt as it penetrates an agglomerate. It has been attempted to follow the process in controlled cylindrical agglomerates immersed in a melt, and the temperature and material transport of such a geometry was described by Walker *et al.* [196]. The experiments were largely reproduced by Kobbeltvedt *et al.* [86], who used alumina saturated melt in a large laboratory furnace. However, agglomeration was not studied on a microstructural level in either case.

The motivation for the current study was to reproduce such agglomerates in the laboratory and to attempt to study the microstructure of the agglomerates thus produced.

It is of particular interest to study the polymorphic $\gamma \rightarrow \alpha$ phase transformation of alumina, i. e. from the metastable transition phases "γ" of SGA to the stable α-alumina (corundum) phase. The phase transform is known to be involved in the agglomeration process [86, 149]. It is postulated here that the presence of fluorides and volatiles at the infiltration front of the

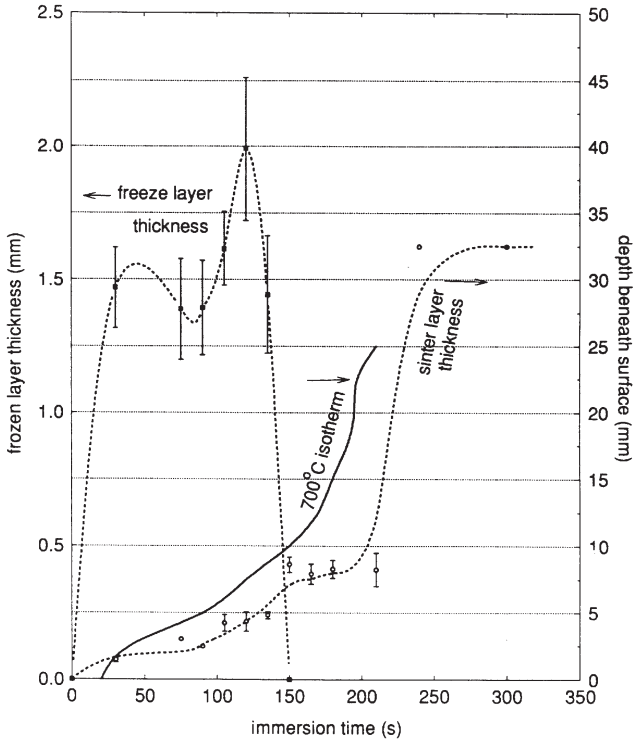

Figure 4.1: *Temperature response curve and thickness of freeze layer and "sinter-layer" obtained in a cylindrical agglomerate in industrial melt by the method described in text. Bath temperature $T = 970\,^{\circ}C$. Bath infiltration follows 700 °C isotherm, corresponding to the lowest melting bath composition. From Walker [195].*

cryolitic melt, as it penetrates a small bed of alumina, will be crucial to the micro-structure of the agglomerates that form, primarily as a function of time and temperature - but probably very dependent on whether the fluorides are in gaseous or liquid form.

A discussion will be given regarding the results of Walker and of Kobbeltvedt in order to complement the results obtained here. As noted by both those authors, we appreciate that agglomeration is a fast and complex process, and that melt penetration in an alumina bed may be unpredictable due to the violent evolution of volatiles from the alumina during rapid heating. As shown and discussed by Walker [196, 195], see figs. 4.1 and 4.2, the infiltration of liquid melt follows the 700 °C isotherm, approximately corre-

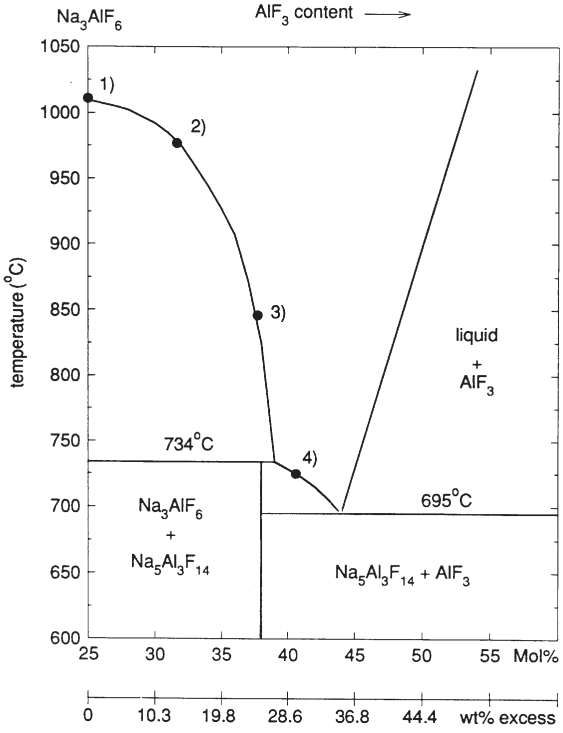

Figure 4.2: *Melt composition (by semi-quantitative XRD) in freeze layer (2), 2nd infiltration layer (3) and 1st infiltration layer (4) obtained in cylinder agglomerate using calcined α-alumina, according to Walker [195]. Pure cryolite composition (1).*

sponding to the lowest melting composition of the electrolyte. In addition, we may expect a certain partial pressure of gaseous $NaAlF_4$ and HF prior to the penetration of liquid fluorides, both with a potential for catalyzing the $\gamma \rightarrow \alpha$ phase transition in the alumina and hence partial recrystallization.

Walker [195] also found a clear correlation of the freeze thickness, which decreased, and the infiltration/ "sinter" layer of the agglomerates with an increasing super-heat. Since this study found that the infiltration front followed the 700 °C isotherm, there is strong evidence to support that the formation and break-up of agglomerates is largely heat transfer controlled.

The temperature response curves of two agglomerates reported by Kobbeltvedt [86] are presented in fig. 4.3. The most striking feature of the presentation is the increased heat transport observed when increasing the superheat in

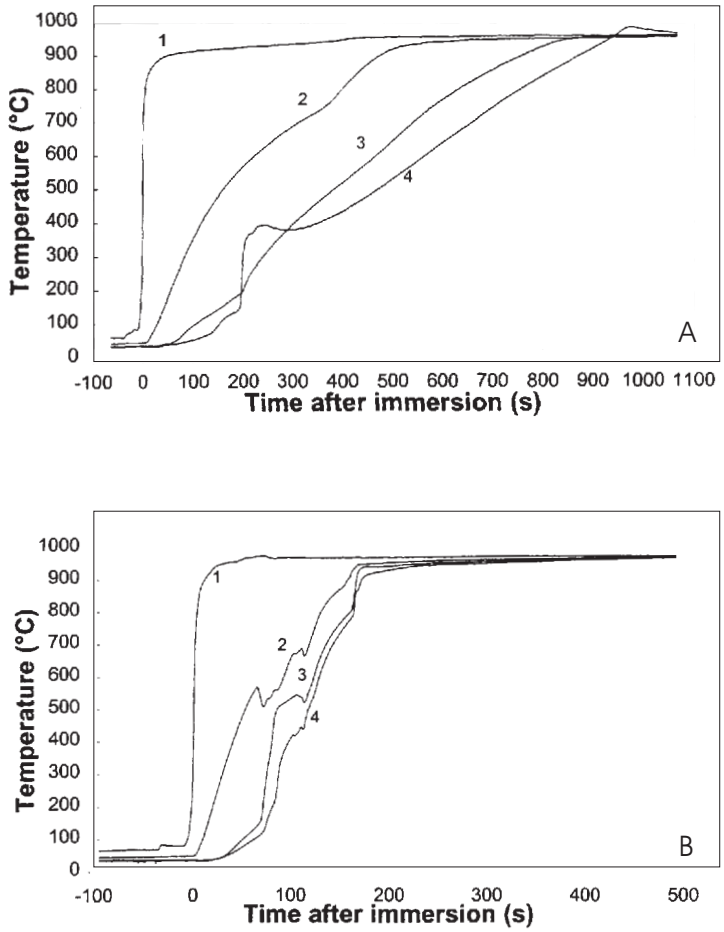

Figure 4.3: *Temperature response curves obtained in a laboratory cylindrical agglomerate by the method described in text. A: Bath temperature T = 962 °C. B: Bath temperature T = 982 °C, else same experimental parameters as in A, showing the effect of increased available heat (super-heat). From Kobbeltvedt [86].*

the melt. An increased "noise" level is also observed when the super-heat is increased, probably due to more violent mixing and stirring of the alumina as volatiles are released in the agglomerate.

An inversion in the response- curve, i. e. a positive increase, recorded by thermocouple 2 is seen in fig. 4.3A as the temperature passed the 700 °C mark, and this is probably due to the penetration of liquid melt at this

temperature.

Kobbeltvedt observed an overshoot in the temperature of the inner thermocouple, (number 4, in the center position), and concluded that it was probably due to the exothermal $\gamma \rightarrow \alpha$ transition, also noted by Gerlach *et al.* [38].

While Kobbeltvedt and Walker are in general agreement,– Kobbeltvedt emphasized the importance of the phase transformation of alumina to provide strength to the agglomerate, and showed that a cylindrical agglomerate does not retain dimensional stability if calcined α-alumina is used. Similar observations were left uncommented by Walker.

4.2 Experimental

Cylindrical agglomerates were prepared using a method similar to that of Walker [195, 196] and Kobbeltvedt [86]. Based on the preliminary results obtained here a different experimental technique was subsequently developed, ref. chapter 5. The experimental technique in Part II (chap.5) may be described as a "one shot" method of data collection using 1.2-1.3 g of premixed (dry) sample, allowing greater repeatability and parameter control.

4.2.1 Procedure: Cylinder Agglomerates

Cylindrical agglomerates were prepared using the method of Walker [196] and Kobbeltvedt [86]. The only major difference is that only one thermocouple is used for each agglomerate, not four. Walker used an electromechanical lowering device for his small cylindrical laboratory agglomerates - and used a crude, but effective, approach for obtaining the larger 65 mm diameter agglomerates in industrial melts. Kobbeltvedt based his study on the latter "industrial" agglomerate cylinder design, and used a semi-manual lowering procedure in the laboratory, also adopted in the present study.

In practice, the industrial melt may have provided easier access than the large laboratory furnace used here. Kobbeltvedt noted that alumina with a high content of moisture was difficult to handle in the laboratory, and used pre-dried samples.

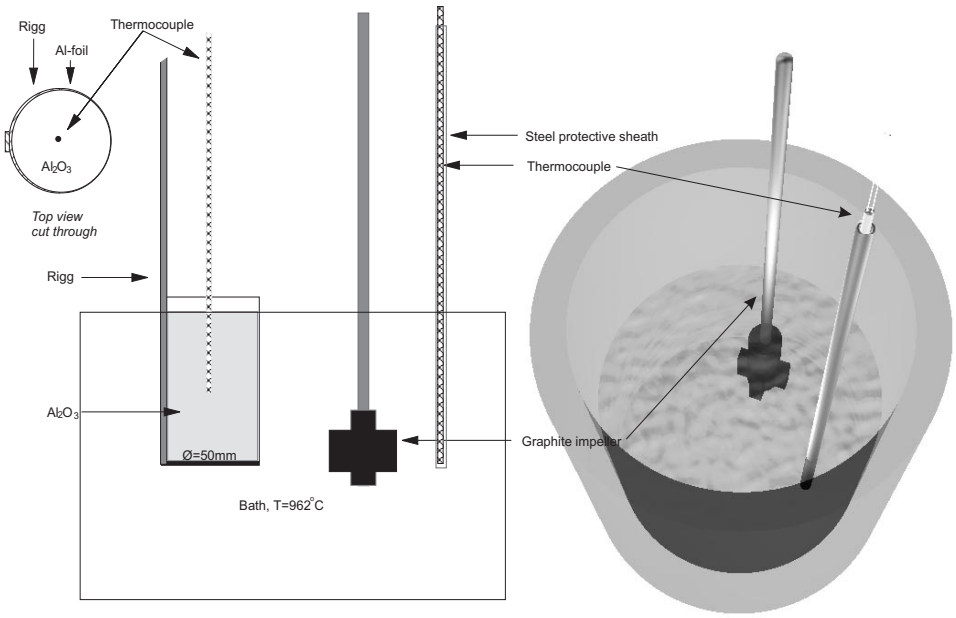

Figure 4.4: *Left:Schematic presentation of the experimental set-up used for preparing cylindrical agglomerates, as described in text. Right: 3D-view of cell.*

A few preliminary experiments and two cylinder agglomerates were prepared under the supervision of Kobbeltvedt, in order to ensure that his results could be reproduced.

4.2.2 Chemicals and Equipment

A schematic presentation of the apparatus used to obtain cylinder agglomerates in the laboratory is shown in fig. 4.4. The key component of the method is the use of aluminium foil to support the alumina powder sample prior to immersion in the melt.

The agglomerate rig, in stainless steel, was contstructed with a bottom and sheath covering about half the circumference of the cylinder. Steel rings at the top and bottom stiffened the construction and defined the cylinder for further wrapping by Al-foil. As indicated in the top-left corner of fig. 4.4, the front was left open, so that only the Al-foil supported the alumina on

the front side of the rig. Alumina powder is poured into the rig, and the top Al-foil folded over it just before the rig is lowered into the melt. If the rig is quickly submerged in the melt, the aluminium foil will melt and immediately be replaced by a freeze layer surrounding the agglomerate - thus maintaining dimensional stability of the cylinder.

In order to minimize the potential for hazardous "explosive" discharges of volatiles upon immersion of the agglomerate rig into the melt, we chose to limit the immersion depth so that the top of the cylinders is flush with the free surface of the melt when fully immersed as indicated in fig. 4.4. This procedure was standard for the entire planned experimental campaign run according to tab. 4.1, but resulted in some limitations in the recorded temperature evolution curves, as will become evident in the following discussion. For some of the secondary alumina samples, the powder was quickly fluidized and allowed to escape the agglomerate at the top, thus exposing the thermocouple to liquid melt that subsequently filled the rig, mostly from above.

A large water-cooled furnace is used, identical to that used by Kobbeltvedt, except for a re-lining of the bottom surface with alumina powder and refractory bricks supporting the graphite crucible with inner diameter of 200 mm. In order to reduce the air- burn of the crucible, we used a stream of argon gas and lining of mineral fiber around the circumference, which also helps support the crucible to the steel cylinder lining of the furnace. One single crucible would thus last the entire experimental campaign described in the following section.

About 7800 g industrial electrolyte with an approximate composition of 11 wt. % excess AlF_3, 5 wt % CaF_2 and about 2 wt % Al_2O_3 was used as the melt, and 700 g alumina powder was added to ensure alumina saturation of the melt which has a calculated liquidus temperature of 939 °C according to the SINTEF liquidus equation [163] with the given composition and alumina saturation. The set-point of the furnace temperature controller was adjusted so that the melt held $T = 962 \pm 2$ °C.

A graphite impeller is used to stir the melt, at 200 RPM, during melting and cooling. In the latter case, temperature cooling curves are used to determine the (experimental) liquidus temperature of the melt.

Alumina of both primary (PA) and reacted, dry-scrubber secondary (SA) samples are used, ref. chapter 5, for tabulated material properties. Kobbeltvedt only reported reproducible results for primary alumina, while Walker used

laboratory prepared aluminas from a Bayer plant hydrate source, using two (extreme) levels of calcination; low (650 °C, γ-alumina) and high (1250 °C, i. e. α-alumina).

For the preliminary agglomerates of the current study only primary alumina was used, of the same quality reported by Kobbeltvedt [86]. An augmented experimental campaign in which both SGA PA and SA was used was subsequently carried out according to the plan described in the next section.

One preliminary agglomerate sample (NPO-01) was obtained by immersing the agglomerate rig shown in fig. 4.4 and held for 3 min in the melt at T = 962 °C before removing the rig and agglomerate thus produced. No temperature recording was made. The cylinder agglomerate was made from 136 g of primary alumina which had been dried for several days at 200 °C. NPO-01 was set to cool to room temperature and subsequently inspected and analyzed by SEM and X-ray diffraction. The same procedure was repeated to obtain sample NPO-02. 140 g alumina was used and a single k-element thermocouple (Thermocoax 30/50/DIN) was used to record the temperature evolution in the center position of the cylinder. The NPO-02 sample was immersed in the melt and removed when the temperature reached 600 °C in the center position after approximately 8 min.

The T_{liq} increased from about 932 °C to 938 °C during the course of the campaign. Assuming alumina saturation, and a CaF_2 content of 5 wt %, this corresponds to a starting composition of 12 wt. % excess AlF_3 and a final composition of 11 wt. % excess AlF_3. Bath samples taken every day were submitted to LECO-analysis, and showed a stable alumina content of 7.3 ± 0.1 wt. %.

4.2.3 Tabulated Experimental Campaign

The experimental plan shown in tab. 4.1 was set up using MINITAB Release 11 statistical software. The experimental plan involved 3 samples a day, each day representing a block of experiments which from a statistical point of view may introduce some bias. The experimental (quasi- 2^3) design is randomized and augmented (including 3 random replicates) involving 2 alumina qualities (PA and SA), 2 levels of volatiles (high and low) and 3 time levels (immersion times 30, 120 and 480 s). The two levels of volatiles was obtained by using alumina samples dried over night at 200 °C, or not dried, but kept in the original air-tight container, used for sampling at the aluminium smelter, until use.

Table 4.1: *Randomized experimental matrix/ plan. 3 randomized copies included, SGA from refinery A used of both primary (PA) and secondary (SA) quality, High/Low level of volatiles in alumina achieved by drying/ not drying at 200 °C over night, and 3 immersion times t.*

Exp. no. (1-15)	Com.	SGA A [P/S]	Volatile Level[H/L]	t [s]
1		S	L	120
2		S	H	30
3		P	L	120
4		P	H	120
5		P	H	30
6		S	L	480
7		P	L	480
8		S	H	120
9	Copy 8	S	H	120
10	Copy 1	S	L	120
11		P	H	480
12		P	L	30
13		S	H	480
14	Copy 3	P	L	120
15		S	H	30

The experimental procedure was described in the previous section. In order to achieve rapid sampling, 3 additional agglomerate rigs, (apparatus for forming ans supporting agglomerate in the melt), were made so that three samples could be obtained in quick succession. It was recognized in the preliminary experiments that it may be difficult to remove samples from the rig after the cylindrical samples had cooled. The alumina- cryolite agglomerates/crust, which formed tends to form a strong bond to the sampling rigs, especially as these became increasingly corroded after several immersions in the cryolitic melt.

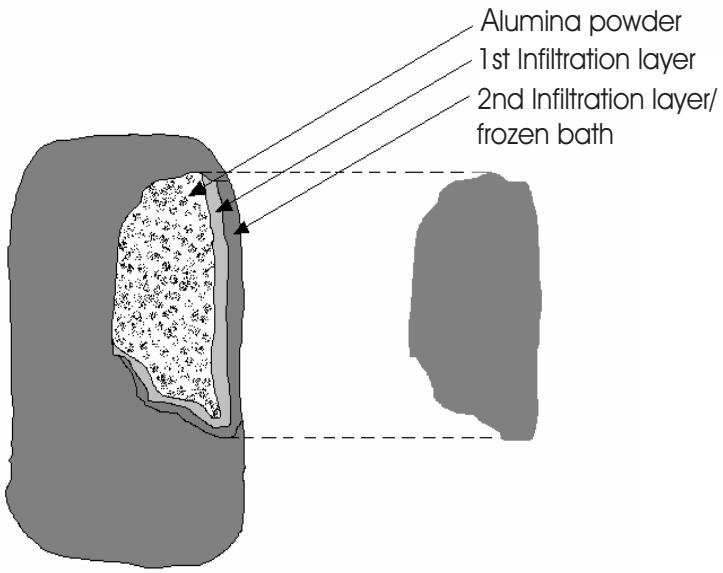

Figure 4.5: *Schematic presentation of the cylindrical agglomerates obtained. Infiltration layer follows the description of Walker [196, 195].*

4.3 Results and Discussion: Cylinder Geometry

The preliminary experiments, using the left-over primary oxide (Alpart source [86]), showed adequate repeatability according to Kobbeltvedt [86]. Generally, the resulting cylindrical agglomerates appeared to be as expected, as described in detail by Walker [196, 195]. The "sinter" layer as depicted in fig. 4.5 consists of a sandwich structure of freeze layer, first and second infiltration layers and loose alumina in the center, in those samples in which the melt had not reached the center. Pieces of the "sinter" layer, or crust layer - could be picked off and the loose alumina was harvested for inspection.

3 distinct layers are observed in parts of both the NPO-01 and NPO-02 samples, which were immersed in the melt for 3 min and about 8 min respectively. The outer layer, consisting of freeze and the 2^{nd} infiltration layer is grayish and porous, while the next layer, the 1^{st} infiltration layer, according to Walker [196, 195], has a distinct pink and peach color. This layer is more compact, and is also noticeably harder as it blends with the

outer layer. An inner-most thin layer of grey/white color could be seen in parts of the agglomerates, this may be a composite of freeze and frozen-inn alumina grains- at least in those parts of the alumina where liquid melt had not yet penetrated the frozen shell.

A sample of crust having a representative layer composition, partly with the sandwich of three discernable layers, was analyzed by qualitative XRD after being finely ground, using a Retsch rotating crusher. The phase composition of the sample compared well with that presented by Walker, showing similar peak intensities of α-alumina, cryolite and chiolite, thus indicating a composition around that indicated by point 3 in fig. 4.2. The crust layer was somewhat thicker for the NPO-02 sample, and while NPO-01 contained free-flowing loose alumina, the alumina powder in NPO-02 had somewhat altered flowability and there appeared to be some traces of small lumps. Such an observation would be consistent with the notion that penetration of melt had started in the latter.

Qualitative powder XRD of the loose alumina powder in NPO-01 and NPO-02 did not show any statistically significant differences between the two however (and similar to primary alumina), so that the lumping observed can mainly be attributed to partial wetting of alumina by penetrating melt.

As shown by XRD however, no detectable phase transition had started in the NPO-02 sample, so we may conclude that the partial agglomeration observed in the inner "loose" alumina body is evidence of initial melt infiltration, in agreement with Walker [196, 195]. The apparent difference in the flowability of the inner "loose" alumina part of NPO-01 and -02, may be explained from the temperature evolution in the latter.

The temperature increased, with a profile of the exponential rise to maximum type, reaching a little over 300 °C, then increasing linearly for over 300 s, probably until the agglomerate was removed, or shortly after, when the temperature was 600 °C. The temperature continued to rise after the agglomerate was set to cool, but at a decreasing rate,– barely reaching 700 °C about 200 s after 600 °C was reached, and then falling off as the agglomerate cooled further, reaching 600 °C after another 300 s. Soon after, the temperature logging was stopped.

Since the center of the agglomerate reached 700 °C, and was within a few degrees of that temperature for at least a minute, some liquid melt may have started to penetrate the alumina from the outer freeze and sinter layers, thus explaining som traces of agglomeration in the "loose" powder of the

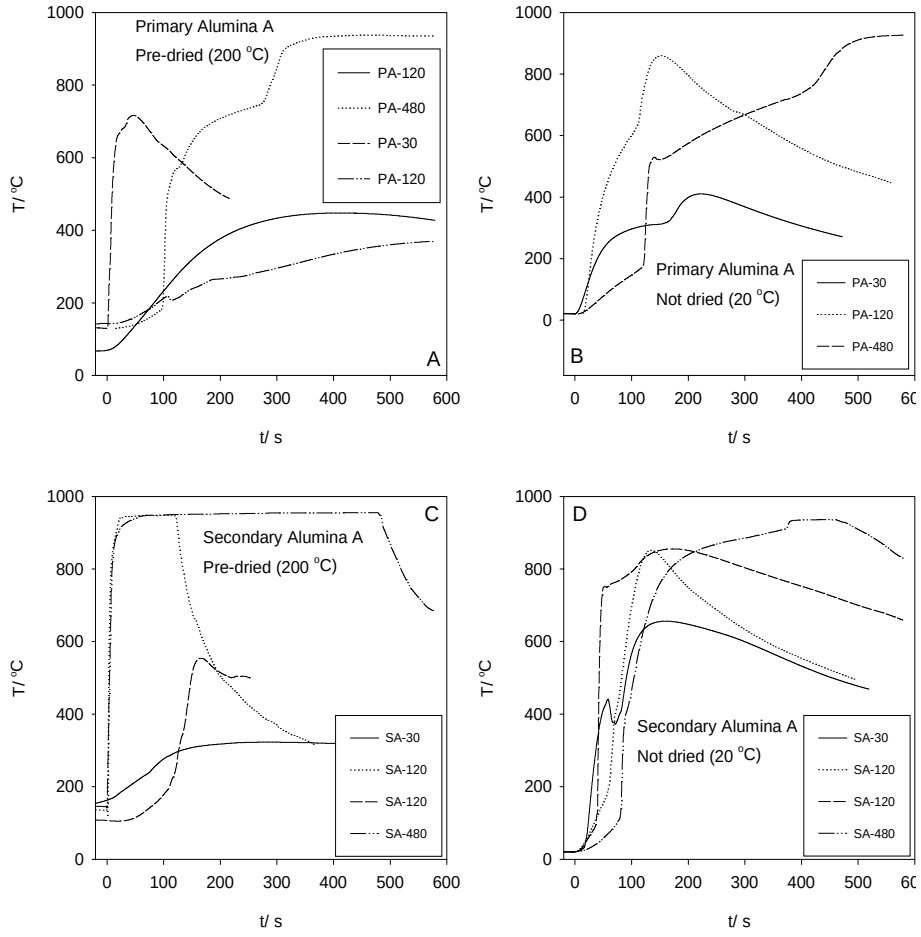

Figure 4.6: *Temperature vs. time data grouped according to alumina quality and moisture content (H/L). See text for details and discussion.*

NPO-sample.

The temperature response curves shown in figs. 4.6 and 4.7, were recorded using a single k-element thermocouple, and in general the response is dependent on the degree of convection in the agglomerates upon immersion into the melt. In several cases, in particular for the secondary samples that had not been dried at 200 °C over night, a fairly large portion of the alumina sample flowed over on to the melt surface forming a thin "raft"-like crust. If this happened, some melt could penetrate the agglomerate from

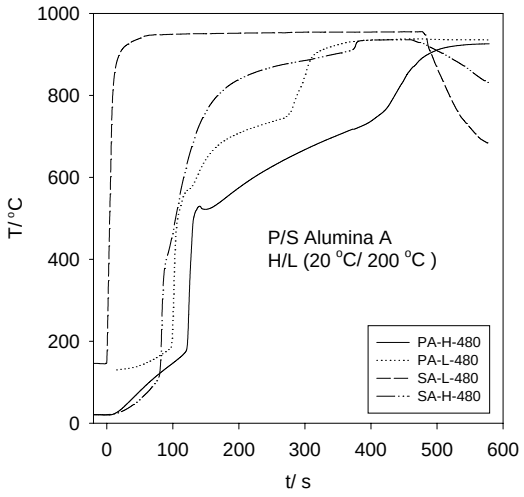

Figure 4.7: *Temperature vs. time data in cylinder agglomerates immersed in melt for 480 s.*

above and the thermocouple might be immediately exposed to the melt. In a few cases, a "geyser" -like shower of alumina would fume fine powder from a small crack in the agglomerate during the experiment. "Geysers" are known to appear in industrial cells also, in particular if the alumina has a high moisture content [3].

However, if little or no such convection occured, the temperature response, as measured in the center position, was seen to be significantly retarded. The alumina will effectively insulate the thermocouple for a significant time period. The convection in the alumina is mainly due to the evolution of moisture, and the temperature response will necessarily be somewhat chaotic, since much of this gas flow is likely to be highly turbulent. However, the qualitative description of the resulting agglomerates shows greater consistency than the different temperature response curves would suggest.

According to the evolution of the isotherms shown by Walker [196, 195], the highly calcined primary alumina samples resulted in the highest predictability in the evolution of volatiles and penetration of melt, and resulted in the well defined 3-layer agglomerate sandwich structure.

For the low-calcined samples in Walker's study, the evolution of volatile moisture generally resulted in a less well defined sandwich structure. This

is also the case here, though rather intermediate results were observed, as could be expected for primary alumina. In the current study, 3 distinct layers are discernable for all samples immersed in the melt for 120 and 480 s. For the shortest immersion time of 30 s, only the freeze layer is seen, in agreement with results of Walker reported in fig. 4.1, since the melt has not yet begun to penetrate the agglomerate. The freeze layer was quite thin and had little mechanical strength, usually not able to contain the loose alumina inside during subsequent cooling, since this led to cracking. The sinter-crust layers for the longer retention times (120 and 480 s), was much more resilient during cooling and later sample collection - though some loose alumina would escape several of those agglomerates also.

The reproducibility of the agglomerate temperature response is demonstrated by the replicate experiments, in particular experiments #3 and # 14, both from dried primary alumina and immersed for 120 s (fig. 4.6A). Due to some evaporation of $NaAlF_4$ during the course of the campaign, the increased temperature response in the former experiment may be partly due to higher superheat of the melt, since a difference of approx. 7 °C in the liquidus was determined. However, the difference is very likely the result of real scatter in this type of experiment.

In theory, one would expect that every response curve should be more or less identical for the first 30 s, at least for the similar alumina qualities grouped in figs. 4.6A-D. In practice, this is obviously not the case, though some trends are evident. Unexpectedly, the secondary samples that were not dried shown in fig. 4.6D, containing the highest level of volatiles, shows the best reproducibility. This may perhaps be due to the violent convection caused by the release of the high level of volatiles, that dominated the more subtle stirring events taking place for the lower levels of volatiles in the other samples.

The 30 s sample shows a distinct peak that may be related to convection due to volatiles as the temperature reaches 400 °C, also evident in for the 30 s and 480 s samples in fig. 4.6B. Inversion points that may be due to the infiltration of liquid melt at approximately 700 °may be seen in the 120 and 480 s curves in fig. 4.6B and the 480 s curve in 4.6B.

In fig. 4.7 all the 480 s agglomerate samples may be compared and we see that the dried secondary alumina sample suffered an exposed thermocouple, and that the other secondary alumina sample with a high level of volatiles had a quicker temperature response than the 2 primary alumina samples.

Secondary alumina has a significantly higher level of moisture. During the course of this campaign, the weight loss of the samples after being dyed over night at 200 °C was measured. For the secondary alumina (SA) a weight loss of 1.3 ± 0.1 wt % was determined, and 0.4 ± 0.1 wt % for the primary alumina samples.

However, in addition to moisture, secondary alumina contains other volatiles, in particular fluorides, and up to 1 wt % carbon which will react with available oxygen. The possible increased heat transport in secondary alumina is discussed in chapter 7. For both primary alumina samples in fig. 4.7 we observe the expected inversion point occurring around 700 °C, corresponding to the penetration of liquid melt. The smaller peaks in those curves at around 500 °C is probably related to the release of chemisorbed and structural water (-OH) from alumina, while the steep inclinations at 200 °C must be related to the release of physisorbed water/ moisture. The dried sample shows the slower response though - and this can only be explained by the inherent variations of this experimental technique.

Photographs of cut-through sections of agglomerates PA-L-480 and SA-L-480 are shown in fig. 4.8. Being closely correlated with the content of solidified melt (ref. chapter 3), the surface was markedly harder towards the outer surface, while the center was scratched easily. The primary alumina sample cylinder (PA-L-480) showed much greater strength and hardness, than that of the secondary sample (SA-L-480), perhaps due to a different temperature history, but probably connected to the increased evolution of volatiles, including the exothermal oxidation of carbon and release of both heat and CO/CO_2 gas. Kheiri *et al.* [82] argued that the content of carbon may explain why secondary alumina forms more porous agglomerates upon addition to melt, and the general appearance of P/S -agglomerate cylinders seems to support their finding.

As may be seen in fig. 4.8, the radial section of the agglomerate layer in contact with the sampling rig had a gray, more smooth outer surface, than that where the alumina had been in direct contact with the melt.

The sampling hole, from which "loose" alumina poured from PA-L-480, and was easily scraped, may be seen in fig. 4.8A (lower left of agglomerate). Concentric rings of pores where volatiles escaped are evident, while concentric infiltration layers, separable by color, are evident throughout. Sample SA-L-480 shows a rather porous, grayish texture (the gray color indicating that not all the carbon had yet burned off), typical of the agglomerates formed by secondary alumina is apparent in fig. 4.8B,D.

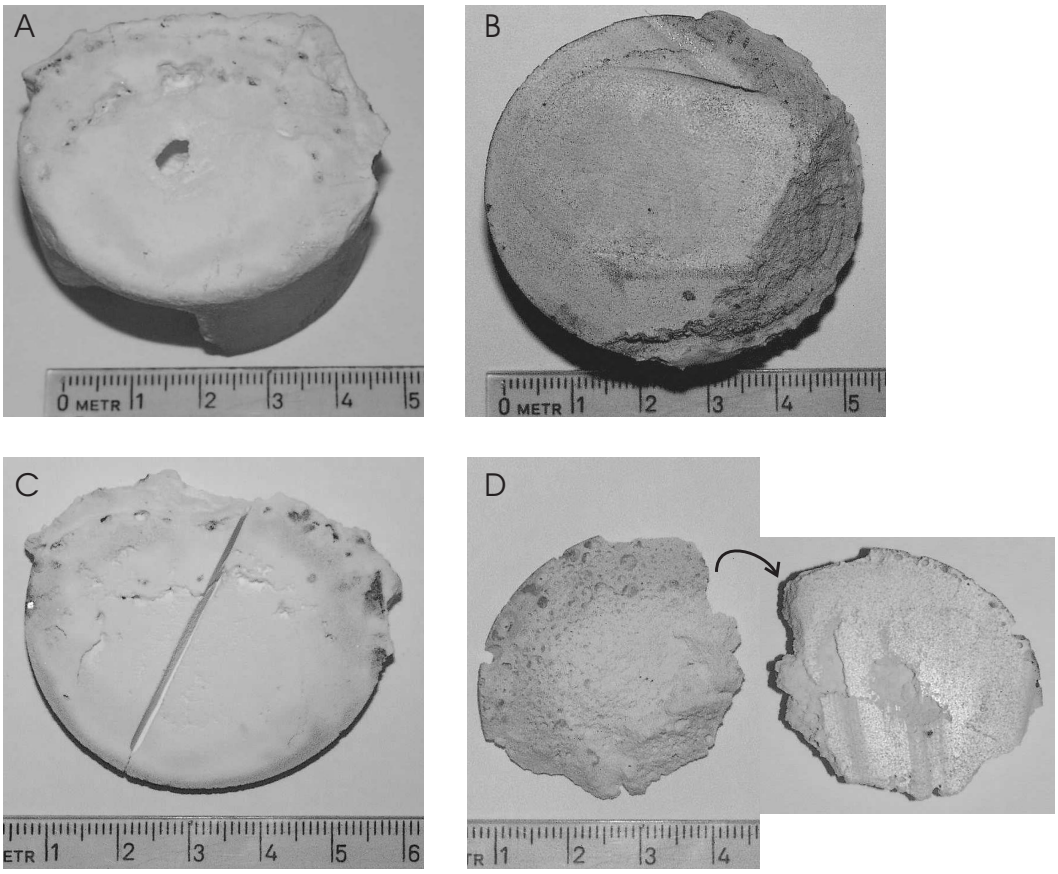

Figure 4.8: *Pictures (edited digital photographs) of cut-through agglomerates with cm scale. A, C: sample PA-L-480, markedly harder surface towards outer surface, while center scratches easily. Sampling hole and concentric rings of pores where volatiles escaped are evident, while radial infiltration layers are evident throughout. Smooth surface facing steel rig at lower end in image A, upper left in image B. B, D: Sample SA-L-480. More porous grayish texture typical of secondary alumina agglomerates.*

The agglomerate samples formed from the primary alumina (PA), dried over night, thus with the lowest content of moisture (L), and with temperature response curves shown in fig. 4.6A, were chosen for further XRD and SEM analysis.

SEM-BSE images of alumina grains and micro-agglomerates at the melt infiltration front are shown in fig. 4.9, including enlarged sections to the right. fig. 4.9A shows a view parallel to the infiltration front (from above), in sample NPO-01 held 3 min in melt. 3 min exposure is obviously sufficient time for the alumina grains at the front to recrystallize and form an interlinking network of α-Al_2O_3 platelets. This is in agreement with the results reported by Townsend and Boxall [185].

fig. 4.9B is a view perpendicular, (side-view), to the same infiltration front in the NPO-01 sample of recrystallized alumina grains. The high magnification view shows alumina crystallites growing as the alumina grain is wetted by melt, and fully recrystallized, thin platelets at the base of the alumina grain.

fig. 4.9C shows a single grain trapped (frozen) at the freeze front of sample PA-L-30, held 30 s in melt, i. e. before melt infiltration has started. The alumina grain bears a striking resemblance to calcined α-Al_2O_3, with typical slit shaped, lamellar pores, and a surface that charges little under the electron beam, unlike primary alumina that charges heavily. From this, it is concluded that the grain has been at least partly calcined and transformed to α-Al_2O_3, but no platelet growth has occured since no liquid melt is present. However, even the short time needed for the near- instantaneous freezing of cryolite melt is apparently sufficient for the (partial) calcination of alumina grains at the front. An enlarged view from above of the solidification front of frozen bath is shown, where it is evident that fine platelets of α-Al_2O_3 have precipitated during solidification. This appears to be the typical microstructure of the solidified melt front, and is evident in other samples, including NPO-01 as well.

A compilation of powder XRD patterns obtained from "loose" powder in the agglomerate samples formed from primary alumina (PA) dried over night, is presented in fig. 4.12. While the "loose" alumina is unchanged in the 30 and 120 s samples, the sample from the 480 s agglomerate shows nearly complete transformation to α-Al_2O_3. Furthermore, traces of cryolite and chiolite is evidence that at least a low melting acidic melt has partly wetted the powder.

SEM-BSE images of a micro-agglomerate present in this sample is shown

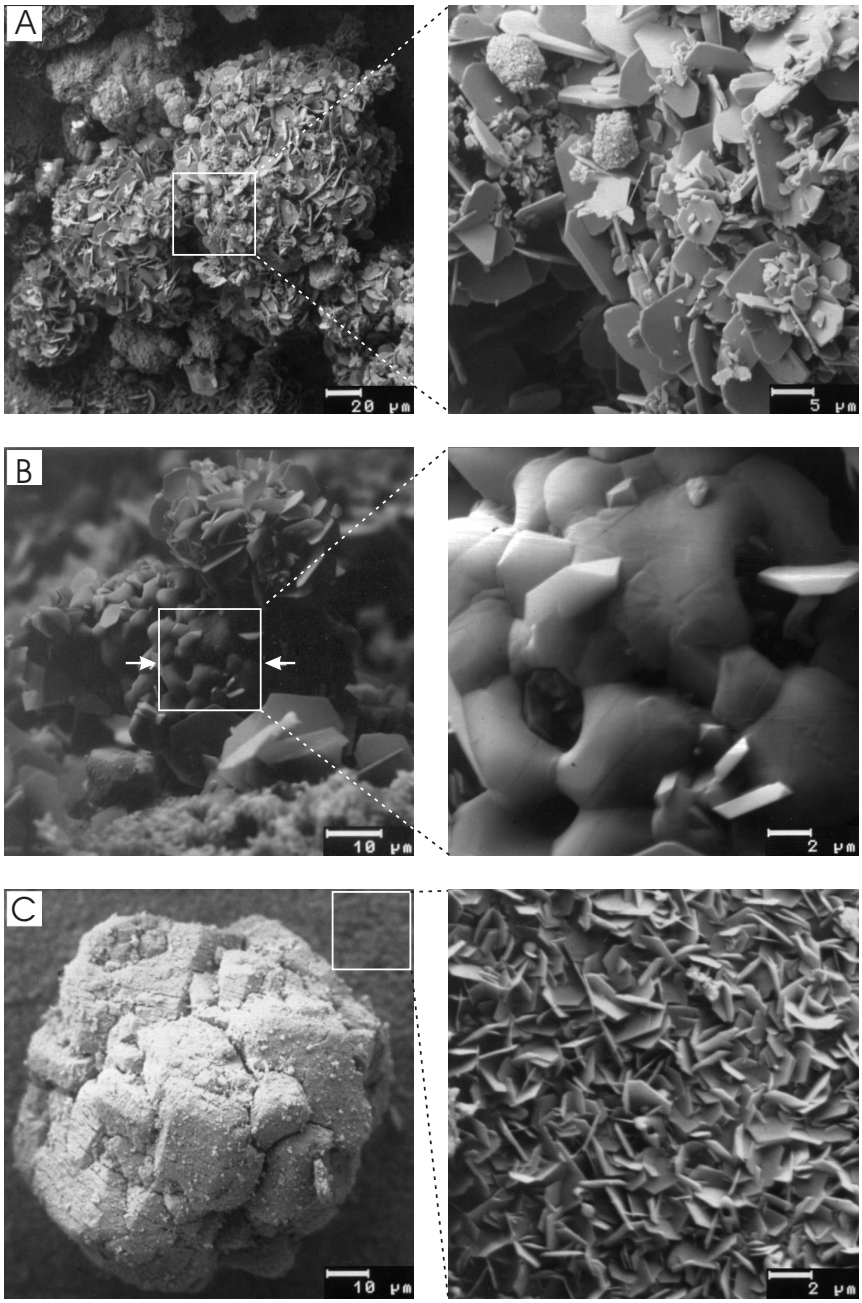

Figure 4.9: *SEM-BSE images of alumina grains/ micro-agglomerates at the melt infiltration front. A: view parallel to (from above), and B: perpendicular to (side-view) of recrystallized alumina grains, sample held 3 min in melt. C: Sample held 30 s in melt. View from above solidification front of frozen bath and attached alumina grain, at least partially calcined and showing evidence of recrystallized micro-structure (α-Al_2O_3).*

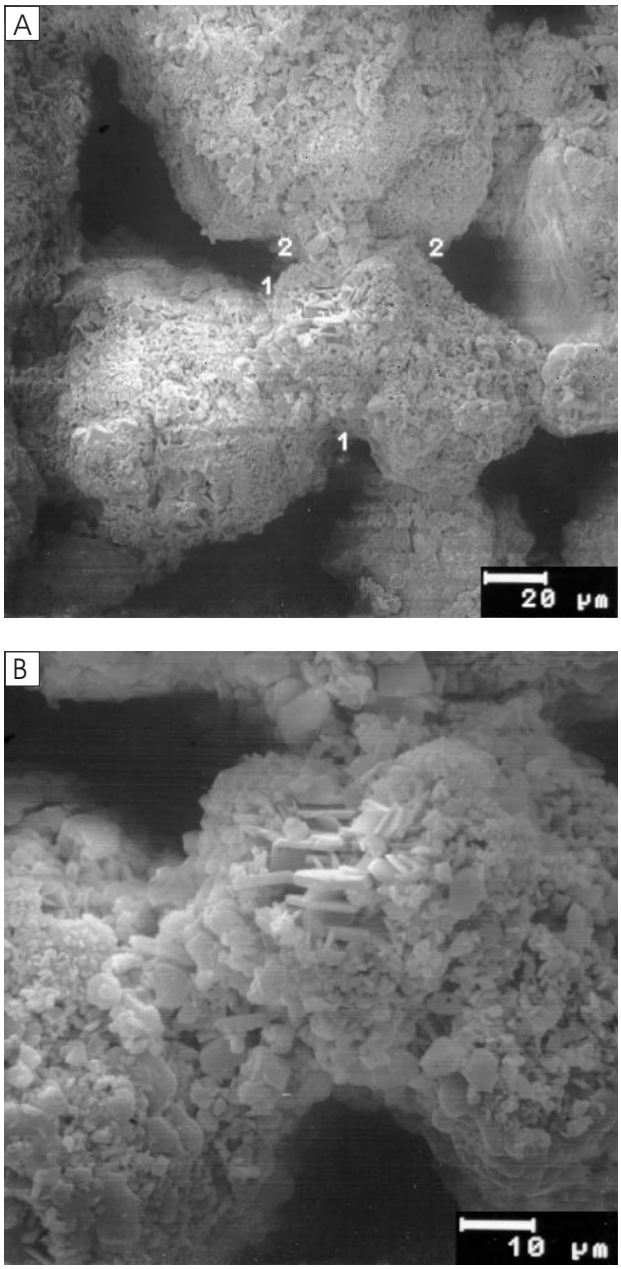

Figure 4.10: *SEM-BSE images of a micro-agglomerate showing characteristic neck formation in regions 1-1 and 2-2 in upper micrograph (A), between grains of SGA. B: Enlarged view of 1-1 and 2-2 grain contact lines.*

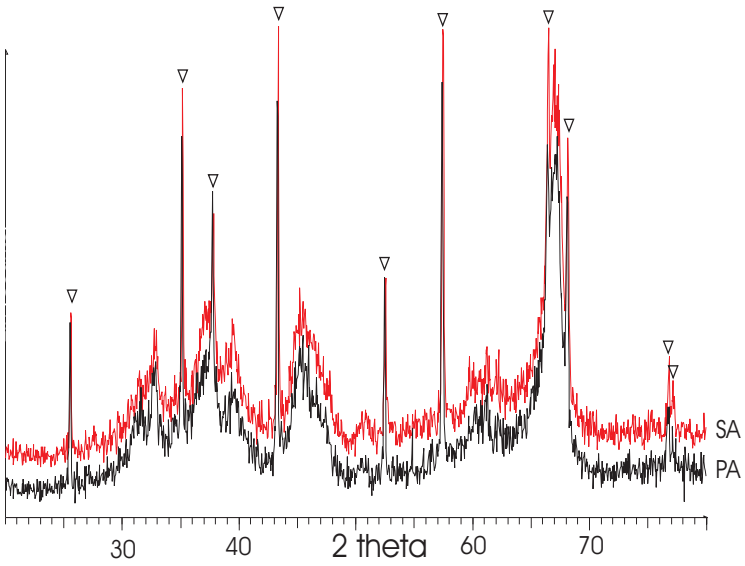

Figure 4.11: *XRD scans, diffracted intensity as a function of scattering angle 2θ. Position of $\alpha - Al_2O_3$ peaks identified $\bigtriangledown$. The scans of primary (PA) and secondary (SA) are statistically identical.*

in fig. 4.10. The sample was easily removed/ lightly scraped from the lower center portion of the cylindrical agglomerate PA-L-480, from the eroded sampling hole evident in fig. 4.8A. The images show typical neck formation between SGA grains having formed at lines 1-1 and 2-2. The higher magnification image 4.10B shows well developed α-Al_2O_3 platelets, together with a more disordered microstructure, perhaps indicative of some cryolitic melt.

Qualitative SEM-EDS (X-ray spectroscopy) showed that the necks, particle-particle contact areas contained significant concentrations of fluoride and sodium. Concentrations of liquid phase may provide strong capillary forces that could result in such densification at the grain particle-particle contact points. Furthermore, fluoride melt will cause effective coarsening and grain growth of α-Al_2O_3 platelets. "Sintering" *per se*, involving macroscopic shrinkage is unlikely at this relatively low temperature, though the initial stage of liquid phase sintering, including some rearrangement and crystallite coarsening may occur, as discussed in chapter 2.

Since the powder sample obtained from the sampling hole in PA-L-480 was

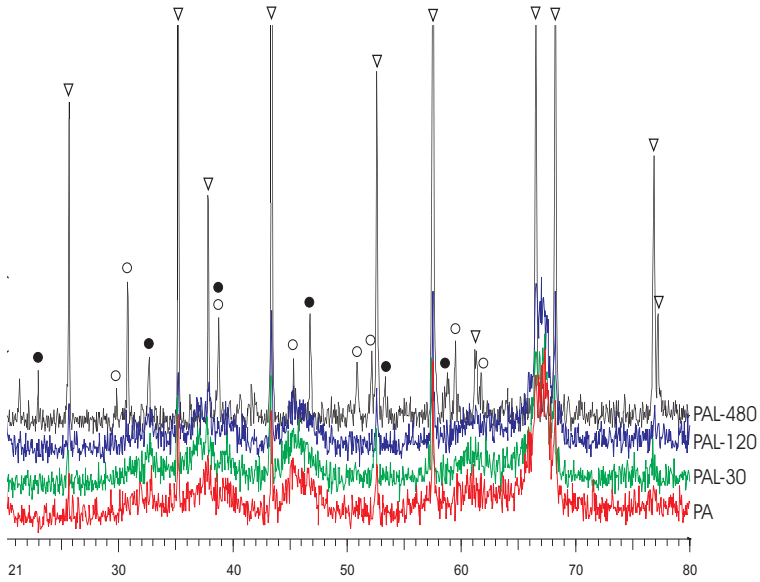

Figure 4.12: *XRD of powder samples from cylinder agglomerates. (Top pattern): Sample PA-L-480, was lightly "sintered"/ agglomerated and shows near complete phase transformation and traces of bath phases, chiolite (∘) and cryolite (•). Other samples (all free flowing powders) identical to that for PA. Position of* $\alpha - Al_2O_3$ *peaks identified* $\bigtriangledown$.

at the lower end of the agglomerate, and not from the area where the thermocouple was partly embedded, the temperature history of this sample is not known. A best "guesstimate" would be that the powder had seen at least 800 °C for several minutes.

4.4 Conclusion

The reproducibility of the cylinder agglomerate method, as applied here, is judged not to be sufficient for further investigation. The violent discharge of volatiles during immersion in melt, results in uncontrollable temperature, time and chemical parameters. The liquid melt composition is not well defined, though the penetration front and at least 2 layers of infiltration may be discerned.

We conclude that the method is well suited to give a general description of events during agglomeration of alumina upon addition to a melt. The experimental conditions applied may well describe the most adverse dissolution conditions in a modern point-fed Hall-Héroult electrolysis cell.

Qualitative differences between secondary (dry scrubber) alumina and its primary derivative are observed, and also between the agglomerates formed from alumina with high and low levels of moisture.

It may be concluded that, in order for an interlinking network of α-Al_2O_3 platelets to form, and contribute to agglomerate strength surpassing that of frozen melt, liquid melt must be present at a temperature close to that required for the phase transformation $\gamma \rightarrow \alpha$ alumina.

In order to study the agglomeration process at the microstructure level, with controlled temperature, exposure times and melt composition the "tablet" method was developed, to be presented in the following chapter, "Agglomeration Part II".

Acknowledgments

I am grateful for the assistance provided by the Electrolysis Group of SINTEF, allowing the use of the same equipment as used by Ove Kobbeltvedt- and indeed the tutoring and advice provided by him. Also Ann-Karin Kvernbråten is acknowledged for providing assistance during the sampling campaign, and for performing the LECO analysis of bath samples.

Chapter 5

Agglomeration Part II

5.1 Summary

Since alumina powder is added "cold" and batchwise to the cryolytic melt in the Hall-Héroult process, a portion of the charge will not disperse as individual grains, but form agglomerates with a much slower dissolution behavior. It was shown in the previous chapter, Agglomeration Part I, that the formation of agglomerates is partly due to recrystallization and interlinking of alumina grains - which may provide significant mechanical strength to the agglomerates even after a layer of frozen bath has melted. Initially a layer of frozen melt, partially infiltrating the alumina, provides the bonding force in the agglomerates.

In order to study the assumed conditions at the electrolyte infiltration front in alumina, we place the system in a controlled environment in shallow Pt-dishes. The method of obtaining thin tablet agglomerates, by addition of fluoride phase, is demonstrated to provide well defined experimental conditions, see chapters 7 and 8, and reproducible data.

A semi-quantitative, comparative study lends evidence to support the hypothesis that alumina qualities with a very low α-alumina content tend to have a greater propensity for agglomeration than those with a medium to high content. We compare the agglomeration behavior of 9 different alumina qualities by using a sinter-scale $0 - 10$, and find a correlation between the degree of agglomeration and loss of moisture (by weight).

The method also allows the control of the fluoride phase additive, so that the effects of the amount of liquid phase present was studied. The effect of the

moisture content on the agglomeration and phase transformation kinetics was found to be significant. It is further concluded, by XRD analysis, that the equilibrium condition in samples with added $NaAlF_4$ is $\alpha + \beta$-Al_2O_3, while fluoride reacts with moisture and is lost, and solid Na_3AlF_6 is probably also formed.

Calcined α-alumina will not form agglomerates in the presence of liquid $NaAlF_4$. In a detailed study of alumina A, with a medium α-alumina content and alumina B, with a low α-alumina content, the kinetics of the $\gamma \rightarrow \alpha$ phase transition are characterized by a nucleation and growth model (JMA). Though the kinetics are significantly faster for alumina B compared to A, they do not explain the observed agglomeration behaviour. Agglomeration is attributed to coarsening and crystal growth of α-alumina platelets.

The method of Warren-Averbach line profile analysis is applied to study the nanostructure (particle size ditribution) of the α-alumina phase in alumina A and B and agglomerates. It is concluded that the α-alumina phase of the two alumina qualities have a significantly different PSD/nanostructure, which partly supports the working hypothesis and the proposed model presented in chapter 2. The Warren-Averbach analysis is supported by other XRD, BET (SSA) and SEM results.

5.2 Background

In order to understand the interlinking and recrystallization process, one must study the advancing front of cryolitic melt as it penetrates alumina. It has been attempted to follow the process in controlled cylindrical agglomerates immersed in melts, as described in the previous chapter. The cylinder agglomerates and crust of alumina infiltrated with melt may thus be collected. However, is was concluded that it is difficult to describe the evolution of the alumina microstructure, as the chemistry, temperature and time variables at, and close to, the melt penetration front are not well defined.

The complex interaction of alumina and melt results in agglomerates with a largely unknown history on the microstructural level since the variables involved encompass a rather wide range of values of temperature, mass-flux, particle-particle contact areas, atmosphere and chemistry. Thus, in order to study the assumed conditions at the alumina-melt interface, i. e. the

electrolyte infiltration front, we place the system in a controlled environment of temperature, time and liquid melt composition in shallow Pt-dishes.

It has been concluded that the "interlinking" of α-alumina platelet-shaped crystals may explain the (increased) strength of crust and alumina agglomerates, and this is the main focus of the present study. The process of heat transfer is also important, as electrolyte will cool rapidly and freeze on the added alumina, which thus consolidates the agglomerates of alumina while the slower process of alumina interlinking may take place. Heat transfer will probably also largely control the process of the break-up and disintegration of agglomerates, and the kinetics of the phase transformation and mass transport events during the coarsening and growth of alumina crystals.

The degree of agglomeration is minimized by available stirring energy and heat in the melt, and by the aluminas' tendency for self agitation, by the release of volatile compounds, mainly water, see chapter 8. The flowability of alumina upon addition is known to be important. The amount of water adsorbed on and structurally a part of the alumina is controlled both by the alumina production (calcination), and by ambient exposure during handling.

Agglomeration is a fast and complex process in cryolitic melt, and bath penetration in an alumina bed may be unpredictable due to the violent evolution of volatiles from the alumina during rapid heating. A systematic study in which the variables may be controlled is necessary in order to study the mechanism in detail.

5.3 Theory

A discussion of the relevant literature and the theory of alumina dissolution and agglomeration is presented elsewhere, see chapters 2, 3 and 6. A presentation of the basic theory and relevant practice using material characterization by X-ray powder diffraction and scanning electron microscopy is given in chapter 3.

5.4 Experimental

Cylindrical agglomerates were prepared using the method of Walker [195, 196], and Kobbeltvedt [86]. The results of that study was presented in the

previous chapter, "Agglomeration Part I". A simplified sintering experimental technique was subsequently developed based on preliminary studies and a comprehensive review of the literature, see chapter 2.

The technique may be described as a "one shot" method of data collection using 1.2-1.3 g of premixed (dry) sample, quickly placed in a pre- heated furnace and held at temperature for a predetermined time interval, hence removed promptly and quenched in air at room temperature by quickly removing the sample from the furnace after the predetermined time had elapsed. Similar techniques have been described in the literature relevant for microstructural studies [212, 158, 8].

The method allows a quite accurate and reproducible data collection. Since the method does not employ a crucible containing liquid cryolytic melt it may well form the basis of a laboratory procedure which may be used by any alumina quality laboratory in the industry having access to a high temperature muffle furnace.

5.4.1 Procedure: Tablet Geometry

Samples of alumina and fluoide additive were mixed batchwise, normally with 16.0 g of sample, and placed in small porcelain dishes in the drying oven, held at 200 °C for at least 2 h, usually over night. The muffle furnace with a spring loaded door was allowed to equilibrate to the set temperature ($700<T<1000$ °C) for at least 2 h, T being electronically regulated to within 2 °C of the set temperature.

For every experiment, the powder sample was manually set and lightly smoothed in one of two (9.0 g) Pt-dishes of 33 mm diameter, using a spoon which held 1.2-1.3 g of sample, taken from the small heap of premixed (dry) sample in the porcelain dish. The sample was usually not weighed, as this required extra time and results in the readsorption of moisture, as described later.

However, for the series of experiments conducted for the comparative study, and for some of the "detailed" studies as well, the samples were carefully weighed in order to determine the weight loss as a function of "sintering". For increasing amounts of fluoride additive, the flowability of the sample is reduced.

The procedure was repeated easily, and the process of removing the bulk sample dish from the drying oven and placing the individual sample in

the preheated furnace took less than 1-2 min every time. The Pt-dish is set to rest on top of the furnace for pre heating and drying, attaining approximately 50 °C, before the powder sample is added. We may assume that every sample held a temperature in excess of 80-100 °C upon manual emplacement in the furnace. According to our findings in chapter 8, this is important in order to avoid re-adsorption of atmospheric moisture. The Pt-dish sample was placed in a centered, fixed location in the furnace provided by a preset piece of porous brick.

All experimental series were conducted according to a semi-randomized plan to minimize the effects of possible systematic experimental errors. A major source of error might otherwise be the bias imposed by the operator upon giving each sample a qualitative "sinter-score". After the predetermined time the samples were promptly removed from the muffle furnace and cooled in air.

5.4.2 Chemicals and Equipment

- Nabertherm muffle furnace, T control at ± 2 °C for 700 < T < 1200 °C
- Termaks drying furnace, T = 200 °C
- Laboratory micro-balance. Model: Sartorius BP61S, with nominal ± 0.1 mg accuracy
- Pt-crucible dishes/"lids", porcelain dishes, ordinary laboratory spoon, scoop etc.

Alumina Quality

Physical properties of the SGAs studied are presented in Tables 5.1 and 5.2, including major and trace chemical impurities, the latter are given in appendix, tab. A.2. The samples were obtained from representative locations in the Hydro Aluminium supply chain, and may be compared with typical qualities reported from 1995,[173] and smelter specifications [9, 173].

The α-alumina content in the samples PA, SA, PE, SE, PF and SF was measured using a modified Australian standard procedure AS2879.3-1991 [33], but augmented by averaging the results of 4 diffraction peaks. The (024) diffraction peak is one of them - and having the peak intensity closest

Table 5.1: *Physical properties of the 9 SGAs studied. Major chemical impurities presented in tab. 5.2. Trace impurities reported in appendix, tab. A.2.*

SGA [P/SA-F]	PD [g/cm^3]	UPBD [g/cm^3]	[α-Al_2O_3] [%]	MOI [%]	LOI_T [$\%_{[^\circ C]}$]	SSA (BET)[m^2/g]
PB	1.21	NA	3.2/2.3	0.16	0.73_{1100}	66.0
PC	1.17	0.97	3.9	0.89	0.80_{1000}	76.8
PD	1.21	0.99	2.1	1.53	0.67_{1000}	72.7
PA	1.24	0.99	9.5	0.83	0.78_{1100}	57.0
SA	-	-	9.3	-	-	-
PE	1.12	0.90	9.6	1.10	0.87_{1100}	81.2
SE	-	-	15.0	-	-	-
PF	1.21	1.04	22.1	2.53	0.73_{1000}	60
SF	-	-	19.2	-	-	-

Table 5.2: *Particle size distributions of the 9 SGAs studied and major chemical impurities. Trace impurities reported in appendix, tab. A.2.*

SGA [P/S], [A-F]	PSD, D[ν,0.1] [μm]	PSD, D[ν,0.5] [μm]	[Na] "Na_2O" [%]	[S] "SO_3 " [%]	[C] [%]	[F] [%]	[Fe] "Fe_2O_3" [%]	[Si] "SiO_2" [%]	[Ca] "CaO" [%]
PB	see	text	0.37	-	-	-	0.015	0.010	0.007
PC	60.6	96.5	0.37	0.059	-	-	0.007	0.018	0.011
PD	NA	NA	0.45	0.004	-	-	0.010	0.016	0.037
PA	45.2	90.5	0.409	0.027	-	-	0.025	0.017	0.032
SA	42.9	91.8	0.697	0.387	0.757	1.676	0.023	0.016	0.043
PE	47.9	89.7	0.428	0.137	-	-	0.015	0.013	0.038
SE	47.9	78.8	0.524	0.586	1.106	1.165	0.089	0.021	0.040
PF	50.4	91.6	0.414	0.132	-	-	0.019	0.012	0.026
SF	29.9	75.6	0.782	0.437	1.287	2.177	0.068	0.021	0.043

to the average in all samples, it is the single peak chosen for most of the quantitative analysis in this work, see chapter 3 for details.

For primary alumina B, two separate determination results are given in table 5.1, each an average over 3 measurements of the single peak (012), of which the (024) is the second order relative. The relative accuracy in the α-alumina content determination will generally decrease with decreasing concentration. A phase content of 1 % is considered to be the general detection limit for ordinary XRD analysis.

The particle size distribution (PSD) is found to be correlated with the α-alumina content in these samples (not shown). Primary alumina B (PB) is known to have little fines, probably due to strong aluminium hydrate precursor grains, and a low attrition index, at 9.2, while alumina PF has a very high attrition index at 29.0 - also seen as a very high fines content in the secondary alumina of the latter quality SF.

The PSD of PB is given as the sample fraction larger than 75 μm and smaller than 45 μm, being 70 % and 7.7 % respectively. For the other aluminas the average diameter of the 10 % smallest fraction, and the 50 % smallest fraction are given, as determined using a combination of sieving and Malvern laser interferometry measurements.

The specific surface area (measured by the BET-method) and the loss-on-ignition (LOI) of volatiles (mostly moisture) is also correlated, both with each other and with the α-alumina content–but only weakly, and with large scatter. Such a correlation is in agreement with the findings of previous workers, see chapters 2 and 8. LOI is given for both 1000 and 1200 °C apart from the usual 1100 °C temperature. LOI has previously been used as a crude measure of specific surface area in chemical compounds [61].

The total moisture content in SGA is MOI + LOI. However, the MOI is very sensitive to the sample treatment, and relative humidity, and is often not cited as a relevant parameter for alumina quality, because it is difficult to determine with any precision and reproducibility. As discussed further in chapter 8, the moisture content of alumina will also influence other parameters, not least the flowability and the packing bulk density, often reported both as unpacked bulk density (UPBD) and packed density. This parameter is very important since the feeding rate of alumina in the modern Hall-Héroult process is based on the volume of alumina.

Chemical impurities are seen to concentrate in the secondary alumina qualities, and the "dirtiest" secondary aluminas are those used in Söderberg

technology cells, as expected.

Quality and Amount of Fluoride Additive

- Synthetic Bayer Cryolite, Na_3AlF_6 + ∼4.5 wt % Al_2O_3 (LECO), T_{liq} determined as 991 °C in our laboratory.
- AlF_3. Norzink: AlF_3 + ∼ 10 wt % Al_2O_3
- Synthesized $NaAlF_4$ (NaF + AlF_3)
  - 40.0 g AlF_3. Alufluor: 97 % + 3.4 wt % Al_2O_3 (LECO)
  - 20.0 g NaF. E. Merck +99 %

$NaAlF_4$ was synthesized from 40.0 g AlF_3 (Alufluor) and 20.0 g NaF (E. Merck). The powders were intimately mixed in a clean Pt-crucible, and heated in an open water-cooled furnace to 1005 °C, and held at temperature for about 1 h and covered with a stream of argon gas. The Pt-crucible and melt sample was subsequently quickly removed and poured over a clean steel plate so that is was very effectively quenched as a large thin flake. Some areas of higher crystallinity (fine needles) were observed.

The "$NaAlF_4$" sample was analyzed by qualitative XRD and determined to contain AlF_3 and chiolite ($Na_5Al_3F_{14}$), as expected. The XRD results did not show any traces of the pattern belonging to meta-stable $NaAlF_4$ phase recently reported by Bruno *et al.* [14, 15], though the crystalline needles would perhaps indicate that they were $NaAlF_4$, since that is the expected crystal habit [12]. $NaAlF_4$ is not a stable compound, but decomposes to AlF_3 and chiolite [176]. According to the phase diagram [176], $NaAlF_4$ is close to the eutectic composition in the system NaF-AlF_3 on the AlF_3 rich side, and the liquidus temperature should be approximately T_{liq}=690 °C, but this was not measured.

5.4.3 Experimental Campaign

Tab. 5.3 gives an overview of the tabulated experimental campaign as divided into series (including duplicates) for the detailed study, of primary and secondary alumina A and primary alumina B. The study includes an investigation into the effect of the operator (NPO, AKK) and of coarse or

Table 5.3: *Tabulated experimental campaign in series (including duplicates) for detailed study, including effect of operator (NPO, AKK) and coarse/ fine ground additive. Fluoride additive given in wt % finely ground, else marked "coarse". See text for details and results.*

Series P/S-A/B + additive	T [°C]	$t \in \{t_0, ..., t_f\}$ [min]
PA + 5 % $AlF_{3,coarse}(g)$	1000	$\{1, 5, 10\}$
PA + 5 % $Na_3AlF_{6,coarse}(l)$	1000	$\{1, 10\}$
PA + 5 % $NaAlF_{4,coarse}(l)$	800	$\{1, .., 20\}$
SA + 5 % $NaAlF_{4,coarse}(l)$	800	$\{1, 5\}$
PA + 5 % $NaAlF_4(l)$	800	$\{1, .., 20\}$
SA + 5 % $NaAlF_4(l)$	800	$\{1, .., 20\}$
PA + 5 % $NaAlF_4(l)$,AKK	800	$\{1, .., 100\}$
PA + 5 % $NaAlF_4(l)$,AKK	800	$\{1, .., 100\}$
PB + 5 % $NaAlF_4(l)$,AKK	800	$\{1, .., 100\}$
PA + 5 % $NaAlF_4(l)$	700	$\{1, .., 30\}$
SA + 5 % $NaAlF_4(l)$	700	$\{1, .., 30\}$
PA + 10 % $NaAlF_4(l)$	800	$\{1, .., 1000\}$
PB + 10 % $NaAlF_4(l)$	800	$\{1, .., 100\}$
PA + 2 % $AlF_3(g)$	800	$\{1, 5, 10\}$
PA + 5 % $AlF_3(g)$	800	$\{1, 5, 10\}$
PA + 15 % $NaAlF_4(l)$	800	$\{1, .., 100\}$
PB + 15 % $NaAlF_4(l)$	800	$\{1, .., 100\}$
α-PB + 5 % $NaAlF_4(l)$	800	$\{1, .., 100\}$
α-PB + 15 % $NaAlF_4(l)$	800	$\{1, .., 100\}$
PA + 20 % $NaAlF_4(l)$	800	$\{1, 2, 5, 10, 100\}$
PB + 20 % $NaAlF_4(l)$	800	$\{1, 2, 5, 10, 100\}$
PA + 5 % $NaAlF_4(l)$	900	$\{1, 2, 5, 10, 30\}$
SA + 5 % $NaAlF_4(l)$	900	$\{1, 2, 5, 10, 30\}$

fine fluoride powder additive in the case of $NaAlF_4$, which melts during the initial period. The fluoride additive described in tab. 5.3 is given in wt % of the finely ground powder, and marked "coarse" powder in the series where this is the case.

A preliminary campaign is reported in appendix B, in tabs. B.1 and B.2

Table 5.4: *Qualitative Scale used to determine degree of agglomeration (termed "sintering" by Kobbeltvedt [86]) in samples prepared as loose SGA and fluoride additive in shallow Pt-dish as described in text.*

Score (1-10)	Qualitative Description of Sample
0	Free flowing powder
1	Traces of agglomeration/ coherent areas
2	Initial agglomeration/ up to 10 % clearly coherent
3	Increasing agglomeration/ up to 25-33 % coherent
4	Predominantly agglomerated/ 50-75 % coherent, flakelike
5	Sample is coherent tablet/ partly sticks to Pt-dish when flipped
6	Up to 50 % sticks when flipped/ rest falls as powder and weak lumps
7	Entire sample sticks when flipped/ removed as lumps and powder
8	Entire sample sticks when flipped/ removed as tablet/ pieces of tablet
9	Mechanically stable tablet/ may be handled carefully
10	Tablet easily removed/ increased coherent strength

using secondary alumina. A semi-quantitative campaign was subsequently conducted in order to compare the agglomeration tendency for 9 alumina qualities, of both primary and secondary qualities.

5.4.4 Semi-Quantitative "Sinter-Scale"

A qualitative "Sinter"-scale, shown in table 5.4, is used to determine the degree of agglomeration in samples prepared as a loose powder of SGA and

the fluoride additive. The tablet samples are formed as previously described, by using approximately 1.2 g of sample set in a shallow Pt-dish and held in a muffle furnace (preheated to set-temperature ± 2 °C) for a preselected duration, t, for t ∈ {1, 1000} min.

The "sinter"-scale is best suited for these experiments, employing a "liquid" phase fluoride additive. In cases where secondary alumina is heat-treated without the liquid additive, the scale is not quite relevant, but does indicate whether the sample sticks to the Pt-dish when flipped. Sticking is in itself proof of at least partial powder consolidation. However, such samples tend to disintegrate into quite free-flowing powder when released from the Pt-dish, see later discussion.

5.5 Results: Tablet Geometry

5.5.1 Preliminary Experiments

A series of preliminary experiments using the same general approach and small Pt-dishes investigated the agglomeration behavior of an unknown secondary oxide. This alumina is almost certainly secondary Alpart alumina, the source and properties being referred by Kobbeltvedt [86]. The results of that experimental series are presented in tables B.1 and B.2 in Appendix B.

The temperatures used were 700, 800, 900 and 1000 °C, while the holding time of the sample in the furnace was 1, 2, 3, 5, 10, 20, 30 and up to 100 min. The sample weight loss, assumed to be mostly adsorbed moisture, was measured as the difference before and after the heat treatment.

A qualitative description of the degree of agglomeration of the sample was correlated to the "sinter-scale" given by Kobbeltvedt [86]. Kobbeltvedt used Roman numerals I to IV, to describe increasing agglomeration in samples of secondary alumina held at temperatures in the range of 500 to 900 °C, and concluded that traces of agglomeration occurred after the sample was held for 10 min at 700 °C. This is within the time-scale relevant for alumina addition and dissolution in modern point-fed Hall-Héroult cells. Increasing temperature resulted in traces of agglomeration after shorter exposure times.

The results in tables B.1 and B.2 are in general agreement with that conclusion. Traces of agglomeration is observed after 30 min at 700 °C, and after

10 min at 800 °C. Also, by comparing the average weight loss of the first 10 min samples at each temperature we also see a clear correlation between the weight loss, heat treatment temperature and the degree of agglomeration, e. g. a mean weight loss of 0.8±0.4 wt % for 700 °C, 1.7±0.2 wt % for 800 °C and 1.9 and 2.4 at 900 and 1000 °C respectively. The greatest increase in weight loss is thus observed when agglomeration occurs. This must be related to an increasing $\gamma \rightarrow \alpha$ conversion, as concluded by Ødegård *et al.* [127].

Most samples disintegrated to a free-flowing powder after being removed from the Pt-dish. It may also be observed that the secondary alumina samples loose their gray hue with time at temperature, and with increasing temperature, probably due to adsorbed carbon dust from the dry scrubbing process, being released as CO/CO_2 upon reacting with oxygen, further discussed in chap. 7.

5.5.2 Semi-Quantitative Comparative Study

A series of experiments was conducted using new Pt-dishes in order to investigate and compare the agglomeration behavior of 9 types of SGA. The results are presented in figs. 5.1, 5.2 and 5.3. For every alumina quality, samples were mixed with 5 wt % $NaAlF_4$, and the heat- treatment was carried out at 800 °C, according to a randomized experimental plan in order to avoid bias imposed by the operator and systematic error, such as varying relative humidity.

For every series a random copy sample was made in order to obtain a measure of the experimental scatter. For a few of the series we see that such scatter is rather large for the weight loss and agglomeration score. The semi-quantitative agglomeration data were obtained by applying the "Sinter-Scale", presented in tab. 5.4, in order to judge the extent of agglomeration and quantify the agglomerate strength on a scale from 0 to 10, 0 being a free flowing powder and 10 describes a pelletized agglomerate of sufficient strength for it to withstand (careful) manual handling.

The degree of weight loss correlated to the degree of agglomeration that occurs for all samples. For SGA SF, with a very high level of fines, the weight loss is linear on the log(t) scale, and shows up to 4.5 wt % relative weight loss after 100 min at 800 °C.

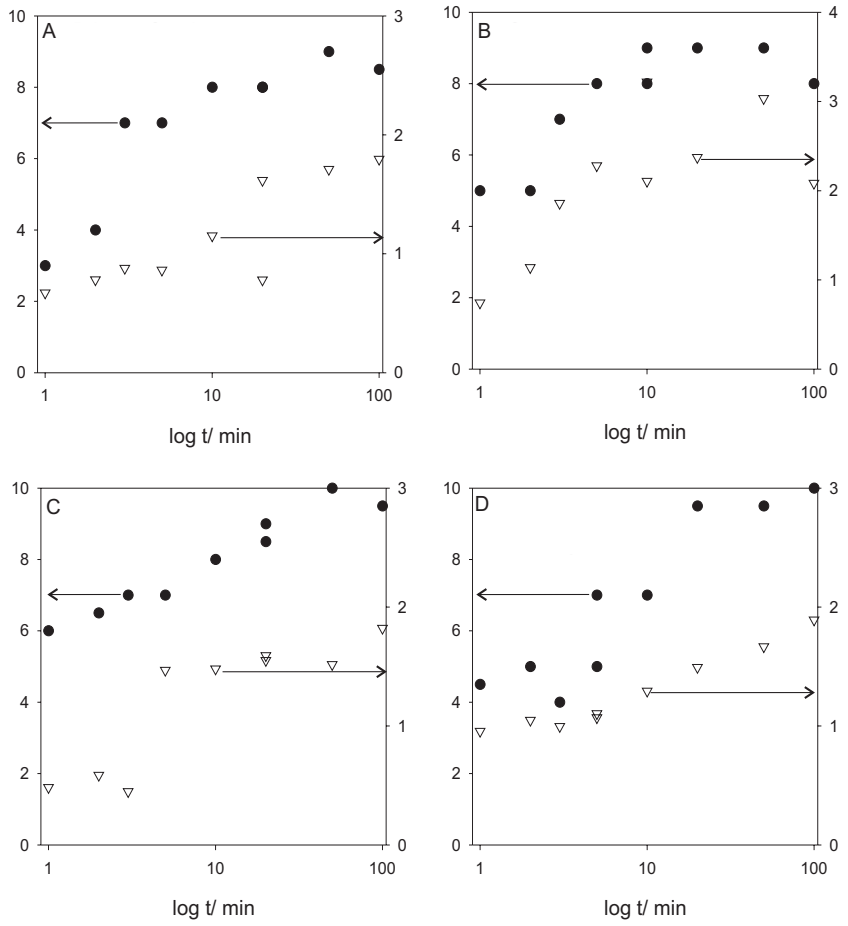

Figure 5.1: *Comparative study of aluminas with 5 wt. % $NaAlF_4$ added. "Sinter-score" and weight loss of samples plotted versus log time at 800 °C. A: Alumina quality PA (primary A), B: SA (secondary A), C: PB, D: PC; Filled circles: Sinter score (0-10); Open triangles: weight loss [wt %]. Weight loss is strongly correlated with the degree of agglomeration.*

Generally, the method gives quite reproducible data. For the semi-quantitative agglomeration score the reproducibility is within ± 1 point between experiments and operator (NPO/ AKK). During the course of the comparative study the weight of the Pt-dishes was observed to increase linearly at 0.1 mg (fig. 5.4) with every experiment, and the Pt-dishes became increasingly gray to white. This observation may be attributed to the formation of some

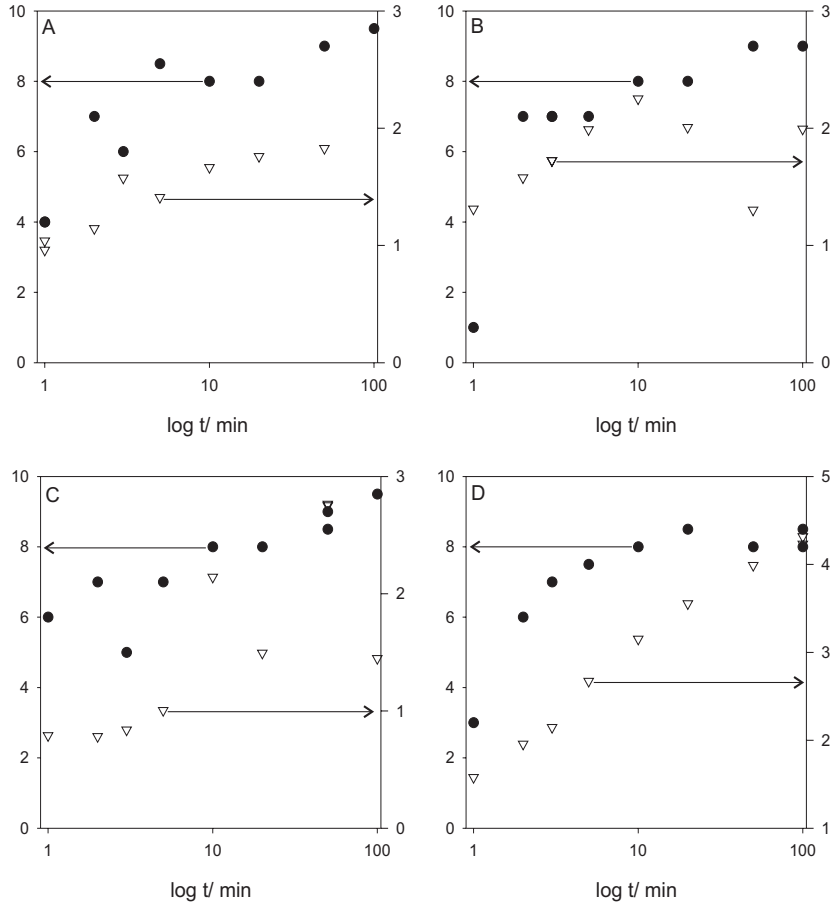

Figure 5.2: *Comparative study of aluminas with 5 wt. % $NaAlF_4$ added. "Sinter-score" and weight loss of samples plotted versus log time at 800 °C. A: PE (primary E), B: SE (secondary E), C: PF, D: SF; Filled circles: Sinter score (0-10); Open triangles: weight loss [wt %].*

cryolite residue as the $NaAlF_4$ phase reacted with moisture in the samples, see the discussion of "hydrolysis" in chapter 8. The Pt-dishes were cleaned in HCl after the series.

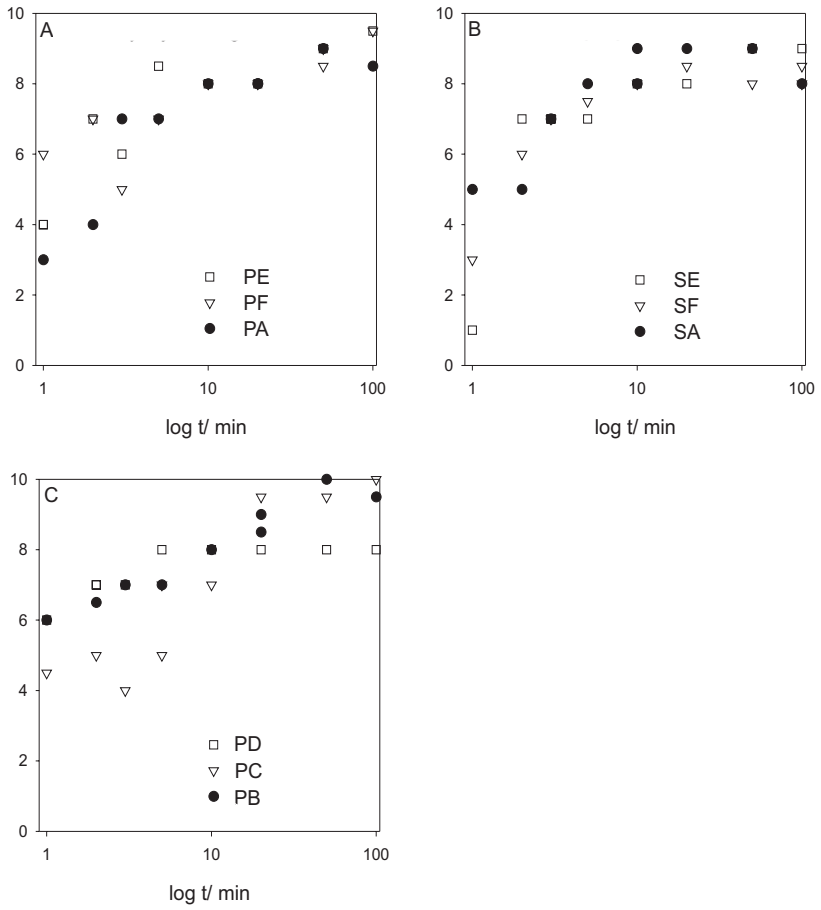

Figure 5.3: *Comparative study "sinter-scores"; A: PE, PF and PA medium α-content primary SGAs; B: SE, SF and SA medium α-content secondary SGAs, C: PD, PC and PB low α-content primary SGAs, which have a greater propensity for agglomeration.*

5.5.3 Detailed Study

Kinetic parameters k and n are obtained according to the JMA-theory, in eq. 5.1, by linear regression analysis of quantitative XRD data. The JMA-theory and eq. 5.1 is presented in section 5.6.7.

In the comparative study primary alumina B is shown to have the highest tendency for agglomeration overall, similar to the other two low α-content

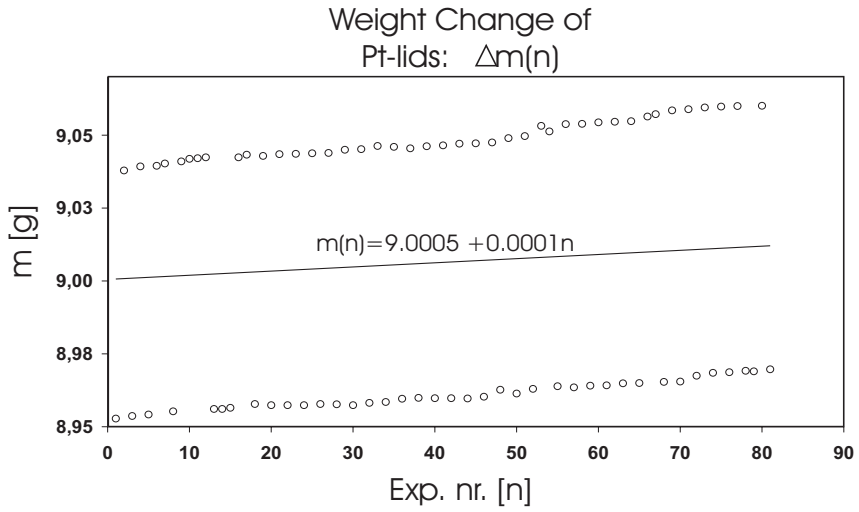

Figure 5.4: *Weight change of Pt-dishes as measured during the series of experiments performed for the comparative study. The small mass difference between the two dishes is apparent. Regression fitted for entire data set.*

aluminas, see fig. 5.3. Aluminas A and B were known to be preferred in modern prebake cells at the time of sampling. Furthermore, alumina B was known to form hard top-crusts, but also to have very low dusting. In a previous study the quality B was found to have rapid dissolution behavior [149].

It seems that alumina B has some distinct properties that may be related to the low α-alumina content, but probably also to more subtle properties. Alumina A has a medium α-alumina content and was chosen as a standard reference for comparison with the B quality.

5.5.4 XRD Results

A comparison of the qualitative degree of agglomeration of primary alumina A and B as a function of time and the amount of $NaAlF_4$ fluoride additive in wt % is presented in figs. 5.5 and 5.6. An increased fluoride level does not alter the general trend in the data, mostly showing the experimental scatter of this qualitative determination. However, for PA there is pronounced

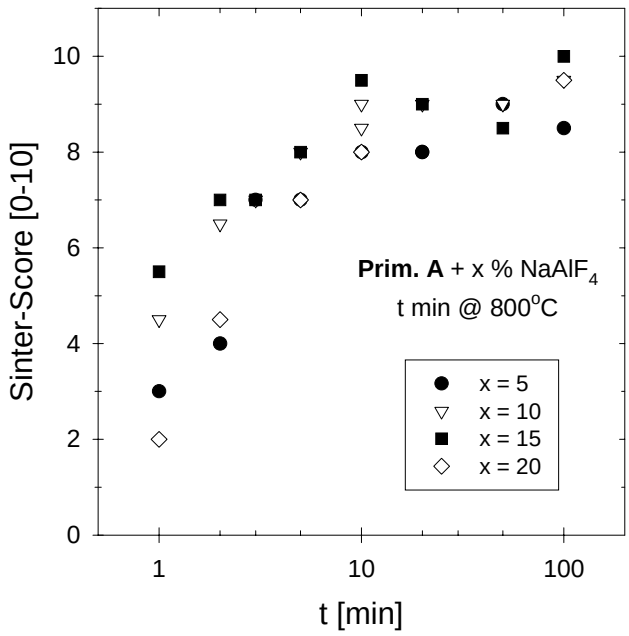

Figure 5.5: *Effect of increasing amount of added fluoride phase on the agglomeration of primary alumina A.*

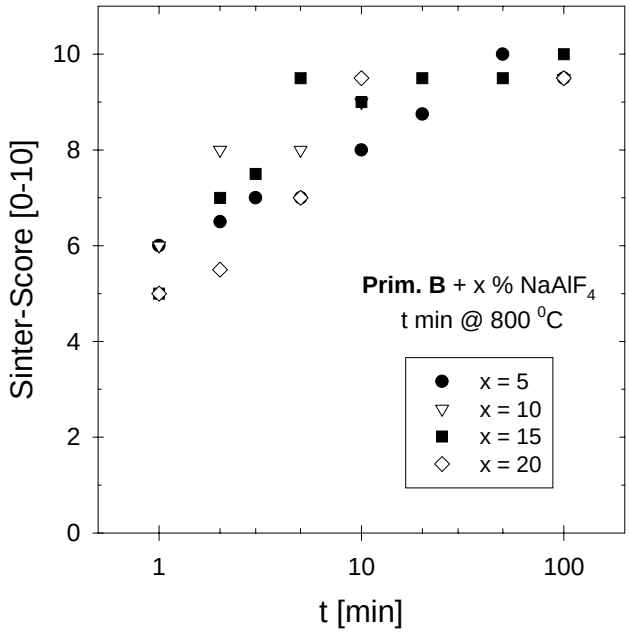

Figure 5.6: *Effect of increasing amount of added fluoride phase on the agglomeration of primary alumina B.*

Table 5.5: *Results from detailed study applying the JMA theory to obtain kinetic parameters k and n in eq.5.1. R^2 is the usual measure of linear model fit.*

Sample P/S-A/B + F-additive	T [°C]	$t \in \{t_0, t_f\}$ [s]	k	n	R^2
PA + 15 % $NaAlF_4(l)$	800	$\{60, 6000\}$	$1.27{\cdot}10^{-2}$	0.53	0.99
PA + 20 % $NaAlF_4(l)$	800	$\{60, 6000\}$	$5.78{\cdot}10^{-3}$	0.67	0.98
PB + 15 % $NaAlF_4(l)$	800	$\{60, 6000\}$	$1.55{\cdot}10^{-3}$	0.76	0.97
PB + 20 % $NaAlF_4(l)$	800	$\{60, 6000\}$	$1.28{\cdot}10^{-3}$	0.80	0.99
PA + 5 % $NaAlF_4(l)$,NPO	800	$\{60, 1200\}$	$3.58{\cdot}10^{-2}$	0.29	0.93
PA + 5 % $NaAlF_4(l)$,AKK	800	$\{60, 1200\}$	$4.98{\cdot}10^{-2}$	0.26	0.96
SA + 5 % $NaAlF_4(l)$,AKK	800	$\{60, 3000\}$	$2.30{\cdot}10^{-2}$	0.47	0.94
PA + 5 % $NaAlF_4(l)$	700	$\{60, 1800\}$	$5.64{\cdot}10^{-2}$	0.14	0.96
SA + 5 % $NaAlF_4(l)$	700	$\{60, 1800\}$	$4.19{\cdot}10^{-2}$	0.20	0.93
PA + 5 % $AlF_3(g)$	800	$\{60, 1200\}$	$3.51{\cdot}10^{-2}$	0.22	0.96
PA + 5 % $AlF_3(g)$	1000	$(60, 300)$, 2 pts.	$2.53{\cdot}10^{-5}$	2.24	1.00
PA + 5 % $Na_3AlF_6(l)$	1000	$(60, 600)$, 2 pts.	$1.29{\cdot}10^{-2}$	0.72	1.00

scatter initially, and the high fluoride contents ensures that PA attains the maximum score after 100 min.

A comparison of the degree of $\gamma \rightarrow \alpha$ transformation of primary alumina A and B as a function of time and the amount of $NaAlF_4$ fluoride additive in wt % is presented in figs. 5.7 and 5.8. An increased fluoride level is seen to slightly decrease the degree of transformation after 1 min at temperature. This is probably due to a longer incubation period while the fluoride additive melts. Generally, the PA quality has a higher α alumina content throughout, starting at 9.5 % compared to around 3 % for PB.

For the lower fluoride addition levels, the $\gamma \rightarrow \alpha$ transformation is seen to halt after a time, 5 - 10 min, while it continues for higher levels of $NaAlF_4$ additive. We attribute this effect to the reaction of the fluoride additive with moisture in the samples, which effectively passivates it, probably by producing solid alumina and cryolite, see later discussion. The same XRD data is presented using the JMA- presentation in figs. 5.21 and 5.22, a linear regression analysis was performed for all the data series, and the kinetic parameters of the JMA-theory were calculated, see tab. 5.5. Based

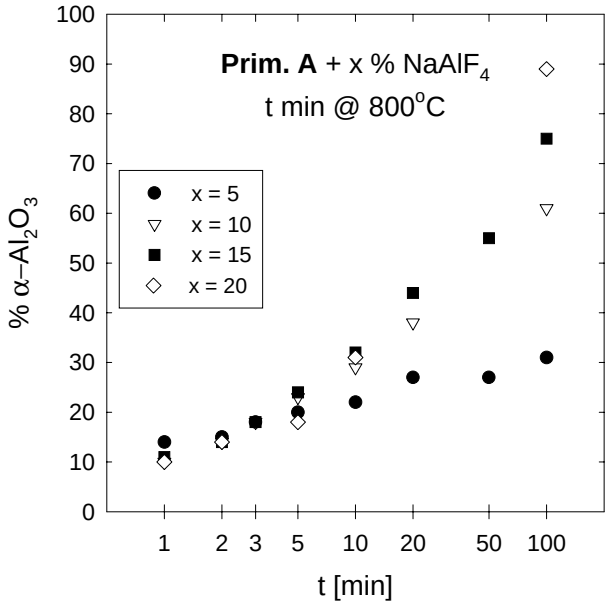

Figure 5.7: *Quantitative XRD data shows effect of increasing amount of added fluoride phase on degree of phase transition to α-Al_2O_3 of primary alumina A.*

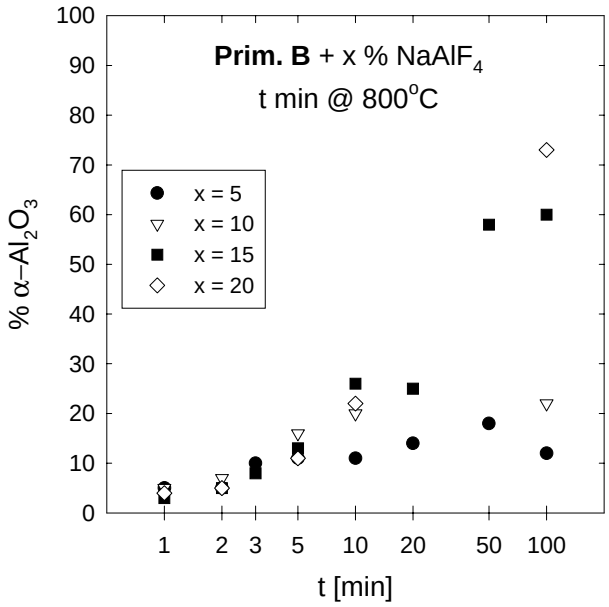

Figure 5.8: *Quantitative XRD data shows effect of increasing amount of added fluoride phase on degree of phase transition to α-Al_2O_3 of primary alumina B.*

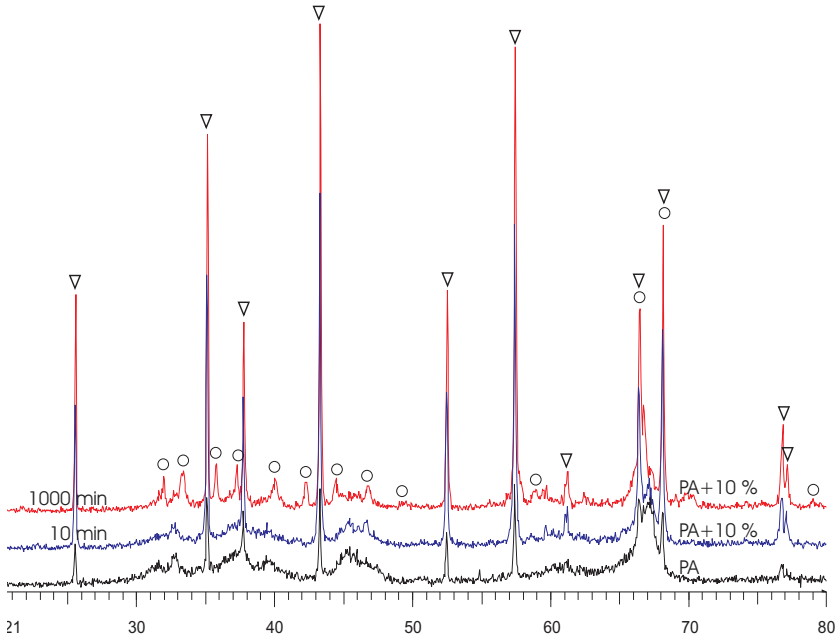

Figure 5.9: *XRD scans, intensity vs. diffraction angle* 2θ *of samples PA + 10 % $NaAlF_4$, held at 800 °C for 1000 min (top) and 10 min (middle). Untreated PA-sample for reference (bottom). Diffraction patterns identified as* α*- (*∇*) and* β*- Al_2O_3 (*$\circ$*).*

on the XRD analysis presented in fig. 5.9 and on the phase diagram by Foster [34], we conclude that the equilibrium condition for the primary alumina + $NaAlF_4$ additive is a mixture of α and β-alumina, see later discussion.

SEM Results

SEM-Back Scatter Electron (BSE) images are presented in figs. 5.10 and 5.11 for two sample series with 5 wt % AlF_3 and cryolite (Na_3AlF_6), respectively, added to primary alumina A and heat-treated in Pt-dishes at 1000 °C.

In both cases in which the sample has been held for only 1 min at temperature, in figs. 5.10A and 5.11A, there is evidence of loosely bound grains, and interconnecting microstructures. The light "wooly" structures seen in the images are due to weak bonding forces of the sub-micron α-Al_2O_3 platelets

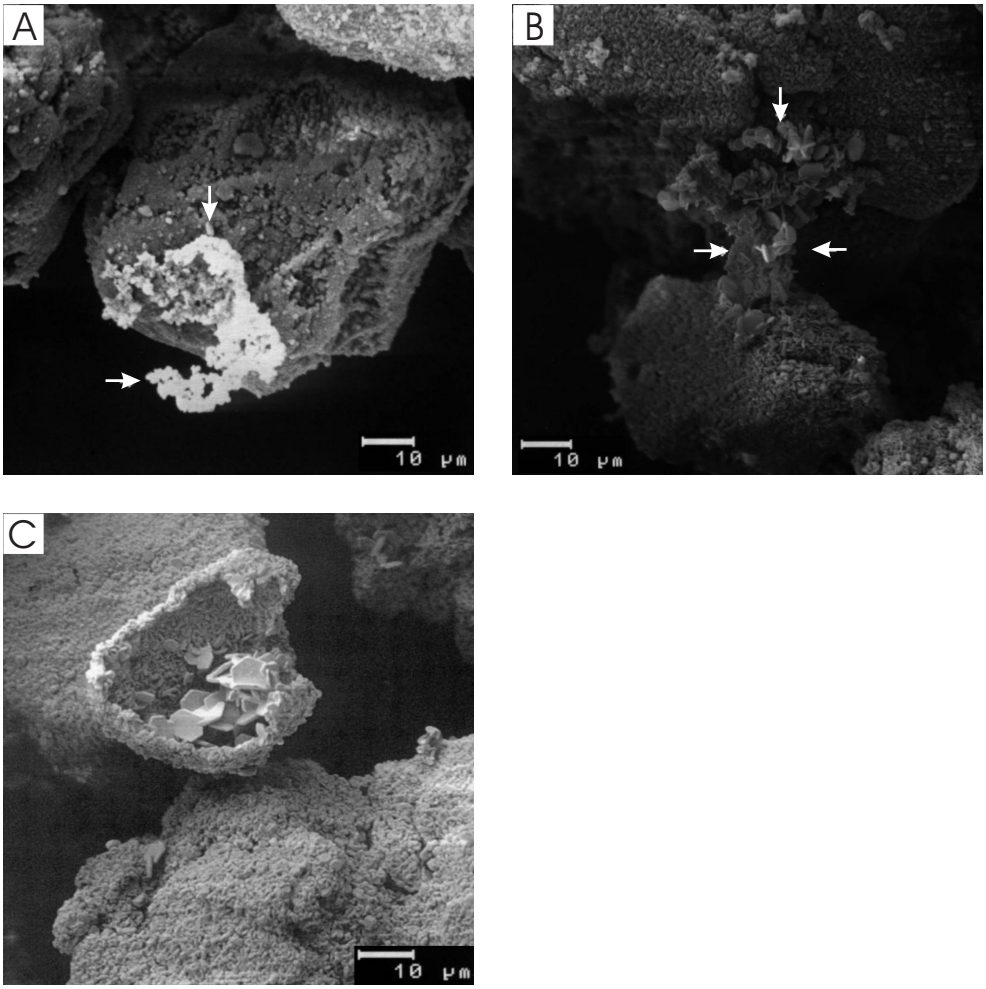

Figure 5.10: *SEM-BSE images. 5 wt % AlF_3 added to primary alumina A. Image A: Light "wooly" structure in center due to sub-micron α-Al_2O_3 platelets. Sample held 1 min at 1000 °C, 1000×. B: Residual interlinking provided by platelets of recrystallized alumina grain-shell, sample held 5 min at 1000 °C, 1000×. C: Image shows coarse platelets in grain center surrounded by finer crystallite shell interlinking the underlying grains, further discussed in text, 1000×.*

that selectively charge under the electron beam. The agglomeration in both

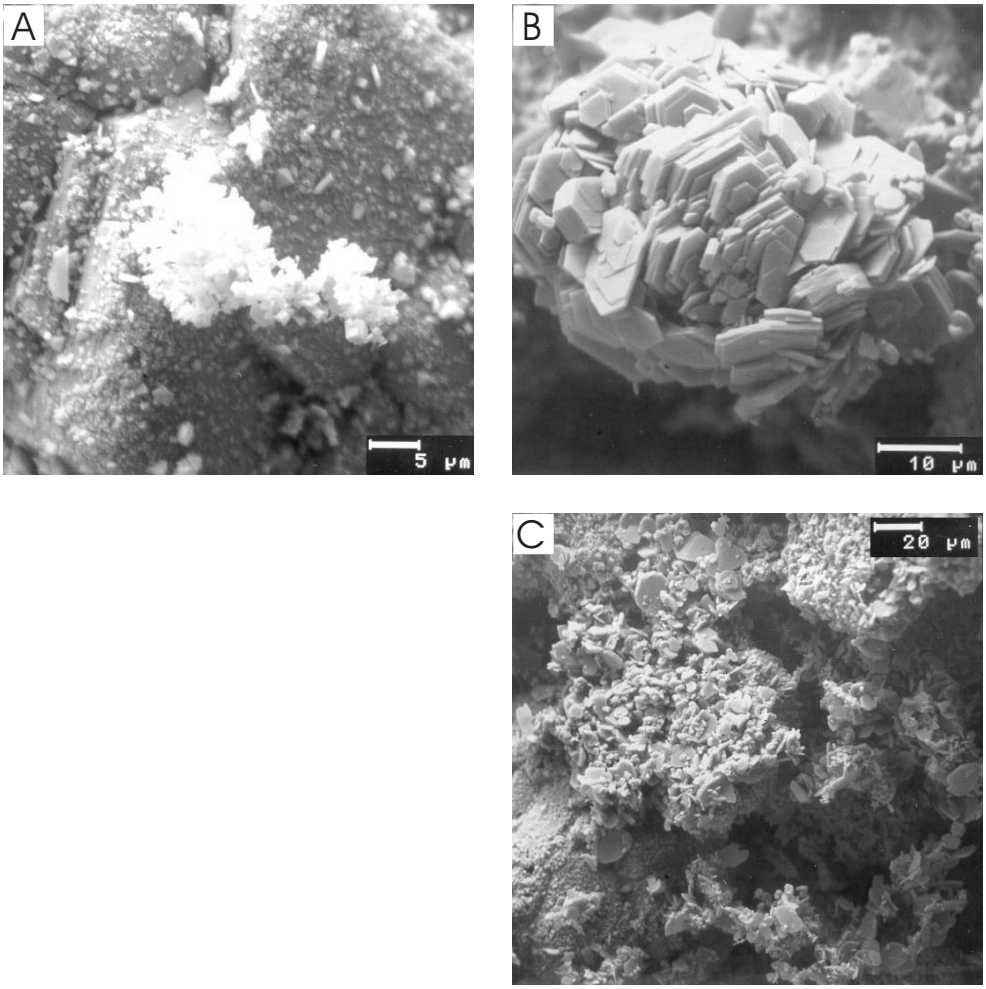

Figure 5.11: *SEM-BSE images. 5 wt % cryolite (Na_3AlF_6) added to primary alumina A. Image A: Light "wooly" structure due to weak bonding of sub-micron α-Al_2O_3 platelets that selectively charge under the electron beam. Sample held 1 min at 1000 °C, 2000×. B: Sample held 10 min at 1000 °C. Alumina grain has collapsed into a dense aggregate of coarse α-Al_2O_3 crystallites, 1700×. C: Typical micro-structure evident in same sample as B, skeletal remains of recrystallized grain-shell evidently interlinking underlying grains, 500×.*

cases was quite light, loose lumps having been formed.

In figs. 5.10B and 5.11C there is evidence to support the notion that the interlinking of neighboring grains is apparently provided by platelets of recrystallized alumina surface "grain-shells". The grain-shells are akin to rough egg-shells. This structure is much further developed in fig. 5.11C, probably due to the presence of the liquid fluoride phase present. The interlinking platelets are less than 4 μm for the AlF_3 sample (fig.5.10) but they are in excess of 10-15 μm for the samples exposed to liquid cryolite held 5-10 min at 1000 °C, ref. fig. 5.11.

In fig. 5.10C we see that coarse platelets of approx. 5 μm in the center of the grains are surrounded by a finer crystallite shell. Since most of the surface area of alumina is internal, it may be argued that the interior of the grain will retain a higher concentration and containment of the gaseous species (AlF_3 and H_2O), thus resulting in the well developed, internal α-Al_2O_3 platelet microstructure.

In fig. 5.11B a single alumina grain (but not the only one observed) has collapsed into a dense aggregate of coarse α-Al_2O_3 platelets with orientations probably resembling the orientation of the aluminium hydrate precursor.

Fig. 5.12 presents SEM-BSE images of the agglomerate sample resulting when primary alumina B and 10 wt % NaAlF4 powder was held for 100 min at 800 °C. Quantitative XRD analysis showed this sample to contain 23 % α-Al_2O_3, while the remainder is probably a mixture of γ- and β-Al_2O_3. The sample obtained an agglomeration "sinter-score" of 9 to 10, and was a fairly strong tablet, showing brittle behavior when the sample had to be crushed for analysis.

Fig. 5.12A shows well developed platelets of about 5 μm in a sub-micron "γ+ β" matrix, while fig. 5.12B shows evidence of the same type of interlinking, recrystallized, alumina grain shell as those in figs. 5.11 and 5.10.

Particle Size and Specific Surface Area

The reduction of the specific surface area (SSA) was measured by the BET method for 3 agglomeration series, as presented in fig. 5.13. The SSA decreases as the overall solid surface area decreases, which correlates to crystallite and microstructre coarsening. The surface area is reduced to about half the initial value after 5 min at 800 °C when 10 wt % $NaAlF_4$ is added.

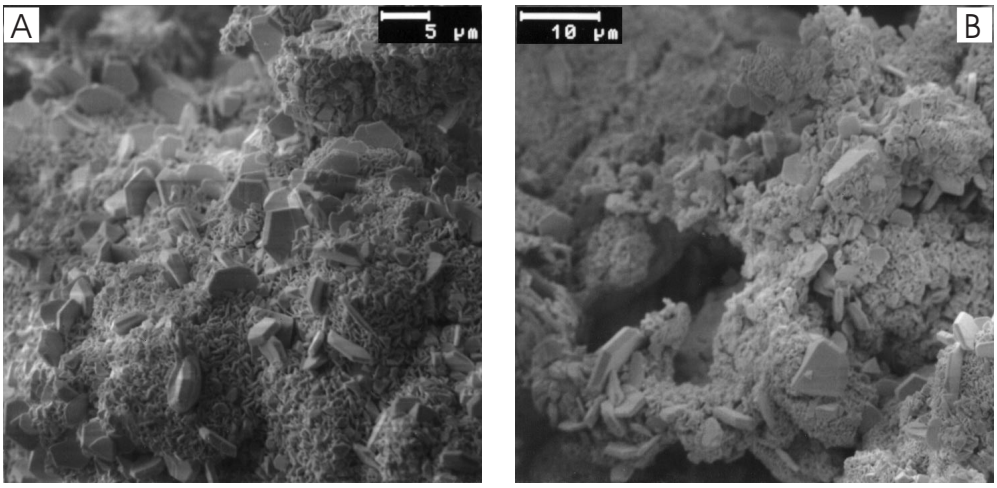

Figure 5.12: *SEM-BSE images of agglomerate sample resulting when primary alumina B and 10 wt % NaAlF−4 powder was held for 100 min at 800 °C. A: Well developed platelets in sub-micron "$\gamma + \beta$" matrix, 2000× B: As in A, but evidence of interlinking recrystallized alumina grain-shell similar to those in figs. 5.11 and 5.10, 1602×.*

On a logarithmic time scale the reduction in SSA is linear for PB + 10 wt % $NaAlF_4$. For PA + 5 wt % $NaAlF_4$ the reduction in SSA is halted after 10 min, while the kinetics of the reduction in SSA seem to increase after 10 min for the SA + 10 wt % $NaAlF_4$ series.

The reduction in the SSA(BET) is correlated to the $\gamma \rightarrow \alpha$ phase transition, but the XRD data (in fig. 5.8) shows that the transformation halted for the PB + 10 wt % $NaAlF_4$ sample series after about 10 min, while the reduction in SSA continues, as seen in fig. 5.13. The microstructural coarsening responsible for the reduction in SSA is obviously not the formation of more α phase, but perhaps coarsening of the transition alumina matrix, and some loss of porosity, perhaps involving moisture. See later discussion.

The initial surface area is quite similar for aluminas A and B at 57.0[63.0] and 66.0 m^2/g respectively. As expected, there was no change in the SSA for a sample of primary alumina A without fluoride additive held at this temperature (800 °C) for 20 min.

The application of the "equivalent diameter" method to the BET data, as-

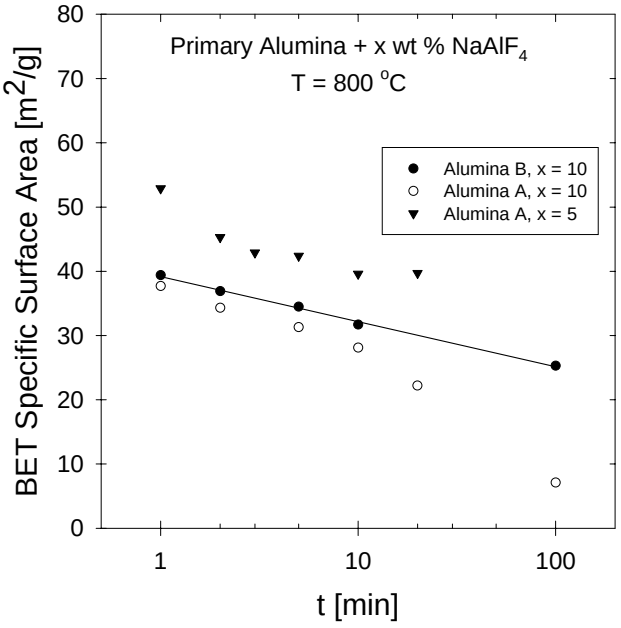

Figure 5.13: *Reduction of surface area showing differences between alumina types A and B. Kinetics are linear in log(t) for alumina B + 10 wt % $NaAlF_4$.*

suming spherical grains, may give a relevant measure of crystal coarsening in simple systems. However, – since most of the loss of surface area is due to the formation of α-Al_2O_3, and probably not coarsening of the transition alumina microstructure, this method is not as relevant as direct size determination (of the recrystallized α-Al_2O_3). Data on particle size evolution (from BET) may however be correlated with results obtained from XRD diffraction peak broadening and SEM topography images in tabs. 5.6 and 5.7.

The distribution of scattered intensity of single XRD peaks may be used to characterize the microstructure of a crystalline powder sample, see chapter 3. In tab. 5.6 the maximum crystallite size d_{max} determined from SEM-images, the equivalent particle diameter, d_{equ}, calculated from the specific surface area (BET) assuming spherical grains and the results from standard XRD data by the Scherrer method (eq. 3.3 in chapter 3) determined from the XRD peak line width, the Full Width at Half Maximum ($FWHM$), presented (as $\bar{L}$), are presented for comparison, to be discussed later.

Table 5.6: *Maximum crystallite size d_{max}(SEM), Eqv. particle diam. d_{eqv}(BET) and results from XRD (FWHM). See text for discussion.*

Sample	Exposure	FHHM [° 2θ]	L [μm]	d_{max} [μm]	BET-SSA [m^2/g]	d_{eqv} [μm]
Alumina A						
PA	RT, Ambient	0.165	0.06	-	65.2	0.023
PA	5 h at 1200 °C	0.135	0.08	0.7	6.1	0.25
PA + 5 % $Na_3AlF_6(l)$	10 min at 1000 °C	0.109	0.12	15.0	-	-
PA + 5 % $AlF_3(g)$	5 min at 1000 °C	0.110	0.12	4.0	-	-
PA + 5 % $AlF_3(g)$	10 min at 1000 °C	0.112	0.11	5.0	-	-
Alumina B						
PB	RT, Ambient	0.151	0.06	-	66.0	0.023
PB	5 h at 1200 °C	0.124	0.09	-	-	-

The Warren-Averbach analysis method may be used to obtain a measure of the particle size distribution (nanostructure) of the α-alumina content of alumina and agglomerate samples. The particle domain size is obtained using one or more diffraction peaks, ref. chapter 3. The PSD results for aluminas A and B, and some agglomerates formed using those SGAs, are presented in figs. 5.14 and 5.15, as relative column length.

Numerical data of the average particle size of aluminas A and B, obtained by the Warren - Averbach analysis of; (1) primary grade alumina, (2) the partly $\gamma \rightarrow \alpha$ transformed agglomerate samples, with added fluorides as previously described, and (3), of calcined 100 % α-aluminas A and B, are presented in table 5.7.

The results may be compared with those obtained by the simple Scherrer equation, also presented in table 5.6 along with the data obtained from SEM micrographs and SSA BET.

When calcining primary alumina in air at 1200 °C, the alumina grains transform to polycrystalline α-Al_2O_3, with a "ceramic" type microstructure as shown in figs. 5.16B,C. The average crystal size is seen to be less than 1 μm, while the typical lamellar pores of calcined SGA. The crushing strength of the transformed grains is markedly lower than that of the primary.

Table 5.7: *Mean particle size (in nm) determined using XRD line profile analysis, using both single line (SL) and Warren-Averbach (WA), and simple Scherrer determination. See text for discussion.*

Sample	Exposure	FHHM [° 2θ]	L [nm]	L_{SL} [nm]	L_{WA} [nm]
Alumina A					
PA	RT, Ambient	0.165	60.8	37.4	26.0
PA + 5 % AlF_3	5 min at 800 °C	0.153	61.8	47.0	52.7
PA + 5 % $NaAlF_4$	5 min at 800 °C	0.157	59.7	45.1	50.1
PA + 10 % $NaAlF_4$	5 min at 800 °C	0.174	52.2	-	46.9
PA + 15 % $NaAlF_4$	10 min at 800 °C	0.164	56.3	36.1	41.9
PA + 5 % $NaAlF_4$	5 min at 900 °C	0.149	64.1	46.2	53.0
PA	5 h at 1200 °C	0.135	80.6	-	66.0
Alumina B					
PB	RT, Ambient	0.151	63.0	39.7	9.2
PB + 15 % $NaAlF_4$	10 min at 800 °C	0.155	60.7	41.3	48.3
PB	5 h at 1200 °C	0.124	92.6	-	73.0

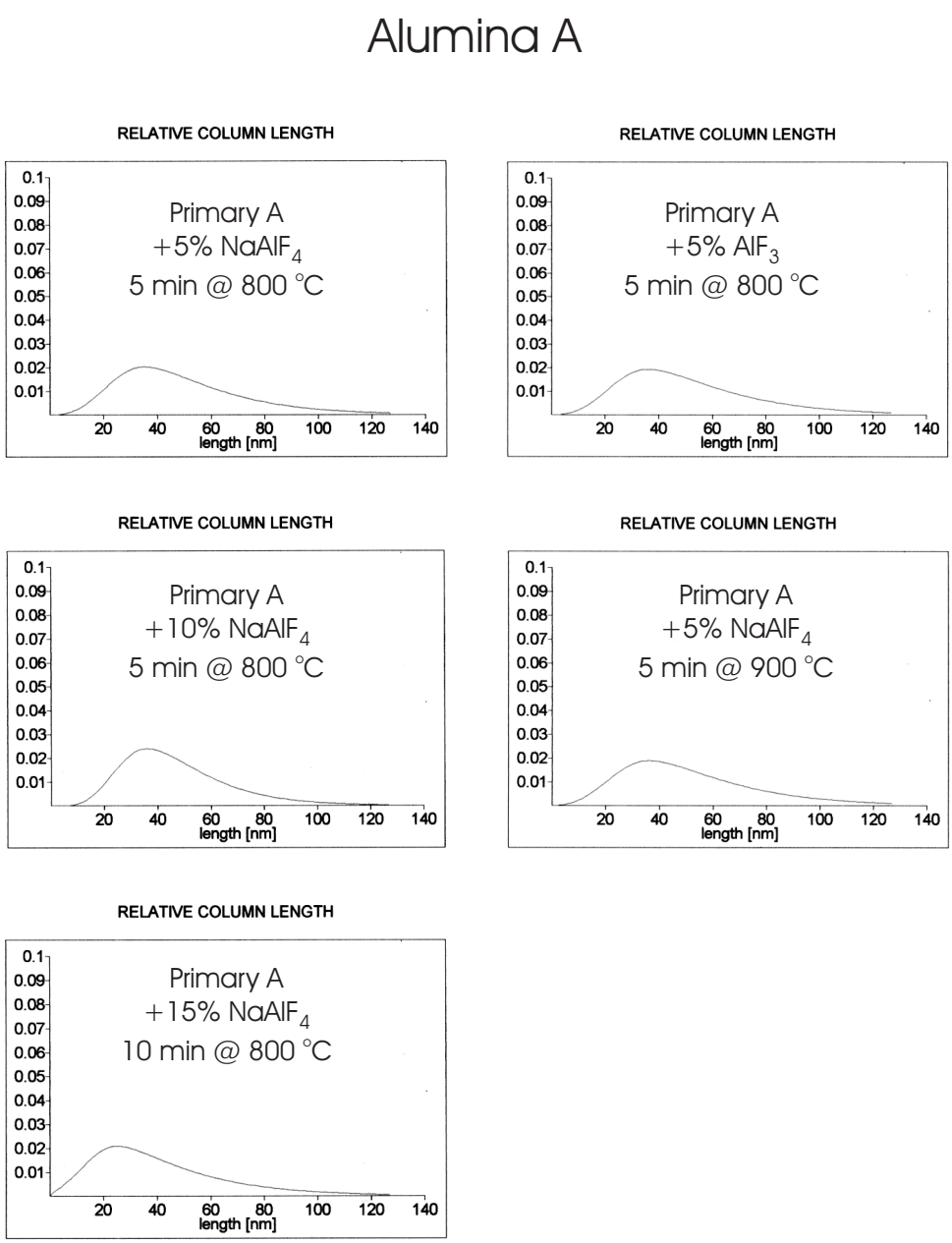

Figure 5.14: *Determination of nano/ micro-crystalline grain structure evolution of α-Al_2O_3. Distribution of relative column lengths (i. e. crystal domain size) determined by Warren-Averbach line profile analysis of the (024) powder X-ray diffraction peak. Effects of fluoride additive, heat treatment time and temperature. Integrated area is unity value.*

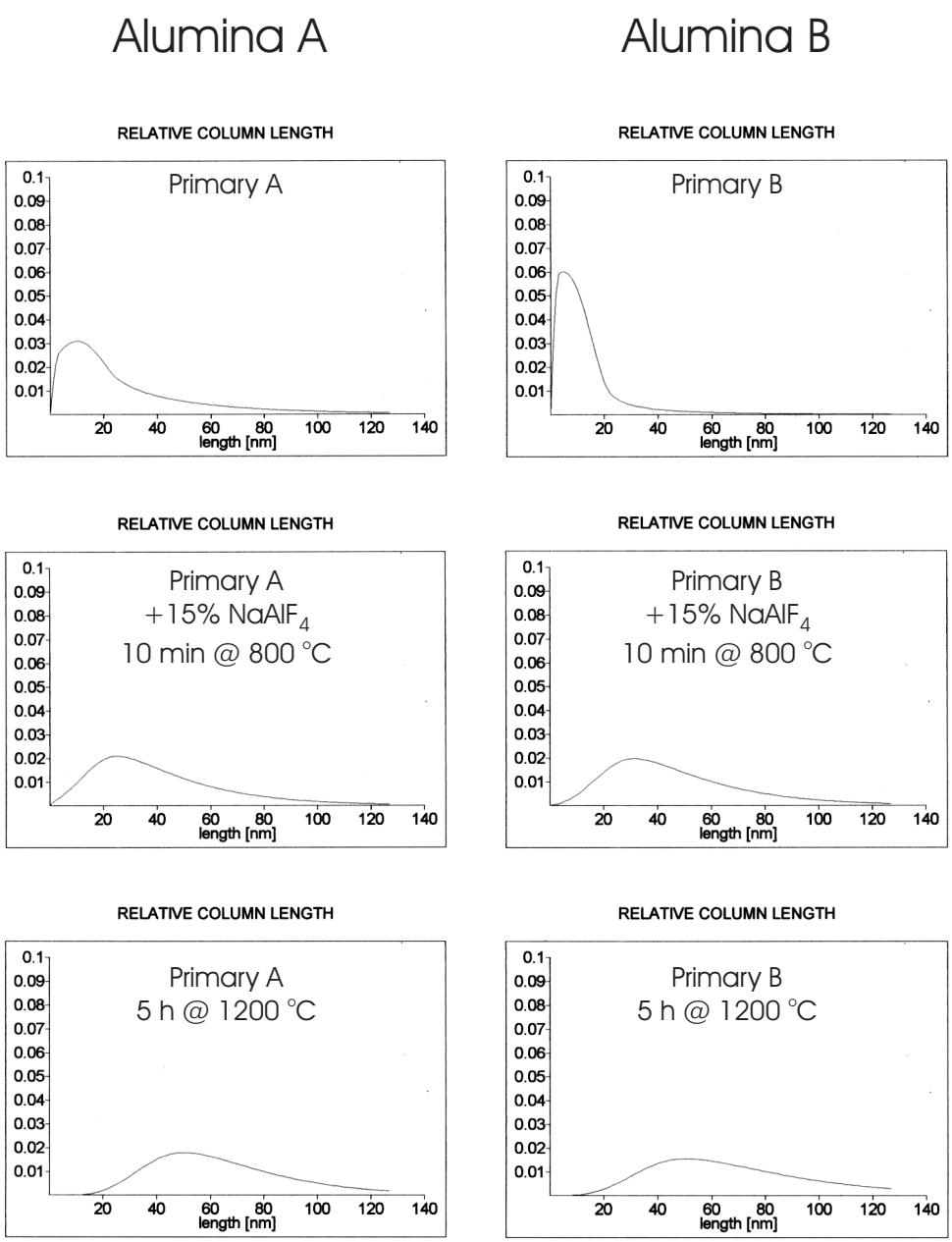

Figure 5.15: *Determination of nano/ micro-crystalline grain structure of α-Al_2O_3. Distribution of relative column lengths (i. e. crystal domain size) determined by Warren-Averbach line profile analysis of the (024) powder X-ray diffraction peak. Integrated area is unity value.*

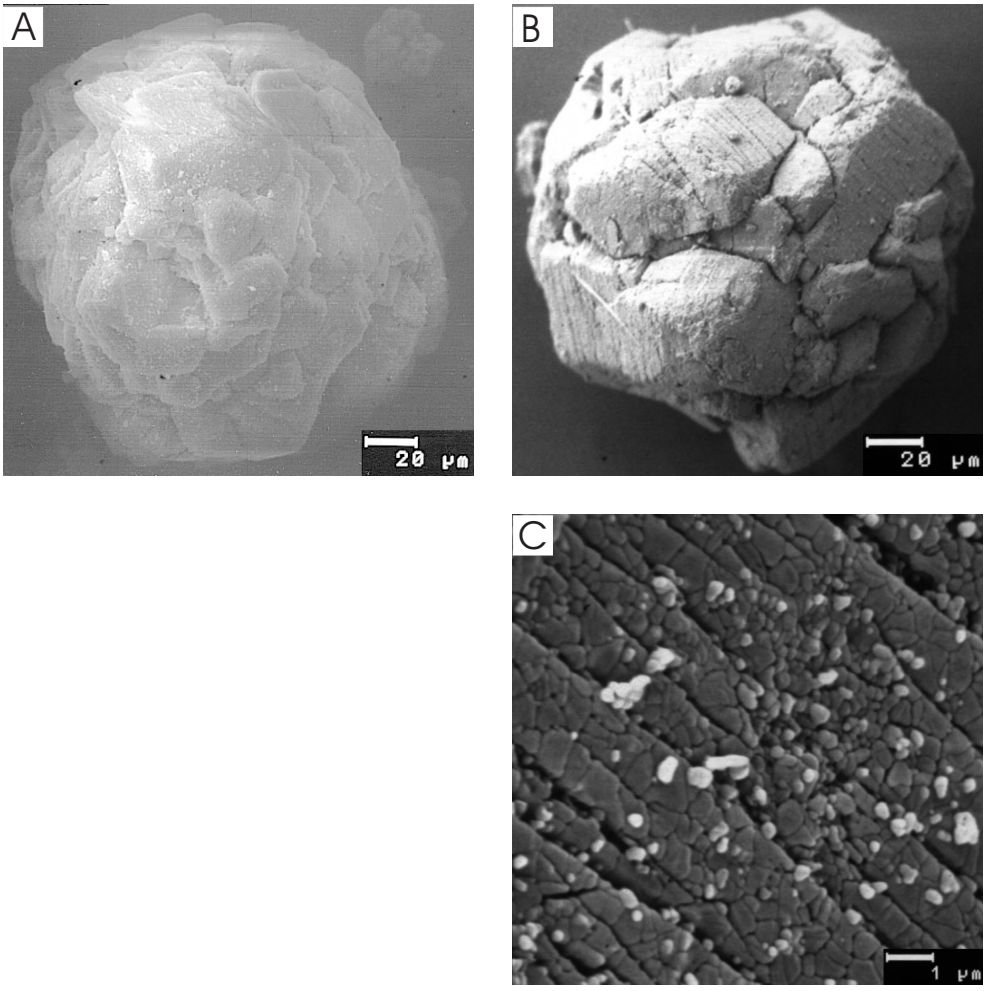

Figure 5.16: *SEM-BSE images. A: Grain of primary alumina A, 500× B: Calcined primary alumina A, 5 h at 1200 °C, 100 % α-Al_2O_3, 500×, C: Detail of image B showing typical "ceramic", unfaceted micro-crystalline grain structure of α-Al_2O_3, and typical lamellar pores, 10000×.*

5.6 Discussion

5.6.1 Relevance for the Industrial Dissolution Process

The tendency for agglomeration of alumina upon addition to the cryolite based electrolyte is well known, and has been linked to sludging by earlier workers, ref. chapter 2. The strength of such agglomerates is highly relevant for the dissolution process since the intrinsic operating factors of the electrolysis cell, such as superheat and convection of the electrolyte must be such that (dense) agglomerate formation is suppressed. Those agglomerates that form should be effectively dispersed and disintegrated so that the added alumina may be available for dissolution and hence electrolysis.

It may be pointed out that the absolute (tensile or compressive) strength of the agglomerate is perhaps not highly relevant. It may be observed that, see chapter 6, that as long as the melt is at or near saturation, even very weak agglomerates will resist disintegration and dissolution if convection is suppressed. Furthermore, the most relevant strength parameter may be toughness, rather than (tensile) strength. It may be argued that the mechanism of agglomeration by interlinking of platelike crystallites provides a system of high toughness, and hence resistance to disintegration even in the presence of adequate convection for agglomerate break-up, see chapter 3 for further discussion.

For direct comparison to alumina feeding events in the modern electrolysis process, the current agglomeration data is perhaps also relevant for understanding the process of "clogging of feeder holes" [120] and also the alumina's adhesion to for instance the feeding hammer, both well known phenomena. In both cases, the alumina is allowed to rest in the presence of rather low levels of fluorides, from splashing (hence liquid phase) or volatile/particulate fluorides escaping the electrolyte as HF and "$NaAlF_4$" [176].

5.6.2 Postulated Model of Agglomeration

It is assumed that the rate of alumina dissolution is basically mass transfer controlled, and the dissolution rate $\frac{dC}{dt}$ is proportional to the effective contact area, A, and the concentration gradient $(C^* - C_{sat})$. The working hypothesis for alumina agglomeration by interlinking is that the agglomerate strength, AS, is proportional to the SGA particle-particle contact area

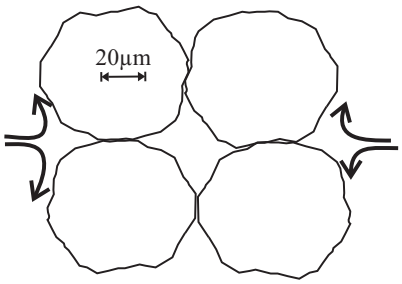

Figure 5.17: *Schematic of alumina particle packing in an agglomerate during initial penetration of bulk electrolyte/ solvent without an interlinking network of platelets.*

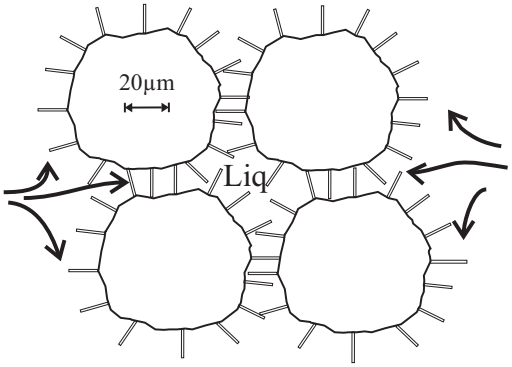

Figure 5.18: *Packing of partly recrystallized alumina particles in agglomerate during initial penetration of bulk electrolyte/ solvent. A matrix of interlocking grains provides strength, but also an open pathway for melt penetration.*

d, related to the "seed concentration" of α-Al_2O_3 in alumina grains, N_α by;

$$AS \propto d_{interface} \propto \frac{[Al_2O_{3(transition)}]}{N_\alpha}$$

It is assumed that the α-alumina content in the alumina will act as crystal seeds during the nucleation and growth transition to the stable alumina as effectively catalyzed by fluorides and high temperature in the cryolitic melt. The nucleation density, N_α should be related to the content of α-alumina, probably in a complex way.

Since every grain of alumina has a specific volume of transition alumina, the average crystallite size (i. e. length, thickness) of the recrystallized new, and potentially cementing and interlinking α-alumina phase, will probably be inversely proportional to N_α. The preferred crystal morphology is platelet form, with the basal plane parallel to the {0001} direction (hexagonal crystal symmetry).

The aspect ratio of the platelets, i. e. the ratio of platelet diameter to thickness, may also be important since the degree of interlinking may be expected to increase with higher aspect ratios due to increased inter- penetration and particle-particle contact area d. The particle-particle contact area is likely the key property when the interparticle interaction is relatively weak. A lower aspect ratio may increase the strength of platelets, but the intrinsic strength of α-alumina is probably high enough to dominate agglomerate strength (in solid state).

It is fairly well established that the content of α-alumina will influence the crust forming and agglomeration behavior of SGAs, see chapter 2.

Low α-aluminas (less than 5 % level)) tend to form hard crusts, [3, 191]. It is postulated that low α-aluminas result in relatively large crystallites/ platelets. Apart from a stronger interlinking force, larger platelets may also result in a more open interlinking structure which may provide an easier pathway for the penetration of liquid melt, as indicated in fig. 5.18. Based on basic ceramic theory, see chapter 2, the primary source of crust strength is the density. Thus, the increased strength of crust is primarily due to the melt having solidified after penetration through an open path-way, thus forming a dense composite structure.

Initially only a "canned" shell of frozen melt would form- and a lot of porosity would still be present within the agglomerate, as shown in fig. 5.17.

This porosity will provide the necessary buoyancy for agglomerates to form "rafts", and later dissolve as flakes.

During alumina feeding and agglomeration, such an interlinked microstructure could be expected to dissolve more quickly in the bulk cryolitic melt if it is allowed to disperse, due to the more open interlinking structure and more effective penetration of melt. On the other hand, if allowed to agglomerate (in analogy to the formation of top-crust), such an effectively filled composite of alumina with solidified cryolitic melt, may form of dense, strong crust. This type of alumina may form agglomerates that have a slower dissolution rate, since the break- up of such dense agglomerates will be more difficult, and they may sink through the metal and form sludge.

A recent study by Oh *et al.* [128] on the fabrication of C-SiC composites by isothermal chemical vapor infiltration found that particles with interconnecting "whiskers" (such as in fig. 5.18), provided an ideal microstructure for subsequent filling, while a particle packing without such an open whisker structure became closed, "canned", resulting in closed porosity unavailable for further filling (such as in fig. 5.17). This finding [128] supports the above argument, and the converse effect, for low α-alumina, as discussed below.

The initial dissolution rate (of dispersed grains) of low α-alumina content may be very high due to "dynamic" recrystallization, rapid crystal growth into the cryolitic melt, which may increase the bath- alumina contact area. Rolseth and Thonstad [149] found that SGA B had the highest "continuous", dispersed, dissolution rate of the aluminas tested. However, such an effect is probably confounded with the rupturing effect due to pressure build-up within each grain due to the high moisture content. Low α-aluminas generally have high surface areas and thus high contents of adsorbed moisture, which must be released upon heating and loss of surface area as the "γ"$\rightarrow$ α phase transition proceeds rapidly. Vaporization of moisture contributes to the explosive expansion of air in the highly porous structure as it is rapidly heated at a rate of up to several thousand °C per min, see further discussion in chapter 8.

High α-aluminas form moderately hard/ weak crusts. Ødegård *et al.* [127] found that an α-alumina content of less than about 50 % produced crust, and agglomerates. It is postulated that high α-aluminas might result in smaller crystallites, and hence lower mechanical strength of crust. The extreme case would be that shown in fig. 5.17, which would be expected if calcined, 100 % α-alumina is used. Fully transformed alumina would result in little or no crystal growth and no interlinking network of α-alumina

platelets. This type of alumina would be expected to have a higher dissolution rate than the low α-aluminas if allowed to agglomerate/ aggregate, since no interlinking network is formed and since little melt penetrates into the agglomerate.

5.6.3 Experimental Sources of Error

The main sources of error relevant for the present work may be summarized as follows, arguably in order of decreasing importance;

- Atmospheric Moisture, ref. chapter 8.
- Temperature Response in samples, ref. chapter 7.
- Effect of operator, AKK, NPO. Qualitative, quantitative exp.
- Instrumental accuracy, precision.

For the comparative study, a few series were analyzed by BET and XRD, otherwise only the "Sinter-Scale" and a simple gravimetric analysis was used. XRD analysis showed that the experimental scatter in all the data was very small for the α-alumina content of every sample, being within the experimental error of the quantitative XRD method of about $\pm$ 1 %-points.

Generally, figs. 5.1, 5.2 and 5.3 show a marked transition in weight loss and agglomeration score for t $\sim$ 5 min. This is assumed to be correlated to the loss of surface area, of around 50 % (see fig. 5.13) associated to a considerable loss of moisture and propensity for readsorbing moisture upon contact with air.

For the comparative study, the samples were weighed before and after the high temperature exposure. The weight loss was ascribed to water for primary aluminas, and mixture of water and other volatiles, such as carbon (C$\rightarrow$ CO_2), HF, $NaAlF_4$ etc., for secondary aluminas [111]. There is an expected correlation of the weight loss due to the moisture content (MOI + LOI) and the specific surface area (BET)- so this provides a simple and very cost-effective method of determining (altered) microstructure, i. e. the surface area, of the samples.

A small series of "blank" control experiments was conducted for 3 SGAs (each run in duplicate) without the addition of $NaAlF_4$, held at 800 °C for

10 min each. For primary alumina A (PA) the weight loss was found to be 0.46 ± 0.30 wt %, for secondary alumina A (SA) it was 1.75 ± 0.14 wt % and for primary alumina B (PB) 0.59 ± 0.07 wt %. The scatter is rather large for SGA A, but the values "blank" agree well with the data plotted in fig. 5.1, but the ranking of SGA A and B is opposite in chapter 8, in which SGA B desorbes less moisture at 100 °C.

For PA "blank" the weight loss is less than for the 1 min sample in fig. 5.1A, where little recrystallization has occurred, while for SA the value corresponds to the weight loss after about 3 min for the SA + 5 wt % $NaAlF_4$ samples and shows that a considerable recrystallization has occurred since fluoride species present in secondary alumina may catalyze the $\gamma \rightarrow \alpha$ transformation, even without liquid fluoride additive. However, the weight loss of secondary alumina samples may also partly be due to loss of fluorides and some C-dust oxidation.

For PB the "blank" weight loss is similar to that of the first samples with the liquid fluoride additive in fig. 5.1C, which is quite stable for the 1, 2 and 3 min samples. This does not quite conform to the observation of the agglomeration score in fig. 5.6, which is high at 6-7 already after 1 min exposure- since this should imply that a considerable transformation has occurred. However, for interlinking to occur, it is probably sufficient that a few large platelets form in every grain (according to the working hypothesis) - and this is really what is to expected for PB which has a very low α-alumina content, see later discussion.

The dynamic moisture content, in quasi-equilibrium with the relative humidity in ambient air, may cause considerable scatter in the data. The samples will re-adsorb moisture during the weighing process to a varying degree, as a function of the residual surface area, moisture content and relative humidity in the laboratory. The scatter in the data is thus to be expected, and the actual weight loss data is best discussed with caution.

5.6.4 Temperature Level

Most of the data was collected at 800 °C, since the kinetics are slow enough for extended study, and this has also been determined as the temperature at which 50% of the phase transformation γ to α-Al_2O_3 is complete within 30 min, when AlF_3 is used as a mineralizer [127]. Manual sample handling is also easier at this temperature, and while the temperature response is

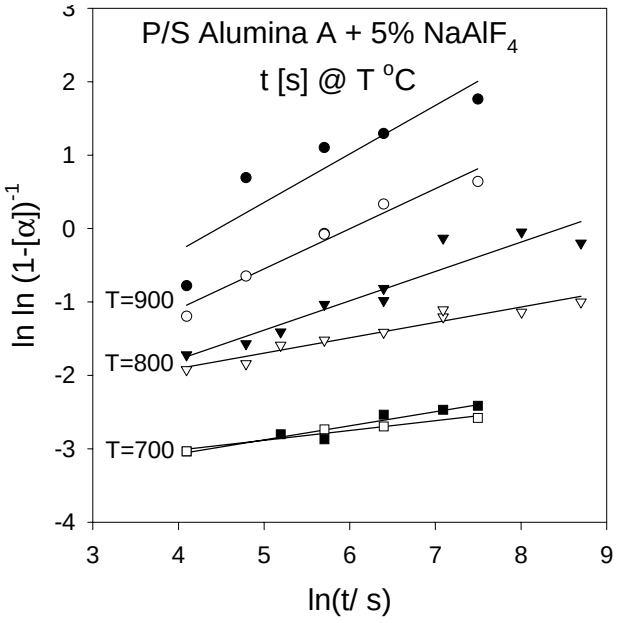

Figure 5.19: *Transformation kinetics (JMA-presentation), as a function of temperature and impurities content (secondary alumina samples, filled symbols).*

slower, (at about 50 s compared to ∼30 s at 1000 °C), it is well defined – as shown in chapter 7.

Transformation kinetics of primary and secondary alumina A are shown using the JMA-presentation in fig. 5.19. The figure shows the effect of temperature in the presence of fluorides, and other impurities, in the case of the secondary alumina samples. Linear regression lines show reasonable agreement with the JMA theory (at least a linear fit), in particular for the primary alumina samples, but the transformation kinetics is obviously more complex for the secondary alumina samples.

In theory it should be possible to obtain a measure of the activation energy for the $\gamma \rightarrow \alpha$ transformation from these data. However, Arrhenius plots ($\ln k$ *vs.* 1000/T) did not give meaningful results for either primary or secondary alumina.

700 - 800 °C is likely to be the highest temperature to be expected for the process of alumina agglomeration, i. e. when the alumina is not in direct

contact with the bulk electrolyte at T ≃960 °C, but the lowest temperature for effective mass transport in this system which is correlated to the $\gamma \rightarrow \alpha$ transformation kinetics.

The nucleation and growth of monodisperse α-alumina platelets has a potential commercial use as additives in ceramics and alloys, and as abrasives. A method of obtaining large α-alumina hexagonal platelets is described in the Elf-Atochem patent by Faure and Bachelard from 1994 [31]. The patent describes a rather wide range of temperature and additives, but the essence of the method resembles the experimental method investigated in the current study.

The patent recommends the use of approximately 100 °C superheat at temperatures up to 800 °C of the added liquid phase fluoride in order to produce platelets of α-Al_2O_3 from low-calcined alumina (and hydrate). This agrees well with our finding, in chapter 4, that, in order for effective recrystallization and interlinking to take place, a liquid fluoride phase must be in direct contact with the alumina (SGA). It is noted in the patent that a rapid heating to the desired temperature is required, with holding times of 30 min up to 2 h. The holding temperature is not critical it seems, as long as the additive is liquid. It may thus be concluded that the results and conclusions reported in this chapter have a "proof of concept" in the reported patent [31].

5.6.5 Time Intervals

The time intervals chosen for most of the experimental series was $t \in 1, 1000$ min. Usually 1, 2, 3, 5, 10, 20, 50 and 100 min were the chosen intervals. For the study of kinetics it is important to cover a time-range of several orders of magnitude. The temperature response data (see chapter 7) showed that for 800 °C the sample attains the set temperature in approximately 50 s, so even at 1 min there is a considerable initiation period that should be considered when discussing the results.

The melting and spreading of the added fluoride, as illustrated in fig. 5.20, takes a period of time. This is obvious from the results presented in figures 5.21 and 5.22. The phase transformation results indicate that incubation time increases somewhat for increasing content of $NaAlF_4$ in the powder sample.

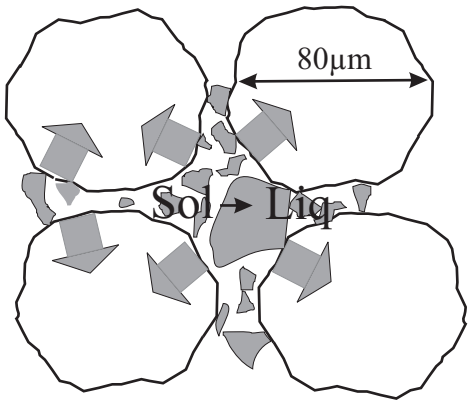

Figure 5.20: *Schematic of initial melting and wetting.*

Since the process of dissolution of alumina is on the second to minute time-scale it is helpful to extrapolate the results towards the second mark (i. e. less than 1 min) in order to describe the initial process. Since the quality of the data obtained is rather good, extrapolation is in order.

No definite macroscopic shrinkage, or signs of cracking was observed in any of the tablet samples after heat-treatment, even when held for 1000 min at 900 °C. This observation supports the conclusion that the mass transport mechanism involved in the agglomeration process is non-densifying in nature, and may be described as microstructure coarsening and crystal growth.

5.6.6 Quality and Amount of Fluoride Additive

The fluoride additive used for most of the experimental series was from the same batch of quenched "$NaAlF_4$", finely crushed and mechanically mixed, (manually, carefully, rigorously), with the alumina sample in batches of 16.0 g each ensuring that each series has homogenous composition.

Results from experimental series comparing "coarse/fine" $NaAlF_4$ showed

the importance of a homogenous sample for reliable agglomeration results. Poor wetting and inhomogeneous agglomeration resulted from the coarse $NaAlF_4$ powder additive, which would weaken the tablets obtained, compared to more homogeneous samples. The purity of the fluoride phase was not considered to be crucial, and has not been measured, though the liquid $NaAlF_4$ phase was synthesized using quite pure chemicals.

The process of adding a solid fluoride phase must involve an "incubation" period during the melting and permeation of this phase in the sample, as previously discussed, see fig. 5.20. During the melting of the added fluoride phase there will be local effects of wetting seen as an initial agglomeration in some of the short time samples obtained.

During wetting there may also be some rearrangement of alumina grains due to strong capillary forces. Since the alumina grains have an exceedingly porous structure, the initial wetting of grains may result in some localized collapse of the grain microstructure, as seen in fig. 5.11. Such local effects are minimized by rigorous mixing and by using sufficiently fine-grained fluoride powder, having an average size an order of magnitude less than that of the alumina powder.

In fig. 5.11B a single alumina grain (but not the only one observed) has collapsed into a dense aggregate of coarse α-Al_2O_3 platelets with orientations probably resembling the orientation of the aluminium hydrate precursor. The grain must obviously have attained a higher than average concentration of liquid cryolite, probably due to improper mixing, since the cryolite was added as a relatively "coarse" powder, with a grain size of the same magnitude or larger than the alumina grains themselves.

Similar, rather beautiful, "rose"-shaped dense aggregates of α-Al_2O_3 platelets formed upon calcination of a mixture of aluminium sulfate and potassium sulfate flux in a study by Hashimoto and Yamaguchi [54]. That study showed that increasing the temperature and the amount of flux increased the platelet size and decreased their number, in accord with the working hypothesis of this study.

Usually, ceramic green bodies are prepared by mechanically mixing and grinding the starting powders, in for instance a ball mill, for several hours. However, for the current work, it was intended to study the agglomeration process under, as far as possible, realistic conditions. Both pre- and post-treatment of the alumina samples where thus kept at an absolute minimum.

The particle size distribution of the alumina sample was not altered, though

that is not a critical parameter for the agglomeration process, at least not in this study in which the alumina sample was fixed to the sample dish. The particle size distribution of SGA is important for the alumina's flowability, and capillary penetration of cryolitic melt. Thus important for the tendency for the SGA powder aggregation prior to melt infiltration during alumina feeding, and the following processes of agglomeration, that is studied here - under controlled conditions minimizing those effects.

5.6.7 Transformation Kinetics

Transformation kinetics of the $\gamma \rightarrow \alpha$ alumina transition may be described by the Johnsen-Mehl-Avrami theory (JMA) [192]. The theory was originally developed for isotropic systems, such as metal solidification and glass crystallization, but it has served to describe the transformation kinetics of transition alumina also [158, 8]. Random nucleation is assumed for simplicity, and a saturation of nucleation sites. The assumption of an isotropic system seems valid for disordered transition alumina in SGA.

The relative degree of transformation as a function of time may be expressed as the volume fraction that has been transformed, i. e. ;

$$X_r = 1 - e^{kt^n} \tag{5.1}$$

so that;

$$ln(ln(1 - X_r)^{-1}) = lnk + n(lnt) \tag{5.2}$$

Thus, we may use the left side of this relation as the dependent variable and lnt as the independent variable in order to obtain values of the kinetic constant k and the time-exponent n from data obtained using quantitative XRD for the relative phase content fraction X_r of α-Al_2O_3, as a function of time (in seconds).

Figs. 5.21 and 5.22 show that the XRD data from the 15 and 20 wt % $NaAlF_4$ series are statistically identical at the 5 % level (i.e. there is a 5 % chance this is wrong) since the data points fall within the 95 % confidence intervals of the linear regression fits to the 20 wt % $NaAlF_4$ series for both aluminas A and B. The lower levels of fluoride additive are shown to fall outside these intervals.

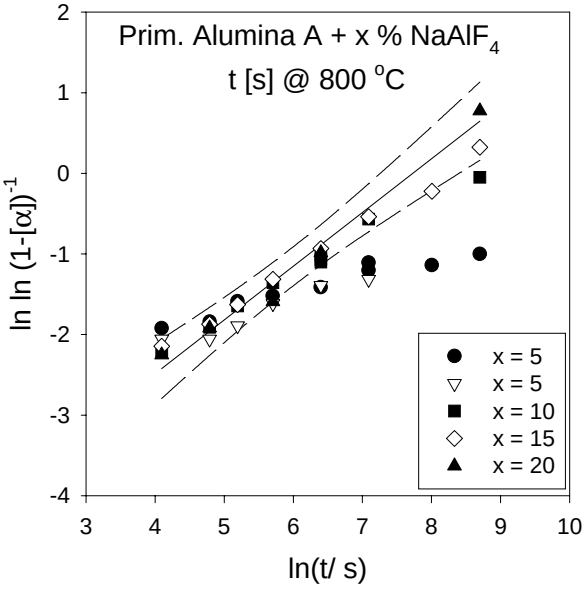

Figure 5.21: *Quantitative XRD data, JMA-pres. Effect of amount of added fluoride phase on degree of phase transition to α-Al_2O_3 of primary alumina A.*

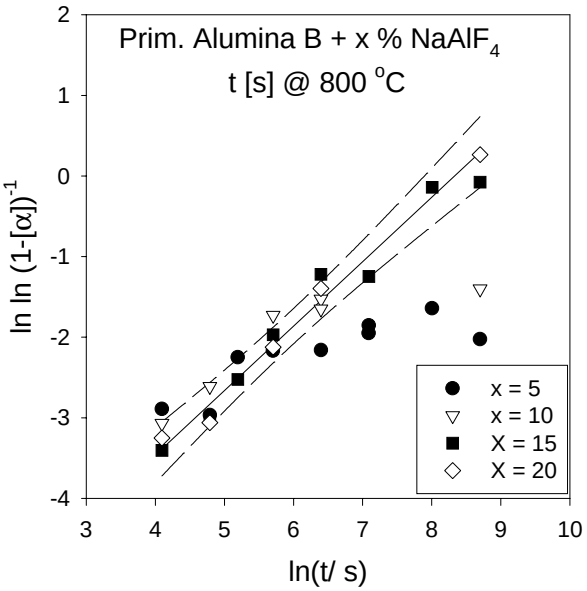

Figure 5.22: *Quantitative XRD data, JMA-pres. Effect of amount of added fluoride phase on degree of phase transition to α-Al_2O_3 of primary alumina B.*

5.6.8 Effect of Fluoride Content

Alumina-cryolite crusts formed above the electrolyte in Hall-Héroult electrolysis cells consists of around 50 wt % bath phase [49, 176]. As a mineralizer, 5 wt % should be more than enough, but it is observed (ref. data in tab. 5.5) that the method of using shallow Pt-dishes and small samples (only in excess of 1 g) gave very slow transformation kinetics for especially 2 % and 5 wt % AlF_3 compared to those of Ødegård *et al.* [127] and Zivkovic *et al.* [189], where larger, partially covered samples were used. Larger, partially covered samples probably retain the gaseous species better. Shacklee and Messing [158] used small 1 g samples, but enclosed them (in gold) in order to ensure recycling of the gaseous species (HF and H_2O).

It was first assumed that a level of 5 % $NaAlF_4$ by weight would be adequate for studying the effects of the liquid phase fluoride assisted transformation and grain growth, but the effects of moisture will "passivate" up to 10 wt % as discussed below. This effect is shown in the SSA(BET) data in fig. 5.13, and the XRD data presented in figs. 5.21 and 5.22.

The effect of adding AlF_3 is to provide a gaseous species intermediate to the HF-water mechanism which adsorbs to the basal $\{0001\}$ plane of $\alpha - Al_2O_3$, enhancing material transport and transformation kinetics and resulting in the characteristic platelet morphology [21].

With reference to the "sintering" theory and discussion in chapter 2, the effect of liquid phase $NaAlF_4$ is probably due to increased surface reactivity and surface diffusion. This may result in very rapid crystal coarsening, perhaps in combination with gas phase evaporation-condensation, by HF, when moisture is available. The effect of moisture is further discussed below.

The kinetic parameters for the two levels of 15 and 20 wt % $NaAlF_4$ in the case of both primary alumina A and B, as presented in tab. 5.5, are statistically identical, also evident by the linear fit in figs. 5.21 and 5.22.

Thus there is an effect of the amount of fluorides added, but it seems that it is in fact mostly due to the effect of moisture, which reacts with the liquid fluoride and halts further mass transport, unless an excess of fluoride is added, to be further discussed below. For alumina A, 10 wt % $NaAlF_4$ is obviously adequate for retaining enough liquid phase $NaAlF_4$, at least up to 100 min, while for alumina B 15 wt % was needed. This may indicate that more water is retained in the B quality, though other explanations may exist, including different pore size distributions. That finding is supported

for the PA + 5 and 10 % $NaAlF_4$ loss of surface area for the sample series in fig. 5.13. 10 wt % $NaAlF_4$ is obviously sufficient for there to remain liquid fluoride after the moisture has reacted and mostly vanished from the sample. While the 10 wt % $NaAlF_4$ level also seems adequate for PB for the loss of surface area past 10 min (fig. 5.13), the phase transformation has ceased, see figs. 5.8 and 5.22. The loss of surface area may continue if moisture is present, [109].

It is concluded that the 15 and 20 wt % level of fluoride additive is sufficient to saturate the catalytic effect even in the presence of moisture, and that the fluoride level is in fact irrelevant for the transformation kinetics, provided there is enough available after a significant amount has reacted with moisture. We may also conclude that there is a significant difference between the transformation kinetics of primary aluminas A and B.

Based on available MOI+LOI data and sample weight loss data obtained in this study, it may be assumed that an alumina sample may contain up to about 2 wt % water. It may be shown that up to about 15 wt % fluoride (liquid) additive may be passivated by a hydrolysis reaction to form solid cryolite and alumina, while the gaseous HF escapes the crucible. The 15 wt % fluoride level is in good agreement with the XRD and BET -data, but such a calculation is only indicative.

Based on the XRD analysis presented in fig. 5.9 and on the phase diagram by Foster [34], it is concluded that the equilibrium condition for the primary alumina + $NaAlF_4$ additive system is a mixture of α and β-alumina, when the alumina content is around 90 %. β-alumina generally has the composition $Na_2O{\cdot}11\ Al_2O_3$, though β-alumina is known to have several possible compositions $Na_2O{\cdot}x\ Al_2O_3$, with a semi-continuous alumina fraction x, for x=8-11 [200]. The following reaction model may be proposed;

$$\gamma + NaAlF_{4,(liq)} + H_2O_{(g)} \rightarrow \alpha + \beta + HF_{(g)} \tag{5.3}$$

A short notation is used, where γ, α and β are the solid alumina phases present. According to the phase diagram, fig. 5.23, the stability field of β-alumina moves to the acidic AlF_3-rich section at higher alumina contents, such as around 90 % in this case, but a move toward a more basic (NaF-rich) composition by hydrolysis of AlF_3 seems necessary in order to explain the presence of β-alumina, and the "passivation" of $NaAlF_4$.

As the fluorides react with moisture in the air and in the sample, by "hydrolysis" (see chapter 8), the liquid phase may become more basic, i. e. NaF-rich

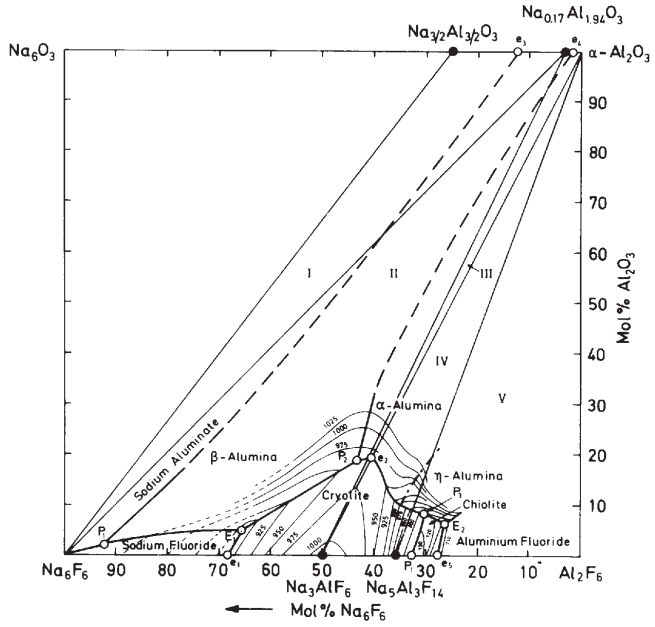

Figure 5.23: *Phase diagram of the reciprocal system Na_3AlF_6- $(NaAlO_2)_3$- $(NaF)_6$- $(Al_2O_3)_2$, from Foster [34].*

melt, so that the composition of the system moves into the stability region of β-alumina according to the phase diagram in fig. 5.23. The sodium ions probably diffuse by intercalation into the α-alumina crystal structure, thus forming β-alumina. The formation of β-alumina from a mixture of alumina and acidic (AlF_3 rich) cryolytic melt has not previously been reported [176].

The postulated reaction (eq. 5.3) warrants further thermodynamic investigation. Such a treatment may however be complicated by the fact that the exact β-alumina content and structure type (sodium content range) should be known, and that the system is open, since moisture is available in the ambient atmosphere while HF is lost, and since HF is also involved in the phase transformation $\gamma \rightarrow \alpha$. Thermodynamically, the α and β-Al_2O_3 phases should not coexist, unless the CR is around 4 [34, 176].

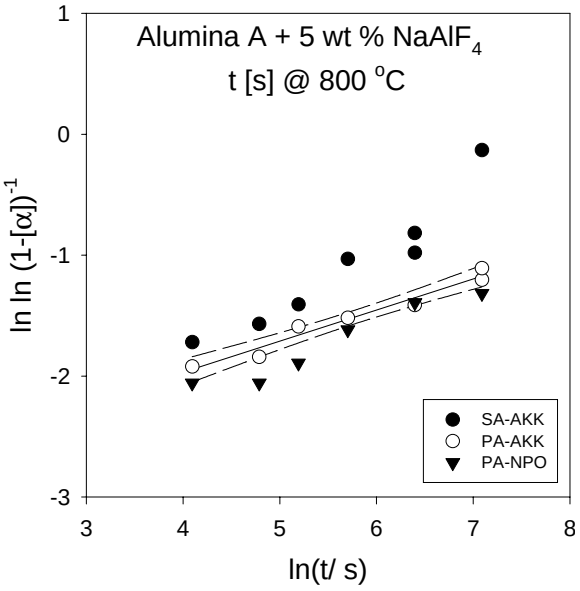

Figure 5.24: *Degree of alumina converted to α-Al_2O_3 using the JMA-presentation showing the effect of an increased level of moisture and other volatiles (in the case of the secondary alumina samples). See text for discussion.*

5.6.9 Effect of Moisture

The effect of moisture on the amount of the liquid fluoride ($NaAlF_4$) added was discussed in the previous section. Moisture may also have other effects on the kinetics of the phase transformation and coarsening of alumina. Moisture is known to provide mass transport and cause coarsening in transition alumina used as catalytic supports [109, 119, 156].

The moisture content in the samples may be influenced by the ambient relative humidity (RH) and the sample temperature, as reported in chapter 8. During the experimental investigation, great care was taken in order to limit the effects of fluctuations in RH and sample temperature. Every experiment was run according to a randomized plan, and performed according to a standard procedure.

The effect of different levels of moisture is presented in fig. 5.24. While the AKK-samples (operator initials AKK) were exposed to ambient air for about 5 min prior to the heat-treatment, the NPO-samples (the authors

initials) were only briefly exposed to air, and only while retaining a high temperature. Linear regression applied to the AKK-primary alumina samples, shows that the 5 min exposure produces statistically significantly (at a 5 % level) faster transformation kinetics.

With reference to the relevant sample geometry results shown in fig. 8.9, in chapter 8, the AKK-samples probably contained around 0.5 wt % more moisture than the NPO samples.

The only viable explanation for the difference between those data-sets is the increased moisture content in the AKK-series. It is possible that slightly less sample would allow a somewhat faster temperature response, and hence a shorter initiation period, but it was determined that the average sample weight in the former series was the same as for the latter.

The samples of secondary alumina contain fluorides and C-dust in addition to an increased level of moisture, and give markedly faster transformation kinetics, also shown in fig. 5.19.

5.6.10 Agglomerate Strength

It could be argued that the added fluoride phase may provide some strength to the agglomerates, by "glueing" of grains or by percolation throughout the sample.

When SGA is calcined in air to a nominal 100 % α-Al_2O_3 quality, the effect of fluoride assisted phase transformation and recrystallization is negligible, and no agglomeration is expected. Fig. 5.25 shows the effect of agglomeration of α-Al_2O_3 (calcined SGA B), with additions of $NaAlF_4$.

All samples show partial agglomeration, according to the "sinter-scores" of 5-7, but when the samples were released from the Pt-dish, they could be described as having free-flowing characteristics indicative of a score of 0 or perhaps 1. Some change in the flowability- perhaps due to altered surface roughness, degree of hydration or the formation of "micro-agglomerates" by weak particle-particle interaction, would imply at least a score of 1 on the sinter-scale. Similar results were also obtained for secondary aluminas without (liquid) fluoride additive at this temperature.

The sinter-scale devised for the current study is very sensitive to whether or not the sample is sufficiently coherent that it partly or entirely sticks to the Pt-dish when flipped. The degree of agglomeration of the "powder" after

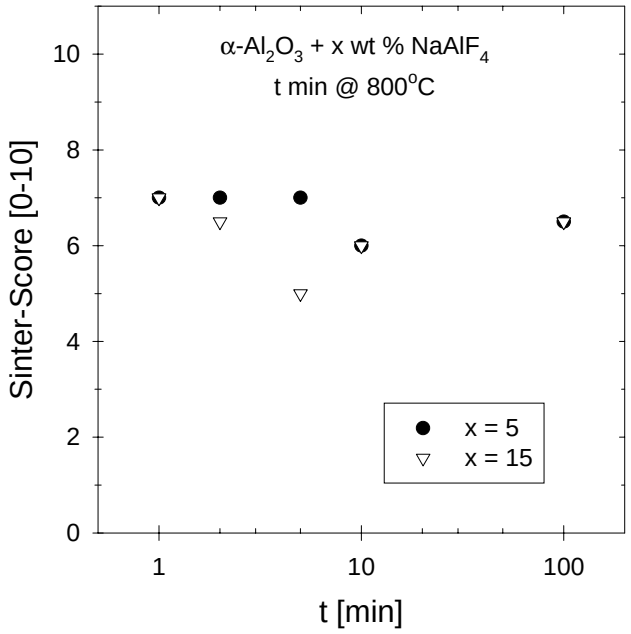

Figure 5.25: *Minimal effect of two levels of added fluoride phase on the agglomeration of α-Al_2O_3 derived from Primary Alumina B. See text for discussion.*

it is released from the crucible, may however not resemble agglomerated powder at all. That is so in the case of liquid fluoride phase added to α-Al_2O_3 from a PB SGA precursor shown in fig. 5.25. The sinter-scale should perhaps be applied twice, once for "sticking" to the Pt-dish, and once for the released sample.

It may be concluded that persistent agglomerates do not form unless coarse α-Al_2O_3 platelets are formed. Some bridging effects due to limited coarsening or effects of dehydration may explain the fact that calcined alumina will stick to the Pt-dish when flipped. The effect of coarsening and moisture could perhaps be tested, by e. g. using very highly calcined or fused alumina. This test was not performed in this study however.

The sinter-scale works best for fluoride additives that are liquid at the heat-treatment temperature, and for samples with transition alumina – as this combination developes the sufficient mechanical strength of the agglomerates.

In order to obtain high quality X-ray diffraction data, the alumina samples must be crushed by hand with a small mortar and pestle (both of dense alumina ceramic). It was thus possible to observe qualitatively the crushing strength of the samples.

For the samples that obtained agglomeration "sinter-scores" of more than 7, the sample was usually partly of tablet form. With increasing strength (score 7 $\rightarrow$ 10) the tablets became increasingly brittle, but were of very limited mechanical strength. The semi-quantitative agglomeration scale (0 – 10, see tab. 5.4), was devised in order to give a measure of the degree of agglomeration and mechanical strength of the samples obtained by heat-treating mixtures of alumina and fluoride powders.

Generally, it was observed that as the $\gamma \rightarrow \alpha$ transition became more complete with increasing time and fluoride phase additive, the crushing strength of the partly or entirely recrystallized alumina powder decreased. Primary alumina A and B has a crushing strength almost as high as some forms of sand. Since alumina dusting is of concern in the modern Hall-Héroult process this is important, since weak alumina grains will lead to high attrition losses and dusting problems. When calcining primary alumina in air at 1200 °C, the alumina grains transform to polycrystalline α-Al_2O_3, with a micro-structure as shown in figs. 5.16B,C. The crushing strength of the transformed grains is markedly lower than that of the primary alumina derivative.

The crushing strength was lowest for the samples known to have developed a highly platelet-like microstructure, with an almost "floury" consistency, again akin to the old nomenclature of "floury" alumina. On the other hand, these samples had the highest mechanical strength of the tablets formed, in agreement to the proposed mechanism of agglomeration involving interlinking and intergrowth of α-Al_2O_3 platelets.

5.6.11 Effect of Alpha Alumina Content

The phase transformation from transition phase alumina to the stable α-Al_2O_3 is a complex process, see chapter 2. The formation of large α-Al_2O_3-platelets in cryolitic melt is the result of the interaction of fluorides and the nano-structure of SGA. The only measure of the nano-structure of SGA, which will vary with alumina quality and calcination, is the content of α-Al_2O_3 and the specific suface area (BET).

The content of α-Al_2O_3 is not a precise parameter, as the α-Al_2O_3 phase also has structure (nano-structure), including a size distribution. The BET value of a given SGA is not a precise parameter either, since it is not only a function of the structure and degree of calcination of SGA, but also of the particle size distribution of the SGA.

In the following discussion, the results reported in this chapter are discussed first for the effect of phase content, then the particle size distribution of the α-Al_2O_3 phase. With reference to the nano-structure of alumina, a clear separation between the two is not possible. Futhermore, the effects of pore size, and total pore size distribution, and the density and crystallinity of the transition alumina matrix in the SGA, i. e. all that is not α-Al_2O_3, is difficult to assess without data, but must also be kept in mind when discussing the nanostructure of SGA.

Effect of Amount of Alpha Alumina

Referring to fig. 5.3 in the results of the comparative study, – similar agglomeration results are obtained for the low α-Al_2O_3 content aluminas, but alumina C shows a significantly different agglomeration behavior initially (for $t < 10$ min) compared to alumina B and D. For the final agglomeration period, for $t > 10$ min, it is alumina D that shows dissimilar behavior.

Only alumina B was studied in further detail, though it would have been interesting to study both aluminas C and D also, in order to better test the proposed model. The low α-content aluminas C and D have similar α-Al_2O_3 contents as alumina B but higher SSA-BET values at 76.8 and 72.7 m^2/g respectively. Alumina C has a similar moisture content as alumina A, while the LOI levels of aluminas B and D are similar.

According to the data presented in tab. 5.5 and in figs. 5.21 and 5.22, there is a significant difference between the agglomeration and transformation kinetics of primary aluminas A and B. Based on the working hypothesis, this difference may be explained by the different levels of α-Al_2O_3, or the nano-structure, including the size distribution (PSD) of the α-Al_2O_3 nuclei in the SGAs.

The primary aluminas A and B have fairly similar specific surface areas at 63 and 66 m^2/g. Other physical properties are probably not relevant to the agglomeration kinetics in this study, less the moisture content, closely linked to the nanostructure (BET) of the transition aluminas. MOI is especially low for alumina B, but this may be due in part to less exposure

to atmospheric moisture compared to the other aluminas (shorter shipping distance). In chapter 8 it was concluded that alumina B had significantly slower moisture desorption kinetics compared to alumina A.

The effect of the α-Al_2O_3 content on the primary alumina's tendency to agglomerate, –supposing that α-Al_2O_3- platelets form,– may be appreciated when considering the following discussion. Alumina A and B have approx. 9 and 3 % α-Al_2O_3 respectively, that may act as seed crystal domains for the further phase transformation upon interaction with fluorides.

If we assume that both qualities A and B have about the same quantity of transition alumina that will serve as feed material for the $\gamma \rightarrow \alpha$ transition, then each α- platelet that forms from the alumina B quality will have about 3 times the volume of the corresponding platelets that form from the A quality, since there are fewer growth areas available. By assuming hexagonal symmetry of the platelets, each platelet is defined by a diameter in the plane D, and a thickness h. The relationship between the platelet diameter D and it's volume may then be expressed as;

$$D = \sqrt{\frac{8\sqrt{3}V}{9h}} \tag{5.4}$$

where V is the volume of the platelet, and the constant $8\sqrt{3}/9$ is derived from the hexagonal geometry.

Similarly, Shacklee and Messing [158] defined the following relation between the density of α-Al_2O_3 nuclei and the resulting average diameter D of the resulting platelets that form in the system γ-Al_2O_3-H_2O-HF;

$$D = \sqrt{\frac{1.24}{Nh}} \tag{5.5}$$

where N is the density of α-nuclei, and the constant 1.24 is derived from the hexagonal geometry and an assumption that the nuclei are evenly distributed in a face centered cubic array.

In either approach, a factor of 3 in either the volume or nucleation density of α-Al_2O_3 will give a factor $\sqrt{3}$ in the platelet diameter D if we assume that the thickness h is the same. The transformed microstructure of alumina B should thus be expected to have an average platelet diameter which is $\sqrt{3}$ (i. e. about 73 %) larger than that expected for alumina A.

When the size of nuclei, as determined by the Warren-Averbach analysis, see below, is figured into the equation, then it may be shown by a similar

volume argument, that the difference in size of a factor of about 2:1 for A:B, equates to a factor of 8:1 by volume per nuclei, assuming spherical shape,– giving a factor of 8/3 in the ratio of N_α in the proposed model. The model thus predicting that SGA A should result in agglomerates that are about twice as "strong" as those from SGA B, in contradiction to the working hypothesis.

Such estimates are probably much too simple however. Basically, it has not been possible to prove or disprove the hypothesis in the present study, since several alumina qualities of similar α-Al_2O_3 content (probably produced using similar calcination technology) would have to be tested for agglomeration and the evolution of nano- and microstructure.

The $\gamma \rightarrow \alpha$ phase transformation is a nucleation and growth type process. The transformation kinetics are tabulated in table 5.5. Though the kinetics is significantly faster for SGA B, with a low α-Al_2O_3 content, the bulk (volume) content of α-Al_2O_3, and further transformation, cannot explain the increased tendency for agglomeration for that alumina quality compared to SGA A. SGA B forms stronger agglomerates than SGA A, at a lower α-Al_2O_3 content, and at a comparable relative increase in the α-Al_2O_3 content, see figs. 5.5 and 5.6 and figs. 5.7 and 5.8.

Thus, some measure of the quality of the α-Al_2O_3 content in the primary alumina must be taken into account.

Effect of Particle Size/Structure of Alpha Alumina

As explained in chapters 2 and 3, many workers have attempted to find fundamental, measurable parameters that may describe the quality of SGA's. This study attempted to investigate the particle size of the α-Al_2O_3 content in SGA by X-ray diffraction, supported by SEM and BET studies.

Differences between aluminas of similar α-Al_2O_3 contents may be due to different nanostructures and microstructure of the α-Al_2O_3 phase content, in accord with the working hypothesis, but may also be related to the transition alumina matrix.

Hamberg [51] hypothesized that the degree of crystallinity of a primary alumina quality, including the degree of order in the disordered transition alumina phases,– could be the reason why some aluminas tended to transform more quickly to α-Al_2O_3 when calcined in air.

Other effects of the nanostructure, including the effects of porosity in the SGA grains, and other effects that may control the mass transfer, such as a difference in the reactivity with, and level of,– residual water, or added fluoride phase, cannot be ruled out.

The reactivity of residual water was found to greatly influence the nucleation density by Shacklee and Messing [158], and this may also explain local differences when the concentration of fluorides is low,- such as during the very initial penetration of fluorides into the SGA matrix.

A patent by Block and Lau from 1992 [13], describes the production of alumina platelets by gas- phase recrystallization of transition (γ-Al_2O_3) alumina using 2 wt %AlF_3 additive, but at a high temperature of 1200 °C for 30 min and rather slow heating at 5 °C/min. It was noted that the source of transition alumina (i. e. product of varying morphology, nanostructure, possibly impurities etc.) will control the size of the alumina platelet product with a range of 1-2 μm up to 40-50 μm (!), for otherwise identical procedures. The role of trace impurities in the source material is probably of little importance when a fluoride flux is used.

This note, [13], supports the argument that the nanostructure of SGA will determine the growth of α- Al_2O_3 from low calcined alumina and hydrate- and hence the degree of interlinking and agglomeration that may be expected for otherwise identical experimental conditions.

In the case of calcined primary alumina without fluoride additive the same general argument may be applied. The average crystallite size of α-Al_2O_3 in both primary and calcined qualities A and B are compared in tab. 5.6. The line broadening of the (024) diffraction peak indicates that the average crystallite size of transformed alumina B, at about 0.09 μm, is in fact only 12.5 % larger compared to that of alumina A, at about 0.08 μm.

The maximum crystal size data obtained from SEM images, d_{max}, is an order of magnitude larger than the domain size L, determined by the Scherrer equation, see eq. 3.3 in chapter 3. This is partly due to the XRD method always giving a low estimate (due to smaller diffraction domains than the apparent crystal size), but is also an effect of the size distribution since the XRD data is an average. The average domain size is not sensitive regarding the α-alumina platelet size for the same reason. While the average domain size was identical, the liquid phase Na_3AlF_6 additive resulted in platelets 3 times as large, at 15 μm, as for the AlF_3 additive (qiving a significant fluoride partial pressure), at about 5 μm, for similar experimental

conditions, see figs. 5.10 and 5.11.

The method of Warren-Averbach line profile analysis, gives a more physical particle (domain) size distribution and a more accurate description of the nanostructure than the simple Sherrer broadening equation. The Warren-Averbach method is described in chapter 3. The graphic results of the PSD curves, are presented in figs. 5.14 and 5.15. The crystal domains, here termed "relative column length", were assumed to be free of residual strain, which is probably a good approximation for recrystallized grains. The crystal domain size data obtained is summarized in tab. 5.7.

It may be assumed that the relative accuracy of the Warren-Averbach method is quite good when comparing results obtained under identical experimental conditions, but the absolute accuracy of the results must be backed up by other methods, and this was not possible in the current study.

The nanostructure and PSD of the α-Al_2O_3 phase in SGA B is concluded to be significantly different from that of SGA A. The mean domain size for SGA A is determined as 26.0 nm *vs* only 9.2 nm for SGA B. Furthermore, the PSD is much more narrow for the latter, see fig. 5.15. The difference between the resulting 100 % α-Al_2O_3 samples after calcination at 1200 °C for 5 h is only about 10 % between the two qualities however, and in fair agreement with the Scherrer data. The results for the α-Al_2O_3 phase in the agglomerates, i. e. PB and PA with an addition of 15 wt % $NaAlF_4$, and held at 800 °C for 10 min differ by even less, at 48.3 nm *vs* 41.9 nm.

The resulting PSD in the partly recrystallized microstructure, see fig. 5.15, is shown to contain a higher density of large α-Al_2O_3 crystallites formed by SGA B, compared to those formed by SGA A. The analysis also shows, see fig. 5.14, that agglomerates formed from SGA A at 900 °C also shows a size distribution slightly skewed toward larger size, compared to agglomerates formed at 800 °C. Also, the PSD tends toward smaller size for the 10 wt % content of $NaAlF_4$ in SA, compared to the lower 5 wt % content, see 5.14, indicative of further nucleation.

The results show that the average nanostructure of α-Al_2O_3 in agglomerates formed by SGA A and B is quite similar, but they also indicate that SGA, having the smallest initial size of α-Al_2O_3 nuclei, results in a coarser microstructure upon interaction with fluorides, but also during calcination in air without fluorides present.

SGA grains retain a nano-crystalline microstructure on average. The formation of large α-alumina platelets in a matrix of nanocrystallites, as shown

in fig. 5.12, may be due to growth kinetics, which are probably faster at preferred sites, with shorter diffusion distances and/ or high mass transport rates and for small domains, i. e. the initial particle size of α-alumina nuclei.

It may be expected that preferred growth sites will exist, due to local effects of mass density and mass transport, and perhaps a general particle coarsening effect, since large particles tend to grow at the expense of smaller particles.

The dominating growth mechanism of the α-Al_2O_3 phase is proposed to be surface diffusion. Surface diffusion depends very strongly on the initial particle size (to the power of four), see chapter 2, so the initial size of α-Al_2O_3 nuclei should be crucial, but also the "particle" domain size and porosity of the transition alumina matrix is important. The reactivity with residual moisture may also be important, as discussed.

The mechanism of agglomeration is concluded to be the coarsening of α-Al_2O_3, with the formation of relatively large platelet-shaped crystallites that form an interlinking matrix between SGA grains, but which contribute relatively little to the diffracted intensity of XRD peaks. The mass transport mechanism is probably by rapid surface diffusion, but also by gas phase evaporation–condensation, when moisture is present, due to the probable formation of HF.

However, the differences in agglomeration behavior between different qualities of alumina cannot be fully explained without further studies of the effect of alumina quality on the coarsening of the nano- and microstructure of SGA and the growth of α-alumina platelets in this system.

5.6.12 Model Predictions

It was hypothesized in chapter 2 that the "average" nano-structure of each SGA grain best explains the propensity for agglomeration of a given SGA quality. A simple model was proposed involving the nucleation density available for further growth of large hexagonal platelets of α-Al_2O_3, correlated to the initial content of α-alumina of the SGA in a complex manner.

It has not been possible to prove or disprove the hypothesis in the present study, since several alumina qualities of similar α-Al_2O_3 content, and similar transition alumina matrix, would have had to be tested for agglomeration and α-nuclei nanostructure.

However, some expected consequences of the main agglomeration mechanism discussed, partly described by the simple model, may include the following effects;

- **A.** SGA with relatively few nucleation sites and/ or ample conditions for mass transport may result in rather large and mechanically strong α-alumina platelets (Alumina B). Such rapid coarsening may be expected to result in platelets of approximately 15μm in length that cement neighboring alumina grains together by forming an interlinking network. A larger quantity of smaller α-crystallites in the grains and/ or limited conditions for mass-transport may result in a finer microstructure with smaller α-crystals in each grain after the $\gamma \rightarrow \alpha$ phase transition is completed. Smaller platelets would be expected to result in weaker interlinking (Alumina A).

- **B.** It may also be hypothesized that, in order for agglomerates of sufficient strength to form, the bulk microstructure of SGA must retain a bimodal size distribution, as illustrated in fig. 5.18. Large (platelet) crystals may provide inter-SGA-particle bonding, while the bulk of each SGA grain retains a fine-grained microstructure, preferably transition alumina, providing sufficient interior (intra-granular) strength.

  The rapid growth of large crystals at the surface, and preferably at the interface between neighboring SGA grains, will most likely result in such a bimodal microstructure (Alumina B), while slower growth may be expected to result in a more homogenous size distribution – presumably giving weaker agglomerates according to the hypothesis.

- **C.** The total resulting (bimodal) microstructure may be expected to have a rather open, and interconnected, pore-structure of much larger dimensions than the original alumina grains. Such a microstructure may be more easily penetrated by liquid melt. However, since the liquid melt within the pore channels of such agglomerates may be expected to be quickly saturated with alumina, the effective alumina - melt contact area for dissolution is the apparent outer surface area of the agglomerate.

  The dissolution of such agglomerates may thus be expected to be rather slow, since the apparent contact area of an agglomerate is easily several orders of magnitude less than that of the dispersed alumina

grains. Rapid dissolution of agglomerates requires their rapid break-up and disintegration.

The same mechanism may explain why low α-alumina content SGAs (Alumina B) form harder crusts. Apart from the formation of larger interlinking alumina crystals, providing initial agglomerate strength, the open pathway produced ensures ample penetration of melt, which upon solidification results in a very dense, thus mechanically strong, composite microstructure.

- **D.** Rapid crystal coarsening of dispersed SGA grains in the cryolitic melt may be expected to provide a larger apparent surface area and hence more rapid dissolution than that observed for α- alumina grains where only very limited "recrystallization" and coarsening occurs, – since no $\gamma \rightarrow \alpha$ transition is possible.

  This effect would is expected to occur in addition to the pressure induced rupture of SGA with high surface areas, due to the release of volatiles, mainly by air expansion and the explosive release of moisture.

These comments and predictions are based on the main experimental results reported here and those reported in the literature, and theory of sintering. The experimental work needed to fully test the working hypothesis is quite involved, as also evidenced in the large amount of work published in the field of alumina ceramics (see chapter 2) and the large number of variables, which may be impossible to control independently.

5.7 Conclusion

The tablet-agglomerate method has been demonstrated to provide reproducible, reliable data for the study of the initial microstructure evolution in agglomerates upon addition of alumina in cryolitic melts. The method shows promise for comparing the agglomeration behavior of different alumina qualities, as done in the semi-quantitative experiments.

It has been shown that aluminas with a low α-alumina content have a greater propensity for agglomeration.

Since the tablet method also allows the control of the fluoride phase additive, we have seen an effect of the amount of liquid phase present, and the effect of

the moisture content of SGA, on the agglomeration kinetics. It is proposed that this is due to the hydrolysis of the $NaAlF_4$ phase, which may also be related to the partial transformation to β-alumina which is observed by XRD of long-term samples.

The $\gamma \rightarrow \alpha$ phase transformation is a nucleation and growth type process. Though the kinetics are significantly faster for SGA B, with a low α-Al_2O_3 content, the bulk (volume) content of α-Al_2O_3, and further transformation, cannot explain the increased tendency for agglomeration for that alumina quality compared to SGA A.

By applying the method of Warren-Averbach line profile analysis, the nanostructure and PSD of the α-Al_2O_3 phase in SGA B is concluded to be significantly different from that of SGA A. The resulting, partly recrystallized microstructure is shown to contain a higher density of large α-Al_2O_3 crystallites formed by SGA B, compared to those formed by SGA A. The analysis also shows that agglomerates formed from SGA A at 900 °C also shows a size distribution slightly skewed toward larger size, compared to agglomerates formed at 800 °C.

The mechanism of agglomeration is concluded to be the coarsening of α-Al_2O_3, with the formation of relatively large platelet-shaped crystallites that form an interlinking matrix between SGA grains, but contribute relatively little to the diffracted intensity of XRD peaks. The mass transport mechanism is probably by rapid surface diffusion, but also by gas phase when moisture is present. SGA grains retain a nanocrystalline microstructure on average. The formation of large α-alumina platelets in a matrix of nanocrystallites may be due to growth kinetics, which are probably faster at preferred sites, with short diffusion distances or high mass transport rates, and for small, initial particle size of nuclei.

However, the differences in agglomeration behavior between different qualities of alumina cannot be fully explained without further studies of the effect of alumina quality on the coarsening of the nano- and microstructure of SGA and the growth of α-alumina platelets in this system.

5.8 Concluding Remarks, Further Work

Further work is needed to test the hypothesis that it is the nano- and microstructure of the SGA, in particular the particle size distribution of α-alumina nuclei, that is largely determining for the agglomeration behavior.

SGAs of identical α-Al_2O_3 contents, but from varying sources – and hence fine- structure, should be carefully compared.

There is a possibility of constructing a controlled "SGA" model by spray-drying well characterized precursor material, or perhaps producing tailored Bayer alumina.

Relevant XRD data suitable for further, more accurate and efficient line profile analysis, may perhaps be obtained by powder synchrotron X-ray diffraction.

In order to have full control over the level of moisture in the samples, a closed environment would have to be used, such as that in a glove-box with controlled atmosphere.

Acknowledgments I am grateful for the assistance provided by Ann-Karin Kvernbråten for many of the tablet experimental series, and Elin Nilsen for performing the BET measurements. Tor Grande gave much helpful advice and criticism.

Chapter 6

Tablet Agglomerate Dissolution

6.1 Background

The literature of alumina dissolution studies is discussed in chapter 2. In spite of considerable effort by many researchers, no single, well defined characterization method has been developed that may measure the dissolution kinetics of smelter grade alumina (SGA) in cryolitic melts.

Two recent studies have reported the use of see-through quartz crucibles in order to visualize the dissolution behavior of SGA upon addition to cryolitic melts [107, 138]. Liu *et al.* [107] constructed flat-sided quartz crucibles measuring 40 x 40 x 80 mm^3 from 3 mm thick plates, and employed backlighting, stirring by impeller at up to 200 RPM, Ar-gas cover and video recording. The study used a melt at T = 895 °C with the composition 3 wt % CaF_2, 25 wt % excess AlF_3 and the balance being cryolite (Na_3AlF_6). The SGA was fed as a free flowing powder through an alumina ceramic tube. The 150 g melt had a height of 50 mm in the crucible. The same experimental set-up was used in the later study by Qiu *et al.* [138], but with dry N_2-gas cover. Liu *et al.* observed that, while calcined α-alumina sank to the bottom and dissolved rather slowly (as a pile of "dispersed" grains), "γ"-alumina formed a floating crust at the melt surface, which tended to break up and dissolve rather quickly.

Qiu *et al.* [138] reported an observation of "snow-flake"-type small agglomerates that sank slowly in the melt. Apparently, the "snow-flakes" were

(gradually) dislodged from the floating crust that had formed after the addition of 1 wt % alumina SGA.

The current study was intended to follow up the reported studies, by attempting to make similar observations of "snow-flake" type agglomerates, observing from below through simpler flat-bottomed cylindrical quartz crucibles. The main objective, however, was to determine the dissolution behavior of well-defined tablet (disc-shaped) agglomerates, see chap. 5, suspended at the surface of the melt. Thus simulating the dissolution of floating "raft" type agglomerates, with a well defined microstructure and history.

6.2 Theory of Dissolution Kinetics

6.2.1 Mass Transfer

The dissolution kinetics of SGA in cryolitic melts is probably under mass transfer control, [180, 147, 85], and may be described by the following relation;

$$\frac{dC}{dt} = k \cdot A(C^* - C_{sat}) \tag{6.1}$$

where the rate of dissolution $\frac{dC}{dt}$ is proportional to the effective contact area, A, between the alumina (solute) and the cryolitic melt (solvent). Thus, the dissolution rate of alumina will largely be determined by the degree of agglomeration upon interaction with the cryolitic melt. The formation and break-up of agglomerates is the subject of this study. The dissolution rate should be proportional to the alumina concentration difference between the (bulk) dissolution area, C^*, and the saturation concentration C_{sat}. A low alumina concentration in the bulk electrolyte is important, but the literature does not show conclusive evidence for the effect of alumina concentration, see chap. 2.

However, the notion that the dissolution kinetics is sensitive to the contact area between the electrolyte and alumina, is generally supported by experimental evidence [180, 149, 63, 147, 107, 85, 86]. If the alumina is not well dispersed upon addition, but is allowed to agglomerate, the dissolution rate may easily be retarded by several orders of magnitude [147, 85]. A simple argument may be made. Allowing for some surface roughness, an alumina disc-shaped tablet may have an outer surface area of about 10^{-3} m^2/g, by assuming a thickness to diameter ratio of 1:10. That is a reduction in

the available surface area of about 5 orders of magnitude compared to the dispersed alumina powder.

The following sections are based on the basic theories of transport phenomena and viscous fluid flow [11, 18] as mostly covered by previous work on alumina dissolution by Thonstad *et al.* [179, 180] and by Hovland, Rolseth and Solheim [63].

Single Alumina Particle

The model treatment of the dissolution of a single (assumed spherical) grain of alumina may be described as a shrinking core model. For a sphere in a fluid with forced convection the following mass transfer relation applies [11];

$$\frac{kD}{\mathcal{D}_a} = 2.0 + 0.60 \left(\frac{D\nu_\infty \rho_f}{\mu_f} \right)^{1/2} \left(\frac{\mu}{\rho_f \mathcal{D}_a} \right)_f^{1/3} \tag{6.2}$$

which corresponds to;

$$Sh = 2.0 + 0.60 Re^{1/2} Sc^{1/3} \tag{6.3}$$

where k is the mean mass transfer coefficient, $\mathcal{D}_a$ is the diffusion coefficient of alumina, D the diameter of the sphere, ν_∞ is the bulk fluid velocity, ρ_f and μ_f is the fluid density and viscosity. Calculations of Sh and Re for various (alumina) particle diameters D in cryolitic fluid melt are given by Thonstad *et al.* [180].

The mass m_a of an alumina particle is $m_a = 1/6 \cdot \pi \rho_a D^3$, and the mass flux of alumina from the surface of the sphere to the bulk of the electrolyte is $dm_a/dt = k \cdot \pi D^2 (C_{sat} - C)$, so that we may obtain the following expression for the dissolution time t [180];

$$t = -\int_D^0 \frac{\rho_a}{2k} (C_{sat} - C) dD \tag{6.4}$$

Since the mass transfer coefficient k is a complex function of the particle diameter (eq. 6.2), the integral must be solved numerically. However, an estimate of t may be obtained by assuming that for low Re-numbers Nu approaches the constant value 2.0 (eq. 6.3), giving $k = 2D/h_m$.

Such an approach gave an estimate of the maximum time t of 4.1 s needed to dissolve an alumina particle of 50 μm diameter using realistic numerical values [180]. This estimate is in fair agreement with observed dissolution times of dispersed alumina grains visually determined by Thonstad *et al.* [179, 180].

Tablet Agglomerate

The dissolution time t for the dissolution of a thin plate, such as a thin tablet, in which all dimensions remain constant except the thickness, may be stated as [63];

$$t = \frac{\rho V}{Ak(C^* - C_\infty)}$$

where $(C^* - C_\infty)$ is the concentration gradient between the local surface and the bulk electrolyte, and ρ and V are the density and volume of the plate respectively. The time of freezing and melt-back of a frozen shell of cryolitic melt on such a plate has been shown to be negligible [63] compared to the total dissolution time. This is provided that the heat transfer rate remains high between the agglomerate and the melt, and little is lost to the surroundings, and that the agglomerate remains coherent after the frozen shell has re-melted.

6.2.2 Heat Transfer

Bulk alumina addition

There is a substantial heat requirement for the endothermal dissolution of alumina in cryolite. The energy needed to heat the alumina from a nominal 200 °C (473 K) to that of the cryolitic electrolyte at around 1250 K (977 °C) is about 94 kJ/mol. The heat of dissolution is a function of the alumina content, but may be assumed to be about 125 kJ/mol [177]. The total heat, L, required to dissolve n_a mol alumina in n_e mol electrolyte assuming that the energy is taken from the electrolyte only, is thus expressed by the relation [177];

$$\Delta T \cdot C_p \cdot n_a = n_e \cdot (125 + 94) kJ/mol$$

By using the specific heat capacity of cryolite $C_p = 0.33$ kJ/mol, and solving for ΔT we obtain that $\Delta T = 13.6$ °C per wt % Al_2O_3. The molar weights were taken as 210 g/mol and 102 g/mol for cryolite and alumina respectively for the conversion to wt % alumina.

An addition of 1 wt % alumina to the electrolyte should thus, theoretically, result in a nearly 14 °C temperature drop in the bulk electrolyte. As noted by Thonstad *et al.* [177], the dissolution of more than 1-2 wt % alumina in an electrolyte with about 10 °C super heat is not possible, even though the

liquidus temperature of the electrolyte will decrease by about 5 °C per wt % alumina. Thonstad *et al.* [180] showed experimentally, in a laboratory cell, that the cryolitic melt dropped to its new liquidus temperature for each batch of 1 wt % alumina added consecutively.

In modern cells, using point feeding technology, alumina additions of around 1 kg per feeder per drop are in the range of only $1 \cdot 10^{-4}$ wt %, assuming about 5-10 t melt in each cell. However, the additions are made locally, with perhaps less than 100 kg melt directly exposed as the "heat affected zone" for dissolution, thus bringing the virtual situation back to a local 1 wt % alumina addition. Thus, before an additional feeder dose is dropped into the melt, the previous batch must have dissolved, or have been carried away in the electrolyte flow [86]. In either case, the same amount of heat must be available, in practice at least 10 °C super-heat, as that before the previous addition was made.

The conditions for heat transfer from the surrounding bulk electrolyte are usually quite good, provided by melt circulation at a rate of around 5-10 cm/s [86], and by the pool of liquid metal. Available heat in the melt must be sufficient if the point feeding of alumina is to remain stable, in which all the alumina added dissolves and is available for electrolysis.

Single alumina grain

The heat transfer between a sphere and a fluid flow field is analogous to mass transfer, and is described by the relation [11];

$$Nu = 2.0 + 0.60 Re^{1/2} Pr^{1/3} \tag{6.5}$$

For very small Re we have that;

$$Sh \simeq Nu \simeq 2 \Rightarrow \frac{Sh}{Nu} = 1$$

while for very large Re we have that;

$$Sh \simeq 0.60 Re^{1/2} Sc^{1/3}, \quad Nu \simeq 0.60 Re^{1/2} Pr^{1/3} \Rightarrow \frac{Sh}{Nu} \simeq (\frac{Sc}{Pr})^{1/3}$$

By definition $Sh/Nu = k\lambda/\mathcal{D}_a h$, where k and h are the mass and heat transfer coefficients respectively, $\mathcal{D}_a$ is the alumina diffusion coefficient and λ is the thermal conductivity. The mass and heat flux from the surface of

an alumina particle (denoted *) to the bulk electrolyte (denoted by ∞) is $|\vec{j}| = k(C^* - C_\infty)$ and $|\vec{q}| = h(T_\infty - T^*)$ respectively. An energy balance argument results in the relation that $\vec{j}/\vec{q} = \Delta H_{diss}$, where H_{diss} is the heat of dissolution which varies for changing alumina concentration [49]. By solving for $\Delta\mathrm{T} = (T_\infty - T^*)$ and using reasonable numerical values, it may be estimated that $\Delta\mathrm{T} = 0.63$ °C for low Re, and $\Delta\mathrm{T} = 0.16$ °C for high Re. This shows that alumina dissolution cannot be controlled by heat transfer [180].

The alumina concentration near the alumina particle must be higher than in the bulk, and the difference may be assumed to be about 5 wt %, thus the gradient in the liquidus temperature is much greater than the above estimated ΔT, since an increase in the alumina concentration by 1 wt % results in an approximately 5 °C decrease in the liquidus temperature [180]. Thus - within the range of primary cryolite crystallization of the alumina – cryolite binary phase diagram [49, 176], it is possible to dissolve alumina into a melt kept at its liquidus temperature by freezing cryolite in the bulk electrolyte, resulting in a lower melt temperature [180].

6.2.3 Viscous Fluid Flow

Spherical grains

A shrinking core model may be envisaged for the rapid dissolution of dispersed alumina grains, as discussed above [180, 57]. Some simple laminar flow calculations based on the near spherical shape of the alumina particles may be made [180, 63, 86]. The terminal velocity of a grain of alumina may thus be expected to be about 70 cm/s in air, after it is discharged from a point feeder and before it reaches the electrolyte – depending on how high above the melt surface it is dropped from. In reality the terminal velocity may be higher due to shielding effects when large quantities of particles interact [18].

Similarly, the terminal velocity ν_{max} for a single free falling small alumina particle (of about 50 μm) in the electrolyte may be estimated by the following relation, derived from Stoke's law and assuming $Re < 2$ [179, 180, 63, 86];

$$\nu_{max} = \frac{gD^2}{18\mu_f}(\rho_a - \rho_f) \tag{6.6}$$

where $\rho_a - \rho_f$ is the density difference between the alumina particle and the (fluid) melt, g is the acceleration of gravity, D is the particle diameter and μ_f is the viscosity of the melt. Thonstad *et al.* [180] thus estimated a ν_{max} of about 0.1 cm/s and 0.3 cm/s for 43 μm and 104 μm particles, Kobbeltvedt [86] estimated a ν_{max} of about 1 cm/s for a 100 μm alumina grain [86]. Such estimates are of course very dependent on the numerical values chosen, themselves often estimates.

For typical electrolyte depths in modern Hall-Héroult cells, and dissolution times of around 5-10 s (see above discussion) it seems very likely that dispersed alumina grains will dissolve completely, even with laminar flow.

Free falling small spherical agglomerates may be treated similarly. By assuming $Re > 500$, D_a of 1 and 5 cm, and density of 2.15 g/cm^3, Stoke's law is no longer valid – but a satisfactory estimate of the drag force [11] gives the following estimate for ν_{max} [11, 86];

$$\nu_{max} = 1.74\sqrt{\frac{gD_a(\rho_a - \rho_f)}{\rho_f}} \tag{6.7}$$

so that ν_{max} is 8.4 and 18.8 cm/s for 1 and 5 cm agglomerates respectively. The agglomerate density will also increase during melt penetration. Obviously, agglomerates must be suspended and broken up in the bulk electrolyte to a certain extent in order to ensure dissolution. Such powerful convective forces may be achieved by upwardly directed turbulent flow at the feeding position, from the release of anode gases [120].

Tablet-Shaped Agglomerates

A tablet (disc) geometry was chosen for the (model) study of agglomerates in this work. This geometry is close to that of "thin" raft-shaped agglomerates. A thin plate, having close to one dimensional heat- and mass-transfer conditions, has previously been described [154, 63, 86]. The behavior of free falling spheroid particles has been described [18], and tablets (i. e. thin cylinders) are a fairly well documented special case. For $1.5 < Re < 133$ the drag coefficient C_D may be described by;

$$C_D = \frac{64}{\pi Re}(1 + 0.138Re^{0.792}) \tag{6.8}$$

which is valid for fixed discs with the axis parallel to the fluid velocity. For higher Re, and when wake shedding occurs, C_D may be approximated as

$C_D = 1.17$. For a tablet-shaped agglomerate (see chap. 5), with $D_a = 3.3$ cm, and using a low relative electrolyte velocity of 1.0 cm/s we obtain the estimate $Re = 220$, so we may use $C_D = 1.17$ in practice. For a disc of thickness to diameter ratio E at its terminal velocity we have that;

$$C_D Re_t^2 = \frac{2\Delta\rho g E D_a^3}{\rho\nu^2} \tag{6.9}$$

which expresses the drag in terms of the particle dimensions. Secondary motion is induced when a disc is free falling, and this will depend on a dimensionless moment of inertia I^*, [18]. The disc will show regular oscillations about the vertical axis diameter, and their amplitude will increase with $(C_D Re_t^2)^{1/3}$ and decrease with I^*. At still higher values of $(C_D Re_t^2)^{1/3}$, the disc's oscillations may be described as a regime of "*glide-tumble*" since the secondary motion will resemble "flight" in a series of curved arcs, and the disc's axis will be inclined at a large angle to the vertical axis at the end of each arc-flight.

At even higher values of $(C_D Re_t^2)^{1/3}$ and moments of inertia the disc will settle into a *tumbling* motion rotating about a diameter and following a rectilinear, but not vertical, trajectory. Such phenomena are not well described quantitatively, but the different regimes and contours of constant Sh and Re are presented by Clift, Grace and Weber [18] (p.149). Most of us have observed falling leaves or pieces of paper to fit such a description of flight.

A fairly high mass transfer coefficient may be expected during such motion, controlled by essentially the same heat and mass transfer mechanisms as for spheres [18]. It seems highly probable that such an agglomerate will disintegrate during secondary axial motion unless it has very high mechanical strength. Thin tablets may also be expected to settle and remain at the aluminium - electrolyte surface and dissolve there [168] described below, unless they dissolve first while "suspended" (in motion) in the bulk electrolyte or while floating on the electrolyte surface.

Cylinder-Shaped Agglomerates

A cylinder geometry was selected as a model study of rather large agglomerates, see chap. 4, based on the work by Kobbeltvedt [86] and Walker [195, 196]. The heat and mass transfer conditions of a cylinder geometry was described by Walker [195]. A cylinder model may be fairly close to

that of a "plugged feeder hole" condition where an agglomerate is allowed to consolidate before being forced into the electrolyte by the steel plunger of the alumina feeder [85].

The drag on discs is relatively insensitive to their thickness, hence the flow behavior of cylinders with thickness to diameter ratios $E < 1$ may be approximated as discs [18]. A cylinder with $E > 1$ and $Re > 0.01$ will fall with its axis horizontal, and secondary motion is induced at around $Re \simeq 100$. This will be the case for a cylinder such as the agglomerate formed in the present study, in chapter 4. Unless the average density of such agglomerates is low so that it may remain buoyant while breaking up and dissolving, such agglomerates are a likely source of alumina sludge [177].

Surface Tension

The part of the alumina charge that does not dissolve while "suspended" in the bulk electrolyte, may form so-called "sludge" under the metal pad [80, 177]. However, a significant amount of alumina, both as dispersed grains and "tablet" agglomerates, may be expected to settle and remain at the aluminium - electrolyte interface, and dissolve and/ or break up there [168, 178]. A force balance was made by Solheim and Rolseth [168] in order to obtain a theoretical expression for the thickness and density limits for agglomerates suspended by surface tension at the liquid aluminium interface. A similar expression will be valid for the surface of the melt.

By considering a tablet (thin cylinder) of thickness H and radius R the following expression may be derived for the maximum tablet thickness [168];

$$H_{max} = \frac{1}{\rho_t - \rho_m}\left(\frac{2\sigma}{Rg} + \sqrt{\frac{2\sigma(\rho_m - \rho_e)}{g}}\right) \tag{6.10}$$

The surface tension force is $2\pi R\sigma cos\theta$, a function of surface tension σ and the angle θ between the vertical and the deformed surface of the metal, and is at its maximum for $\theta = 0$. The surface tension force was used for the derivation of eq. 6.10 [168]. The densities ρ_t, ρ_m and ρ_e are for the agglomerate tablet (t), Al-metal (m) and electrolyte (e) respectively, while $g = 9.81 m/s^2$ and $\sigma = 0.55 N/m$. H_{max} will decrease for increasing tablet density ρ_t and tablet radius R.

Calculations made for ρ_t in the range 2.5 – 3.2 g/cm^3 and R in the range of about 2.5 – 20 cm, using eq. 6.10 were reported [168]. The maximum

H_{max}, for $\rho_t = 2.5 g/cm^3$ and $R = 3$ cm, was determined to be about 4.5 cm. The authors comment that this is probably on the high side, since in reality the agglomerates would be irregularly shaped, and it is also noted that the situation in which agglomerates remain suspended is likely to be metastable only. Furthermore, electrolyte penetration into the agglomerate will increase its density.

6.2.4 Effects of Alumina Moisture Content

Agglomeration and Dissolution

Explosive desorption of moisture and expansion of air within grains and agglomerates will likely result in some shattering of individual grains as discussed (and shown) by Liu *et al.* [107], and quite effective dispersion of alumina powder and agglomerates.

The discharge of moisture and air will probably increase the flowability of the alumina, and may ensure that the alumina is largely fluidized when it contacts the hot electrolyte. Fluidization of the alumina powder will ensure that thin agglomerates are formed, resembling "rafts" (flakes, tablets) that float at the electrolyte surface, [176]. Such rafts may be expected to be broken up by the undulating electrolyte and discharge of anode gas from under the anodes during electrolysis. The microstructure, and mechanical strength, of such agglomerates is the main subject of this study, see chap. 5.

The content of moisture in smelter grade alumina (SGA) is known to be beneficial for the *dissolution process* up to a level of approximately 1 wt % [59]. As discussed in chapters 2 and 8, an excess of water may give entrainment of alumina upon addition, producing a so-called "volcano" or"geyser" effect, which may lead to alumina feeding problems as a mound of agglomerated SGA may form [3]. A "plugged" feeder hole may result, where the alumina charge is not fed as a free flowing powder but as lumps, perhaps with inadequate dissolution and distribution rates, causing bottom sludge, current interruptions and low alumina concentrations in the electrolyte [177, 120].

Haverkamp *et al.* [59] found that reacted dry scrubber alumina dissolved 30-40 % faster than primary SGA, see chap. 8 for further discussion.

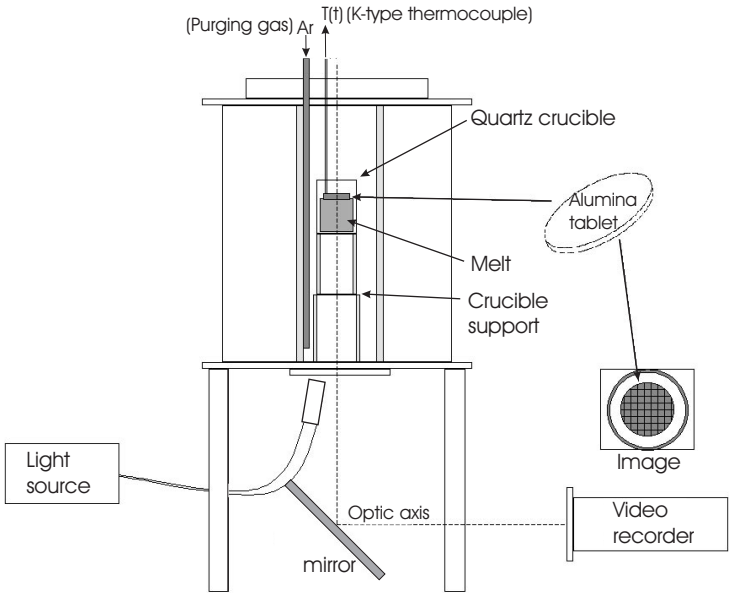

Figure 6.1: *Schematic of the experimental set-up used.*

6.3 Experimental

The experimental set-up chosen for this study is shown schematically in figure 6.1. It allows the simultaneous visual determination of the break-up and dissolution of a tablet (disc-shaped) alumina agglomerate and the possibility to observe "snow-flakes" in the melt. By using a side view set-up, [55, 107], it would be nearly impossible to discern the dissolution time of a thin tablet at the melt surface.

Since the view from below is not cluttered by other components of the set-up, such as thermocouples, tablet suspension rig, stirring etc., an accurate positioning of the video camera along the optical axis is straight forward by the use of a simple mirror. Observation from below will also make it possible to observe small "snow-flake" agglomerates, as described in the literature.

A view from below, using a see-through crucible has several advantages. A flat bottomed cylindrical quartz crucible is more easily obtained than the specially made, orthorhombic crucibles used by Liu *et al.* [107]. Flat windows are important for visual observations with minimal distortion. Furthermore, a view from below allows closer, more consistent observation,

since the observer and instruments are protected from heat and fluoride vapors- compared to a top view. More importantly it makes it possible to make visual observations in a semi-closed furnace, with a controlled, stable temperature and temperature gradient.

The solubility of SiO_2 in cryolite is significant (5 wt % at 1010 °C), and increases with increasing content of Al_2O_3 [49], and a quartz crucible is thus not chemically stable. However, Liu *et al.* [107] reported that their crucible remained translucent for up to 2 h.

6.3.1 Chemicals and Equipment

- Specially reconstructed open ended vertical furnace, electronic temperature control ± 2 °C
- High luminance light source, Zeiss, with Ø=15 mm fiber optic light guide (with Al-foil protection)
- Canovision EX1, Hi-8 video camera, aperture F:1.4-2.1, 15× optical zoom, remote control; Olympus digital SLR camera.
- Thermocoax thermocouples, k-type (chromel-alumel alloy), Ø=3 mm, accuracy better than ± 1 °C
- AlF_3. Norzink: AlF_3 + ∼ 10 wt % Al_2O_3; Alufluor: ∼97 % (+ 3.4 wt % Al_2O_3, LECO
- NaF. E. Merck: +99 %
- Ar-gas: 99.99%

Special flat bottom quartz crucibles were prepared from a quartz tube with ID=50 mm. Unless otherwise mentioned, 130 g melt was used, so that tablets of 1.2-1.3 g would constitute a 1 wt % addition, in line with previous work, see chapters 2 and 5. The alumina concentration was kept below saturation. The cryolitic melts was prepared using quite pure chemicals, since the melts should be as translucent as possible, and when cooled, the melts appeared to be quite pure (white), while the crucibles disintegrated into thin flakes.

The tablet rig used to suspend a disc-shaped alumina agglomerate just below the melt surface was prepared by shaping a Zn-coated steel wire

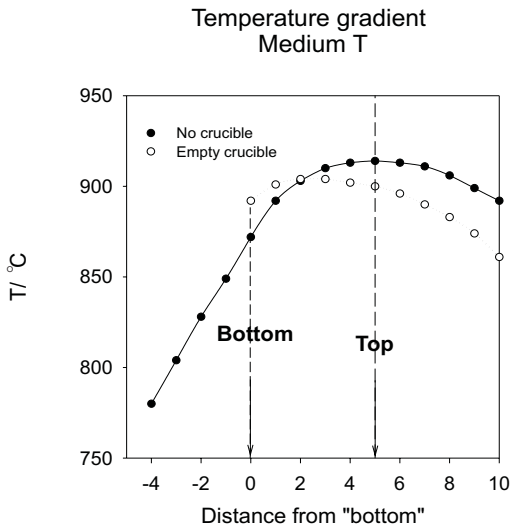

Figure 6.2: *Temperature gradients measured along the optical axis.*

mesh (1.5 mm mesh spacing, 0.2 mm wire) to an ID=34.7 mm, adequate to hold the 33 mm diameter tablet. A clamp was fixed to the mesh using steel wire, and a 3 mm k-type thermocouple could be squeezed tight. The total mass of the rig, not including the thermocouple, was 2.15 g. The corrosion resistance of the rig was satisfactory for a melt temperature of around 800 °C. Ideally, a Pt-mesh should be used.

6.3.2 Controlled Temperature Gradient

An open ended vertical furnace will generally act as a chimney stack air heater, by the principle of sucking in cool air at the bottom and expelling hot air from the top.

The furnace must be closed at least at one end, and it was observed that a stable (but very large) temperature gradient was obtained when only the top furnace lid (insulation plate) was used.

Figure 6.2 shows stable gradient with and without an empty crucible in place. At this medium temperature, T = 900 °C, similar to that used by Liu *et al.* [107], the effect of adjusting the height of the crucible support was studied. It was observed that the gradient within a lengthened alumina cylinder section of the crucible support was linear, and smaller than that

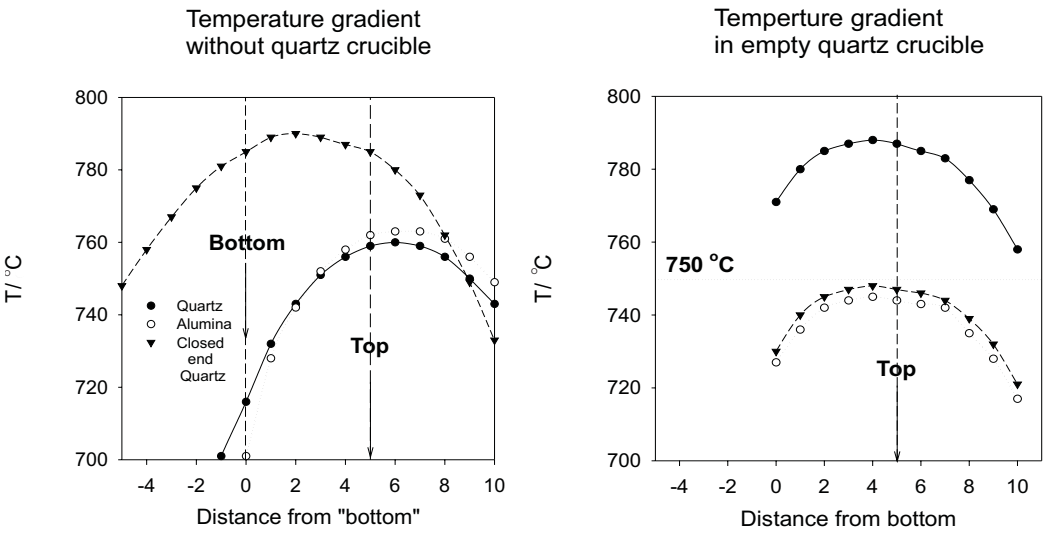

Figure 6.3: *Temperature gradients measured along the optical axis. A:(Left) Stable gradient with no crucible for 3 different top sections of the crucible support. B:(Right) Stable gradient with empty crucible in place. Identical gradients measured at several set temperatures during furnace temperature calibration.*

observed by shortening the support (same as that measured for z $<$ 0 cm in fig. 6.2). The optimal position of the crucible, centered in the hottest zone of the furnace, was confirmed.

Figure 6.3A:(Left) shows the effect of using 3 different top sections of the crucible support. While the difference between using open cylinders of either quartz of alumina is minimal, a closed quartz cylinder (empty crucible) showed a favorably small gradient in the z-position where the crucible was to be placed -between the "Top" and "Bottom" marks in the figure.

The temperature gradients were measured using a k-type thermocouple along the optical axis of the set-up (see fig. 6.1). By using a simple tube guide and clamp the z-position was measured with an accuracy of $\pm$ 1 mm. The thermo-couple was allowed to equilibrate at the new z-position for 1 min prior to every recorded temperature reading.

Figure 6.3B:(Right) shows the stable gradient with empty crucible in place

when using the standard alumina cylinder top section of the crucible support. Identical gradients were measured at several set temperatures during set-temperature calibration to T = 750 °C, prior to the low temperature experiments .

6.4 Results and Discussion

In general the open ended furnace was observed to perform satisfactorily, producing a stable, reproducible temperature gradient, see above. It became clear that corrosion of the quartz crucible was too serious for reliable alumina dissolution results to be obtained. The corrosion was most serious in a band around the inner circumference of the crucible, at the melt meniscus. In practice a compromise between rapid melting and good temperature control had to be made. A set temperature of a nominal 30 to 50 degrees super-heat had to be used, and as the melting temperature of the melt in order to minimize the preparation time before each experiment.

Preliminary experiments at $890 < T < 990$ °C, and $1.67 < CR < 2.35$ where failures since the crucible was observed to corrode catastrophically during melt down. The effects of using variable levels of Ar-gas were studied, and pre-heating the crucible, and varying the alumina and CaF_2 concentrations, but the severe quartz corrosion was always observed. A melt composition allowing a still low temperature of 750 °C was chosen. A 130 g mixture was prepared giving a melt composition of CR=1.22, i. e. close to the eutectic. No CaF_2 additive was used, and a nominally alumina-free melt (sublimated AlF_3) gave a nominal liquidus temperature of 715 °C. The corrosion rate at these conditions was sufficiently slow to perform further experiments, but melt down was rather slow, much like melting snow in a bucket at room temperature.

For a test of the tablet rig and tablet "dissolution", crushed melt with ca. 1.5 wt % alumina was used. The alumina content was introduced by the AlF_3 (Alufluor) impurity, not sublimated in this case. This melt composition has an alumina solubility only of about 2 wt % [163], so that only 0.5 g alumina could now be expected to dissolve. The melt was pre-melted in a Pt-crucible held at 960 °C for 1 h, then quenched and crushed). The observed events are now cited for reference.

The crushed melt was introduced through a funnel directly into the hot crucible at T = 750 °C in order to minimize the melting time. This time

Figure 6.4: *View of quartz crucible with melt seen from above. The rough surface that has developed on the crucible bottom after melt-down is evidently of the order of ∼1 mm. Under-exposed image due to intense light source from below.*

Figure 6.5: *Tablet agglomerate in place just below the melt surface. The tablet suspension rig is a steel wire mesh fixed at the end of a 3 mm k-type thermocouple.*

was termed $t = t_0$. A high level of Ar-gas flow was used, and video recordings were made. The resolution of the video-images was observed to be better than 0.5 mm prior to melting.

After t_0 + 60 min at least 50 % had melted, and after another 10 min the melt is almost entirely liquid. The crucible bottom became difficult to see through. The melt was determined to be 33 ± 1 mm. The melt was stirred regularly at about 5 min intervals. A melt sample was quenched for later (LECO) analysis. At t_0 + 80 min a few small lumps are still present at the crucible bottom, total mass of these lumps was estimated as 0.5 g. The crucible bottom had become rough, with a roughness of about 1-2 mm, see fig. 6.4, and a corrosion band around the inner circumference of the crucible, at the melt meniscus was evident.

At t_0 + 95 min the small lumps on the bottom resemble a few grains of sand at the bottom of a glass of water. The temperature was lowest at the crucible bottom, at T = 721 °C– which is barely above the liquidus temperature for this melt - explaining why the melting was so slow.

After t_0 + 120 min the tablet and rig was lowered to just below the melt surface, after being pre-heated for a few minutes just above the surface. The dimensionally stable tablet was prepared by the procedure described in chap. 5, from SGA B with 15 wt % $NaAlF_4$ held at 800 °C for 10 min. Only a section of 0.91 g (of a total of 1.2 g) was used in order to fit the tablet into the rig.

Initially the tablet seemed to float, but was rapidly penetrated by melt and settled on the steel wire mesh, see fig. 6.5. The crucible lid was kept closed. At about t_0 + 125 min, i. e. after 1-2 min, what appears to be "snow-flakes" in the melt become evident when viewed from above. They do not appear to be caused by contamination from other parts of the equipment, such as the insulating lid. After a further 10 min period the tablet suspension rig loosens from the thermocouple it is fastened to and sinks to the bottom. By this time the crucible bottom is so opaque that it is very difficult to observe this major event, – much less very small "snow-flake" agglomerates. The experiment was terminated after a final bath sample was quenched for later analysis. By then the corrosion at the meniscus had reached about 2 mm in depth. This had been observed in previous experiments also. In order to test the visibility from below, a few flashes from the laboratory digital camera were fired above the melt. These are not visible on video.

6.4.1 Quartz Corrosion

The high temperature melts had a nominal liquidus temperature of about 975 °C, and a melting temperature of 1020 °C was used, giving a 45 °C super-heat. After about 60 min the melt was liquid, but rather viscous, and lumps persisted on the crucible bottom. The crucible disintegrated after 90 min, melt running through at the meniscus and on the outside surface of the crucible.

The medium temperature melts had a nominal liquidus temperature of 854 °C. A melting temperature of 900 °C was used. After 40 min melting started, and possible traces of "smoke" was observed. After about 60 min the melt was liquid, but a few lumps persisted on the crucible bottom. The melt height was 30 mm. A temperature gradient was measured along the optical axis, and this confirmed the temperature to be lowest at the crucible bottom. The temperature continued to rise at a rate of about 0.3 °C/min until the melt corroded through the crucible at the melt meniscus position, after 95-110 min. Typical corrosion observations for the low temperature melts was described above, involving the rough bottom surface, and the pitting band along the inner circumference of the crucible, at the melt meniscus. The latter progressed steadily until the crucibles were removed, the pits reaching 2 mm in depth, i. e. just before melt-through.

The set-up in this study was not stable enough to allow the (rather risky) introduction of liquid melt to a pre-heated crucible at correct temperature in place in the furnace. This may be considered as perhaps the best solution to optimize the time available for experiments before the quartz crucible becomes corroded by the cryolitic melt. Such an approach is described in the literature [55]. The observations of severe corrosion of the crucible may be explained by the following reactions;

$$\begin{aligned} 4Na_3AlF_6(l) + 3SiO_2(s) &= \\ 2Al_2O_3(s,diss) &+ 3SiF_4(g) + 12NaF(s,l) \end{aligned}$$

$$\begin{aligned} Na_3AlF_6(l) + 4SiO_2(s) &= \\ NaAlSi_3O_8(s,l) &+ 2NaF(s,l) + SiF_4(g) \end{aligned} \tag{6.11}$$

$$\begin{aligned} 2Na_3AlF_6(l) + 2Al_2O_3 + 9[21]SiO_2(s) &= \\ 6NaAlSiO_4[NaAlSi_3O_8] &+ 3SiF_4 \end{aligned} \tag{6.12}$$

$$2Na_3AlF_6(l) + 2Al_2O_3 + 3[9]SiO_2(s) = 3NaAlSiO_4[NaAlSi_3O_8] + 3NaAlF_4 \quad (6.13)$$

The upper-most reaction, which has a very high positive ΔG, (ΔG_{1300K} = +375.4 kJ/mol) is very unlikely, even in this open system. It is more likely that a reaction involving silica, and perhaps alumina, will produce a viscous sodium-alumina-silicate product and SiF_4 and $NaAlF_4$ gases, as discussed by Rutlin [150]. The melt quickly became very viscous for the high temperature experiments before the crucibles were completely corroded through.

For the lower temperature experiments the corrosion rate was significantly lower. However, the corrosion was still serious and resulted in an opaque, rough crucible bottom not suitable as an optical window. Bath samples were taken after about 27 min and 80 min exposure to liquid melt, i. e. 27 and 80 min after melting had definitely started. LECO analysis was used in order to obtain a measure of the oxygen content of the melt, which was initially low at $\sim$ 1.5 wt % Al_2O_3. The LECO analysis gave estimated "Al_2O_3"-contents of 8.1 $\pm$ 0.2 wt % and 14.4 $\pm$ 0.2 wt % respectively, using the standard alumina calibration curve.

Since the solubility limit of alumina in this melt is about 2.0 wt %, these data must be attributed to quartz corrosion and dissolved SiO_2-containing species in the melt. Liu *et al.* [107] reported that their crucible lasted about 2 h before becoming opaque, and that the SiO_2 concentration in the melt was only 0.12 wt % after the experiment. The method of determining the quartz content in the melt was not stated however. It may be concluded that the quartz crucible used in that study had much better corrosion resistance than those used in the present study, perhaps due to the completely flat surface and perhaps better quality of the fused quartz plates. The crucible was perhaps better protected by the inert atmosphere used in that study (closed system). It is also possible that the melt had a low silica content, but contained other oxygen containing species, as suggested in the reactions above.

6.4.2 Crucible Bottom

Because the temperature was lowest at the crucible bottom, this was the last place the bath melted prior to experiments, and the preferred location for reaction products to freeze out later. In addition, small pieces of top cover

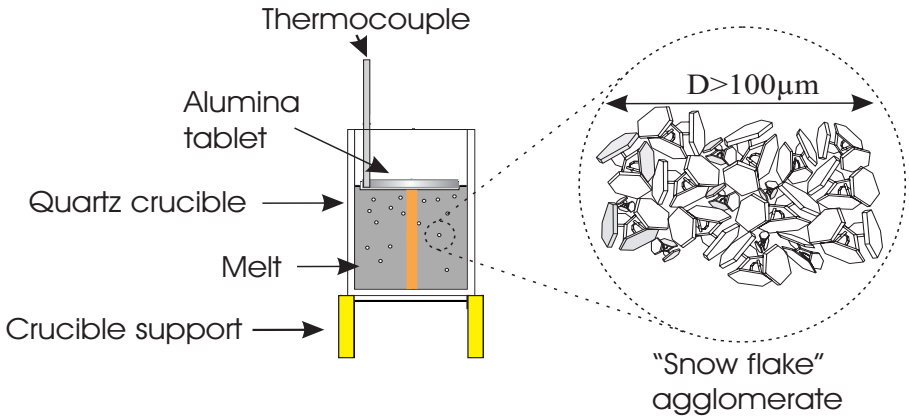

Figure 6.6: *Detail of the experimental set-up, and "snow flake" as discussed in text.*

insulation plate and other trace solid state impurities were unavoidable. These would also tend to hamper the visibility through the crucible bottom and could be confusing for later analysis of the video recordings. By having a side view set-up such problems are avoided.

By only using a single quartz surface the temperature gradient will be large at the bottom, through the quartz layer. It was observed that the temperature gradient could be much improved be using two quartz layers, in practice by using an empty quartz crucible as the top-most section of the crucible support. Since the crucible bottoms were not completely flat, the combined distortions became too large for high definition visual study. A flat quartz plate could have been used however.

6.4.3 "Snow-flake" Observations

Visual observation requires that "snow-flakes" have to be larger than about 0.1 mm in order to be observed without magnification. This limit may be improved by using optical equipment, such as reported here, but the resolution is limited by the melt and flatness of the windows used. In practice the detection limit would be governed by imperfections in the optics (mainly the observation window/ crucible bottom). Surface roughness on

the order of 1-2 mm as observed after corrosion had taken place, and this makes any visual observation almost impossible.

Small snow flake type agglomerates may be expected to have a microstructure consisting of interlinked, fairly coarse α-alumina platelets, as shown in fig. 6.6. A certain spalling and break-up of the alumina agglomerate will take place as the cryolitic melt penetrates it. It seems reasonable to assume that the current set-up, by including a well defined supporting mesh for a well characterized alumina microstructure, could provide a measure of the "dissolution resistance strength" of such agglomerates. The mesh size was supposed to have been varied in later experiments on the assumption that: the larger the mesh size the – "stronger" the agglomerate must be in order to withstand disintegration for a given set of other conditions, including temperature and fluid (melt) flow.

Further work was terminated due to the severe crucible corrosion problems, however. Though the results reported in this study are uncertain, it seems highly probable that the "snow-flakes" observed at t_0+ 125 min in the final low temperature experiment, as recorded on video - are in fact small agglomerates, in agreement with Qiu *et al.* [138] and others [176].

6.4.4 Further Work

Other more advanced optical techniques were looked into for the possibility of using a similar set-up as used here, in order to obtain more precise data on the dissolution behavior of alumina agglomerates and dispersed grains.

Ultrasound might be attempted, and quartz is a good candidate transducer material available, the resolution may be limited however [32]. Low coherence laser interferometry has recently been developed for the *in vivo* study of blood vessels. A technique using a laser probe, scanning horizontal sections of the cryolitic melt under a suspended tablet, would be able to gauge the mean light scattering amplitude of a two dimensional plane, – as a function of time and vertical distance from the tablet [131]. The scattering amplitude would be a function of the (alumina) particle size and number of dissolving grains in each plane.

A modern approach of window-less crucibles for optical studies of fluoride melts, such as low-temperature "FLINAK" might be a possibility for small scale agglomerates.

However, quartz corrosion renders such methods nearly impossible, since a stable transducer, clear transparent window and/or crucible bottom is required. Fused quartz plates, as used by Liu *et al.* [107], could perhaps be re-investigated for such studies. Exotic materials, such as a diamond crucible could be envisioned.

6.5 Conclusion

Because the temperature was lowest at the crucible bottom, this was the last place the bath melted prior to experiments, and the preferred location for reaction products to freeze out later. Corrosion of the quartz crucibles was very serious, even at the lowest temperature employed.

The results obtained are uncertain, but it seems highly probable that small "snow-flake" agglomerates were observed after a tablet agglomerate was suspended just below the melt surface at 750 °C.

Acknowledgments

Many thanks are due to glass blower Astrid Salvesen for preparing the flat bottomed quartz crucibles. I would also like to thank colleagues and visiting researchers, for many interesting discussions on this difficult subject.

Chapter 7

Tablet Temperature Response

7.1 Motivation

In order to study the assumed conditions at the electrolyte infiltration front in alumina agglomerates, as discussed in chapters 2,4 and 5, the system is placed in a controlled environment using small tablet-shaped samples. The aim of this study was to determine the characteristic temperature response time of the samples studied in chapter 5.

7.2 Background

In order to understand the "interlinking" and agglomeration process, one must study the advancing front of the cryolitic melt as it penetrates an alumina agglomerate.

This allows precise control of the experimental conditions of the system including SGA, temperature, time and melt composition. A simplified sintering experimental technique was developed. The technique may be described as a "one shot" method of data collection, using about 1.2 g of pre-mixed, dry powder sample, quickly placed in a pre-heated furnace, and then held at temperature for a pre-determined time interval. The sample is subsequently quenched in air at room temperature by quickly removing the sample from the furnace after the predetermined time had elapsed.

Differential Thermal Analysis (DTA) has been used for measurements of transition alumina, with [189, 127] and without [156] the presence of fluo-

rides. Usually a controlled temperature increase of only 5 - 10 °Cmin^{-1} is employed for DTA, in which exothermal/ endothermal processes are determined against a stable (α-alumina) reference material. Lossius [110, 111] used a combination of Thermo-Gravimetric Analysis (TGA) and subsequent XRD analysis to determine most of the chemical reactions of secondary alumina heated in air. The identification of desorbed chemical species and reactions were discussed as a function of weight loss and temperature within the range of 30 - 830 °C, at a heating rate of 20 °Cmin^{-1}. Desorbed water and -OH groups has the largest thermal effect, while some fluoride species (e.g. HF, $AlF_2(OH)$) and SO_2 were also significant. The removal of moisture and the effect of fluorination on the desorption of -OH and HF is further discussed in chapter 8 in the present work.

The thermal conductivity k of a porous composite material is a quite complex function of temperature, microstructure (i.e. porosity), material and lattice defects (ceramics), [141, 200]. For low temperatures $k \propto 1/T$, directly related to the mean free path of phonon scattering in the material. For higher temperatures thermal heat radiation becomes more important, with $k \propto T^3$. Heat transport rates in a convective fluid may be much higher. The heat transport equations for an alumina grain (sphere) is discussed in chapter 6, and should be relevant for the thermal response of dispersed alumina grains in air.

Østvold *et al.* [132, 133, 50] studied the thermal conductivity of a bed of alumina with additions of $NaAlF_4$ using a hot strip (using Pt) method. The samples were held 20 h at temperatures in the range likely in top crust and cover of modern Hall-Héroult cells. Generally, k increased as a function of temperature in the range 700 - 900 °C and this was attributed to the "sintering" of alumina induced by the liquid fluoride additive. The thermal conductivity was observed to peak at around 2 wt % addition of $NaAlF_4$. Na-incorporation into the alumina may have reduced k however due to increased phonon scattering for higher contents of $NaAlF_4$, [133, 141]. A significant increase in the thermal conductivity is observed by this method for temperatures as low as 600 °C,[133, 132]. Micro-structural coarsening may improve the particle-particle contact of alumina, ref. chapter 2 and 5, thereby increasing the thermal conductivity by increasing the alumina connectivity. The effect increases with increasing temperature and soaking time.

For normal top-crust containing up to 60 % electrolyte (frozen and liquid) the porosity is greatly reduced and the thermal conductivity is much higher

than for loose alumina powder with around 75 % porosity. The thermal conductivity of top-crust in modern Hall-Héoult electrolysis cells is important for the heat balance of the cells, [153, 176].

A mathematical model was developed by Rye and Solheim [152] in order to estimate k for a porous material such as unpacked bulk alumina. A matrix of continuous (air) and discontinuous material (alumina) with cubic symmetry was devised. The porous material has a mixed k which is a function of material properties, the temperature and the relative fraction of discontinuous material, and the connectivity of the two phases. At the limit of zero porosity the model will reproduce the k of the discontinuous phase material. For polycrystalline, fully dense, alumina $k = 32$ $\mathrm{Wm^{-1}K^{-1}}$ at room temperature [200].

The (molar) heat capacity at constant pressure, C_p of alumina is a function of temperature [200];

$$C_p(T) = a + \frac{b}{T} - \frac{c}{T^2}, \tag{7.1}$$

where a, b and c are material specific parameters. The C_p for high quality alumina (corundum) is well documented, having a = 114.77, b = 12.80 and c = 35.44 [200].

7.3 Experimental

A simple apparatus, shown in figure 7.1, was constructed for determining the thermal response time of tablet type agglomerates, as studied in chapter 5. The supporting structure was made from a cylinder section of sintered aluminium oxide, "Alsint" , (tube Ø= 57.0 mm outer and Ø= 65.6 mm inner), and steel wire (Kanthal type, Ø= 1.2 mm). The thermocouple used was a commercial grade k-type (Thermocoax TKI-10/50) with a diameter of only 1.0 mm and a documented intrinsic response time of under 100 ms in air. A few initial experiments were conducted using a larger diameter thermocouple (Thermocoax TKI-30/50).

Apart from holding the thermocouple, the function of the support structure was also to define the location for emplacing the sample given by the opening in the support structure and center. The thermocouple was set in the starting position above the spot where the sample is placed. Heating rates up to 2000 $^{\circ}\mathrm{Cmin^{-1}}$ were attained.

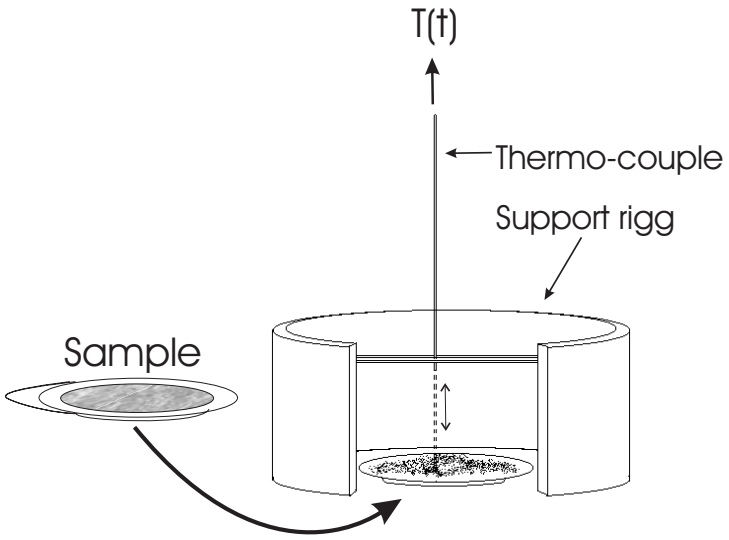

Figure 7.1: *Schematic presentation of the experimental set-up used for determining the temperature response time of the agglomerate samples. The sample is quickly placed in a predetermined location in a hot furnace (at set-temperature), before the thermocouple (also preheated) is quickly lowered into it.*

The thermocouple and support structure used was equilibrated for at least two hours in the Nabertherm furnace at the set temperature T_{sp}, which was controlled electronically within ± 2 °C. Alumina samples of ca. 1.2 g were quickly filled flat in the Pt-"dish", (9.0 g) sample container – prior to emplacing the sample in the furnace. The alumina sample was each time removed from a pre-heated, dried batch held at 200 °C. The spring-loaded door was opened to insert the preheated (T ∼100 °C) sample. The preheated thermocouple was quickly lowered into the sample as soon as the furnace door was shut. The entire process took approximately 3 seconds. A data- logger (21X micrologger, Campbell Scientific LTD.) was used to record data during each experiment, starting 10 min before and ending 10 min after the sample was emplaced.

Both primary and secondary alumina samples of the A quality were used, see chapter 5. The set temperature levels were 800, 900 and 1000 °C. After performing the temperature response measurement, the samples were subsequently analyzed by XRD in order to determine the degree of phase

Table 7.1: *Randomized experimental matrix and results including 3 randomized copies. Commented experiments identified as S1, S2 and S3 demonstrate effect of varying the type of Pt-dish and diameter of the thermocouple used (exp. cond.). Temperature response time τ defined as time at which sample has reached 95 % of furnace temperature.*

Exp. no. (1-11)	Com.	Pt-dish (#) [0,1,2]	Thermo-couple Ø[mm]	SGA A [P/S]	Temp. T_{sp} [°C]	τ, t(0.95T_{sp}) [s]
1	Copy 2	0	3	P	800	65
2	S1	0	3	P	800	57
3		1	1	S	800	31
4	S2	0	1	P	800	54
5	Copy 3	1	1	S	800	35
6	S3	2	1	P	800	44
7		2	1	S	900	33
8	Copy 7	1	1	S	900	33
9		2	1	P	900	36
10		1	1	S	1000	31
11		2	1	P	1000	32

transformation $\gamma \rightarrow \alpha$.

7.3.1 Tabulated Experimental Campaign

The experimental design matrix is presented in table 7.1. A few preliminary experiments were performed in order to determine the effects of varying the sample container (Pt-dish) and the diameter of the thermocouple. A semi- randomized experimental plan was used in order to minimize effects of possible systematic error. The plan included 3 randomized duplicate experiments in order to estimate the standard error of the results.

Two types of Pt-dishes were used, Pt-dish no. 1 and 2 being similar, with inner diameter Ø= 33 mm, but with slightly different mass (9.05 g and 8.95 g), while Pt-dish no. 0 was of a different, (old) type with Ø= 32 mm, (7.90 g).

The temperature response time τ was defined as the time at which the

temperature in the sample had reached 95 % of the set-temperature of the furnace. The time τ was thus determined from the T(t) response curves logged using the data logger. The accuracy of this determination was approximately $\tau \pm$ 2 s, and about $\pm$ 4°C in the recorded temperature. The experimental campaign, and the temperature response time results, are presented in tab. 7.1.

7.3.2 1-D Model

A one-dimensional mathematical model was developed based on previous work [152], using the assumption that the heat was provided through the sample bottom and conducted vertically through the Pt-dish and alumina bed. The top surface of the alumina bed is in thermal contact with the surroundings (furnace walls) by heat radiation, and a significant amount of heat is absorbed by the sample surface. The alumina bed is fixed at 1.9 mm, divided into 20 equal vertical cells of 0.095 mm each, while the Pt-dish is a single cell. The heat affected zone of the (bottom) furnace lining is assumed to be 15 mm deep, divided into 25 equidistant vertical cells. The bottom-most cell is fixed at the furnace set temperature.

The thermal conductivity of the alumina layer is assumed to vary linearly from 0.12 $Wm^{-1}K^{-1}$ at 20 °C to 0.32 $Wm^{-1}K^{-1}$ at 1000 °C. The temperature at each nodal point is determined by the mean temperature of two neighboring cells. The thermal conductivity of the furnace lining is fixed at 0.2 $Wm^{-1}K^{-1}$, while that of Pt is not applied (assumed to be infinite). The (specific) heat capacity C_p, with dimension $Jkg^{-1}K^{-1}$, of alumina is assumed to be a function of temperature, ref. eq. 7.1, with a = 1071.4, b = 0.18 and c = 2.9817. Again, the mean temperature of neighboring cells is used.

The temperature dependence of the heat capacity of Pt is of the same form as for alumina, but with a = 123.1, b= 0.1203 and a positive c-term = 214500, while the heat capacity of the furnace lining material is fixed at 1150 $Jkg^{-1}K^{-1}$. The mass (density) of the Pt-dish is 5.4 kgm^{-2}, while the density of alumina is 1.0 gcm^{-3} and the density of the furnace lining is assumed to be 0.8 gcm^{-3}.

The emissivity of the alumina is very important for the results obtained, as this parameter will control the amount of heat absorbed from the surroundings (furnace) by radiation. In the final model result an emissivity of 0.2

was used, which is on the low side of a realistic value [152]. The starting temperature of the alumina bed and Pt-dish is set as 50 °C.

The model calculates the temperature in each cell by time increments of Δt 0.01 s per cycle, according to the relation;

$$T_{2,new} = T_{2,old} + \frac{\Delta t \left\{ \frac{k_{12}}{\Delta x}(T_{1,old} - T_{2,old}) + \frac{k_{23}}{\Delta x}(T_{3,old} - T_{2,old}) \right\}}{\rho C_p \Delta x} \qquad (7.2)$$

where T_i is the temperature in the cell for the previous (old) and present (new) calculation cycle respectively for cell i = 1, 2, 3,.... (i=1 is the cell below and i=3 above cell no. 2). k_{ij} is the mean thermal conductivity of two neighboring cells.

7.4 Results and Discussion

By using a small sample, the effects of volatilization by loss of moisture etc. upon heating, are minimized. A rapid thermal response may also be expected, though the effects of the experimental set-up, including the sample container, limits the heating rate compared to the situation upon addition of free flowing alumina to a cryolitic melt.

7.4.1 Thermal Response Data

The thermal response time data is presented in table 7.1. 3 experimental copies, exp. numbers 2, 5 and 8, were used in order to estimate the standard deviation of the data.

At 800 °C, and using primary alumina sample, the response time is 61 ± 4 s with Pt-dish #0 and thermocouple diameter of 3 mm. At 800 °C and using secondary alumina the response time is reduced to 33 ± 2 s with Pt-dish #1 and thermocouple diameter 1 mm. The measurement error in reading off the temperature and response time data from the response curves is estimated as ± 4 °C and ± 2 s respectively, in fair agreement with the observed data scatter. In general, the replicates (exp. 1, 2;3, 5;7, 8) demonstrate satisfactory reproducibility in the experimental technique, see data in table 7.1. As stated above, at 800 °C and using primary alumina, the response time τ is 61 ± 4 s with Pt-dish #0 and thermocouple diameter of 3 mm (exp. 1 and 2), while the response time is 44 s with Pt-dish #1 and thermocouple

diameter of 1 mm (exp. 6). The difference of 39 % is due to the experimental conditions, further discussed in the following sections along with the effect of the sample (P/S alumina).

Qualitative Results

In the samples of secondary alumina some traces of agglomeration was observed for the samples heat treated at 800 °C, and the sample was a coherent agglomerate for the 900 and 1000 °C samples. The agglomerates disintegrated into a less free-flowing powder compared to the original powder sample, indicating some grain coarsening and phase transformation, later confirmed by XRD analysis. The samples of primary alumina showed no signs of agglomeration, and no $\gamma \rightarrow \alpha$ phase transformation (XRD). The thermocouple contact point in the samples treated at 900 and 1000 °C showed a yellow hue that may be due to traces of Ni impurity from the thermocouple.

The secondary alumina samples have a grey hue, mostly due to the content of carbon-dust, [110]. After heat treatment, the sample becomes increasingly white as a function of time and temperature, evidence of carbon combustion in air, to be further discussed later.

7.4.2 Effect of Experimental Conditions

Fig. 7.2 shows the temperature response curves for the experiments S1, S2 and S3, demonstrating the effect of the Pt-dish and thermocouple for the observed response time τ at constant temperature and using primary alumina samples. The greatest qualitative difference is obviously due to the thermocouple, while the greatest difference in the recorded response time is due to the Pt-dish. The recorded response times are presented in table 7.1.

The *thermocouple*, having cylinder geometry, is much more massive at a diameter of 3 mm compared to 1 mm, so that extra heat is provided since the thermocouple is pre-heated, and the larger thermocouple is more exposed to absorb radiated heat in the furnace. The heat dissipated through the larger diameter thermocouple is therefore reduced. Experiments S1 and S2 demonstrate this effect of the diameter of the thermocouple, which resulted in a difference in the response time of only 13 % (61 s *vs* 54 s) in favor of the smaller diameter. The qualitative difference of the temperature response

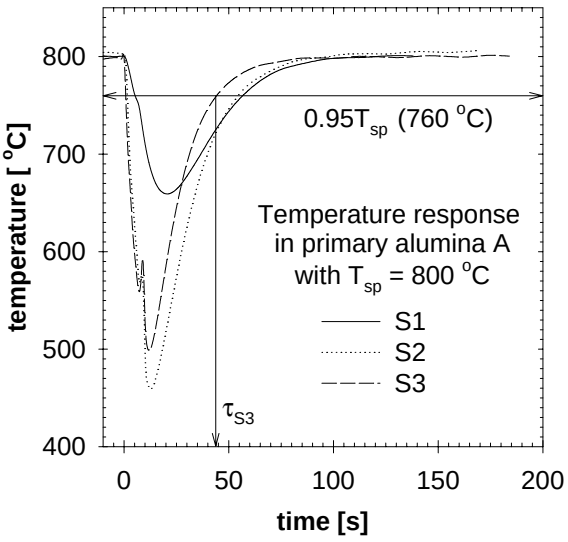

Figure 7.2: *Temperature response curves demonstrating the effect of the Pt-dish and thermocouple for the exp. S1, S2 and S3 (see table 7.1).*

curves is striking however, the larger diameter resulting in a much lower temperature (∼140 *vs.* 340 °) drop upon contact in the alumina sample.

The data in table 7.1 for exp. S2 and S3 shows the *effect of the Pt-dish* to result in a 23 % quicker response time for Pt-dish type # 1,2 compared to the old type Pt-dish #0. The projected area of dish # 1,2 is estimated as 19.5 cm^2 and as 13.7 cm^2 for the old type #0, while the exposed area of the alumina sample is very similar. By assuming the response time to be proportional to the exposed surface area, mainly due to heat radiation, (differing by +42 %) and inversely proportional to the sample weight - mainly the difference in mass of the Pt-dishes, (at -14 %), the total (product) difference, due to the Pt-dish type, could be expected to be about 22 % slower for dish #0, compared to #1 and 2. This estimate compares very well with the recorded difference of about 23 %.

The total difference in the recorded response time τ, of 39 %, due to the combined effect of thermocouple and Pt-dish, compares favorably with the total estimated (product) difference of ∼38 %, and is well within the estimated experimental error.

7.4.3 Effect of Alumina Quality and Temperature

The abrupt drop when the thermocouple contacts the alumina sample has been discussed, but the most striking difference in the temperature response curves of primary and secondary alumina A is the exothermal response attributed to the fluoride assisted $\gamma \rightarrow \alpha$ phase transition, see chapter 2, [38]. The response peak sharpens and occurs more quickly with increasing temperature, ref. figures 7.4, 7.5 and 7.6.

The effect of liquid phase fluoride "$NaAlF_4$" on the phase transformation kinetics of $\gamma \rightarrow \alpha$ in controlled alumina samples is studied in chapter 5. Significant phase transformation $\gamma \rightarrow \alpha$ and crystal growth requires liquid $NaAlF_4$. Apart from the thermal effects discussed for samples of primary and secondary alumina discussed in this chapter, the presence of $NaAlF_4$ will require additional heat of fusion for melting. Phase transformation results, ref. chapter 5, indicate that an increasing amount of $NaAlF_4$ added to the alumina leeds to a longer initiation period of melting and wetting of alumina by the added fluoride phase.

An estimate of the heat required for increasing levels of "$NaAlF_4$" fluoride phase may be obtained as follows. Thermodynamic data for the following reactions, [176];

$$\begin{aligned} Na_5Al_3F_{14}(s) &\rightleftharpoons 5NaF(l) + 3AlF_3(s) \qquad (7.3) \\ &\quad (\Delta H^\circ_{1000K} = 252kJ/mol) \\ NaF(l) + AlF_3(s) &\rightleftharpoons NaAlF_4(l) \qquad (7.4) \\ &\quad (\Delta H^\circ_{1000K} = 27kJ/mol) \end{aligned}$$

may be combined to find the equivalent of "heat of fusion" of $NaAlF_4$ as;

$$\frac{1}{5}Na_5Al_3F_{14}(s) + \frac{2}{5}AlF_3(s) \rightleftharpoons NaAlF_4(l), \quad \Delta H^\circ_{1000K} = 77.4kJmol^{-1} \qquad (7.5)$$

The $\Delta H^\circ_{fusion}(NaAlF_4)$, is thus approximately 7.4 J per wt % added to an alumina sample when converted to a wt % basis. Assuming the specific heat of alumina to be C_p=79 $JK^{-1}mol^{-1}$, the thermal effect of "$NaAlF_4$"-fusion is 48 °C for 5 wt % and 191 °C for 20 wt % $NaAlF_4$ additions respectively.

Below, a similar estimate of the thermal effect of the presence of carbon in secondary alumina samples is derived. The estimate predicts the heat released by carbon combustion to correspond to a temperature increase of

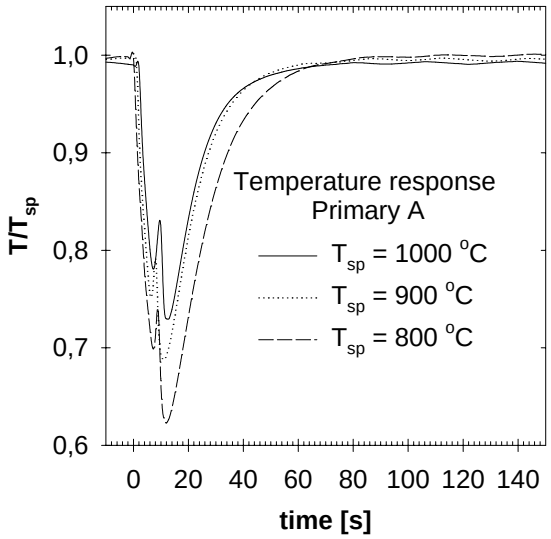

Figure 7.3: *Effect of temperature on the response curves for primary alumina A.*

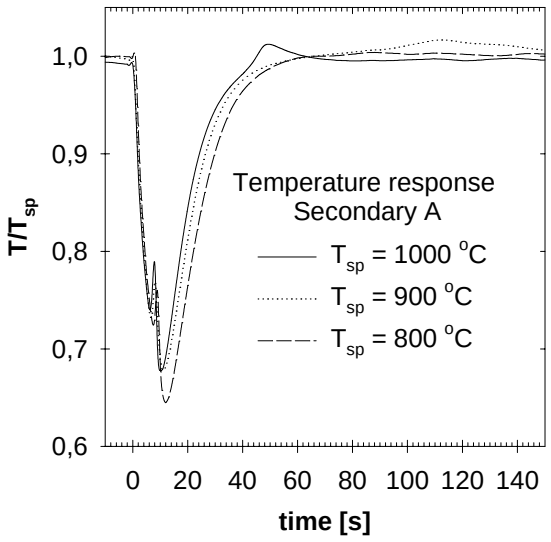

Figure 7.4: *Effect of temperature on the response curves for secondary alumina A.*

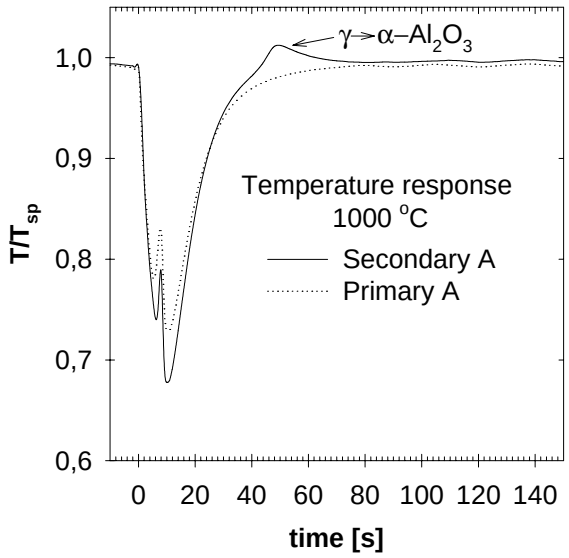

Figure 7.5: *Comparison of primary and secondary alumina A at 1000 °C. Exothermal peak attributed to $\gamma \rightarrow \alpha$ transformation.*

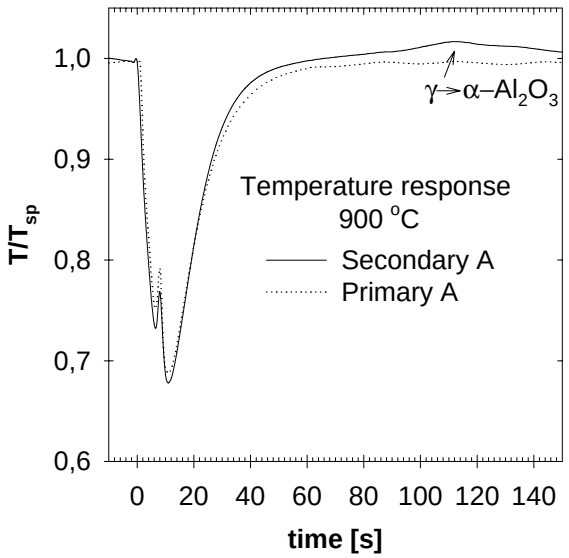

Figure 7.6: *Comparison of primary and secondary alumina A at 900 °C. Exothermal peak attributed to $\gamma \rightarrow \alpha$ transformation.*

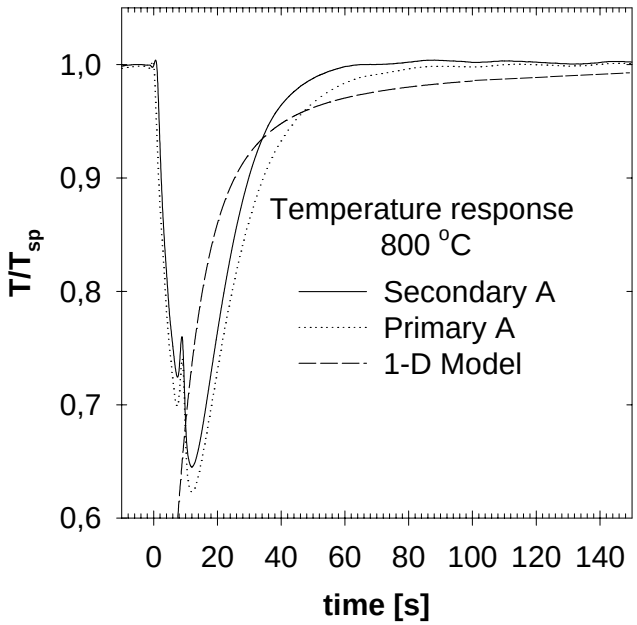

Figure 7.7: *Comparison of primary and secondary alumina A at 800 °C. No temperature effect of the $\gamma \rightarrow \alpha$ transformation is observed. The 1-D model response curve is plotted for comparison.*

about 400 °C assuming the same C_p of alumina as above. If we assume a proportional thermal effect of "$NaAlF_4$"-fusion on the temperature response time, τ could be expected to increase by 1-5 s in samples of primary alumina with added solid phase $NaAlF_4$.

Effect of Carbon Content

The data in table 7.1 shows a difference in the response time of primary and secondary alumina to be 9 s at 800 °C, being shorter for secondary alumina, and this difference is mainly attributed to the carbon content of the secondary alumina. The difference decreases to 3 s at 900 °C and only 1 s at 1000 °C, seemingly obeying an exponential decay type relation with increasing heat treatment temperature. Thus, the increased level of volatiles and effect of carbon combustion seems to be more important than the limited $\gamma \rightarrow \alpha$ transformation at the lower temperatures.

The shorter response time τ of secondary alumina is attributed to the effect of the *carbon content* in the secondary alumina sample. XRF results indicate a C-content of around 0.8 wt % in this quality (SA, ref. chapter 5). Carbon combustion occurs at temperatures over ∼400 °C by the reaction;

$$C + O_2 \rightarrow CO_2, \qquad \Delta G_f^{\circ}(CO_2) = -394kJ/mole$$

perhaps first via the formation of CO, since the oxygen air content is limited in the sample. By assuming the heat capacity of alumina to be 79 $JK^{-1}mol^{-1}$ and that 1 wt % carbon is equivalent to about 8 mole % of the secondary alumina sample, the available combustive heat could result in a ∼400 °C temperature increase in the sample, provided that the heat is not dissipated to the surroundings. The reaction is likely to be limited by mass transport of oxygen into the bulk sample. Kheiri *et al.* [82] found that an increasing carbon content of alumina explained the increased porosity of alumina-cryolite agglomerates that form upon addition of alumina to cryolitic melt.

Effect of Moisture Content

The transient peak occurring after 7 - 8 s in all the temperature response curves is probably due to the sudden release of moisture at above about 200 °C. The steam will increase the heat transport in the sample, but may also form a momentary barrier layer on the thermocouple. The effect of *moisture and dehydration* kinetics of alumina is complex, and further discussed in chapter 8. The loss of moisture is likely to be chaotic when the temperature is increased rapidly. Furthermore, the moisture content will ensure a local temperature of ∼100 °C until the physisorbed water is evaporated. A temperature shock may result as the sample suddenly becomes "dry", and moisture trapped in micro-pores will probably induce cracking and rupture of the alumina grains [107].

Lossius [110] found that dehydration caused the greatest weight loss in secondary alumina samples. Combined MOI and LOI for primary alumina A is 1.61 wt %, ref. chapter 5, and the moisture content of the secondary alumina may be[1] another 1.0 wt % or so. Secondary alumina contains adsorbed

[1]Data for weight loss obtained in chapter 4 by drying samples of primary and secondary alumina over night at 200 °C giving 0.4 ± 0.1 wt % for primary and 1.3 ± 0.1 wt % for secondary alumina A respectively.

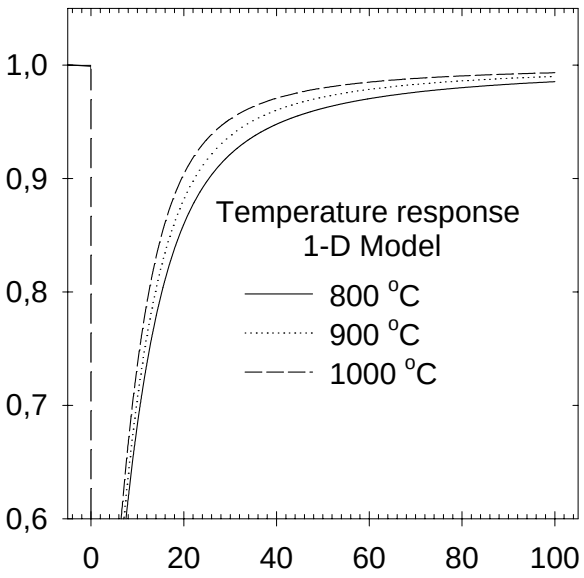

Figure 7.8: *1-D model response curves. A simple physical model assuming one -dimensional thermal conductivity and radiation was assumed, see details in text.*

fluorides that catalyze the $\gamma \rightarrow \alpha$ transformation, which results in the loss of surface area - and more hydroxylated moisture at higher temperatures, when the samples also tend to agglomerate, ref. chapter 5 and Appendix B. As discussed in chapters 5 and 8, moisture also has the potential to react, with for instance fluorides, by hydrolisis.

7.4.4 1-D Model Fit

Fig. 7.8 shows the simulated temperature response obtained by the 1-D Model. The model may give quite accurate response times: τ_{800}= 41 s, τ_{900}= 34 s and τ_{1000}= 29 s. Within a reasonable range of the parameter data used in the model, the greatest effect on τ is caused by varying the sample emissivity. The emissivity of a radiating black-body is 1.0 by definition, and decreases for increasing body reflectivity. The results shown in figure 7.8 were obtained by setting the alumina emissivity as 0.2. This number is

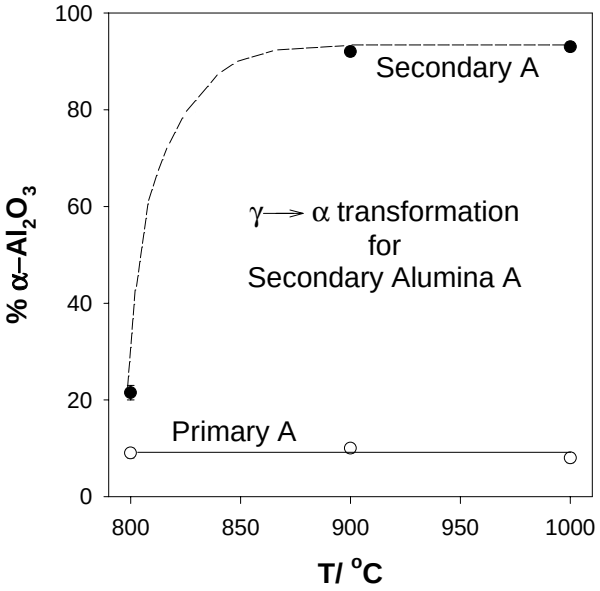

Figure 7.9: *XRD results of samples after temperature response times were measured. Samples held 10 min at temp. Trend line for the secondary samples intended only to aid the eye.*

on the low side of that assumed for crust by Rye *et al.* [153, 152], but is quite reasonable given that is the only fitted parameter in the model. The effect of the absorbed heat by radiation to the sample is confirmed to be important, however.

The rather poor curve fit is evident in figure 7.7, and this is probably due to convection and thermal events in the sample that are not accounted for in the model. The desorption of moisture is probably the dominant endothermal reaction at lower temperature, 100 $°C < T < 400°C$, [110, 156]. The oxidation of carbon is probably dominant at intermediate temperature, ($400°C < T < 800°C$) while the fluoride assisted $\gamma \rightarrow \alpha$ phase transition produces an exothermal peak for higher temperatures, evident in the temperature response curves for $T \geq 900$°C. The model fit cannot be expected to improve without incorporating these effects into the model.

7.4.5 XRD Characterization

Results are shown in fig. 7.9 to support the identification of the exothermal peaks, evident in figures 7.5 and 7.6, to be due to the $\gamma \rightarrow \alpha$ phase transition. The relative standard error of the determined α-Al_2O_3 phase content (duplicate samples) is less than $\pm$ 1.5 % for all samples. The α-Al_2O_3 content in the secondary alumina samples (with a nominal F-content of 1-2 wt %) is 22$\pm$1 % after 10 min at 800 °C, in good agreement with the results obtained in chapter 5 and in the literature [127, 89, 44]. The results for 900 and 1000 °C are identical at 92$\pm$1 %. The lack of full transformation may be due to the loss of HF from the samples, [59, 158].

7.4.6 Suggestions for Further Work

Temperature response measurements in samples with carbon dust (powder) added to primary alumina should be conducted. As indicated by this study, for secondary alumina, the presence of C will probably result in a faster heating response above ~400 °C in the sample, due to the combustion of C in air.

Temperature response measurements in samples with added "$NaAlF_4$" powder to primary alumina could also be conducted in order to verify the effect of the heat of fusion of the added fluoride phase. Results in chapter 5 indicate that increasing amounts of $NaAlF_4$ leeds to a longer initiation period of melting and wetting of alumina by the added fluoride phase. Thermal response experiments for added fluoride phase would be expected to show slower response time τ, but also perhaps an increased exothermal response around 800 °C, corresponding to increased phase transformation and coarsening of the microstructure.

7.5 Conclusion

The temperature response time is defined as the time at which the sample temperature is at 95 % of the furnace temperature. With reference to the primary motivation for the work reported here, the temperature response time is determined to vary from 30 - 50 s. The results are relevant as the same samples and Pt-dishes are used for the tablet agglomerate study reported in chapter 5. The response time varies depending on the furnace

temperature and sample quality (primary/secondary), and the shortest response time τ recorded is 31±2 s, for secondary alumina at 1000 °C.

The effect of the carbon content, fluorides and increased levels of moisture in secondary alumina is discussed as the reason why secondary alumina samples have shorter response times, in particular at lower temperature. The carbon content may be important for the dissolution behavior of secondary alumina. This study indicates that, for secondary alumina, the presence of carbon dust will probably result in a faster heating response over ∼400 °C due to carbon combustion in air. However, the effect of C in this study is confounded with effects of F and increased levels of moisture compared to primary alumina A.

Acknowledgement Asbjørn Solheim is acknowledged for helpful discussions and implementing the 1-D model in an Excel spread-sheet.

Chapter 8

Dynamic Moisture Content of Alumina

8.1 Motivation

The moisture content of smelter grade alumina (SGA) influences the fluoride emissions from the Hall-Héroult process by reacting with bath fluorides to produce volatile hydrogen fluoride. Most of the fluorides are recovered in the dry scrubbing process in which (primary) SGA acts as the absorbant and reacted dry scrubber (secondary) SGA is fed to the electrolysis cells.

The moisture and volatiles content in SGA is also known to be beneficial for the dissolution process. However, an excess of moisture may give unwanted entrainment of alumina upon addition, producing what is known as a "volcano-" or "geyser-" effect.

A study of water absorption and desorption kinetics in SGA is also relevant for the agglomeration kinetics, which is the main focus of the present study, ref. chapter 5. The dynamic moisture content of SGA under normal laboratory and industry feeding conditions is the main motivation for the work described here.

8.2 Background

Smelter grade alumina (SGA) contains residual water from the calcination of $Al(OH)_3$ [200]. Residual $Al(OH)_3$ is unacceptable to most smelters,

though traces of the hydrate are not uncommon, especially in fines from the alumina refineries' electrostatic precipitators (ESP-dust). SGA has a large capacity to absorb moisture in the porous structure, and may act as a desiccator. Surface hydroxyl (OH-)groups are also associated to the transitional crystallographic phases of calcined alumina, which have complex surface structures and are catalytically active [119], while OH- groups may also adsorb at the highly ordered crystal faces of corundum [123].

There is still some controversy regarding what part the hydroxyl groups and moisture play in the transition aluminas crystallographic phase structures, in particular the cubic spinel types of γ-,η- and ρ-Al_2O_3. It may be argued that hydroxyl groups are only a part of the surface structure of transition aluminas, having a range of defect cation vacancy sites explaining some features of porosity and limitations in surface areas [167, 206]. The role of H_2O as a surface stabilizer for nano-crystalline alumina (both γ- and α-Al_2O_3) is fairly well established [117, 119]. Hydrogen has also been suggested to be a component of the bulk structure of the spinel-type transition aluminas. Sohlberg, Pennycook and Pantelides [166] favor the latter view and conclude that the transition aluminas γ-,η- and ρ-Al_2O_3 are a group of hydrogen spinels, with a propensity for absorbing dissociated water while maintaining stoichiometry and charge neutrality.

SGA is used as the absorber in the dry scrubbing process to remove the harmful hydrogen fluoride emission from the smelters. It is thus required to have a relatively high specific surface area, in the range of 60-80 m^2/g, as measured by the BET nitrogen adsorption method. SGA may in fact absorb in excess of 20 wt % water at RT without appearing moist or noticeably altering its flowability [168], but will also desorb water when the ambient becomes relatively less humid. SGA is in near quasi-equilibrium with the ambient surroundings. Secondary (reacted, dry scrubber) SGA contains fluorides, both gaseous "HF" and particulate "$NaAlF_4$", along with carbon dust, adsorbed sulphuric oxides and other volatile impurities such as phosphorous - and increased levels of moisture, see analysis results in chapter 5 [176].

8.2.1 Moisture in the Hall-Héroult Process

A discussion of the available literature on the detrimental effects of water and other impurities to the Hall-Héroult process is given in the monographs

by Grjotheim *et al.* and Thonstad *et al.* [49, 176]. It may be concluded that the primary concerns regarding moisture are;

- The reaction with the electrolyte to produce HF
- The possible hydrogen contamination of the aluminium metal product
- A slight reduction of the current efficiency

Direct contact between water and electrolyte is very hazardous due to the explosive evaporation reaction. The moisture content of SGA is normally determined as the sample weight loss upon heating within a specified temperature range. The "loss on ignition" (LOI) is determined from the sample weight loss between 300 °C and 1000 °C [70]. LOI is sometimes referred to as LOI_{1000}, LOI_{1100} or LOI_{1200} in analysis reports depending on the upper temperature used, and this makes a direct comparison more difficult. The "moisture on ignition" (MOI), sometimes denoted LOI_{300}, is the weight loss determined between room temperature (RT) and 300 °C, [69]. It is noted in the ISO standards that the alumina sample is sensitive to the ambient conditions of the storage facility, transportation and analysis in the temperature interval of RT and 100 °C, [69, 70].

Effect on Handling Properties

Though very high moisture contents up to 20-25 wt % does not appear to change the flowability or appearance of SGA, lower levels may influence its handling properties. In particular, as studied by Davies and Mercer [22], moisture will affect the unpacked bulk density (UPBD), flowability (sometimes measured as the flow funnel time) and the degree of particle break-down (attrition index, AI) of the alumina. Fresh, calcined (kiln) SGA was reported to be highly charged, resisting flowability through a fairly coarse mesh, but the flowability improved after exposure to air [22]. In that study, the LOI_{300} increased from 0 to 3 wt % after 180 min exposure to ambient air, while the LOI_{1000} remained essentially constant at around 1 wt %.

Hartman [53] argues that the platelike morphology of α-alumina grown in fluxes may be due to the fact that anions (alumina-flux complexes) will preferentially adsorb on the {0001} planes since these are terminated by Al cations. Growth involving adsorption of an intermediate anion will therefore

involve increased growth rate on the other crystal planes - and the exposed {0001} planes will dominate the crystal habit (preferred shape).

It seems likely that a majority of surfaces in calcined aluminium hydrate (SGA) may thus be terminated by Al cations also, since an excess of hydroxide is present and probably involved in the growth process of the α-alumina phase from the transition alumina matrix [200]. Al cations may also be expected to be available in the many crystal defects in SGA due to OH-desorption and pore formation. Surface termination by Al cations should thus result in a positive surface charge on SGA, which could explain the observations by Davies and Mercer. Exposure to ambient air, containing moisture, will result in the adsorption of OH- thus neutralizing the surface charge so that SGA becomes free flowing. However, even moisture adsorption on α-alumina is very complex, as has been studied using atomistic simulation techniques [23]. That study confirmed the Al-terminated {0001} surface to be the most stable non-hydroxylated surface - with preferential OH-adsorption, and also demonstrated a very flat physisorption of water. Both physisorption and hydroxylation of all the surfaces studied was energetically favorable. It may be expected that physisorption will be followed by chemisorption (hydroxylation), since hydroxylation energies are always higher.

Since alumina is a dielectric material (electrical insulator), relative movement may cause so-called tribocharging on the SGA particle surfaces. Large voltages may thus build up during handling of SGA, [139]. Moisture may provide some electrical conductivity, so that the charge may dissipate rather easily in ambient air - but not in dry storage facilities. The effect of tribocharging may easily be observed in the laboratory during handling of SGA, especially if a small amount of alumina powder is poured from a large plastic container onto an electrical insulator material, such as paper. But, its influence on handling properties, and in particular dusting, needs further research [130].

It seems rather obvious that the unpacked bulk density of alumina is a function of the density of SGA grains (agglomerates) and the loose packing fraction of such particles. However, as discussed by Kong and Lanutti [88], the effect of the particle size distribution is quite complex. Theoretically, a rather wide particle size distribution (PSD) will result in the highest packing density, if adequate mixing energy is provided. However - fines will decrease the loose packing density due to particle bridging effects [88], which are probably affected by the moisture content and “gas-like” behavior

of the fines fraction.

Though the exact mechanism is not known, electrostatic interactions (depending in part on the SGA's moisture content), may also explain the observed correlation between the dustiness of SGA and the LOI. The effect of LOI on dusting is of the same order of magnitude as the SGA's content of fines ($\leq$44 μm) and super-fines ($\leq$20 μm) [9, 130]. Dusting in pot rooms is a complex issue involving other materials also, such as anode dust - and bath-containing top-cover material [122].

Moisture and Fluoride Emissions

Fluoride emissions from Hall Héroult electrolysis cells are affected by moisture since it will react with electrolyte fluorides to produce volatile hydrogen fluoride (HF), see [49, 176, 135]. The *hydrolysis* of the cryolitic melt containing "NaF, AlF_3, $NaAlF_4$ and Na_3AlF_6" may occur by the following reactions;

$$3H_2O_{(g)} + 2Na_3AlF_6 = Al_2O_3 + 6NaF + 6HF_{(g)} \quad (8.1)$$
$$(\Delta G = +187kJ/mol)$$

$$3H_2O_{(g)} + 2AlF_3 = Al_2O_3 + 6HF_{(g)} \quad (8.2)$$
$$(\Delta G = -19kJ/mol)$$

$$3H_2O_{(g)} + 3AlF_3 + 3NaF = Al_2O_3 + Na_3AlF_6 + 6HF_{(g)} \quad (8.3)$$
$$(\Delta G = -282kJ/mol)$$

The ΔG values stated above are all for 900 °C and calculated using HSC software with JANAF data. The heat of formation of cryolite should probably be subtracted from the last equation stated above, in which 3(NaF+AlF_3) is used in stead of 3$NaAlF_4$, and this would roughly halv the negative ΔG value [176]. The fluoride species present in the melt is still a matter of debate, chapter 2.

The considerable discharge of gaseous HF from the electrolysis cells by the hydrolysis reactions above must be adsorbed on the primary alumina particles in the dry scrubbing process for environmental reasons and most of the fluorides lost as HF are thus also recovered. Surface hydroxyl groups has been concluded to be the preferred adsorption sites for HF on SGA in the dry scrubbing process, [56], probably by providing hydrogen bonding sites to the HF. Adsorbed HF is not released before the reacted alumina

reaches 700 °C [67, 56]. A hydrogen "mass balance" may be expected as an equilibrium of HF and H_2O is established.

An XPS study on laboratory hydro-fluorinated samples, conducted by Hyland and Haverkamp *et al.* [67, 56], showed initial F surface concentrations of 13 % (in % of full coverage). No desorption of F was recorded even after 3 h exposure at 200 °C. 33 % of the initial F coverage was desorbed after 1 h exposure at 500 °C and 72 % after 1 h at 700 °C. A sample of dry scrubber alumina was concluded to be significantly different to the laboratory samples, with 18 % of the initial F coverage desorbed after 3 h at 200 °C, 68 % after 1 h at 500 °C and 82 % after 1 h at 700 °C. The secondary alumina contained $NaAlF_4$, assumed to be responsible for the trace Al-F bonding and some evidence of Na-F bonding.

Further results of the XPS study showed that nearly 45 % surface coverage of F was achieved with dried alumina (12 h at 300 °C) and dry HF, but only in excess of 10 % was achieved for undried alumina with wet or dry HF, [56]. No desorption of F was observed after samples were annealed for 1 h at 500 °C, while less than 50 % of the initial coverage of F remained after 1 h at 700 °C. Only trace amounts (about 1 %) of surface adsorbed F remained after 1 h exposure at 1000 °C for the former sample, in which a 45 % surface coverage of F had been achieved. While the study showed some evidence of AlF_3 formation (during dry alumina adsorption of HF), and some Na-F bonding, the study supports the mechanism of HF-OH bonding.

Haverkamp *et al.* [59] studied the influence of controlled fluorination of SGA on alumina dissolution and compared the results obtained to those for secondary alumina. Reacted dry scrubber alumina was concluded to dissolve 30-40 % faster than primary SGA. The laboratory samples were fluorinated by streaming HF/N_2, $HF/H_2O/N_2$ or $NaAlF_4/N_2$ mixtures through a bed of SGA. These samples showed insignificant change in dissolution behavior compared to untreated SGA, even though the fluoride content of the samples was positively correlated with MOI and LOI. Laboratory samples were thus concluded to be significantly different from dry scrubber alumina.

Gillespie *et al.* [41] also studied laboratory prepared samples of SGA (hydro-fluorinated) and revealed by XRD and SEM that the process of aging the hydro-fluorinated samples in moist air at RT resulted in some crystallization on the surface of SGA. XPS spectra and MAS-NMR data supported the formation of a disordered aluminium hydroxy-fluoride layer after the laboratory fluorination. DSC showed (weight) loss of water between 100 and 440 °C and that F losses started above 440 °C. Dehydration of the

underlying (substrate) SGA occurred above 540 °C.

Hyland *et al.* [66] measured water isotherms in SGA at 20, 40 and 50 °C and concluded that at these temperatures the moisture content in the alumina is primarily a function of RH. Initial changes of the moisture content in the alumina samples were observed to be in excess of 0.03 wt %/min, and in one case changed by 1.3 wt % in 10 min.

Effect on Dissolution Kinetics

The content of water (and other volatiles) in SGA is known to be beneficial for the *dissolution process* up to a level of approximately 1 wt % [7, 59]. However, an excess of moisture may give entrainment of alumina upon addition, producing a "volcano"- or"geyser"- effect which may lead to alumina feeding problems as a mound of partly recrystallized (and "sintered") SGA may form [3]. A "plugged" feeder hole may result where the alumina charge is no longer effectively fed as a free flowing powder but as lumps. Such lumps have inadequate dissolution and distribution rates causing bottom sludge, interruptions of the cell current distribution, and low alumina concentrations in the electrolyte [120]. The formation of agglomerates is the subject of this study and is relevant for the process of the formation of the above-mentioned plugged feeder holes also.

The evolution of moisture from SGA upon interaction with the electrolyte is rather complex, a function both of temperature and structural rearrangement in the alumina, see chapters 2,4 and 5. The basic principle of steam formation and explosive expansion is the driving force for alumina fluidization and disruption of agglomerates.

Trapped air, initially at atmospheric pressure p_{atm} within pores will, by assuming ideal gas $pV = nRT$ during heating to about 1000 °C, have a pressure of $p_f \sim 4p_{atm}$. We may also assume that the alumina contains 1-2 wt % water, and this may be shown by a similar argument to give an additional 10-fold increase ($p_f \sim 69p_{atm}$) in the internal pressure of an alumina agglomerate/ particle! The (explosive) discharge of this pressurized water vapor will give rise to a considerable convection within alumina agglomerates submerged in the electrolyte. The release of moisture must explain the rapid convective heat transport observed above ∼200 °C in the T *vs.* t measurements in chapter 4.

Studying high alumina refractory castables, Innocentini *et al.* [68] recently reported that water may be released as steam in a controlled manner for low

heating rates (1 °C/min) but a clear transition to chaotic release occurs as the heating rate is increased to 5 °C/min, or higher. This was attributed to moisture and steam being trapped in pores. The same study concluded from thermal analysis that endothermal boiling of water may result in thermal shock, and hence cracking. This finding is probably also valid for SGA upon addition to cryolitic melts, in which heating rates may exceed 2000 °C/min, see chapter 7.

Liu *et al.* showed evidence to support the assumption that violent desorption of moisture from modern SGA causes individual alumina grains to shatter [106, 107]. This will presumably occur for SGA in addition to the fluidization of alumina powder undergoing rapid heating and moisture/ steam desorption.

Moisture and Agglomeration

Water absorption and desorption kinetics in SGA is also directly relevant for the study of *agglomeration kinetics*, and this is the main motivation for the work described here, see chapters 4 and 5. A partial pressure of water is known to affect the mass transport rate of alumina during sintering, see chapter 2, and may affect the thermal response upon heating, in addition to the other effects relevant for alumina dissolution as previously described. In conclusion, a study of the moisture content dynamics of SGA is, therefore, highly relevant in a contribution to attempt to understand the alumina dissolution process.

8.3 Experimental

A two-part experimental approach was chosen. By placing alumina samples in a fan-regulated oven, a series of *controlled temperature* recordings were made. Desorption kinetics are quite fast as the oven heats up rapidly to 100 °C. However, the cooling rate in the oven and sample is quite slow, so a different *rapid absorption* experiment was performed.

8.3.1 Controlled Temperature

The moisture desorption and adsorption kinetics is studied by gravimetric analysis, the weight change simply being ascribed to water. Samples are

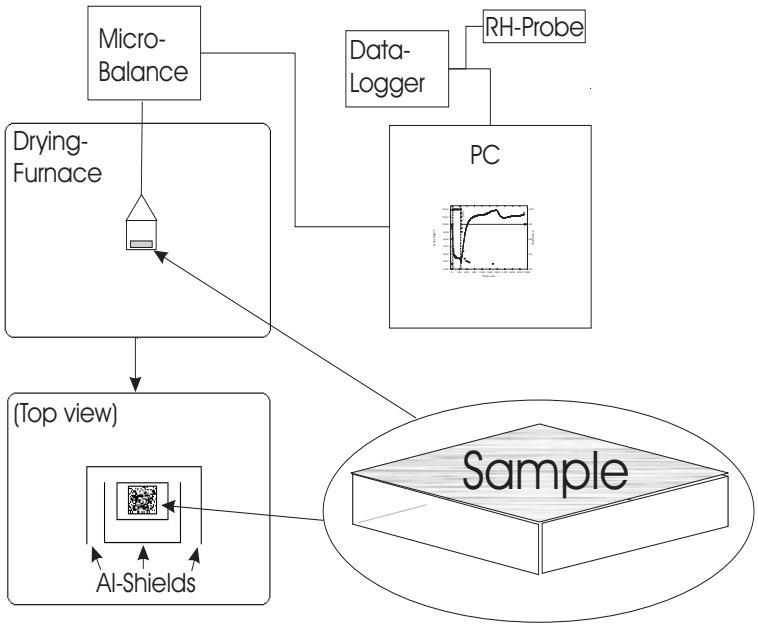

Figure 8.1: *Schematic of the experimental set-up used.*

prepared by pouring alumina into a small open aluminium box container measuring $62 \times 62 \times 7$ mm^3. The box was made from a 0.5 mm plate and the sides of the open box was sealed by two-component, heat resistant, glue (Araldit). The alumina sample is scraped flush with the container using a plastic card, thus presenting a well defined, flat surface. The sample is then set in the aluminium sample holder which is suspended through a small hole from the fine analysis balance (Mettler AT200) mounted on top of the furnace. The furnace door is closed after the sample is emplaced having attained equilibrium with the ambient.

The experimental setup is shown in figure 8.1, and the experimental procedure is described in table 8.1. The room temperature (RT) and relative humidity (RH) is monitored using a Vaisala HMP 35E probe and Vaisala HMI 38 data logger with display. The RH was not under direct control, but we aimed for a high/ low level of RH, conducting the low RH-level experiments during a period of fine, stable and relatively cold (sub-zero °C) high pressure weather conditions. The ambient of the room in which the

Table 8.1: Experimental Procedure of Controlled Temperature Program

1	Micro-balance set-up and calibration
2	Sample preparation and placement
3	Start data collection, 10- 15 min stabilization ($t=t_0$)
4	Heat-up to 100 °C with approx 6 hrs holding time
5	Cool-down to RT with at least 12 hrs holding time ($t=t_1$)
6	Stop data collection

experiments were conducted are controlled by the ambient outside the building. The "high" RH- level experiments were conducted during less stable weather conditions, and also using a simple air moisturizer to ensure that the RH-level was always above 12 % of saturation. This RH level is, however, much lower than that which may be expected during summer, even in Norway. Indeed – a RH of close to 100 % may be expected in many parts of the world.

The drying oven (Termax) is fan-regulated and, in order to minimize the disturbance of the forced air circulation, a shielding was constructed from Al-plates (figure 8.1) and the inlet valve on the furnace was fixed to mid-range (5 on a scale of 1 to 10). A steady aerodynamic lift on the sample was observed during the experiments when the fan was turned on before every experiment, and some of the sample data showed a small negative response peak, again indicating some aerodynamic lift, when the temperature was set back to RT on the temperature controller. The sample weight data was logged every minute, while the RH/RT data was logged every 30 minutes.

Temperature Control

The furnace attained 100 °C within 15 min, but the temperature response from 100 °C back to RT was much slower, shown in figure 8.2, approaching RT after 5 h. The samples were run through a semi-randomized data collection program according to the data collection cycle described in table 8.1. Every experiment was run through the same temperature program, and at the same time of day, in order to minimize the possible effects of fluctuations in the ambient and the building ventilation.

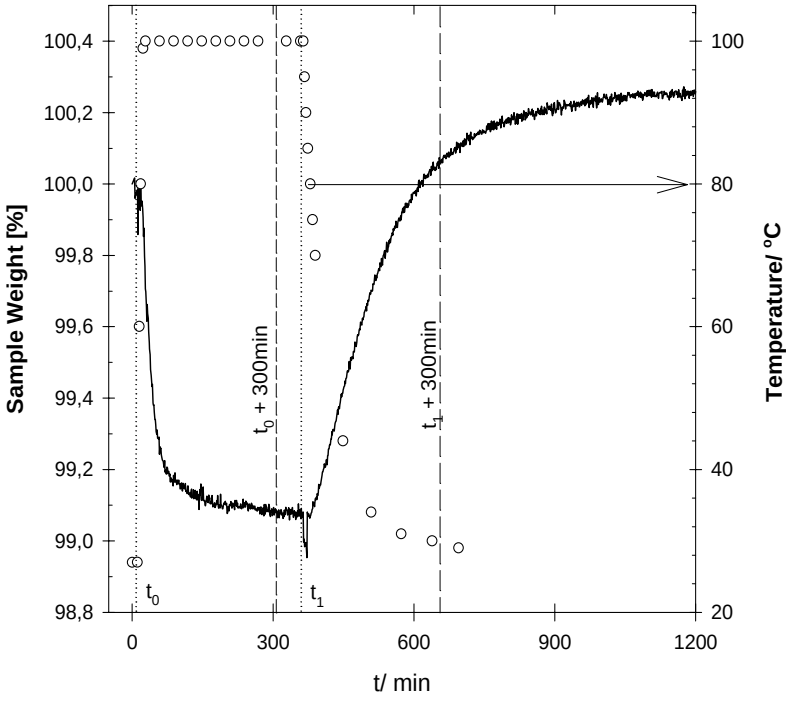

Figure 8.2: *The weight change of a sample of secondary alumina A as a function of the temperature program. The figure shows the defined time values t_0 and t_1, as used for the data analysis for each response curve, further described in the text.*

The initial sample weight, M_0 (i. e. the first recorded), is defined as 100 %. After the temperature is set to 100 °C, at t_0, there is initially a rapid weight loss in the sample until a minimum is approached after approximately 1 h. The initial maximum weight loss data are obtained from the best linear fit (by the method of least sum of squares) of 10 points for each sample.

The time at which the temperature is set to 100 °C is defined as t_0, and the local average after 300 min at 100 °C (really t_0+ 300 min), is taken

as the minimum value, M_{min}. The time at which the temperature is set back to RT is defined as t_1, and the weight gain at t_1+ 300 min compared to M_{min} is taken as the maximum value, M_{max}. The M_{min} and M_{max} data thus obtained are plotted against the average RH measured during the 300 min time periods. The effect on the sample weight as a function of the temperature program is shown in figure 8.2, and t_0 and t_1 are defined by dashed vertical lines.

8.3.2 Rapid Absorption

In order to obtain a measure of the instantaneous water absorption kinetics a different set-up was used. This data is most relevant for discussions of the sample preparation method in chapter 5, since we find that the sample's moisture content influences the "Agglomeration" results obtained in that study.

For this experiment 3 different sample holders were used, thus measuring each of the two relevant sample configurations used in chapter 5, in addition to the Al- box used for the controlled experiments here. Moisture absorption kinetics may be expected to be a function of the sample container, geometry and sample mass. The samples were preheated to T_{sp} = 150 °C since that was the maximum possible for the current set-up.

Two 1.32 g alumina samples where prepared in shallow Pt-dishes, of ID = 33 mm, and mass of 9.0 g, i. e. of the same type as used for the "agglomeration" tablet samples of this study, see chapter 5. Furthermore, 2 alumina samples (16.04 g and 14.06 g) were prepared as loose cone shaped piles, in flat bottom glass dishes of 53.49 g and 53.09 g respectively. The cone of alumina powder was naturally determined by the angle of repose of the alumina. Finally, the Al-box as described above was used.

After more than 3 h the samples are removed successively from the oven and placed on the micro-balance in ambient air. The sequence of removing samples was alternated according to the sample holder type in order to minimize systematic error. The manual transfer of the sample, including the operation of opening and closing the furnace door, was completed within about 5 to 10 s. The first data point was thus recorded about 5-10 s after the sample was removed from the drying oven. The weight data was subsequently logged every minute as for the controlled temperature experiments. All SGA samples were of primary type A. The maximum initial

weight gain per minute was determined from a linear fit of the first 3 data points, while the final data point collected after 15 min was taken as the maximum weight.

8.4 Results and Discussion

Generally the results obtained show good reproducibility and qualitative consistency. Typical (long term) examples are shown in figures 8.3 and 8.4 for the set-up with a controlled sample temperature, as shown in figure 8.1.

8.4.1 Controlled Temperature

Initially, the samples show a slight but steady weight gain when exposed to air, and most of the samples tend to absorb moisture compared to the initial content. This may be expected since the alumina samples were collected under different ambient conditions, most likely at a higher temperature and relatively low moisture content. It appears as though even a very low RH level of approximately 12 % at RT is sufficient for the sample to absorb moisture to a level surpassing that of the starting weight (at 100 %). Figures 8.3 and 8.4 show that, for longer holding times at RT, the sample weight is strongly correlated with fluctuations in RH, a change in RH of 10 %-points leads to a weight change of about 0.2 %-points for alumina A.

A steady aerodynamic lift on the sample was observed when the fan was turned on before the oven temperature was set to 100 °C. The maximum weight loss is observed during the first 15 min or so after the oven has attained 100 °C, and after about 5 h the sample weight approaches the minimum value recorded, M_{min}. Observations of a few long term samples, ref. figs. 8.3 and 8.4, indicated that the sample weight attains the true minimum only after more than 12 h at this temperature. After the heater in the furnace was turned off, at t_1, the samples reattained RT, for t>1200 min during the data collection cycle.

Desorption Kinetics

The desorption kinetics data for the samples are denoted in table 8.3 according to alumina quality and experiment, for example, SA-1L is [S:secondary][alumina

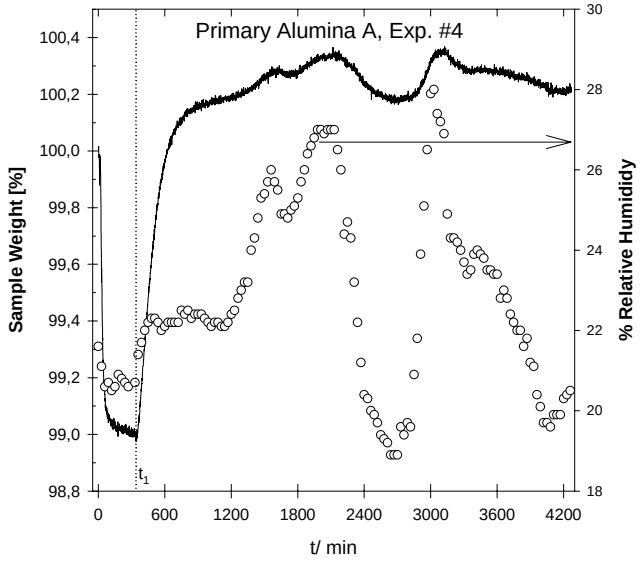

Figure 8.3: *The weight change of a sample of primary alumina A as a function of the temperature program and ambient relative humidity.*

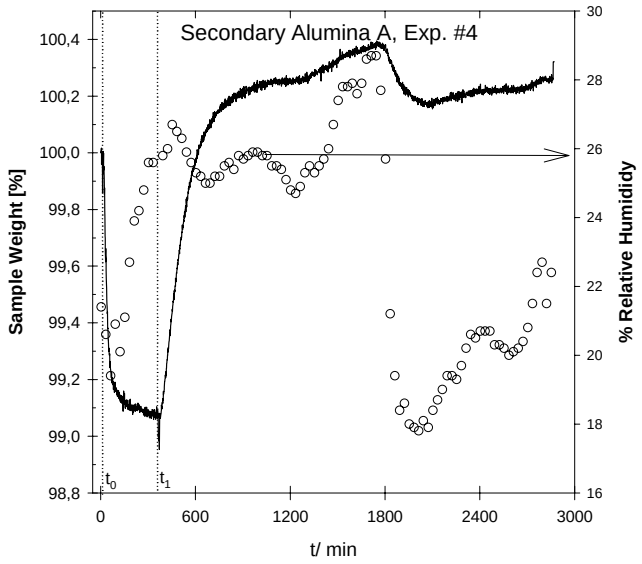

Figure 8.4: *The weight change of a sample of secondary alumina A as a function of the temperature program and ambient relative humidity.*

Table 8.2: *Desorption Kinetics Data: Samples are denoted in the table according to alumina quality and experiment, as explained in text.* ΔM_{max} *is the maximum rate of the weight loss determined as a linear fit over at least 10 measurements, the statistical coefficient* R^2 *is close to 1, indicating an adequate fit.*

Sample	M_0 [g]	RH [%]	M_{min}-M_0 [%]	ΔM_{max} [%/min]	R^2
SA-1L	22.91	12	-0.96	-0.021	0.97
SA-2L	22.50	8	-1.07	-0.025	0.99
SA-3H	26.37	12	-0.89	-0.025	0.92
SA-4H	27.14	21	-0.92	-0.026	0.93
Average	24.73		-0.96	-0.024	
PA-1L	26.18	9.5	-0.98	-0.038	0.99
PA-2L	26.39	8.5	-0.97	-0.038	0.90
PA-3H	26.32	12.5	-0.98	-0.040	0.99
PA-4H	26.49	21	-0.98	-0.037	0.91
Average	26.35		-0.98	-0.038	
PB-1L	26.89	7	-0.55	-0.013	0.76
PB-2L	26.68	9	-0.57	-0.018	0.86
Average	26.79		-0.56	-0.016	

quality:A] - [experiment nr.1] [L:low level of relative humidity].

M_0 is the starting weight of the sample, M_{min}-M_0 is the weight difference between the starting weight and the sample weight determined 300 min after the temperature was adjusted to 100 °C. ΔM_{max} is the maximum rate of the weight loss determined as a linear fit over at least 10 measurements, while the statistical coefficient R^2 is close to 1 for most samples, indicating an adequate fit. Desorption data for the alumina samples are presented in table 8.2 and in figures 8.6 and 8.5. There is no significant dependence on RH, but markedly slower kinetics for the secondary alumina A compared to primary alumina A. Primary alumina B shows the slowest desorption kinetics, - indicating a low adsorbed moisture content or a strong affinity to adsorbed water. The total weight loss M_{min} is 0.56 wt % for alumina B compared to 0.98 wt % for alumina A. The difference between primary and secondary SGA A is apparently no longer significant for the total weight loss, M_{min} determined at t_0+300 min, see fig. 8.6.

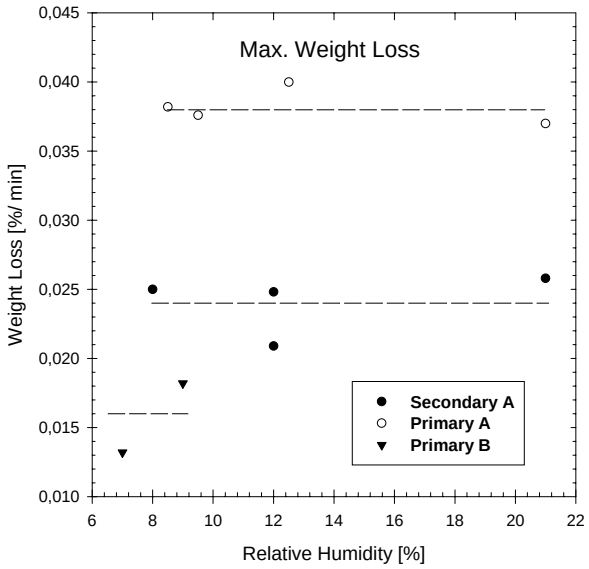

Figure 8.5: *Max. rate of wt loss of samples determined by linear regression of 10 data points, after furnace set-temp. was adjusted to 100 °C (t_0) from RT.*

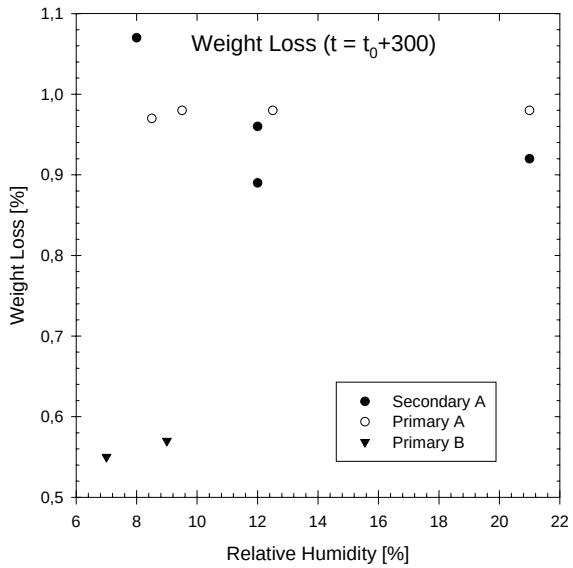

Figure 8.6: *The maximum weight loss of all samples taken 300 min after the furnace set- temperature was set to 100 °C.*

Table 8.3: *Absorption Kinetics Data: Samples are denoted as for table 8.2.* ΔM_{max} *is the maximum rate of the weight gain determined as a linear fit over at least 50 measurements.*

Sample	RH [%]	M_{max}-M_{min} [%]	ΔM_max [%/min]	R^2
SA-1L	8	0.34	0.0030	0.98
SA-2L	11	0.80	0.0037	0.99
SA-3H	13	0.86	0.0035	0.99
SA-4H	25	1.00	0.0054	1.00
PA-1L	10	0.59	0.0033	0.85
PA-2L	9.5	0.53	0.0033	0.99
PA-3H	13	0.81	0.0040	0.99
PA-4H	22	1.00	0.0053	1.00
PB-1L	7	0.55	0.0023	1.00
PB-2L	14	0.78	0.0039	0.99

Available LOI data[1] for the samples also show that alumina B has a considerably lower MOI content, at 0.16 % by weight, compared to alumina A, at 0.83 %. The slow kinetics we observe here may thus in part be due to the lower moisture content of those samples, but the micro- and pore- structure is also thought to be important which, in part at least, must account for the lower moisture content in the first place.

The observation here that data for primary and secondary alumina A show no significant difference in M_{min}, but considerably slower initial desorption for the secondary quality is surprising. The weight loss of secondary alumina should tend to be higher following the dry scrubber process, since that process will increase the levels of moisture as well as fluorides, and other volatiles in the alumina[2]. The increased affinity to moisture demonstrated by secondary alumina A initially may probably be attributed to the content of HF, since HF is known to bond relatively strongly to OH-groups [41].

Absorption Kinetics

Absorption kinetics data are presented in table 8.3, where the samples studied are denoted as for table 8.2. M_{max}-M_{min} is the weight difference between the relative minimum weight of the sample as defined in table 8.2 and the weight determined 300 min after the temperature was adjusted from 100 °C back to RT. ΔM_{max} is the maximum rate of the weight gain, as determined from a (very good) linear fit over at least 50 measurements. R^2 is approximately 1 for all samples.

The time at which the temperature is set back to room temperature (RT) is defined as t_1, and the weight gain at t_1 + 300 min compared to M_{min} is taken as the maximum value, M_{max}. Though all samples attain a higher true maximum, this is strongly influenced by fluctuations in the RH. The maximum rate is determined from a linear fit using at least 50 data points. The slow linear absorption kinetics observed are probably due to the rather slow temperature response in the oven, see figure 8.2. The temperature approaches the set temperature (RT) only after 5 h, compared to less than 15 min for the up-ramping RT → 100 °C for the desorption data.

Moisture adsorption data is presented in table 8.3. While there are no significant differences between the alumina qualities studied here, there is obviously a strong dependence on the RH as shown in figures 8.7 and 8.8. Since the weight gain is linear with time in most of the time interval there is also a strong correlation between the measured data for the maximum absorption rate ΔM_{max} and M_{max}.

With reference to fig. 8.2, the desorption data in table 8.2 appear to support the finding that, at a relatively stable temperature below approx. 80 °C, the moisture content in SGA is primarily a function of the ambient RH, in agreement with the study by Hyland *et al.* [66].

8.4.2 Rapid Absorption

While key data and details of the experimental conditions are given in table 8.4, the initial absorption kinetics data is best presented in fig. 8.9. ΔM_{max}

[1]See chapter 5, alumina quality.

[2]Data for weight loss obtained in chapter 4, "Agglomeration Part I", by drying samples of primary and secondary alumina over night at 200 °C giving 0.4 ± 0.1 wt % for primary and 1.3 ± 0.1 wt % for secondary alumina A respectively.

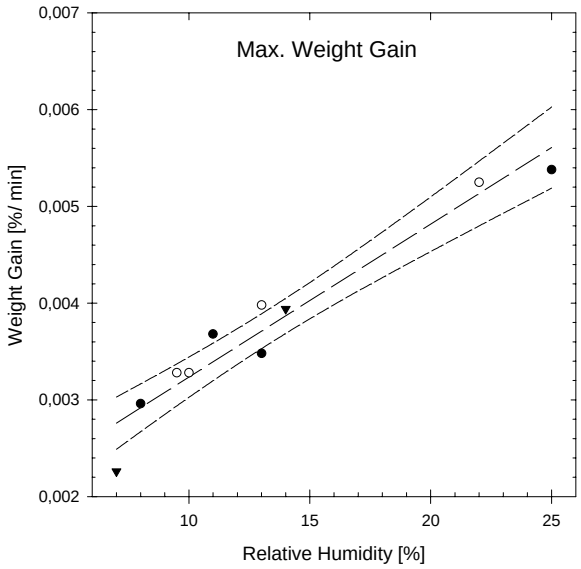

Figure 8.7: *Maximum rate of absorption (weight gain) of samples as determined by linear regression fit of 50 data points after* t_1. *Lin. regr. with 95 % confidence intervals.*

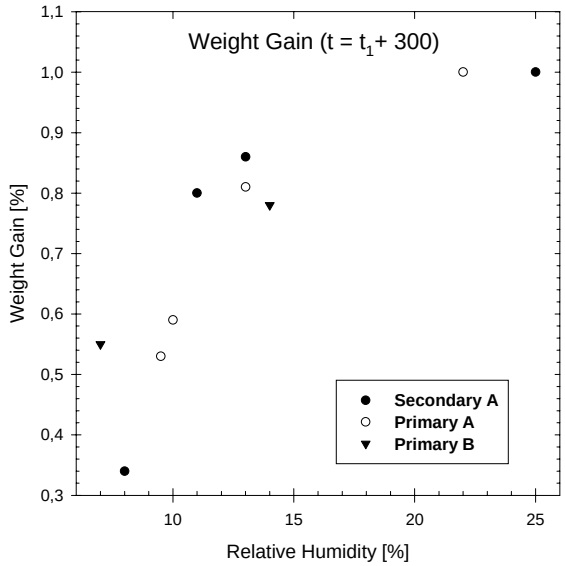

Figure 8.8: *The maximum weight gain of all samples as determined after 300 min after* t_1. *No longer linear correlation.*

Table 8.4: *Initial Absorption Kinetics Data.* ΔM_{max} *is the maximum rate of the weight gain determined from a linear fit over the first 3 measurements, i. e. during the first 2 min of exposure.*

Sample	$M_{0,alumina}$ [g]	$M_{container}$ [g]	$SA_{alumina}$ (est.) [cm^2]	M_{max}-M_0 [%]	ΔM_{max} [$\%/min$]
PA-A1	1.32	9.11	8.6	1.18	0.119
PA-A2	1.32	9.13	8.6	1.13	0.162
Average				1.16	0.141
PA-B1	16.04	53.49	31.2	0.59	0.081
PA-B2	14.06	53.09	28.6	0.70	0.095
Average				0.65	0.088
PA-C	26.58	4.68	38.4	0.25	0.023

is the maximum rate of the weight gain determined from a linear fit over the first 3 data points, i. e. during the first 2 min of exposure to ambient air.

Only primary alumina quality A was used, and the samples are denoted [Primary][Alumina A]-[Sample geometry A, B or C][exp. #]. $M_{0,alumina}$ is the starting weight of the alumina sample, and $M_{container}$ is the weight of the alumina sample container, of Pt, glass and Al respectively. $SA_{alumina}$ is the estimated apparent sample surface area of the SGA. For geometry B, the available geometric surface area is cone-shaped, and only a rather rough estimate is stated, based on the mass of alumina and typical angle of repose ($\sim$40 °). M_{max}-M_0 is the weight difference between the starting weight and the sample weight determined after 15 min of exposure to the ambient on the micro-balance.

The recorded RH value was fairly stable at 24.1 ± 0.5 % during the data collection period, but no effect of possible RH variations could be noted during a single experiment sequence. For the sample with Al box container, i. e. geometry C in table 8.4, the response is linear over 5 min intervals. The absorption rate for that sample geometry decreases to 0.012 % per min for 10< t< 15 min, which is about half the initial rate of 0.023 %/min (table 8.4). For comparison, the absorption rate for similar samples in the controlled temperature experiments varied with RH at around 0.004 wt %/min, while the desorption rate for primary alumina A was higher, by an order of magnitude, at 0.039 %/min at 100 °C, see table 8.2. It may be

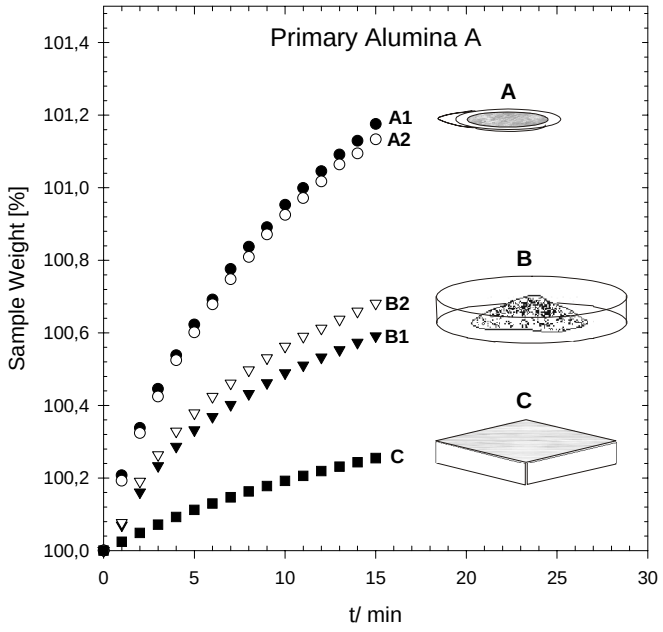

Figure 8.9: *The initial weight gain of samples during quench after removal from furnace at 150 °C to the ambient of the micro-balance at room temperature. There is a large effect of sample mass and geometry.*

concluded that the slow thermal response in the controlled experiment is responsible for the slow absorption kinetics observed in table 8.3.

Sample geometry A is most relevant for the agglomeration study reported in chapter 5. We obtain a weight gain, i. e. moisture absorption, equivalent to nearly 1 wt % during only 10 min exposure to the ambient, 0.6 wt % after 5 min and 0.2 wt % after 2 min respectively. The absorption levels must be less for samples held at 200 °C, in containers similar to geometry B and C. For comparison, Hyland *et al.* [66] measured initial changes of the moisture content in their 1 g SGA samples in excess of 0.03 wt %/min, and in one case changed by 1.3 wt % in 10 min, under isothermal conditions, by varying the RH.

By quenching the samples, as done in the present study, we obtain absorption kinetics data comparable to (but differing by a factor of 2) the desorption kinetics in the controlled temperature experiment, table 8.2, indicating that the mechanisms are similar. For moisture diffusion in these

samples, the driving force should be a function of the concentration gradient and equilibrium conditions of the surroundings, temperature and relative humidity, and also the sample thickness and available sample surface area.

Unfortunately, the effect of the available sample surface area is confounded with the thermal effect of a relatively high heat capacity (high total mass to sample mass ratio) in the samples with a higher available surface area. Our data show a linear dependence of the desorption kinetics with respect to the mass ratio of the alumina sample compared to the total mass, sample container included, as may be expected if thermal effects are important. However, in this study there is also a linear relationship between the observed absorption kinetics and the ratio of the available geometric surface area of the sample to the sample mass. The two effects could probably be separated in future work, perhaps by first effectively quenching the samples in a dessicator before the adsorption kinetics are measured.

8.4.3 Further Work

The simple experimental approach chosen for the present study has considerable potential. In particular, it would be interesting to further explore the differences between various SGA qualities, also for the rapid absorption kinetics study. The topic of SGA nanostructure, pore size distribution and moisture content warrants further study.

As SGA is sensitive to ambient moisture, it has been shown that care must be taken to handle each alumina sample according to a fixed procedure, and to standardize the geometry and exposure conditions for any major study. Obviously, the variations with RH recorded here show that a controlled atmosphere should be used, though systematic RH data recording is also very helpful. The effect of RH was only explored over a narrow, low range in this study- and should be further pursued.

Work continues at Hydro Aluminium to study the effects of moisture absorption and handling of SGA.

8.5 Conclusion

Desorption/ absorption kinetics is shown to be a function of the surroundings, the relative humidity and temperature, but also of the alumina quality. In particular, at 100 °C, the data shows markedly slower desorption

for secondary alumina A compared to the primary, unreacted alumina A, which must be attributed to HF-OH bonding. The desorption kinetics are slower still for primary alumina B, and the total weight loss is at 0.56 wt% compared to 0.98 wt% for alumina A. The different desorption kinetics for SGA A and B, having similar specific surface areas (BET), may be due the different pore- and nano-structures, as discussed in chapter 5.

Starting at 100 °C, and approaching room temperature, the absorption kinetics does not vary significantly among the alumina qualities in this study, probably due to relatively slow cooling of the samples. There is, however, a pronounced variability of the absorption kinetics as a function of the RH, at temperatures less than about 80 °C.

It appears that if SGA (smelter grade alumina) retains a temperature of 80 °C or more, then moisture adsorption is not significant under conditions comparable to those in this study. This is an important finding, and supports the experimental approach chosen for the laboratory experiments conducted in chapter 5. Variations in the MOI of alumina should be minimized if alumina is maintained at least at this temperature.

The alumina sample geometry affects the absorption kinetics, which are probably sensitive to both the water diffusion and heat transfer conditions. In this study the effect of the available surface area is confounded with the thermal effect of a relatively high heat capacity.

Acknowledgments We are grateful for the assistance provided by the Light Metals Division of the Hydro Research Center in Porsgrunn, in particular Jørn Tonheim and Kjell Hamberg, who where responsible for the experimental set-up and gave some helpful advice.

Bibliography

[1] Encyclopædia Britannica Online. Feb:, 2001.

[2] Z. Akdeniz, Z. Cicek, G. Pastore, and M.P. Tosi. Ionic clusters in aluminium-sodium fluoride melts. *Modern Physics Letters B*, 12[23]:995–1002, 1998.

[3] B. Allais. Alumina quality: Smelters experience with fluctuating and out of bound alumina: Point feeding and side break technologies, environmental and other costs to a smelter when using out of specifications alumina. *Fourth International Alumina Quality Workshop, Darwin, NT, Australia*, pages 9–20, 1996.

[4] J. Anwar. Analysis of time-resolved powder diffraction data using a pattern-decomposition method with restraints. *J. Appl. Cryst.*, 26:413–421, 1993.

[5] P.A. Badkar and J.E. Bailey. The Mechanism of Simultaneous Sintering and Phase Transformation in Alumina. *J. Mater. Sci.*, 11:1794–1806, 1976.

[6] A.N. Bagshaw, G. Kuschel, M.P. Taylor, S.B. Tricklebank, and B.J. Welch. Effect of operating conditions on the dissolution of primary and secondary (reacted) alumina powders in electrolytes. *Light Metals 1985*, pages 649–659, 1985.

[7] A.N. Bagshaw and B.J. Welch. The influence of alumina properties on its dissolution in smelting electrolyte. *Light Metals 1986*, pages 35–39, 1986.

[8] R.B. Bagwell and G.L. Messing. Effect of seeding and water vapor on the nucleation and growth of α-Al_2O_3 from γ-Al_2O_3. *J. Am. Cer. Soc.*, 82[4]:825–832, 1999.

[9] O. M. Bakkerud, J. A. Larsen, and B. Lillebuen. Evaluation of alumina quality parameters. *Third International Alumina Quality Workshop, Hunter Valley, NSW, Australia*, pages 48–67, 1993.

[10] T.R. Barton, T.J. Bastow, J.S. Hall, B.J. Robson, and M.E. Smith. Flash calcination of alumina: An NMR perspective. *Light Metals 1995*, pages 71–74, 1995.

[11] R.B. Bird, W.E. Steward, and E.N. Lightfoot. *Transport Phenomena*. John Wiley & Sons Inc., New York, NY, 1960.

[12] O. Bjørseth, O. Herstad, and J. L. Holm. On the physical and thermodynamic stability of solid sodium tetrafluoroaluminate. *Acta Chemica Scandinavica*, A40:566–571, 1986.

[13] J. Block and J.W.D. Lau. Thermally conductive elestomer containing alumina platelets. *United States Patent number 5,137,959*, pages 1–6, 1992.

[14] M. Bruno, O. Herstad, and J. L. Holm. Stability and structure of sodium tetrafluoroaluminate, $NaAlF_4$. *Acta Chem. Scan.*, 52:1399–1401, 1998.

[15] M. Bruno, O. Herstad, and J. L. Holm. Calorimetric investigations of some phases in the system sodium fluoride- aluminium fluoride. *J. Therm. Anal. Cal.*, 56:51–57, 1999.

[16] A.H. Carim, N.R. Dando, S.-Y. Tzeng, C.L. Rohrer, and A.J. Perotta. Conversion of diaspore to corundum: A new α-alumina transformation sequence. *J. Am. Cer. Soc.*, 80[10]:2677–80, 1997.

[17] T.J. Carnheim and D.J. Green. Mechanical properties of dry-pressed alumina green bodies. *J. Am. Cer. Soc.*, 84[7]:1405–1410, 2001.

[18] R. Clift, J.R. Grace, and M.E. Weber. *Bubbles, Drops and Particles*. Academic Press, New York, San Francisco and London, 1978.

[19] R.L. Coble. Initial sintering of alumina and hematite. *J. Am. Cer. Soc.*, 41[2]:55–62, 1958.

[20] M.P. García Coque, M.A. Llavona, J.M. Ayala, L.F. Verdeja, and J.P. Sancho. New trends in characterizing industrial bayer aluminas. *J. of Metals*, November:20–21, 1990.

[21] K. Daimon and E. Kato. Morphology of corundum crystallized by heating mixture of $\eta - Al_2O_3$ and AlF_3. *J. of Crystal Growth*, 75:348–352, 1986.

[22] T. J. Davies and A. E. Mercer. Bulk density. *Third International Alumina Quality Workshop, Hunter Valley, NSW, Australia*, pages 186–99, 1993.

[23] N.H. de Leeuw and S.C. Parker. Effect of chemisorption and physisorption of water on the surface structure and stability of α-alumina. *J. Am. Cer. Soc.*, 82[11]:3209–3216, 1999.

[24] Z. Deng, T. Fukasawa, and M. Ando. Microstructure and mechanical properties of porous alumina ceramics fabricated by the decomposition of aluminum hydroxide. *J. Am. Cer. Soc.*, 84[11]:2638–2644, 2001.

[25] Z. Deng, T. Fukasawa, M. Ando, G.-J. Zhang, and T. Ohji. High-surface-area alumina ceramics fabricated by the decomposition of $Al(OH)_3$. *J. Am. Cer. Soc.*, 84[3]:485–491, 2001.

[26] A. Derdacka-Grzymek, Z. Konik, A. Stok, and J. Iwanciw. The MgF_2 and AlF_3 influence on α-Al_2O_3 formation as well as form and size of grains in calcination process. *Light Metals 1990*, pages 115–119, 1990.

[27] S.A. Deshpande, T. Bhatia, H. Xu, N.P. Padture, A.L. Ortiz, and F.L. Cumbrera. Microstructural evolution in Liquid-Phase-Sintered SiC: Part II, Effects of planar defects and seeds in the starting powder. *J. Am. Cer. Soc.*, 84[7]:1585–1590, 2001.

[28] E.R. Dougherty. *"Probability and Statistics", For the engineering, computing, and physical sciences.* Prentice-Hall International, Inc., Englewood Cliffs, N.J., USA, 1990.

[29] EAA. Supply and demand primary aluminium markets up to 2003. *http://www.aluminium.org/downloads/Primaryoct2001.pdf*, Feb:, 2002.

[30] ESRF. ESRF highlights 2000, "time-resolved study of grain growth in nanocrystalline Fe". *http://www.esrf.fr/info/science/highlights/2000/ materials/MAT6.html*, Feb:, 2002.

[31] A. Faure and R. Bachelard. Macrocrystalline α-alumina hexagonal platelets. *United States Patent number 5,296,085*, pages 1–6, 1994.

[32] K. Fossheim. Private communication, NTNU.

[33] G. Foster, G. Power, and G. Yaxley. Recent developments in standard procedures for the analysis and testing of smelter grade alumina. *Fourth International Alumina Quality Workshop, Darwin, NT, Australia*, pages 43–50, 1996.

[34] P.A. Foster. Phase diagram of a portion of the system Na_3AlF_6-AlF_3-Al_2O_3. *J. Am. Cer. Soc.*, 58[7-8]:288–291, 1975.

[35] Y.R. Gan, Z.S. Gao, A.L. Zhang, and J. Thonstad. Multifunctional sensor for use in aluminium cells. *Light Metals 1995*, pages 233–241, 1995.

[36] S. Gautier, E. Champion, and D. Bernache-Assollant. Processing, microstructure and toughness of Al_2O_3 platelet-reinforced hydroxyapatite. *J. Eur. Cer. Soc.*, 17:1361–69, 1997.

[37] J. Gerlach, M. Henning, and K. Kern. The dissolution of aluminium oxide in cryolite melts. *Met. Trans. B*, 6B:83–86, 1975.

[38] J. Gerlach and G. Winkhaus. Interactions of alumina with cryolite-based melts. *Light Metals 1985*, pages 301–313, 1985.

[39] R.M. German. *Sintering Theory and Practice*. John Wiley & Sons, Inc., New York, 1996.

[40] C. Giacovazzo, editor. *Fundamentals of Crystallography*. Oxford University Press, Walton Street, Oxford, 1995.

[41] A.R. Gillespie, M.M. Hyland, and J.B. Metson. The surface chemistry of secondary alumina from the dry scrubbing process. *Light Metals 2000*, pages 345–350, 2000.

[42] S.J. Glass and D.J. Green. Permeability and infiltration of partially sintered ceramics. *J. Am. Cer. Soc.*, 82[10]:2745–2752, 1999.

[43] J.I. Goldstein, editor. *Scanning Electron Microscopy and X-ray Microanalysis*. Plenum Press, New York, 1992.

[44] G.N. Gopienko. Formation of $\alpha - Al_2O_3$ in the presence of Alf_3. *Inorg. Mater. (Eng. Transl. from Izvestiya Akademii Nauk SSSR, Neorganicheskie Materialy)*, 8[4]:681–682, 1972.

[45] G.N. Gopienko, T.A. Zavaritskaya, and O.I. Arakelyan. Changes in the physico-chemical properties of aluminium oxide during the calcination of hydrargillite and boehmite. *Sov. J. Non Ferrous Met. (Tsvetnye Metally)*, 13[3]:32–33, 1972.

[46] A.P. Goswami, S. Roy, M.K. Mitra, and G.C. Das. Impurity-dependent morphology and grain growth in liquid-phase-sintered alumina. *J. Am. Cer. Soc.*, 84[7]:1620–1626, 2001.

[47] D.J. Green. Comment on "correlation between surface area reduction and ultrasonic velocity in sintered zinc oxide powders". *J. Am. Cer. Soc.*, 81[6]:1698, 1998.

[48] C. Greskovich and K.W. Lay. Grain growth in very porous Al2O3 compacts. *J. Am. Cer. Soc.*, 55[3]:142–146, 1971.

[49] K. Grjotheim, C. Krohn, M. Malinovský, K. Matiašovský, and J. Thonstad. *Aluminium Electrolysis, Fundamentals of the Hall-Héroult Process, 2nd Edition.* Aluminium-Verlag, Düsseldorf, Germany, 1982.

[50] Ø.T. Gustavsen, T. Haarberg, H. Mediaas, and T. Østvold. Heat conductivity of alumina sintered at varying temperatures with varying concentrations of $NaAlF_4$. *Ninth Intl. Symp. "Light Metals Production", Hurtigruta, Norway, 1997*, pages 31–43, 1997.

[51] K. Hamberg. Aluminakvalitet. Kvantitativ analyse av mellomfaser i alumina. Sammenligning mellom litteraturdata og diffraktogrammer av kommersielle kvali- av gamma og delta-alumina. *Rapport, Doc. nr. 89C.FW1, Hydro Forskningssenter Porsgrunn*, Okt. 16:, 1989.

[52] K.R. Han, C.S. Lim, M.-J. Hong, J.W. Jang, and K.S. Hong. Preparation method of submicrometer-sized α-alumina by surface modification of γ-alumina with alumina sol. *J. Am. Cer. Soc.*, 83[4]:750–54, 2000.

[53] P. Hartman. The attachment Energy as a Habit Controlling Factor. *J. of Crystal Growth*, 49:166–170, 1980.

[54] S. Hashimoto and A. Yamaguchi. Formation of porous aggregations composed of Al_2O_3 platelets using potassium sulfate flux. *J. Eur. Cer. Soc.*, 19:335–339, 1999.

[55] W.E. Haupin and W.C. McGrew. See-through hall-heroult cell. *Light Metals 1974*, pages 37–47, 1974.

[56] R.G. Haverkamp, J.B. Metson, M.M. Hyland, and B.J. Welch. Adsorption of hydrogen fluoride on alumina. *Surface and Interface Analysis*, 19:139–144, 1992.

[57] R.G. Haverkamp and B.J. Welch. Modelling the dissolution of alumina powder in cryolite. *Chem. Eng. Processing*, 37:177–187, 1998.

[58] R.G. Haverkamp, B.J. Welch, S. Bouvet, and P. Homsi. Alumina quality testing procedure. *Light Metals 1997*, pages 119–126, 1997.

[59] R.G. Haverkamp, B.J. Welch, and J.B. Metson. The influence of fluorination on the dissolution rate of alumina in smelter electrolyte. *Light Metals 1994*, pages 365–70, 1994.

[60] R.F. Hill and R. Danzer. Synthesis of Aluminium Oxide Platelets. *J. Am. Ceram. Soc.*, 84[3]:514–520, 2001.

[61] J. Hlaváč. Reactivity of solids in high temperature processes. *In "Sintering Key Papers", editors S. Somiya and Y. Moriyoshi, Elsevier Applied Science, London and New York*, 1987.

[62] D.S. Horn and G.L. Messing. Anisotropic grain growth in TiO_2-doped alumina. *Mater. Sci. Eng.*, A195:169–178, 1995.

[63] R. Hovland, S. Rolseth, and A. Solheim. On the alumina dissolution in cryolitic melts. *Proc. of the Intl. Symp. on Light Metals Processing and Applications, Quebec City, Quebec, Canada. August 29-September 1.*, pages 3–16, 1993.

[64] L.K. Hudson. Alumina production. *In Series "Production of Aluminium and Alumina", ed. A.R. Burkin, John Wiley & Sons, Chichester*, pages 11–46, 1987.

[65] L.M. Hunt and R.G. Haverkamp. Determination of the phases of alumina in quenched cryolite melts using X-ray powder diffraction crystallography. *Unpublished work, Massey University, NZ*, pages 1–6, 1999.

[66] M.M. Hyland, A.R. Gillespie, and J.B. Metson. Predicting moisture content on smelter grade alumina from measurement of the water isotherm. *Light Metals 1997*, pages 113–117, 1997.

[67] M.M. Hyland, J.B. Metson, R.G. Haverkamp, and B.J. Welch. Surface studies of hydrogen fluoride adsorption on alumina. *Light Metals 1992*, pages 1323–1327, 1992.

[68] M. D. M. Innocentini, C. Ribeiro, L. R. M. Bittencourt, and V. C. Pandolfelli. Fluid dynamics and thermal aspects of the dewatering of high-alumina refractory castables: Removal of physically absorbed water. *J. Am. Cer. Soc.*, 84, No. 11:2696–2698, 2001.

[69] ISO. ISO 803-1976(E): Aluminium oxide primarily used for the production of aluminium- determination of loss of mass at 300 °c (conventional moisture). Technical report, International Organization for Standardization, 1976.

[70] ISO. ISO 806-1976(E): Aluminium oxide primarily used for the production of aluminium- determination of loss of mass at 1000 °c and 1200 °c. Technical report, International Organization for Standardization, 1976.

[71] L.A. Issaeva, P.V. Poliakov, V.A. Blinov, I.G. Mikhalev, and V.I. Buzunov. Rates of dissolution of commercial aluminas with different physical properties. *Light Metals 1998*, pages 507–512, 1998.

[72] R.K. Jain, M.P. Taylor, S.B. Tricklebank, and B.J. Welch. A study of the relationship between the properties of alumina and its interaction aluminium smelting electrolytes. *1^{st} Intl. Symp. Molten Salt Chem. and Tech. , Kyoto, Japan*, pages 59–64, 1983.

[73] R.K. Jain, S.B. Tricklebank, B.J. Welch, and D.J. Williams. A study of the relationship between the properties of alumina and its interaction aluminium smelting electrolytes. *Light Metals 1983*, pages 59–64, 1983.

[74] D.D. Jayaseelan, N. Kondo, M.E. Brito, and T. Ohji. High-stregth porous alumina ceramics by the pulse electric current sintering technique. *J. Am. Cer. Soc.*, 85[1]:267–269, 2002.

[75] A.R. Johnson. Alumina crusting and dissolution in molten electrolyte. *JOM*, 3:63–68, 1982.

[76] T.J. Johnston and N.E. Richards. Correlation between alumina and properties of crust. *Light Metals 1983*, pages 623–639, 1983.

[77] I.S. Kachanovskaya, V.I. Osovik, and T.N. Kukhotkina. Phase transformations and alumina dissolution in cryolite. *Tsvet. Met. (translated)*, 44:40–42, 1971.

[78] H. Kao and W. Wei. Kinetics and microstructural evolution of heterogeneous transformation of θ-alumina to α-alumina. *J. Am. Cer. Soc.*, 83[2]:362–368, 2000.

[79] T. Kathrina and R.D. Rawlings. Acoustic studies of the effect of SiC particle reinforcement on the compaction alumina powder. *J. Eur. Cer. Soc.*, 17:1157–1166, 1997.

[80] R. Keller. Alumina dissolution and sludge formation. *Light Metals 1984*, pages 513–518, 1984.

[81] M. Kheiri, J. Gerlach, U. Hennig, and R. Kammel. Bildung und verhalten von krusten sowie boden-schlamm bei der aluminium- reduktionselektrolyse. *Erzmetall*, 40[3]:127–131, 1987.

[82] M. Kheiri, U. Hennig, and R. Kammel. Krustungbildung und krusteneigenschaften beim einsatz sekundärer aluminiumoxide für die aluminium- reduktionselektrolyse. *Metallwissenschaft+Technik*, 43[9]:858–862, 1989.

[83] A. Kidron, R.J. De Angelis, and P.J. Reucroft. Particle-size distribution of NiO in coprecipitated NiO-Al_2O_3 powders. *J. Appl. Phys.*, 48[12]:5296–5300, 1977.

[84] H.P. Klug and L.E. Alexander. *"X-ray Diffraction Procedures", For Polycrystalline and Amorphous Materials.* John Wiley & Sons, Inc., New York, 1959.

[85] O. Kobbeltvedt, S. Rolseth, and J. Thonstad. On the mechanism of alumina dissolution with relevance to point feeding aluminium cells. *Light Metals 1996*, pages 421–427, 1996.

[86] Ove Kobbeltvedt. *Dissolution kinetics for alumina in cryolite melts. Distribution of alumina in the electrolyte of industrial aluminium cells.* PhD thesis, NTNU, Institutt for teknisk elektrokjemi., 1997.

[87] T. Kogure. Dehydration sequence of gibbsite by electron-beam irradiation in a TEM. *J. Am. Cer. Soc.*, 82[3]:716–720, 1999.

[88] C.M. Kong and J.J. Lannutti. Effect of agglomerate size distribution on loose packing fraction. *J. Am. Cer. Soc.*, 83[9]:2183–2188, 2000.

[89] V.N. Kuklina, É.A. Levitskii, L.M. Plyasova, and V.I. Zharkov. The role of a mineralizer in the polymophic transition of aluminium oxide. *Kinetika i Kataliz (Translated)*, 13[5]:1269–1274, 1972.

[90] G.I. Kuschel and B.J. Welch. Further studies of alumina dissolution under conditions similar to cell operation. *Light Metals 1991*, pages 299–305, 1991.

[91] H. Kvande. The structure of alumina dissolved in cryolitic melts. *Light Metals 1986*, pages 451–459, 1986.

[92] H. Kvande and K. Grjotheim. Operation/process control of alumina reduction cells.

[93] S. Kwon and G.L. Messing. Sintering of mixtures of seeded boehmite and ultrafine α-alumina. *J. Am. Cer. Soc.*, 83[1]:82–88, 1999.

[94] V. Lacassagne, C. Bessada, B. Ollivier, D. Massiot, P. Florian, and J.-P. Coutures. Étude de la transtition solide/liquide de la cryolithe par résonance magnétique nucléaire de ^{27}Al, ^{23}Na et ^{19}F. *C.R. Acad. Sci. Paris*, 325[Série II]:91–98, 1997.

[95] F.F. Lange. Sinterability of Agglomerated Powders. *J. Am. Cer. Soc.*, 67[2]:83–89, 1983.

[96] J.I. Langford and D. Louër. Powder diffraction. *Rep. Prog. Phys.*, 59:131–234, 1996.

[97] H. Ledbetter, S. Kim, M. Dunn, Z. Xu, S. Crudele, and W. Kriven. Elastic constants of mullite containing alumina platelets. *J. Eur. Cer. Soc.*, 21:2569–2576, 2001.

[98] C. Legros, C. Carry, P. Bowen, and H. Hoffman. Sintering of a transition alumina: Effects of phase transformation, powder characteristics and thermal cycle. *J. Eur. Cer. Soc.*, 19:1967–78, 1999.

[99] L.N. Less. The crusting behavior of smelter aluminas. *Met. Trans. B*, 8B:219–225, 1977.

[100] I. Levin and D. Brandon. Metastable alumina polymorphs: Crystal structures and transition sequences. *J. Am. Cer. Soc.*, 81[8]:1995–2012, 1998.

[101] I. Levin, W.D. Kaplan, D.G. Brandon, H. Mullejans, and M. Ruhle. Phase boundaries among the metastable precursor phases to alpha-Al_2O_3. *Mater. Sci. forum*, 207-209:749–752, 1996.

[102] W. Limper, J. Ihringer, K. Knorr, W. Prandl, and T. Wroblewski. Particle size determination from multiwavelength powder diffraction at a synchrotron radiation source. *Nucl. Instr. Meth. Phys. Res.*, A316:437–441, 1992.

[103] J.-D. Lin and J.-G. Duh. The use of X-ray line profile analysis to investigate crystallite size and microstrain for zirconia powders. *J. Mater. Sci.*, 32:5779–5790, 1997.

[104] J.-D. Lin and J.-G. Duh. Crystallite size and microstrain of thermally aged low-ceria-and low yttria-doped zirconia. *J. Am. Cer. Soc.*, 81[4]:853–860, 1998.

[105] B.C. Lippens and J.H. de Boer. Study of phase transformations during calcination of aluminium hydroxides by selected area electron diffraction. *Acta Cryst.*, 17:1312–1321, 1964.

[106] X. Liu, S.F. George, and V.A. Wills. Effect of alumina phase structure on its dissolution in cryolitic melt. *Third International Alumina Quality Workshop, Hunter Valley, NSW, Australia*, pages 213–222, 1993.

[107] X. Liu, S.F. George, and V.A. Wills. Visualisation of alumina dissolution in cryolitic melts. *Light Metals 1994*, pages 359–364, 1994.

[108] M.A. Llavona, L.F. Verdeja, R. Zapico, F. Alvarez, and J.P. Sancho. Density, hardness and thermal conductivity of hall-heroult crusts. *Light Metals 1990*, pages 429–437, 1990.

[109] C.-K. Loong, J.W. Richardson Jr., and Masakuni Ozawa. Structural phase transformations of rare earth modified transition alumina to corundum. *J. of Alloys and Compounds*, 250:356–359, 1997.

[110] Lorentz Petter Lossius. *Removing Impurities from Secondary Alumina*. PhD thesis, NTH, Institutt for uorganisk kjemi., 1991.

[111] P. Lossius and H.A. Øye. Removing impurities from secondary alumina fines. *Light Metals 1992*, pages 249–258, 1992.

[112] H. Maeda, S. Matsui, and A. Era. Measurement of dissolution rate of alumina in cryolite melt. *Light Metals 1985*, pages 763–780, 1985.

[113] L.P. Martin and M. Rosen. Correlation between surface area reduction and ultrasonic velocity in sintered zinc oxide powders. *J. Am. Cer. Soc.*, 80[4]:839–846, 1997.

[114] V. Massardier, R. Fougeres, and P. Merle. Mechanical properties of aluminium-based metal matrix composites reinforced with α-alumina platelets. *J. de Physique IV*, 3[nov]:703–708, 1993.

[115] J.L. McArdle and G.L. Messing. Transformation, microstructure development, and densification in α-Fe_2O_3-seeded boehmite-derived alumina. *J. Am. Cer. Soc.*, 76[1]:214–22, 1993.

[116] I.C. McColm and N.J. Clark. *High-Performance Ceramics*. Blackie and Son, Glasgow and London, 1988.

[117] J. M. McHale, A. Novrotsky, and A. J. Perrotta. Effects of increased surface area and chemisorbed H_2O on the relative stability of nanocrystalline γ-Al_2O_3 and α-Al_2O_3. *J. Phys. Chem. B*, 101:603–13, 1997.

[118] C. Misra. *Industrial Alumina Chemicals, ACS Monograph 184*. American Chemical Society, Washington, DC, 1986.

[119] C. Morterra and G. Magnacca. A case study: surface chemistry and surface structure of catalytic aluminas, as studied by vibrational spectroscopy of adsorbed species. *Catalysis Today*, 27:497–532, 1996.

[120] B.P. Moxnes, B.E. Aga, and J.H. Skaar. How to obtain open feeder holes by installing anodes with tracks. *Light Metals 1998*, pages 247–255, 1998.

[121] R.G. Munro. Effective medium theory of the porosity dependence of bulk moduli. *J. Am. Cer. Soc.*, 84[5]:1190–92, 2001.

[122] D. Neesen-Drack, J. Lay, R. Shaw, and W. Thomas. Laboratory and plant studies of alumina containing smelter dusts. *Fourth International Alumina Quality Workshop, Darwin, NT, Australia*, pages 77–85, 1996.

[123] C. E. Nelson, J. W. Elam, M. A. Cameron, M. A. Tolbert, and S. M. George. Desorption of H_2O from a hydroxylated single-crystal α-Al_2O_3 (0001) surface. *Surf. Sci.*, 416:341–53, 1998.

[124] F. Noguchi, T. Nakamura, Y. Ueda, and T. Yanagase. Mechanisms of Al_2O_3 dissolution into cryolite melt. *1st Intl. Symp. Molten Salt Chem. and Tech. , Kyoto, Japan*, pages 13–16, 1983.

[125] E. Nonnet, N. Lequeux, P. Boch, S.L. Colston, and P. Barnes. *In Situ* X-ray diffraction and Young's modulus measurement during heat treatment of high-alumina cement castables. *J. Am. Cer. Soc.*, 84[3]:583–587, 2001.

[126] M.J. O'Brien and B.W. Sheldon. Porous alumina coating with tailored fracture resistance for alumina composites. *J. Am. Cer. Soc.*, 82[12]:3567–3574, 1999.

[127] R. Oedegard, S. Roenning, S. Rolseth, and J. Thonstad. Crust formation in aluminium cells. *J. of Metals*, 11:25–28, 1985.

[128] B.J. Oh, Y.J. Lee, D.J. Choi, G.W. Hong, J.Y. Park, and W.J. Kim. Fabrication of Carbon/Silicon Carbide Composites by Isothermal Chemical Vapor Infiltration, Using the *in situ* Whisker-Growing and Matrix-Filling Prosess. *J. Am. Cer. Soc.*, 84[1]:245–247, 2001.

[129] B. Ollivier, R. Retoux, P. Lacorre, D. Massiot, and G. Frérey. Crystal structure of κ-Al_2O_3: An X-ray powder diffraction, TEM and NMR study. *J. Mater. Chem.*, 7[6]:1049–1056, 1997.

[130] D. Olsen. Alumina dustiness related to physical quality parameters-user experience and R&D in Hydro Aluminium. *Fifth International Alumina Quality Workshop, Bunbury, WA, Australia*, pages 1–11, 1999.

[131] D. Østling. Private communication, SINTEF. 1999.

[132] T. Østvold. Private communication, NTNU. 1999.

[133] T. Østvold, Ø.T. Gustavsen, and H. Mediaas. Sintering and heat conductivity of alumina. *Light Metals 1997*, pages 127–131, 1997.

[134] H. Øye. Materials used in aluminium smelting. *Light Metals 2000*, pages 3–15, 2000.

[135] E.C. Patterson, M.M. Hylland, V. Kielland, and B.J. Welch. Understanding the effects of the hydrogen content of anodes on hydrogen fluoride emissions from aluminium cells. *Light Metals 2001*, pages 365–370, 2001.

[136] G. Pezzotti, H. Okuda, N. Muraki, and T. Nishida. *In-Situ* determination of bridging stresses in Al_2O_3/Al_2O_3-platelet composites by fluorescence spectroscopy. *J. Eur. Cer. Soc.*, 19:601–608, 1999.

[137] A. Pinoncely and K. Tsouria. FCB flash calcination technology: Ten years performances. *Light Metals 1995*, pages 113–120, 1995.

[138] Z. Qiu, Z. Yang, B. Bingliang, Z. Wang, S. Sun, and W. Li. Dissolution of alumina in molten cryolite (A video recording study). *Light Metals 1999*, pages 467–471, 1999.

[139] N.E. Richards. Alumina in smelting. *Presented during "The 20th International Course on Process Metallurgy of Aluminium"*, pages 511–561, 2001.

[140] N.E. Richards, S. Rolseth, J. Thonstad, and R.G. Haverkamp. Electrochemical analysis of alumina dissolved in cryolite melts. *Light Metals 1995*, pages 391–404, 1995.

[141] D.W. Richerson. *Modern Ceramic Engineering, Second Edition Revised and Expanded*. Marcel Dekker Inc., New York, Basel and Hong Kong, 1992.

[142] G.I.D. Roach and J.B. Cornell. Alumina and hydrate-unmasking their mysteries, eight years on. *Fourth International Alumina Quality Workshop, Darwin, NT, Australia*, pages 1–8, 1996.

[143] G.I.D. Roach, J.B. Cornell, and A. Antonovsky. Hydrate and alumina-unmasking their mysteries. *"Smelter Grade Alumina for the 1990's and Beyond". An International Alumina Quality Workshop, Gladstone, QLD, Australia*, pages 137–148, 1988.

[144] G.I.D. Roach, J.B. Cornell, D.Y. Li, and B.H. O'Connor. Quantifying alumina phases in smelter-grade alumina by X-ray diffraction. *Second International Alumina Quality Workshop, Perth, WA, Australia*, pages 209–223, 1990.

[145] G.I.D. Roach and G. Reid. Flowability of smelting grade alumina. *"Smelter Grade Alumina for the 1990's and Beyond". An International Alumina Quality Workshop, Gladstone, QLD, Australia*, pages 186–96, 1988.

[146] R.K. Roeder, K.P. Trumble, and K.J. Bowman. Microstructure development in Al_2O_3-platelet-reinforced Ce-ZrO_2/Al_2O_3 composites. *J. Am. Cer. Soc.*, 80[1]:27–36, 1997.

[147] S. Rolseth, R. Hovland, and O. Kobbeltvedt. Alumina Agglomeration and Dissolution in Cryolitic Melts. *Light Metals 1994*, pages 351–357, 1994.

[148] S. Rolseth, S. Rønning, A. Solheim, J. Thonstad, and R. Ødegård. Non-conventional methods for alumina testing. *Aluminium*, 62[4]:286–290, 1986.

[149] S. Rolseth and J. Thonstad. Agglomeration and dissolution of alumina. *Proc. of the Intl. Symp. on Extraction, Refining and Fabrication of Light Metals, Ottawa, Ontario, Canada. August 18-21.*, pages 177–190, 1991.

[150] Jørn Lone Rutlin. *Chemical reactions and mineral formation during sodium aluminium fluoride attack on aluminiosilicate and anorthite based refractories*. PhD thesis, NTNU, Institutt for uorganisk kjemi., 1998.

[151] K.Å. Rye, M. Köingsson, and I. Solberg. Current redistribution among individual anode carbons in a hall-heroult prebake cell at low alumina concentration. *Light Metals 1998*, pages 241–46, 1998.

[152] K.Å. Rye and A. Solheim. Thermal conductivity of alumina and crust measurements and model. *CIM, Proc. Intl. Symp. "Light Metals Processing and Applications", Quebec, 1993*, pages 29–43, 1993.

[153] K.Å. Rye, J. Thonstad, and X. Liu. Heat transfer, thermal conductivity, and emissivity of Hall-Heroult top crust. *Light Metals 1995*, pages 441–449, 1995.

[154] Ketil Ålstedt Rye. *Crust Formation in Cryolite Based Baths.* PhD thesis, NTH, Institutt for teknisk elektrokjemi., 1992.

[155] Y. Saito, T. Takei, S. Hayashi, A. Yasumori, and K. Okada. Effects of Amorphous and Chrystalline SiO_2 Additives on γ-Al_2O_3-to-α-Al_2O_3 Phase Transitions. *J. Am. Cer. Soc.*, 81[8]:2197–2200, 1998.

[156] H. Schaper and L.L. van Reijen. A quantitative investigation of the phase transformation of gamma to alpha alumina with high temperature DTA. *Thermochimica Acta*, 77:383–393, 77.

[157] C.H. Schilling, V.J.Garcia, and R.M. Smith. Ultrasonic and Mechanical Behavior of Green and Partially Sintered Alumina: Effects of Slurry Consolidation Chemistry. *J. Am. Cer. Soc.*, 81[10]:2629–2639, 1998.

[158] C.A. Shacklee and G.L. Messing. Growth of α-Al_2O_3 platelets in the HF-γ-Al_2O_3 system. *J. Am. Cer. Soc.*, 77[11]:2977–2984, 1994.

[159] P.K. Sharm, M.H. Jilavi, D.Burgard, R. Nass, and H. Schmidt. Hydrothermal Synthesis of Nanosize α-Al_2O_3 from Seeded Aluminum Hydroxide. *J. Am. Cer. Soc.*, 81[10]:2731–2734, 1998.

[160] R.A. Shelleman and G.L. Messing. Liquid-phase-assisted transformation of seeded γ-alumina. *J. Am. Cer. Soc.*, 71[5]:317–322, 1988.

[161] T.W. Simpson, Q. Wen, N. Yu, and D.R. Clarke. Kinetics of the Amorphous $\rightarrow \gamma \rightarrow \alpha$ Transitions in Aluminum Oxide: Effect of Crystallographic Orientation. *J. Am. Cer. Soc.*, 81[1]:61–66, 1998.

[162] S. Skirl, R. Krause, S.M. Wiederhorn, and J. Rödel. Processing and mechanical properties of Al_2O_3/Ni_3Al composites with interpenetrating network microstructure. *J. Am. Cer. Soc.*, 84[9]:2034–2040, 2001.

[163] E. Skybakmoen, A. Solheim, and Å. Sterten. Alumina solubility in molten salt systems of interest for aluminium electrolysis and related phase diagram data. *Met. Mater. Trans. B*, 28B:81–86, 1997.

[164] P.J. Slikkerveer, H. in't Veld, M. Verspui, B. de With, and D. Reefman. Alumina particle degradation during solid particle impact on glass. *J. Am. Cer. Soc.*, 83[9]:2263–2266, 2000.

[165] R.L. Smith, G.S. Rohrer, and A.J. Perrotta. Influence of diaspore seeding and chloride concentration on the transformation of "diasporic" precursors to corundum. *J. Am. Cer. Soc.*, 84[8]:1896–1902, 2001.

[166] K. Sohlberg, S. J. Pennycook, and S. T. Pantelides. Hydrogen and the structure of the transition aluminas. *J. Am. Chem. Soc.*, 121:7493,7499, 1999.

[167] S. Soled. Gamma-Al_2O_3 viewed as a defect oxyhydroxide. *J. of Catal.*, 81:252–257, 1983.

[168] A. Solheim and S. Rolseth. Some surface and interfacial phenomena encountered in aluminium electrolysis. *Light Metals 2001*, pages 469–474, 2001.

[169] A. Solheim and Å. Sterten. Activity of alumina in the system NaF-AlF_3-Al_2O_3 at NaF/AlF_3 molar ratios ranging from 1.4 to 3. *Light Metals 1999*, pages 445–452, 1999.

[170] H. Song and R.L. Coble. Morphology of platelike abnormal grains in liquid-phase-sintered alumina. *J. Am. Cer. Soc.*, 73[7]:2086–90, 1990.

[171] H. Song and R.L. Coble. Origin and growth kinetics of platelike abnormal grains in liquid-phase-sintered alumina. *J. Am. Cer. Soc.*, 73[7]:2077–85, 1990.

[172] H. Song, R.L. Coble, and R.J. Brook. Applicability of Herring's Scaling Law to the Sintering of Powders. *In "Sintering and Heterogeneous Catalysis", edited by G.C. Kuczynski, A.E. Miller and G.A. Sargent, Plenum Press, New York*, pages 63–80, 1984.

[173] D. Syltevik, B. Lillebuen, and J.A. Larsen. Alumina quality-user perspective. *Fourth International Alumina Quality Workshop, Darwin, NT, Australia*, pages 21–31, 1996.

[174] H. t. Wang, X. q. Liu, F. l. Chen, G. y. Meng, and O.T. Sørensen. Kinetics and machanism of a sintering process for macroporous alumina ceramics by extrusion. *J. Am. Cer. Soc.*, 81[3]:781–784, 1998.

[175] P. Thompson, D.E. Cox, and J.B. Hastings. Rietveld refinement of debye-scherrer synchrotron x-ray data from Al_2O_3. *J. Appl. Cryst.*, 20:79–83, 1987.

[176] J. Thonstad, P. Fellner, G.M. Haarberg, Ján Híveš, H. Kvande, and Å. Sterten. *Aluminium Electrolysis, Fundamentals of the Hall-Héroult Process, 3rd Edition*. Aluminium-Verlag, Düsseldorf, Germany, 2001.

[177] J. Thonstad, P. Johansen, and E.W. Kristensen. Some properties of alumina sludge. *Light Metals 1980*, pages 227–239, 1980.

[178] J. Thonstad and Y.-X. Liu. *Light Metals 1981*, pages 303–312, 1981.

[179] J. Thonstad, F. Nordmo, and J.B. Paulsen. *Met. Trans.*, 3:403–408, 1972.

[180] J. Thonstad, A. Solheim, S. Rolseth, and O. Skar. The dissolution of alumina in cryolite melts. *Light Metals 1988*, pages 655–660, 1988.

[181] I.I.M. Tijburg, H. De Bruin, P.A. Elberse, and J.W. Geus. Sintering of pseudo-boehmite and γ-Al_2O_3. *J. of Mater. Sci.*, 26:5945–49, 1991.

[182] L. Tikasz, R.T. Bui, V. Potocnik, and M. Barber. Simulation of different alumina feeding strategies on a training workstation. *Proc. of the Intl. Symp. on Extraction, Refining and Fabrication of Light Metals, Ottawa, Ontario, Canada. August 18-21.*, pages 329–338, 1991.

[183] A. Tonejc, A.M. Tonejc, and D. Bagovi c. Comparison of the transformation sequence from γ-AlOOH (boehmite) to α-Al_2O_3 induced by heating and by ball milling. *Mater. Sci. Eng.*, A181/A182:1227–1231, 1994.

[184] K. Tørklep, K. Kalgraf, and T. Nordbø. Alumina distribution in point-fed Hall-Héroult cells. *Light Metals 1997*, pages 377–387, 1997.

[185] D.W. Townsend and L.G. Boxall. Crusting behaviour of smelter aluminas. *Light Metals 1984*, pages 649–665, 1984.

[186] D.S. Tucker. Gamma-to-alpha transformation in spherical aluminum oxide powders. *J. Am. Cer. Soc.*, 68[7]:C163–C164, 1985.

[187] Ž. Lubyová and V. Daněk. Control mechanism for alumina dissolution in cryolite melts. *Chem. Papers*, 49[2]:59–63, 1995.

[188] Ž. Lubyová and V. Daněk. Empirical equation for the dissolution rate of alumina in cryolite melts. *Aluminium*, 71[3]:346–349, 1995.

[189] Ž. Živković, N. Štrbac, and J. Šestác. Influence of fluorides on polymorphous transformation of α-Al_20_3 formation. *Thermochimica Acta*, 266:293–300, 1995.

[190] A. Vázquez, T. López, R. Gómez, Bokhimi, A. Morales, and O. Novaro. X-ray diffraction, FTIR, and NMR characterization of sol-gel alumina doped with lanthanum and cerium. *J. of Solid State Chem.*, 128:161–168, 1997.

[191] T.A. Venugopalan. Experiences with gas suspension calciner alumina. *"Smelter Grade Alumina for the 1990's and Beyond". An International Alumina Quality Workshop, Gladstone, QLD, Australia*, pages 53–66, 1988.

[192] J.D. Verhoeven. *Fundamentals of Physical Metallurgy.* John Wiley & Sons, New York, 1975.

[193] A. Viola, R. Baratti, and A. Teodosi. Analysis and simulation of the alumina calcination process. *Light Metals 1986*, pages 179–189, 1986.

[194] N. Wai-Poi and B.J. Welch. Comparing alumina specification and smelter expectations in cells. *Light Metals 1994*, pages 345–350, 1994.

[195] David I. Walker. *Alumina in Aluminium Smelting and its Behaviour After Addition to Cryolite-Based Electrolytes.* PhD thesis, University of Toronto, 1993.

[196] D.I. Walker, T.A. Utigard, and W.P. Taylor. Alumina agglomerates in aluminum smelters. *Light Metals 1995*, pages 425–434, 1995.

[197] X. Wang. Alumina dissolution in cryolitic melts: A literature review. *CIM: Light Metals 2000 Métaux Légers, Proceedings*, pages 41–54, 2000.

[198] Y.G. Wang, P.M. Bronsveld, J.Th.M. DeHosson, B. Djuričić, D. McGarry, and S. Pickering. Ordering of octahedral vacancies in transition aluminas. *J. Am. Cer. Soc.*, 81[6]:1655–1660, 1998.

[199] B.E. Warren. X-ray studies of deformed metals. *Prog. Metal Phys.*, 8:147–202, 1959.

[200] K. Wefers and C. Misra. "oxides and hydroxides of aluminum", techn. paper no. 19, revised. Technical report, Alcoa Laboratories, 1987.

[201] H.-L. Wen and F.-S. Yen. Growth characteristics of boehmite-derived ultrafine theta and alpha-alumina particles during phase transformation. *J. of Crystal Growth*, 208:696–708, 2000.

[202] E.A.D. White and J.D.C. Wood. The growth of highly perfect alumina platelets and other oxides by solvent vapour transport. *J. of Mater. Sci.*, 9:1999–2006, 1974.

[203] S.J. Wilson and J.D.C. McConnell. A kinetic study of the system γ-AlOOH/Al_2O_3. *J. of Solid State Chem.*, 34:315–322, 1980.

[204] G. Winkhaus. Gewüschte eigenschaften des aluminiumoxids für die elektrolyse. *Aluminium*, 6:593–602, 1988.

[205] M.A. Wójcik, T. Gajda, B. Meiners, K. Volker, J. Plewa, and H. Altenburg. High temperature modification of the morphology of corundum primary crystals of special alumina during calcination of aluminium trihydrate with mineralizers. *Light Metals 1998*, pages 205–209, 1998.

[206] C. Wolverton and K. C. Hass. Phase stability and structure of spinel-based transition aluminas. *Phys. Rev. B*, 63:1–16, 2000.

[207] H. Xu, T. Bhatia, S.A. Deshpande, N.P. Padture, A.L. Ortiz, and F.L. Cumbrera. Microstructural evolution in Liquid-Phase-Sintered SiC: Part I, Effect of starting powder. *J. Am. Cer. Soc.*, 84[7]:1578–1584, 2001.

[208] C.C. Yong and J. Wang. Mechanical-activation-triggered gibbsite-to-boehmite transition and activation-derived alumina powders. *J. Am. Cer. Soc.*, 84[6]:1225–30, 2001.

[209] Y. Yourdshahyan, C. Ruberto, M. Halvarsson, L. Bengtsson, V. Langer, I. Lundquist, S. Ruppi, and U. Rolander. Theoretical structure determination of a complex material: κ-Al_2O_3. *J. Am. Cer. Soc.*, 82[6]:1365–80, 1997.

[210] W. Zeng, L. Gao, L. Gui, and J. Guo. Sintering kinetics of α-Al_2O_3 powder. *Ceramics International*, 25:723–726, 1999.

[211] G.-D. Zhan, R.-J. Xie, M. Mitomo, and Y.-W. Kim. Effect of β-to-α phase transformation on the microstructural development and mechanical properties of fine-grained silicon carbide ceramics. *J. Am. Cer. Soc.*, 84[5]:945–950, 2001.

[212] R.-S. Zhou and R.L. Snyder. Structures and transformation mechanism of the η, γ and θ transition aluminas. *Acta Cryst.*, B47:617–630, 1991.

[213] Y. Zhou, J. Vleugels, T. Laoui, and O. Van der Biest. Toughening of x-sialon with Al_20_3 platelets. *J. Eur. Cer. Soc.*, 15:297–305, 1995.

APPENDIX

Appendix A

Alumina Quality

Table A.1: *Decoding of alumina quality, source identity.*

Code	Alumina Refinery
PA	Primary Suralco
SA	Secondary Suralco
PB	Primary Aughinish
PC	Primary Alunorte
PD	Primary Bauxilum/Interalumina
PE	Primary Aljam
SE	Secondary Aljam
PF	Primary Frigiua
SF	Secondary Frigiua

Table A.2: *Trace impurities of 9 SGAs (XRF)*

SGA [P/S], [A-F]	[Ti] "TiO_2" [%]	[V] "V_2O_5" [%]	[Zn] "ZnO" [%]	[Mn] "MnO" [%]	[Ni] "NiO" [%]	[Cu] "CuO" [%]	[Ga] "Ga_2O_3" [%]	[Pb] "PbO" [%]	[P] "P_2O_5" [%]
PB	0.001	0.002	0.002	0.001	-	-	-	-	0.001
PC	0.0035	0.0018	0.0027	0.0005	0.0009	0.0009	0.0084	0.0014	0.0006
PD	0.0037	0.0003	0.0004	0.0004	0.0009	0.001	0.0084	0.001	0.0005
PA	0.005	0.001	0.001	0.001	0.003	0.001	0.016	0.001	0.001
SA	0.004	0.001	0.001	0.0	0.008	0.003	0.016	0.002	0.003
PE	0.002	0.002	0.008	0.001	0.002	0.001	0.008	0.001	0.001
SE	0.001	0.005	0.008	0.001	0.002	0.004	0.008	0.003	0.005
PF	0.005	0.002	0.001	0.0	0.002	0.001	0.007	0.001	0.001
SF	0.005	0.003	0.001	0.0	0.009	0.001	0.008	0.004	0.008

Appendix B

Exploratory Tablet Agglomeration

Table B.1: *Preliminary Results from Qualitative "sintering" determination using secondary alumina in shallow Pt-crucibles, weight loss and qualitative sintering scale (I-IV) according to AKK/ [86]. Estimated "sinter-score" (0-10) based on the scale used in this study is also presented.*

Temp/Time [°C]/[min]	Sample Mass [g]	Mass loss [wt %]	Score AKK (I-IV)	Score NPØ (0-10)
700				
1	1.0029	0.87		0
2	1.0010	1.37		0
3	1.0042	0.43		0
5	1.0003	1.03		0
10	1.0015	0.38		0
Mean		0.8(4)		
20	1.0051	1.52		0
30	1.0035	0.44	I	2-4
30	2.0541	0.42	I	2-4
102	2.0852	1.24	I	2-4
800				
1	2.0030	1.46		0
2	2.0024	1.84		0
3	2.0047	1.75		0
5	2.0039	2.04		0
10	2.0032	1.53	I	2-4
Mean		1.7(2)		
21	2.0027	1.52	I	2-4
30	2.0014	0.44	II	∼5
34	2.0610	1.30	II	∼5
60	2.0452	0.46	II	∼5

Table B.2: *Preliminary Results from Qualitative "sintering" determination using secondary alumina in shallow Pt-crucibles, weight loss and qualitative sintering scale (I-IV) according to AKK/ [86]. Estimated "sinter-score" (0-10) based on the scale used in this study is also presented.*

Temp/Time [°C]/[min]	Sample Mass [g]	Mass loss [wt %]	Score AKK (I-IV)	Score NPØ (0-10)
900				
1	2.0026	1.02	I	1-3
2	2.0022	1.52	I	2-4
3	2.0045	NA	I	2-4
5	2.0060	2.29	I+	2-4+
10	2.0047	1.95	II-	4-5
Mean		1.7(5)		
950				
1	2.0184	1.16	II	2-4+
2	2.0019	NA	II	2-4+
3.33	2.0299	2.83	III-	7-8
5	2.0325	1.87	III-	7-8
10	2.0375	1.82	III	∼8
Mean		1.9(7)		
20	2.0074	2.19	III	∼8
1000				
1	2.1333	NA	III	7-8
2	2.0128	2.04	III	7-8
3	2.0569	2.27	III+	∼9
5	2.0273	2.48	III+	∼9
10	2.0602	2.66	IV	∼10
Mean		2.4(3)		

Appendix C

PearsonVII

A mathematical model function Φ must be used in order to fit single diffraction peaks according to the function;

$$y_{calc}(x_i) = \sum_j A_j \Phi(x_i - x_j) + b(x_i),$$

for every position x_i, where A_j is the calculated area of the j'th peak. For diffractograms with recorded intensity as a function of the scattering angle 2θ, x is defined as the distance $2\theta - 2\theta_0$ from the position of the maximum intensity. The Pearson VII function is given as,[96];

$$\Phi(x) = \Phi(0)\frac{1}{(1 + Cx^2)^m}$$

where m is the Pearson index, $\Phi(0)$ is the maximum intensity of the (lineless) background and w is the Full Width at Half Maximum intensity (FWHM) of the fitted peak. The other parameters are defined as;

$$\begin{aligned} C &= \frac{2^{1/m} - 1}{w^2} \\ w &= \beta(Ln2/\pi)^{1/2} \\ \beta &= \frac{\pi 2^{2(1-m)}\Gamma(2m-1)w}{(2^{1/m} - 1)[\Gamma(m)]^2} \end{aligned}$$

where L is the Lorentzian function given as;

$$\Phi(x) = \Phi(0)\frac{w^2}{(w^2 + x^2)}, \;\; \beta = \pi w$$

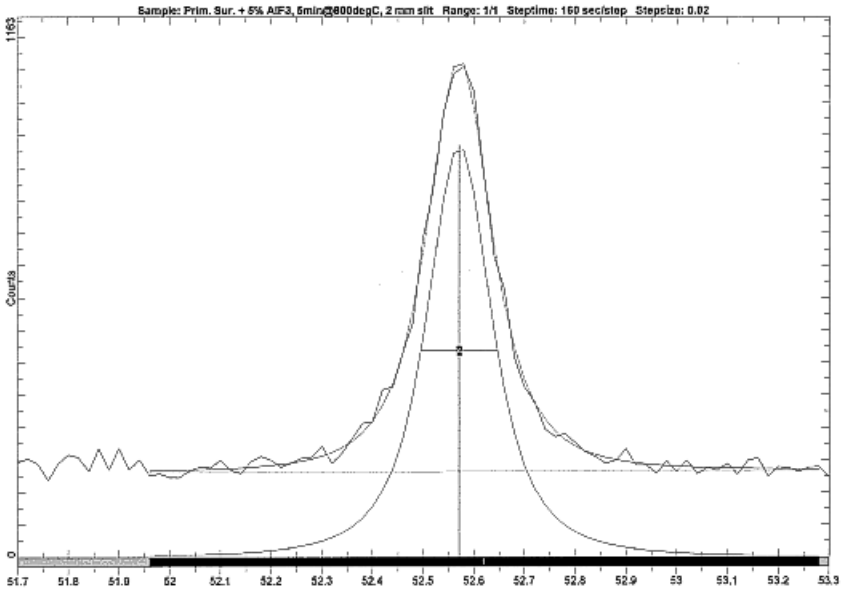

Figure C.1: *Sample Profile fit of the (024) α-Al_2O_3 peak using the Pearson VII function. Linear background is subtracted.*

The Pearson VII function is equivalent to L^m, and reduces to the Lorentzian function for m=1, while tending towards a Gaussian function as $m \to \infty$. The common Γ-function, defined for any $n > 0$, is given as;

$$\begin{aligned} \Gamma(n) &= \int_0^\infty x^{n-1} e^{-x} dx \\ &= \int_0^1 (ln\frac{1}{x})^{n-1} dx \end{aligned}$$

Appendix D

Crysize Output

```
WIN-CRYSIZE  Ver. 3.04 © Sigma-C GmbH 1991-97        Date: 27:11:01
             Siemens Analytical X-Ray Systems        Time: 17:10:35
Licensed to: Faculty of Chemistry and Biology, NTNU

Sample Name:   Peter's alpha Suralco, 2 mm
Sample File:   FWHM_024_1_7-9.dpf
Standard File: LaB6_20_100.PST
================================================================
```

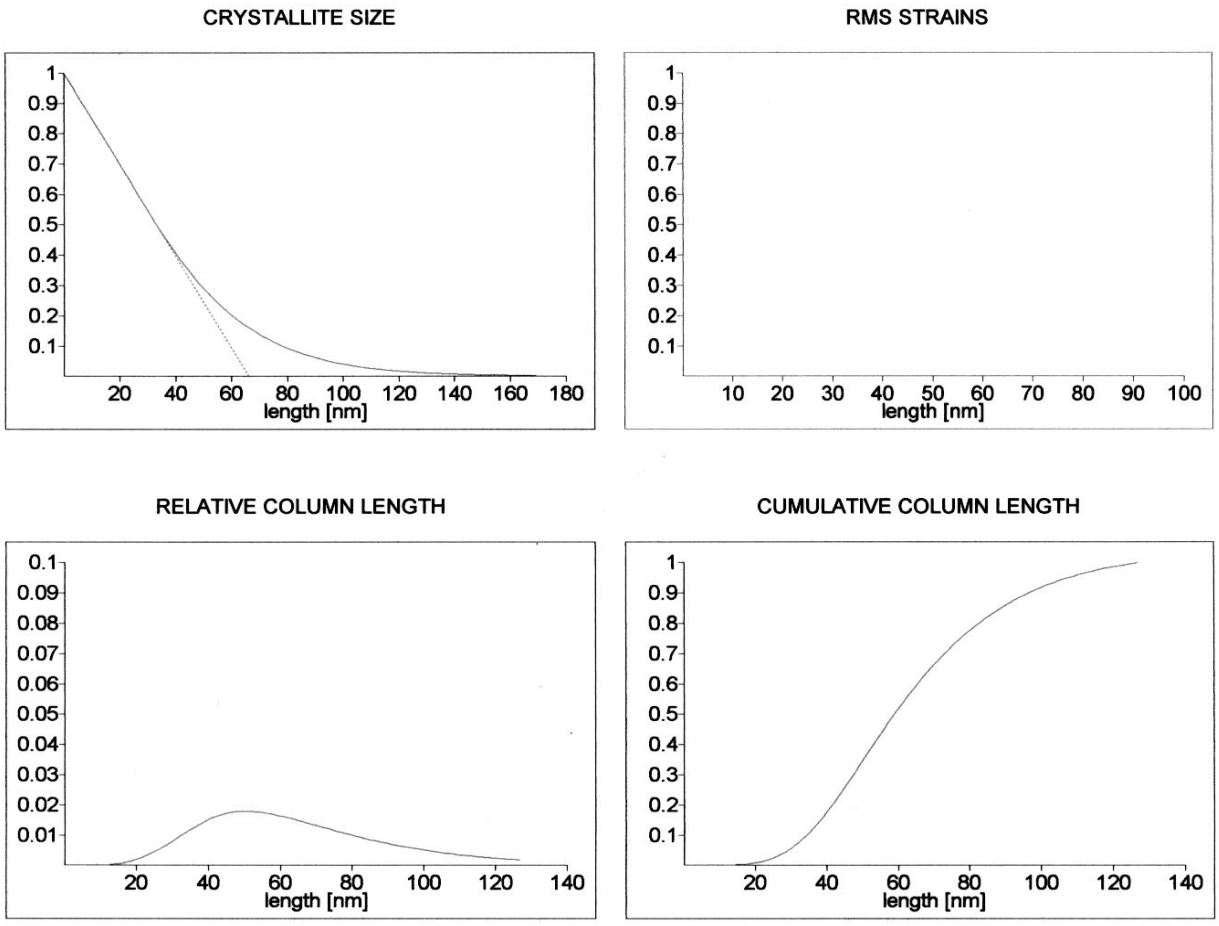

Figure D.1: *Sample output file from Crysize Line Profile Analysis Program.*